Mechanistic studies of H_2 oxidation and evolution catalysed by NiFe hydrogenase enzymes



Sophie Kendall-Price
Christ Church
Trinity Term 2022

A Thesis submitted to the Board of the Faculty of Physical Sciences, for the degree of Doctor of Philosophy, University of Oxford

Mechanistic studies of H_2 oxidation and evolution catalysed by NiFe hydrogenase enzymes

Sophie Kendall-Price, Christ Church, University of Oxford

A thesis submitted for the degree of Doctor of Philosophy, Trinity Term 2022

The complexity of metalloenzyme catalysis has led to the development of a range of techniques, broadly separated into those that probe activity, and those that provide structural information. However, reconciling data from each of these approaches is challenging due to the differences in the physical form of samples, and that most methods cannot simultaneously provide both structural insight and information on catalytic activity.

Two IR spectroelectrochemical techniques are utilised in this Thesis to provide insight into the catalytic mechanism of [NiFe]-hydrogenases.

In situ protein film infra electrochemistry bridges the gap between activity- and spectroscopic-based measurements and has revealed that the rate determining step in H^+/H_2 catalysis is different for the O_2-tolerant Hyd-1 and O_2-sensitive Hyd-2.

A technique is developed which combines single crystal IR spectroscopy with electrochemical control to unify structural and spectroscopic information of metalloenzymes. With this technique, a complete redox characterisation of single crystals of *E. coli* Hyd-1 is described, demonstrating that proton transfer equilibria and electron transfer redox equilibria are maintained *in crystallo*. Thus the crystalline state can be thought of as a dynamic system, much like in solution.

Studies on single crystals of *E. coli* Hyd-2 provide evidence of the Ni_a-L species which was not conclusively identified before for Hyd-2. The observation of the Ni_a-C species in frozen solution converting into Ni_a-L upon illumination confirms the assignment of the Ni_a-L species in Hyd-2.

Overall this work highlights the necessity for utilising a variety of techniques when investigating metalloenzyme catalysis. The single crystal IR microspectroscopic-electrochemical technique developed in this Thesis will provide valuable opportunities for unifying the structural and spectroscopic insights on the catalytic mechanisms of hydrogenases and other metalloenzymes in the future.

Acknowledgements

There are so many people that without I would not have been able to accomplish this mountain of a degree.

My first and largest thanks must go to Kylie for allowing me to work in the Vincent group as both an MChem and DPhil student. Your guidance, encouragement and kindness has been unrivalled. It has been such a privilege to work with you.

My thanks also go to Phil who has been so kind to impart his vast scientific and practical knowledge during my time at Oxford. I can only hope to retain it all and pass it on.

Thank you Non for teaching me the ins and outs of protein preparations and for being someone I could always rely on if I needed help or just company. Thanks go to Steve as well for accompanying me through all the long protein preps and revealing to me the mysterious ways of protein crystallisation.

Thanks must of course be extended to the rest of the Vincent group for providing such a great atmosphere over the past 5 years. I'm sad to finally be leaving as I feel I have truly blossomed during my time at Oxford.

Sincere thanks to all my friends and family, both in Oxford and at home, for your unwavering support and motivation, particularly in the final few months. To my parents: you may never have exactly understood what I've been researching these past 5 years but that has never stopped you from encouraging me even when I was at my lowest and about to give up. Dad, thanks for being bossy when telling me to focus and for the endless cups of tea! Mum, I truly don't know where I'd be without you. This is just as much your success as it is mine. Thank you for everything. Special thanks to Rosie for always cheering me up and making me go out for a walk to get some fresh air every day. Not sure I would be sane if I didn't!

This Thesis is dedicated to my grandfather, Victor George Kendall

without whom I would have never discovered my love of chemistry or dreamed of attending Oxford, let alone walk in your footsteps at Christ Church. I am sorry I was unable to finish before you passed. You supported me unconditionally throughout my journey, and I know you will continue to do so in spirit.

Abbreviations

A. aeloicus/Aa	*Aquifex aeolicus*
Arg	arginine
CE	counter electrode
CV	cyclic voltammetry
Cys	cysteine
cyt*b*	cytochrome *b*
***D. vulgaris* MF/ *Dv*MF**	*Desulfovibrio vulgaris* Miyazaki F
delta TM	delta transmembrane
DFT	density functional theory
E. coli*. /*Ec	*Escherichia coli*
EPR	electron paramagnetic resonance
FTIR	fourier transform infrared
FWHM	full width half maximum
Hase	hydrogenase
IR	infrared
IRE	internal reflection element
MBH	membrane bound hydrogenase
OCP	open circuit potential
P. furiosus/Pf	*Pyrococcus furiosus*
PCET	proton coupled electron transfer
PFE	protein film electrochemistry
PFIRE	protein film infrared electrochemistry
R. eutropha/Re	*Ralstonia eutropha*
RE	reference electrode
Ser	serine
SH	soluble hydrogenase
SHE	standard hydrogen electrode
ν_{CN}	cyanide vibrational stretch
ν_{CO}	carbon monoxide vibrational stretch
WE	working electrode
XAS	x-ray absorption spectroscopy

Table of Contents

Chapter 1. Introduction 1

1.1. Techniques and challenges for studying metalloenzyme mechanisms 2

1.1.1. Current approaches: activity-based, spectroscopy-based, structure-based 2

1.1.2. Challenges faced in understanding metalloenzyme catalysis 6

1.1.3. Combining simultaneous activity measurements with structural and spectroscopic insight 7

1.2. [NiFe]-hydrogenases 8

1.2.1. Introduction 8

1.2.2. Classification 9

1.2.3. Structure 10

1.2.4. Catalytic mechanism 19

1.2.5. *Escherichia coli* [NiFe]-hydrogenases 21

1.3. Aims of this Thesis 23

1.4. References 25

Chapter 2. Experimental theory and methods 34

2.1. Infra-red spectroscopy 35

2.1.1. General principles 35

2.1.2. Sampling geometries 42

2.1.3. IR microspectroscopy 49

2.1.4. IR spectra of carbonyl and cyanide ligands 50

2.1.5. Data processing 55

2.2. Protein film electrochemistry 60

2.2.1. Redox reactions in enzymes 60

2.2.2. Principles of protein film electrochemistry 62

2.2.3. IR spectroelectrochemistry 69

2.3. Protein preparations 70

2.4. Crystallisation 71

2.4.1. Buffer solutions 71

2.4.2. Procedure 72

2.5. Protein film IR electrochemistry set-up 74

2.5.1. Reagents and equipment 74

2.5.2. Experimental procedure 76

2.6. IR microspectroscopic-electrochemical set-up 78

2.6.1. Reagents and equipment 78

2.6.2. Experimental procedure 80

2.7. IR cryo-spectroscopy set-up 83

2.7.1. Reagents and equipment 83

2.7.2. Experimental procedure 84

2.8. References 85

Chapter 3. Characterisation of Hyd-1 using PFIRE 89

3.1. IR spectroelectrochemical studies of [NiFe]-hydrogenases 90

3.1.1. Introduction 90

3.1.2. Inactive states 91

3.1.3. Active states 92

3.1.4. *E. coli* hydrogenase-1 95

3.2. Results and discussion 99

3.2.1. Redox states of Hyd-1 99

3.2.2. The effect of pH 113

3.2.3. Comparing O_2-tolerant and O_2-sensitive [NiFe]-hydrogenases under catalytic turnover 124

3.2.4. Conclusion 131

3.3. References 135

Chapter 4. Single crystal IR microspectroscopic-electrochemistry 140

4.1. Introduction 141

4.2. Method development 143

4.2.1. Previous designs and limitations 143

4.2.2. Cell design 145

4.2.3. Redox mediators 146

4.2.4. Experimental procedure 151

4.3. Spectroelectrochemical characterisation of Hyd-1 crystals 152

4.3.1. Initial characterisation 152
4.3.2. Detailed redox titrations 159
4.3.3. Comparison to other IR spectroelectrochemical techniques 177
4.4. Time-resolved experiments 181
4.4.1. Time-resolved IR spectroelectrochemistry of [NiFe] hydrogenases 181
4.4.2. Ni_a-L as a precursor to Ni_a-SI 182
4.4.3. Discussion 185
4.5. Summary 188
4.6. References 190
Chapter 5. Proton transfer equilibria within single crystals of Hyd-1 193
5.1. Introduction 194
5.2. Results and discussion 196
5.2.1. High pH 196
5.2.2. Low pH 206
5.3. Summary 210
5.4. References 211
Chapter 6. Comparing different preparations of Hyd-1 crystals 213
6.1. Introduction 214

6.2. The impact of the cytochrome *b* subunit 217

6.2.1. Initial characterisation 218

6.2.2. Oxidative titration 220

6.2.3. Discussion 225

6.3. Delta transmembrane Hyd-1 230

6.3.1. Initial characterisation 231

6.3.2. Electrochemical oxidation 234

6.3.3. Discussion 235

6.4. Summary 237

6.5. References 238

Chapter 7. Redox characterisation of O_2-sensitive Hyd-2 241

7.1. Introduction 242

7.2. Single crystal IR spectroelectrochemical characterisation 244

7.3. Investigating a new low wavenumber ν_{CO} species 248

7.4. Discussion and summary 250

7.5. References 252

Chapter 8. Conclusions and Outlook 254

Chapter 1. Introduction

1.1. Techniques and challenges for studying metalloenzyme mechanisms

1.1.1. Current approaches: activity-based, spectroscopy-based, structure-based

Metalloenzymes are ubiquitous throughout nature, catalysing biochemical reactions with high regio- and stereoselectivity.[1–3] Predominantly containing naturally abundant metals, their superior selectivity and efficiency results in metalloenzymes being used directly in biotechnology whilst also inspiring the design of artificial catalysts for sustainable industrial synthesis and energy production.[4] As such, understanding their structure, function and dynamics is crucial.

Approaches to studying metalloenzymes can be broadly separated into three fields: activity-based, spectroscopy-based, and structure-based. To obtain a complete understanding of complex metalloenzyme mechanisms, data from all three must be considered together. A brief overview of various techniques within each field is presented below.

1.1.1.1. Activity-based

Solution assays

Biochemical assays are the traditional way of measuring the catalytic activity of enzymes. By mixing substrate and enzyme in solution, the rate of substrate oxidation or reduction can be monitored by spectrophotometry either directly if the substrate absorbs light or indirectly with artificial electron acceptors/donors.[5,6]

Protein film electrochemistry (PFE)

By directly immobilising redox active proteins onto an electrode surface, catalytic activity can be controlled and measured electrochemically. This technique is known as protein film electrochemistry (PFE).[7,8] The enzyme can readily exchange electrons with the electrode

surface without necessarily the need for diffusion which allows the electron transfer properties of the system to be recorded in detail. Information including transitions between the catalytically active and inactive redox states, the onset and rate of catalysis, and the impact of inhibitors can be obtained by PFE. The principles behind PFE are discussed in Chapter 2.

1.1.1.2. Spectroscopy-based

There are a plethora of spectroscopic techniques that have been utilised to investigate metalloenzyme catalysis.

Infrared (IR) and Raman

Various aspects of metalloenzymes can be examined using IR and Raman spectroscopies. Several vibrational modes within the peptide backbone can be probed allowing the secondary structure of a metalloenzyme to be investigated.[9–11]

If a metalloenzyme contains species within its active site that are IR or Raman active, such as the CO and CN ligands in hydrogenases, or whose substrate/inhibitor is IR/Raman active, such as CO dehydrogenase, then IR/Raman spectroscopy can also provide information on the different redox states of the active site. If steady state catalysis is maintained throughout the spectroscopic measurement, then these redox species are likely to be catalytically relevant.[12] Furthermore, time-resolved methods can be utilised to monitor catalysis following initiation of a specific part of the catalytic cycle.[13]

IR spectroscopy is the primary technique used throughout this Thesis and its principles are discussed in more detail in Chapter 2.

Electron Paramagnetic Resonance (EPR)

Metalloenzymes that contain systems with one or more unpaired electrons can be studied using electron paramagnetic resonance spectroscopy. Briefly, this is achieved by examining the interaction of an external magnetic field with the unpaired electrons in the molecule. A variety of information can be obtained including the oxidation state and spin state of a metal, the reduction potentials of metalloclusters, and the interactions between metal centres within the metalloenzyme.[14] As such, EPR is a widely used technique to probe paramagnetic metals within metalloenzymes.

X-ray absorbance spectroscopy (XAS)

X-ray absorbance spectroscopy is a technique which provides insight on the oxidation state, ligand type and geometry of a metal centre. A major benefit of XAS is that EPR-silent paramagnetic states can be examined. One disadvantage of XAS for studying metalloenzymes, however, is that samples must be frozen to prevent photoreduction and damage caused by the high intensity x-ray beams that are required for long periods of time during measurements (more so for protein samples as they are often relatively dilute).

Mössbauer

Metalloenzymes that contain iron are often probed using Mössbauer spectroscopy to investigate the electronic structure, spin state and coordination sphere of the Fe ions.[15] Iron-sulfur clusters exhibit distinct Mössbauer signals due to their diverse electronic states and so this technique has often been used to detect individual clusters within multicluster enzymes along with monitoring their coordination.[16,17] However, experiments must be performed on either solid or frozen samples to ensure that the nuclei do not recoil upon

absorption and emission of the gamma radiation, and isotopic labelling of the Fe sites to ^{57}Fe is required.

Nuclear Resonance Vibrational Spectroscopy (NRVS)

When a synchroton source is used, fine vibrational structure coupled to Mössbauer nuclei, such as ^{57}Fe, can be resolved using nuclear resonance vibrational spectroscopy (NRVS). This technique allows more detailed analysis of metalloenzymes that contain iron-sulfur clusters, as well as the ability to characterise the strength of iron coordination in heme proteins.[18]

Similar to Mössbauer spectroscopy, isotopic labelling of Fe sites is required although samples can be either crystalline or in solution.

1.1.1.3. Structure-based

X-ray crystallography has long been an important tool in the structural characterisation of metalloproteins. By exposing a crystallised sample to an x-ray beam, the three-dimensional atomic arrangement of the sample can be extracted from the resulting diffraction pattern. As such, providing the metalloenzyme can be crystallised, obtaining the x-ray crystal structure is usually one of the first techniques performed.[19] However there are limitations to x-ray crystallography. Hydrogen atoms are not easily identifiable by x-ray diffraction: even with ultra-high resolutions (< 1 Å), highly polarised H atoms and protons are invisible to x-rays. Furthermore, the crystal structure obtained is not dynamic and thus does not necessarily represent the metalloenzyme as it is in solution.

1.1.1.4. Other approaches

Density functional theory (DFT) is a quantum mechanical method used to calculate the electronic structure of atoms and molecules. DFT can be utilised for analyses of

spectroscopic experiments whilst also predicting the electronic structures of active site species involved in metalloenzyme catalysis.[20] Thus it is a widely applicable and useful technique that can support other experimental methods.

Another established technique for aiding interpretation of metalloenzyme structure and activity is site directed mutagenesis. By selectively changing certain amino acid residues and then performing other analytical techniques, such as PFE, x-ray diffraction or FTIR spectroscopy to name a few, the role of the altered residue can be examined.[21–23]

It is not necessarily possible to investigate exchange every residue within a metalloenzyme with site directed mutagenesis as some mutants can result in either immature enzyme or no enzyme production at all.[24]

1.1.2. Challenges faced in understanding metalloenzyme catalysis

The main issue involved in collating data obtained using the various techniques described in the previous Section is that they are not all performed under the same conditions and state of metalloenzyme. X-ray crystallography requires crystalline samples whereas biochemical assays are generally performed on enzyme solutions. In PFE studies, on the other hand, enzyme samples are adsorbed onto an electrode. There is also variation in sample conditions, primarily temperature. Whilst some spectroscopic techniques can be carried out under ambient conditions, such as FTIR and Raman, other techniques including EPR and XAS are performed on frozen samples. There is a tacit assumption that these variations do not impact the catalytic properties of the metalloenzyme, i.e. features, such as the range of redox states, observed in solution or at ambient temperatures match those seen *in crystallo* or frozen samples, even if unobserved.

Essentially, most traditional methods for investigating metalloenzyme catalysis either focus on providing structural insight or information on catalytic activity, but not both

simultaneously. As a result, relating structural features observed by EPR, XAS, and x-ray crystallography to catalytically relevant states is challenging. One of the main hurdles in combining the two approaches is the difficulty of controlling turnover, as simply saturating a metalloenzyme with substrate does not necessarily replicate turnover conditions. Therefore *in situ* techniques that can monitor spectroscopic or structural changes whilst under turnover conditions are crucial in developing understanding of complex metalloenzyme mechanisms.

1.1.3. Combining simultaneous activity measurements with structural and spectroscopic insight

A field of research which has seen success in unifying various approaches to provide thorough mechanistic understanding is that of heterogeneous catalysis. There is a heavy emphasis on using *in situ* approaches where collection of spectra occurs under conditions relevant to catalytic operation, and *operando*, which combines *in situ* characterisation with simultaneous measurement of catalytic activity, when studying heterogeneous catalysis.[25–27] In fact, nowadays it is almost assumed that multiple *in situ*, or *operando*, characterisation methods are combined within a single experimental set-up.[28,29] Computational methods have also widely used in heterogeneous catalysis to aid mechanistic understanding and the development of new catalysts.[30] Scott and co-workers have emphasised the importance of benchmarking to assess different theoretical methods along with combining and comparing multiple *in situ* and *operando* experimental techniques applied to catalysis.[31]

A similarly wide range of approaches and techniques are not only available but required for an in depth understanding of enzymatic catalysis. Currently, there are few methods that can simultaneously measure or control catalytic activity along with spectroscopic or

structural measurements. In this Thesis, two IR spectroelectrochemical techniques that bridge the gaps between activity-, spectroscopy- and structural-based approaches are utilised. Protein film IR electrochemistry combines electrochemical control under turnover with infrared spectroscopic sampling.[12] The second method developed is single crystal IR microspectroscopic-electrochemistry. Whilst not providing direct information on catalytic activity, this method instead links traditional IR spectroscopic methods with electrochemical control over single crystals, uniting solid state and solution spectroscopic information.[32,33] The metalloenzymes studied using these two techniques are two well-characterised [NiFe]-hydrogenases from *Escherichia coli*. An overview of these enzymes, their function and known catalytic behaviour is discussed next.

1.2. [NiFe]-hydrogenases

1.2.1. Introduction

Molecular hydrogen has been used as a source of energy in nature for millions of years through the interconversion of H_2/H^+ (Equation [1.1]). The metalloenzymes known as hydrogenases are the biocatalysts that enable this process.[34,35]

$$H_2 \rightleftharpoons 2H^+ + 2e^- \qquad [1.1]$$

By using the naturally abundant metals iron and nickel, hydrogenases catalyse hydrogen oxidation and evolution with high turnover frequencies (> 1000 s^{-1}) coupled with low overpotentials under ambient conditions.[7,36] This ideal efficiency inspires the development of technologies that aim to harness H_2 as a renewable form of energy. Recent research has shown the application of hydrogenases in biocatalytic heterogeneous hydrogenations[37] and H_2/O_2 enzyme fuel cells.[38] Furthermore, studies to elucidate their mechanism promise fundamental insight into how to activate or form H_2 at cheap, non-noble metal catalyst

sites and thus pave the way for cheaper, bio-inspired synthetic catalysts for energy chemistry.

Hydrogenase enzymes can be classified into three categories based on the metals in their active sites: bimetallic nickel-iron [NiFe], mono-iron [Fe] and di-iron [FeFe]. [NiFe]-hydrogenases are widely abundant and more resilient to inhibition by O_2 and CO, and therefore are of high interest, despite their lower activity when compared to [FeFe]-hydrogenases.[36,39] This, and the fact that they are a widely studied and well-characterised group of metalloenzymes, makes [NiFe]-hydrogenases an ideal choice for a model metalloenzyme for developing new spectroelectrochemical techniques.

1.2.2. Classification

[NiFe]-hydrogenases are generally separated into 4 groups based on their full sequence alignments and cellular function[40]:

1. Membrane-bound respiratory H_2-uptake hydrogenases: hydrogen oxidation is linked to quinone reduction by the reduction of anaerobic electron acceptors such as fumarate, CO_2 or O_2. Examples include *W. succinogenes* [NiFe]-hydrogenase, *Escherichia coli* hydrogenase-2
2. Cytoplasmic cyanobacterial H_2-uptake (2a) and H_2-sensing (2b) hydrogenases: cyanobacterial uptake hydrogenases are linked to nitrogenases whereas H_2-sensing regulatory hydrogenases are involved in controlling hydrogenase gene transcription in response to H_2. Examples include *A. aeolicus* hydrogenase-3 (Group 2a), and *R. eutropha* H16 RH (Group 2b).
3. Cytoplasmic cofactor-coupled bidirectional hydrogenases: include subunits that can bind soluble cofactors such as F_{420}, NAD or NADP and function reversibly by using protons from water to re-oxidise cofactors under anaerobic conditions.

Examples include *M. marburgensis* F_{420}-reducing [NiFe]-hydrogenase (Group 3a), *P. furiosus* hydrogenase-1 (Group 3b)

4. Membrane-bound H_2-evolving respiratory hydrogenases: these multimeric enzymes remove excess electrons from the anaerobic oxidation of small organic compounds like CO or formate by reducing protons from water. Examples include *E. coli* hydrogenase-3, *R. rubrum* CO-induced hydrogenase

[NiFe]-hydrogenases can also be separated into two categories based on their response to O_2. The large majority of [NiFe]-hydrogenases function under anaerobic conditions *in vivo* and are inactivated in the presence of O_2. These 'standard', or O_2-sensitive, hydrogenases are inhibited by trace amounts (μM) of O_2 but can be slowly re-activated *via* reduction under anaerobic conditions.[41] However, several [NiFe]-hydrogenases have been found to maintain catalytic activity in the presence of O_2 and are often involved in aerobic respiration.[42] These enzymes are known as O_2-tolerant [NiFe]-hydrogenases.

The enzymes that are studied in this Thesis, *E. coli* Hyd-1 and Hyd-2, are both Group 1 [NiFe]-hydrogenases, but while Hyd-1 is classified as O_2-tolerant, Hyd-2 is a standard, O_2-sensitive [NiFe]-hydrogenase.

1.2.3. Structure

The basic unit of a [NiFe]-hydrogenase is an αβ heterodimer. The larger α-subunit contains the bimetallic [NiFe] active site and the smaller β-subunit contains the electron relay chain of iron-sulfur clusters that allow the transfer of electrons to and from the active site. Crystal structures of various [NiFe]-hydrogenases show that the main catalytic core is formed of a dimer of heterodimers, $(\alpha\beta)_2$, within the crystal unit cell. [43–49] Selective gas channels throughout the hydrogenase are also present, to allow the movement of substrates and products. Efficient removal of protons produced by H_2 cleavage is crucial

for a high turnover frequency. The exact mechanism of proton transfer has yet to be fully determined although various pathways have been proposed, which are discussed below (Section 1.2.4)

1.2.3.1. Active site

The large α-subunit contains the [NiFe] active site. The nickel and iron adopt different coordination geometries within the bimetallic cluster. The Ni is bound to four cysteine ligands (two of which bridge the Ni and Fe atoms) in a distorted see-saw geometry that promotes binding of H_2.[50] The Fe, on the other hand, adopts an approximate octahedral environment that allows binding to the two bridging thiolates and the three biologically unusual ligands, one CO and two CN. These ligands participate in hydrogen bonding with surrounding Ser and Arg amino acid residues.[36,51,52] The final coordination site around the Fe is left vacant and can be occupied by a third bridging ligand.[53] The Ni is the only redox active metal, with its oxidation state fluctuating between Ni(I), Ni(II) and Ni(III) during catalysis. The Fe, instead, remains in the low oxidation state Fe(II) throughout catalysis and is stabilised by the electron-accepting CO and CN ligands.

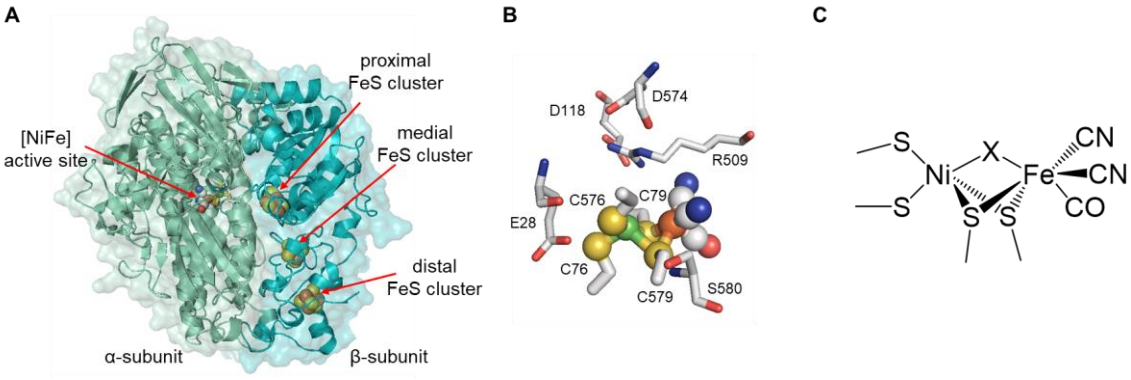


Figure 1.1 X-ray crystal structure of Hydrogenase 1 from *E. coli* (*E. coli* Hyd-1, PDB 3USE) in the as-isolated state. A: Arrangement of the α (large) and β (small) subunits, [NiFe] site and FeS clusters. B: [NiFe] active site with neighbouring cysteine (C), aspartic acid (D), arginine (R), serine (S) and glutamic acid (E) amino acid residues labelled C: Schematic representation of the [NiFe] active site. The bridging ligand X varies with the redox state of the [NiFe] hydrogenase. A and B were prepared using Pymol.

The [NiFe] active site can form a wide range of redox states, not all of which are part of the catalytic cycle. Multiple different spectroscopic and structural techniques have been used to identify the structure of the various active site redox species. An overview of these species is provided in Figure 1.2.

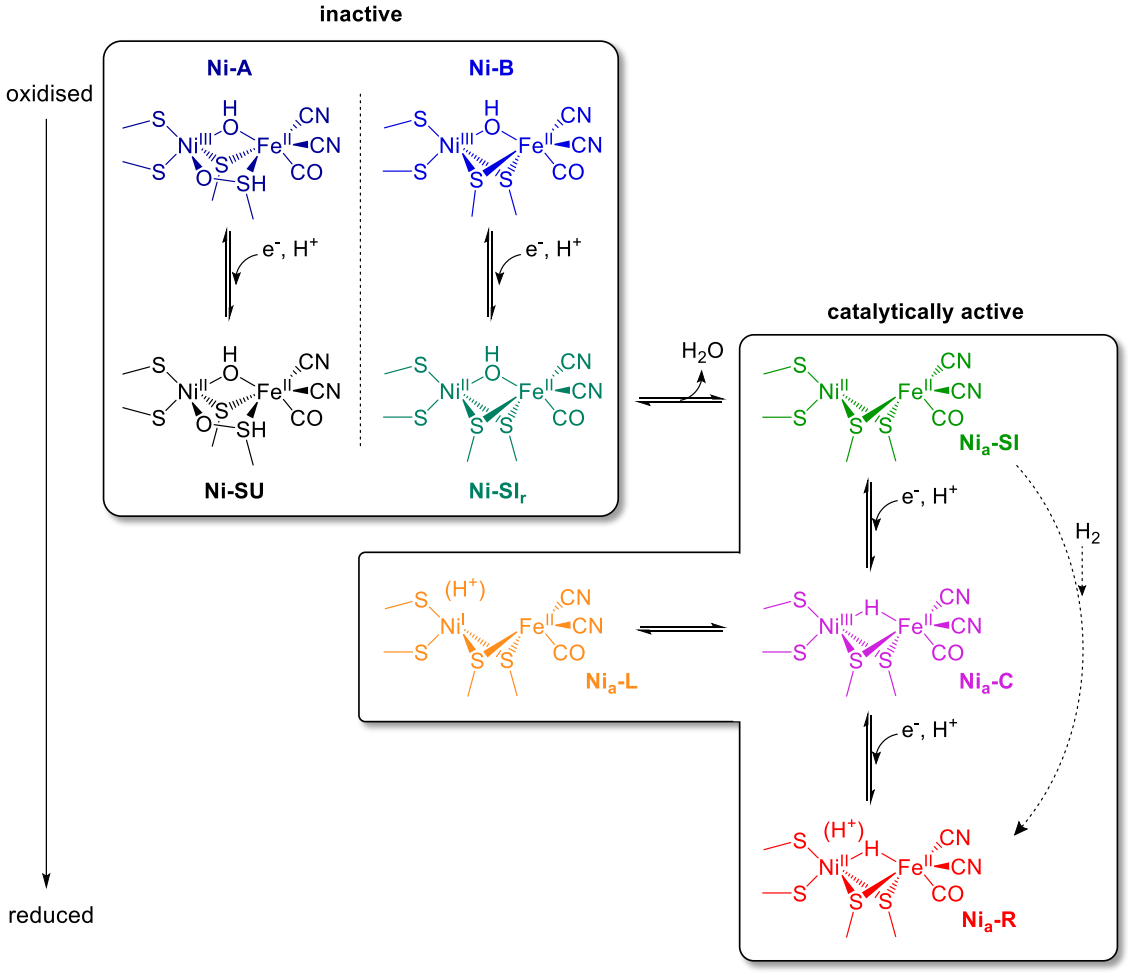


Figure 1.2 Overview of the active site redox states present in [NiFe]-hydrogenases (colour coding used throughout this Thesis. The states are ordered by redox level, with the most oxidised species at the top and the most reduced species at the bottom of the Figure. Inactive and catalytically active states are separated by two boxes for clarity. The subscript "a" signifies the state is catalytically active, while the subscript "r" represents a "ready" state, i.e., the species is inactive but on the same redox level as an active species which it can be activated into.

The inactive states

The two most oxidised active site redox states are the catalytically inactive Ni-A and Ni-B species. These species are formed upon exposure to O_2 and possess a paramagnetic $Ni^{III}Fe^{II}$ (S=½) active site. Whilst Ni-B has been confirmed to have a hydroxide bridging ligand,[54] there is still controversy over its identity in Ni-A. The most supported assignment

is a hydroxido bridging ligand, similar to Ni-B, alongside an oxygenated bridging cysteine coordinated to the Ni.[51,54,55] Due to their similar structures, it is difficult to distinguish between Ni-A and Ni-B using IR spectroscopy, although they do possess different *g*-tensors in EPR measurements and have vastly different rates of activation. Ni-A requires several hours to be reduced to a catalytically active species, whereas Ni-B can usually be reduced within a few minutes.[36]

One-electron reduction of the Ni-A and Ni-B species leads to the formation of the 'unready' Ni-SU and 'ready' Ni-SI_r states respectively.[56] These retain an oxygenic bridging ligand, which prevents the species from being active, but have a diamagnetic $Ni^{II}Fe^{II}$ active site. There is some debate as to whether the formation of the Ni-SI_r state is a concerted or step-wise proton-coupled electron transfer. One mechanism predicts the bridging ligand is protonated to H_2O either by transfer of a proton directly to the active site or through protonation of a Ni-coordinated cysteine.[57] Others suggest the Ni-SI_r species is in an acid-base equilibrium with a protonated version which has a loosely bound H_2O bridging ligand.[58–60] Recent DFT analysis has proposed the Ni-SU state has a terminal coordinated water molecule to the Fe atom with a modified coordination of Ni, along with the oxygenated Cys seen in Ni-A.[61] Slow activation of the Ni-SU state leads to the Ni-SI_r species. Subsequent release of a water molecule activates the hydrogenase and forms the catalytically active Ni_a-SI species.

The active states

The active site redox species that are known to participate in the catalytic cycle are called the 'active' states. In this Thesis, these states are annotated with the subscript 'a' to denote this.

The most reduced active species is known as Ni_a-R. Nuclear resonance vibrational spectroscopy and DFT calculations have revealed that a hydride bridging ligand sits between the diamagnetic Ni(II)Fe(II) active site in the Ni_a-R state.[62] The common representation also includes protonation of the terminal cysteine thiolate bound to the Ni, implying its involvement as the primary proton acceptor. Evidence for this interpretation was given by a high resolution (0.89 Å) crystal structure of chemically reduced [NiFe]-hydrogenase from Desulfovibrio *vulgaris* Miyazaki F (MF) which showed residual electron density at the cysteine thiolate.[46] This observation agreed with previous DFT calculations which also predicted the Ni-bound cysteine as the primary proton acceptor.[62,63] However, this interpretation of the Ni_a-R species is rather simplified. IR spectroscopic studies of reduced [NiFe]-hydrogenases show that there are at least three different species at the Ni_a-R redox level (Ni_a-R_I, Ni_a-R_{II} and Ni_a-R_{III}). These three sub-species are pH dependent and thus are predicted to be caused by different protonation sites.

One electron oxidation of the Ni_a-R state results in Ni_a-C. Unlike Ni_a-R, this state is EPR-active due to its Ni(III)Fe(II) active site. Single crystal EPR techniques and ENDOR spectroscopic studies also revealed that a hydride remains at the bridging site.[64,65] Only one Ni_a-C species has been identified for most [NiFe]-hydrogenases, although Greene *et al.* observed a pH-dependent Ni_a-C peak shift during photo-triggered FTIR studies of *Pyrococcus furiosus* SH1, hypothesised to be due to protonation of a nearby glutamate residue.[66] A similar observation during IR spectroelectrochemical studies of *Escherichia coli* hydrogenase-1 is discussed during this Thesis.[33]

Another paramagnetic state at the same redox level as Ni_a-C is the Ni_a-L species. This Ni(I) species is essentially a tautomer of Ni_a-C, where the electrons from the hydride are

transferred to the Ni to produce the formally Ni(I) species, with the proton residing on a neighbouring basic residue. Recent light-triggered FTIR experiments have suggested that the terminal cysteine thiolate coordinated to Ni is this basic residue, similar to its role as a proton acceptor in the Ni_a-R species.[67] Another similarity between the Ni_a-R and Ni_a-L states is they have at least three different pH-dependent sub-species, speculated to represent different protonation states during the removal of a proton from the active site.[68] Ni_a-L was initially thought to not be catalytically relevant due to its lack of presence under normal physiologically conditions. Instead, it was only observed upon illumination of the Ni_a-C species under cryogenic conditions.[65,69] However, various FTIR and photo-triggered time-resolved studies have highlighted the role of the Ni_a-L species as an intermediate in the Ni_a-C / Ni_a-SI transition.[12,70,71] A nickel-iron bond also been suggested in the Ni_a-L state, consistent with observation of low wavenumber ν_{CO} IR bands for a terminal CO ligand due to delocalisation of electron density onto the Fe.[72]

The most oxidised but still catalytically active species is the Ni_a-SI state. This state contains a diamagnetic Ni(II)Fe(II) cluster and vacant bridging coordination site, as confirmed by x-ray crystallography.[73] This is the species at which H_2 binding occurs and it is also susceptible to attack by CO.[73–75] Further oxidation of the [NiFe] active site leads to the inactive Ni-B state.

1.2.3.2. Iron-sulfur clusters

The small β-subunit contains three iron-sulfur clusters that act as the electron relay chain between the surface of the αβ heterodimer and the buried [NiFe] active site. These are called the proximal, medial and distal clusters based on their distance from the active site (with proximal being the closest). The medial and distal clusters are common across [NiFe]-hydrogenases, being [3Fe4S] and [4Fe4S] respectively. The proximal cluster,

however, differs between standard and O_2-tolerant [NiFe]-hydrogenases: a [4Fe4S] cubane cluster, coordinated by four cysteines, is found in standard [NiFe]-hydrogenases, whereas a [4Fe3S] proximal cluster coordinated by six cysteines, is present in O_2-tolerant hydrogenases.[48,76] Exceptions are known. The membrane bound [NiFe]-hydrogenase from *Citrobacter* sp. S-77 contains a [4Fe4S] proximal cluster, similar to standard [NiFe]-hydrogenases, whilst still exhibiting catalytic activity in the presence of O_2.[77,78] This hydrogenase is known as O_2-stable rather than O_2-tolerant.

A second difference between the iron-sulfur clusters of standard and O_2-tolerant [NiFe]-hydrogenases is their reduction potentials. EPR and Mössbauer spectroscopies have been utilised to investigate the reduction potentials of the iron-sulfur clusters in various [NiFe]-hydrogenases. Table 1.1 shows that O_2-tolerant [NiFe]-hydrogenases tend to have much higher reduction potentials than standard hydrogenases. This has been purported to be important for the O_2 tolerance, whilst also impacting the distributions of the active site redox states present at equilibrium, which is discussed later in this Thesis.

Table 1.1 Reduction potentials of the EPR active Fe-S clusters of [NiFe]-hydrogenases. The potentials for *Ec* Hyd-1, *Re* MBH and *Dv*MF were obtained at pH 6.0, 6.4 and 7.7 respectively. For *Aa* Hase I and *D.gigas*, measurements were performed at pH 7.0. The subscript 'app' represents the apparent reduction potential, i.e. the potential at which the uncoupled $[3Fe–4S]^{+}$ cluster signal is at half its maximum intensity.

[NiFe]-hydrogenase	**Reduction potentials / mV *vs* SHE**				
	Proximal		**Medial**		**Distal**
O_2-tolerant	**$[4Fe3S]^{5+/4+}$**	**$[4Fe3S]^{4+/3+}$**	**$[3Fe4S]^{+/0}$**	**$[3Fe4S]^{+/0}_{app.}$**	**$[4Fe4S]^{2+/+}$**
Ec Hyd-1[79]	+ 230 ± 15	+ 30 ± 30	+ 190 ± 30	+ 130 ± 15	-
Re MBH[80]	+ 160	-	-	+ 25	-60
Aa Hase I[81]	+ 232 ± 20	+ 98 ± 20	-	+ 78 ± 20	-65 ± 20
Standard	**$[4Fe4S]^{2+/+}$**		**$[3Fe4S]^{+/0}$**		**$[4Fe4S]^{2+/+}$**
Dv MF[82]	< -300		-70 ± 10		<-300
D. gigas [83]	< -250		-70 ± 10		< -250

1.2.3.3. Gas channels

X-ray structures of Xe-infused crystals of [NiFe]-hydrogenase from *Desulfovibrio fructosovorans* and Kr-infused crystals of *Ralstonia eutropha* MBH along with molecular dynamic simulations have revealed the presence of defined hydrophobic gas channels that run from the surface of the enzyme to the buried [NiFe] active site.[84,85] These allow the diffusion of H_2 substrate, along with other non-polar inhibitors of hydrogenases such as O_2 and CO, to reach the active site. Hydrophilic gas channels have also been detected in hydrogenases. Scheer and co-workers identified a hydrophilic tunnel at the medial [3Fe4S] in standard [NiFe]-hydrogenases that is otherwise blocked by a tryptophan residue in O_2-tolerant hydrogenases. They proposed that by blocking the medial cluster to

accessibility to solvent may be influencing the medial cluster reduction potential.[85] Hydrophilic gas tunnels were also identified in *D. vulgaris* Hildenborough [NiFeSe]-hydrogenase which allow O_2 to access the active site, in contrast with the assumption that only hydrophobic channels provide access for inhibitors.[86]

1.2.4. Catalytic mechanism

The [NiFe]-hydrogenase catalytic mechanism is composed of several active site redox species, most of which interconvert *via* specific proton-coupled electron transfer steps. The outline mechanism for H_2 oxidation (the reverse of proton reduction) is detailed in Figure 1.3.

Reductive activation of the inactive Ni-B state *via* the 'ready' Ni-SI_r state results in the formation of Ni_a-SI, considered to be the initial state that reacts with H_2. The highly electron dense $Ni^{II}Fe^{II}$ centre polarises the H–H bond, with subsequent heterolytic cleavage forming the Ni_a-R species. Multiple Ni_a-R species have been spectroscopically characterised which are thought to represent transfer of a proton away from the active site. The exact mechanism of H_2 cleavage, the identity of the initial proton acceptor and subsequent proton transfer pathway have all been debated. The most substantiated theory involves H_2 initially binding side-on to the Ni in a Kubas-type complex, with H–H bond cleavage forming the bridging hydride and protonation of the terminal cysteine thiolate coordinated to the Ni. This is supported by DFT calculations and high-resolution x-ray crystallographic studies showing protonation of the thiolate along with a shorter Ni-H^- distance compared to Fe-H^-.[46]

A second mechanism involving a highly-conserved arginine group was proposed by Armstrong and co-workers based on the decrease in enzyme activity upon substitution of the arginine residue for lysine in *E. coli* Hyd-1.[23] Here, the pendant arginine, which sits

4.4 Å above the [NiFe]-active site, acts as the base that polarises the H–H bond, similar to a frustrated Lewis pair. This mechanism is controversial as at neutral pH the arginine residue is likely protonated due to its high pK_a and thus cannot act as a base.[87] Furthermore, protein film IR electrochemical experiments under turnover conditions on the same R → K mutant in *E. coli* Hyd-1 (R509K) revealed that the arginine residue was not crucial for H_2 splitting although still important for proton-coupled electron transfer, either by acting as a direct proton acceptor or by stabilising a surrounding transient solvent network.[88]

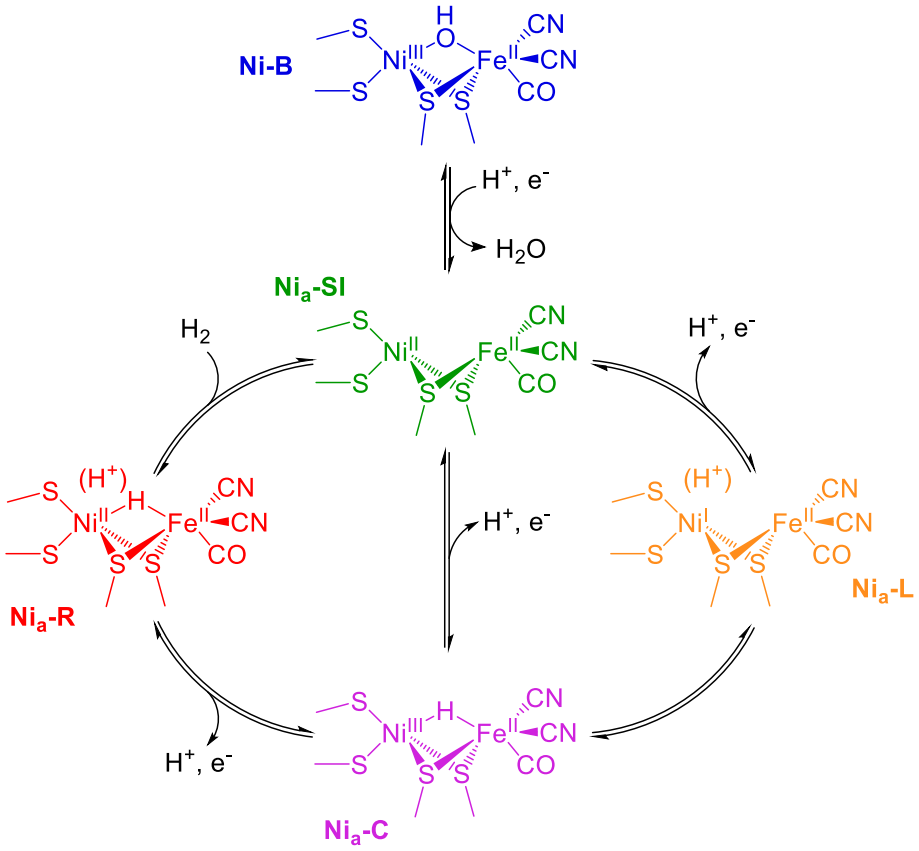


Figure 1.3 The outline catalytic cycle of [NiFe]-hydrogenases, showing catalytically active and inactive states (colour-coding used throughout this Thesis). The proton (H^+) acceptor sites are not specified as their identity is still under investigation.

Following H_2 cleavage, removal of the proton from the active site vicinity has been proposed to proceed *via* glutamate and threonine residues.[76,89] However Evans *et al.* showed that the glutamate residue was not necessary for the initial H^+ transfer between the Ni_a-R and Ni_a-C species in *E. coli* Hyd-1 but instead facilitates removal of the bridging hydride as a proton between Ni_a-C and Ni_a-SI.[90] Furthermore, an alternative proton transfer pathway involving histidine and water molecules connected by a hydrogen bonding network has also been proposed in the O_2-tolerant [NiFe]-hydrogenase from *R. eutropha*.[89,91]

Complete removal of the proton from the active site combined with one electron oxidation of Ni_a-R leads to the Ni_a-C species. From the Ni_a-C state, oxidation to Ni_a-SI can proceed via two pathways: direct loss of a second electron and proton; or, by means of the Ni(I) intermediate Ni_a-L. Similar to Ni_a-R, multiple Ni_a-L states have been spectroscopically characterised. Various FTIR and crystallographic studies also support the involvement of the terminal cysteine thiolate and the glutamate residue as steps along the proton transfer pathway between Ni_a-L.[67,90] One electron oxidation of the Ni_a-L state results in reformation of the initial Ni_a-SI state.

1.2.5. *Escherichia coli* [NiFe]-hydrogenases

Escherichia coli (*E. coli*) synthesises four membrane-bound reversible [NiFe]-hydrogenases: two respiratory H_2-uptake Group 1 hydrogenases, and two H_2-evolving, energy-conserving Group 4 hydrogenases.[92] Work in this Thesis focuses on the former two Group 1 [NiFe]-hydrogenases: hydrogenase-1 (Hyd-1) and hydrogenase-2 (Hyd-2).

Hyd-1 is an O_2-tolerant Group 1 hydrogenase as it is able to oxidise H_2 when O_2 is present, due to its unique [4Fe3S] proximal cluster. Furthermore, at neutral pH, Hyd-1 is unable to catalyse H_2 production and thus is exclusively an H_2-oxidiser. Hyd-2, on the other hand,

behaves like a standard Group 1 [NiFe]-hydrogenase. It is reversibly inactivated in the presence of O_2, is an efficient bidirectional H_2 catalyst without a large overpotential, and is strongly inhibited by CO.[35]

Differences between the two Group 1 hydrogenases also lie in their subunit composition (Figure 1.4). Both Hyd-1 and Hyd-2 contain a [NiFe] αβ heterodimer anchored to the periplasmic side of the membrane by a single C-terminal transmembrane (TM) alpha-helix attached to the small β sub-unit. However, Hyd-1 is also anchored by a TM cytochrome *b* (cyt*b*) subunit which acts as a redox couple between the FeS clusters and the quinone pool. The cyt*b* subunit can disassociate from the HyaAB heterodimer during protein purification. The effect this has on the behaviour of the [NiFe] active site is investigated in Chapter 6.[45,93]

Hyd-2 does not contain a heme *b* subunit. Instead, the [NiFe] αβ heterodimer (HybOC) associates with a ferredoxin (HybA) that contains four [4Fe4S] clusters anchored at the periplasmic side of the membrane by a C-terminal TM domain, and with HybB, an integral membrane protein comprised of 10 TM helices. These allow the HybOC heterodimer to couple to the quinone pool.[43]

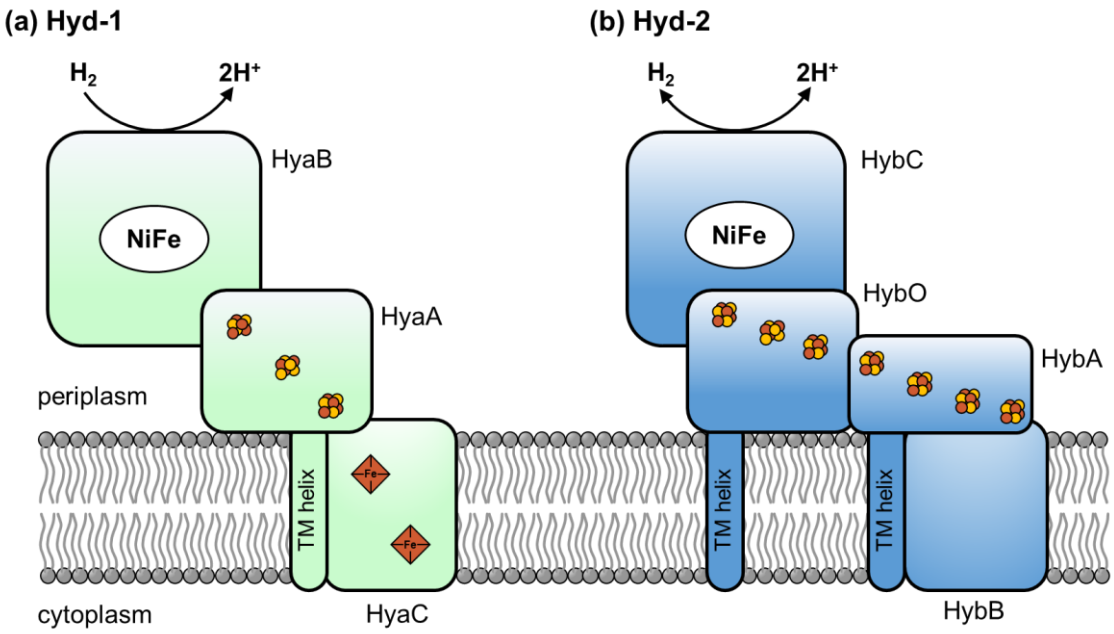


Figure 1.4 Cartoon representation of the two periplasmic-bound *E. coli* hydrogenases: (a) Hyd-1 and (b) Hyd-2. The groups of red and yellow circles represent the FeS clusters and the red diamonds symbolise the heme *b* groups.

Both Hyd-1 and Hyd-2 are well characterised and have been studied in solution using a range of IR spectroscopic techniques. This provides a good reference for comparison to IR studies on their crystallised forms.

1.3. Aims of this Thesis

The wide array of techniques present for studying metalloenzyme mechanisms means that there is a wealth of information available for interpretation. However, as these methods often handle the enzyme in disparate ways, with many only focusing on obtaining either kinetic, structural or spectroscopic information, reconciling all of this data can be challenging. This Thesis aims to demonstrate how important it is to utilise a range of different approaches to provide a more holistic view of an enzyme mechanism. In particular, methods of combining IR spectroscopy with electrochemical control are shown to extend from *in situ* electrode-adsorbed to the crystalline state, demonstrating the

enzyme can be regarded as a dynamic system throughout. A new IR microspectroscopic-electrochemical technique is used to study the redox behaviour of two [NiFe]-hydrogenases from *E. coli*, Hyd-1 and Hyd-2, providing fresh insight into the general mechanism of [NiFe]-hydrogenases.

Initially, in Chapter 3, the behaviour of electrode-adsorbed Hyd-1 is investigated using the established *in situ* protein film IR electrochemical (PFIRE) technique. Whilst similar studies have been performed before on Hyd-1, there is a question as to whether they were mass transport limited, particularly those performed under catalytic turnover conditions. By repeating these PFIRE experiments, this query is addressed along with providing a complete redox characterisation of Hyd-1 for comparison with other IR spectroelectrochemical techniques.

Chapter 4 involves the development of the single crystal IR microspectroscopic-electrochemical technique and its application in revealing the redox behaviour of Hyd-1 *in crystallo*. A detailed electrochemical titration is performed and compared to similar titrations performed on Hyd-1 in solution and electrode-adsorbed. Specific attention is given to the IR spectra recorded during the equilibration periods of the electrochemical redox titration determine whether the kinetics of the transitions can be observed.

Chapter 5 investigates whether proton transfer equilibria are maintained in the crystalline state, whilst Chapter 6 focuses on different preparations of Hyd-1 single crystals and whether the presence of the redox partner cytochrome *b* impacts active site redox behaviour.

Finally, the single crystal IR microspectroscopic-electrochemical technique is applied to a different [NiFe]-hydrogenase, namely the O_2-sensitive Hyd-2 from *E. coli*., in Chapter 7. To

aid identification of the active site redox states responsible for new low wavenumber IR bands visible in the single crystal IR spectra, low temperature light-triggered IR spectra of Hyd-2 solution were also performed.

1.4. References

1 M. Hoppert, in *Encyclopedia of Earth Sciences Series*, Springer Netherlands, 2011, pp. 558–563.

2 C. E. Valdez, Q. A. Smith, M. R. Nechay and A. N. Alexandrova, *Acc Chem Res*, 2014, **47**, 3110–3117.

3 E. Torres and M. Ayala, in *Comprehensive Inorganic Chemistry II (Second Edition): From Elements to Applications*, Elsevier, 2013, vol. 6, pp. 685–735.

4 H. J. Davis and T. R. Ward, *ACS Cent Sci*, 2019, **5**, 1120–1136.

5 K. Schneider and H. G. Schlegel, *BBA - Enzymology*, 1976, **452**, 66–80.

6 H. Bisswanger, *Perspect Sci (Neth)*, 2014, **1**, 41–55.

7 K. A. Vincent, A. Parkin and F. A. Armstrong, *Chem Rev*, 2007, **107**, 4366–4413.

8 C. Léger, S. J. Elliott, K. R. Hoke, L. J. C. Jeuken, A. K. Jones and F. A. Armstrong, *Biochemistry*, 2003, **42**, 8653–8662.

9 A. Rygula, K. Majzner, K. M. Marzec, A. Kaczor, M. Pilarczyk and M. Baranska, *J. Raman Spectrosc.*, 2013, **44**, 1061–1076.

10 D. M. Byler and H. Susi, *Biopolymers*, 1986, **25**, 469–487.

11 H. Yang, S. Yang, J. Kong, A. Dong and S. Yu, *Nat. Protoc.*, 2015, **10**, 382–396.

12 R. Hidalgo, P. A. Ash, A. J. Healy and K. A. Vincent, *Angew. Chem., Int. Ed.*, 2015, **54**, 7110–7113.

13 B. L. Greene, G. E. Vansuch, B. C. Chica, M. W. W. Adams and R. B. Dyer, *Acc Chem Res*, 2017, **50**, 2718–2726.

14 C. More, V. Belle, M. Asso, A. Fournel, G. Roger, B. Guigliarelli and P. Bertrand, *Biospectroscopy*, 1999, **5**, S3-18.

15 V. Schünemann and H. Paulsen, *Mössbauer Spectroscopy*, John Wiley & Sons, Ltd, Chichester, UK, 2011.

16 D. Sedney and W. M. Rieff, *Inorganica Chim Acta*, 1979, **34**, 231–236.

17 S. J. Yoo, H. C. Angove, B. K. Burgess, M. P. Hendrich and E. Münck, *J Am Chem Soc*, 1999, **121**, 2534–2545.

18 W. R. Scheidt, J. Li and J. T. Sage, *Chem Rev*, 2017, **117**, 12532–12563.

19 S. E. J. Bowman, J. Bridwell-Rabb and C. L. Drennan, *Acc Chem Res*, 2016, **49**, 695–702.

20 T. Lovell, F. Himo, W. G. Han and L. Noodleman, *Coord Chem Rev*, 2003, **238–239**, 211–232.

21 S. Shin, E. T. Yukl, E. Sehanobish, C. M. Wilmot and V. L. Davidson, *Biochemistry*, 2014, **53**, 1342–1349.

22 A. Ciaccafava, D. Tombolelli, L. Domnik, J. Fesseler, J. H. Jeoung, H. Dobbek, M. A. Mroginski, I. Zebger and P. Hildebrandt, *Chem Sci*, 2016, **7**, 3162–3171.

23 R. M. Evans, E. J. Brooke, S. A. M. Wehlin, E. Nomerotskaia, F. Sargent, S. B. Carr, S. E. V. Phillips and F. A. Armstrong, *Nat Chem Biol*, 2016, **12**, 46–50.

24 A. L. DeLacey, V. M. Fernandez, M. Rousset, C. Cavazza and E. C. Hatchikian, *J. Biol. Inorg. Chem.*, 2003, **8**, 129–134.

25 M. A. Bañares, *Catal Today*, 2005, **100**, 71–77.

26 H. J. Freund, *Rendiconti Lincei*, 2017, **28**, 5–18.

27 B. M. Weckhuysen, *Chem Soc Rev*, 2010, 39, 4557–4559.

28 U. Bentrup, *Chem Soc Rev*, 2010, **39**, 4718–4730.

29 X. Li, X. Yang, J. Zhang, Y. Huang and B. Liu, *ACS Catal*, 2019, **9**, 2521–2531.

30 B. W. J. Chen, L. Xu and M. Mavrikakis, *Chem Rev*, 2021, **121**, 1007–1048.

31 T. Bligaard, R. M. Bullock, C. T. Campbell, J. G. Chen, B. C. Gates, R. J. Gorte, C. W. Jones, W. D. Jones, J. R. Kitchin and S. L. Scott, *ACS Catal*, 2016, **6**, 2590–2602.

32 P. A. Ash, S. E. T. Kendall-Price and K. A. Vincent, *Acc Chem Res*, 2019, **52**, 3120–3131.

33 P. A. Ash, S. E. T. Kendall-Price, R. M. Evans, S. B. Carr, A. R. Brasnett, S. Morra, J. S. Rowbotham, R. Hidalgo, A. J. Healy, G. Cinque, M. D. Frogley, F. A. Armstrong and K. A. Vincent, *Chem Sci*, 2021, **12**, 12959–12970.

34 P. M. Vignais and B. Billoud, *Chem Rev*, 2007, 107, 4206–4272.

35 M. J. Lukey, A. Parkin, M. M. Roessler, B. J. Murphy, J. Harmer, T. Palmer, F. Sargent and F. A. Armstrong, *J Biol Chem*, 2010, **285**, 3928–38.

36 W. Lubitz, H. Ogata, O. Rüdiger and E. Reijerse, *Chem Rev*, 2014, 114, 4081–4148.

37 H. A. Reeve, L. Lauterbach, O. Lenz and K. A. Vincent, *ChemCatChem*, 2015, **7**, 3480–3487.

38 L. Xu and F. A. Armstrong, *Energy Environ Sci*, 2013, **6**, 2166.

39 M. Frey, *Chembiochem*, 2002, **3**, 153–60.

40 P. M. Vignais, B. Billoud and J. Meyer, *FEMS Microbiol Rev*, 2001, **25**, 455–501.

41 P. P. Liebgott, S. Dementin, C. Léger and M. Rousset, *Energy Environ Sci*, 2010, **4**, 33–41.

42 J. A. Cracknell, K. A. Vincent, M. Ludwig, O. Lenz, B. Friedrich and F. A. Armstrong, *J. Am. Chem. Soc.*, 2008, **130**, 424–425.

43 S. E. Beaton, R. M. Evans, A. J. Finney, C. M. Lamont, F. A. Armstrong, F. Sargent and S. B. Carr, *Biochem. J.*, 2018, **475**, 1353–1370.

44 A. Volbeda, M.-H. Charon, C. Piras, E. C. Hatchikian, M. Frey and J. C. Fontecilla-Camps, *Nature*, 1995, **373**, 580–587.

45 A. Volbeda, P. Amara, C. Darnault, J.-M. Mouesca, A. Parkin, M. M. Roessler, F. A. Armstrong and J. C. Fontecilla-Camps, *Proc. Natl. Acad. Sci. U.S.A.*, 2012, **109**, 5305–5310.

46 H. Ogata, K. Nishikawa and W. Lubitz, *Nature*, 2015, **520**, 571–574.

47 H. Ogata, P. Kellers and W. Lubitz, *J Mol Biol*, 2010, **402**, 428–444.

48 J. Fritsch, P. Scheerer, S. Frielingsdorf, S. Kroschinsky, B. Friedrich, O. Lenz and C. M. T. Spahn, *Nature*, 2011, **479**, 249–253.

49 P. Wulff, C. Thomas, F. Sargent and F. A. Armstrong, *J. Biol. Inorg. Chem.*, 2016, **21**, 121–134.

50 M. Bruschi, M. Tiberti, A. Guerra and L. de Gioia, *J Am Chem Soc*, 2014, **136**, 1803–1814.

51 A. Volbeda, E. Garcin, C. Piras, A. L. de Lacey, V. M. Fernandez, E. C. Hatchikian, M. Frey and J. C. Fontecilla-Camps, *J Am Chem Soc*, 1996, **118**, 12989–12996.

52 A. J. Pierik, W. Roseboom, R. P. Happe, K. A. Bagley and S. P. J. Albracht, *J Biol Chem*, 1999, **274**, 3331–7.

53 S. Kaur-Ghumaan and M. Stein, *Dalton Trans.*, 2014, **43**, 9392–9405.

54 J. L. Barilone, H. Ogata, W. Lubitz, M. van Gastel, A. Pamplona, J. Telser, I. Moura, J. J. G. Moura, B. M. Hoffman and J. C. Fontecilla-Camps, *Phys. Chem. Chem. Phys.*, 2015, **17**, 16204–16212.

55 A. Volbeda, L. Martin, E. Barbier, O. Gutiérrez-Sanz, A. L. de Lacey, P.-P. Liebgott, S. Dementin, M. Rousset and J. C. Fontecilla-Camps, *J. Biol. Inorg. Chem.*, 2015, **20**, 11–22.

56 M.-E. Pandelia, H. Ogata, L. J. Currell, M. Flores and W. Lubitz, *J. Biol. Inorg. Chem.*, 2009, **14**, 1227–1241.

57 T. Krämer, M. Kampa, W. Lubitz, M. van Gastel and F. Neese, *ChemBioChem*, 2013, **14**, 1898–1905.

58 H. Tai, L. Xu, K. Nishikawa, Y. Higuchi and S. Hirota, *Chem. Commun.*, 2017, **53**, 10444–10447.

59 A. L. de Lacey, V. M. Fernández, M. Rousset and R. Cammack, *Chem Rev*, 2007, 107, 4304–4330.

60 B. Bleijlevens, F. A. van Broekhuizen, A. L. de Lacey, W. Roseboom, V. M. Fernandez and S. P. J. Albracht, *J. Biol. Inorg. Chem.*, 2004, **9**, 743–752.

61 R. Breglia, C. Greco, P. Fantucci, L. de Gioia and M. Bruschi, *Inorg Chem*, 2019, **58**, 279–293.

62 H. Ogata, T. Krämer, H. Wang, D. Schilter, V. Pelmenschikov, M. van Gastel, F. Neese, T. B. Rauchfuss, L. B. Gee, A. D. Scott, Y. Yoda, Y. Tanaka, W. Lubitz and S. P. Cramer, *Nat Commun*, 2015, **6**, 1–8.

63 T. Krämer, M. Kampa, W. Lubitz, M. van Gastel and F. Neese, *ChemBioChem*, 2013, **14**, 1898–1905.

64 M. Brecht, M. van Gastel, T. Buhrke, B. Friedrich and W. Lubitz, *J Am Chem Soc*, 2003, **125**, 13075–13083.

65 S. Foerster, M. Stein, M. Brecht, H. Ogata, Y. Higuchi and W. Lubitz, *J Am Chem Soc*, 2003, **125**, 83–93.

66 B. L. Greene, C. H. Wu, G. E. Vansuch, M. W. W. Adams and R. B. Dyer, *Biochemistry*, 2016, **55**, 1813–1825.

67 H. Tai, K. Nishikawa, Y. Higuchi, Z. Mao and S. Hirota, *Angew. Chem.*, 2019, **131**, 13419–13424.

68 P. A. Ash, R. Hidalgo and K. A. Vincent, *ACS Catal*, 2017, **7**, 2471–2485.

69 H. Tai, K. Nishikawa, S. Inoue, Y. Higuchi and S. Hirota, *J Phys Chem B*, 2015, **119**, 13668–13674.

70 B. L. Greene, C. H. Wu, P. M. McTernan, M. W. W. Adams and R. B. Dyer, *J Am Chem Soc*, 2015, **137**, 4558–4566.

71 H. Tai, K. Nishikawa, M. Suzuki, Y. Higuchi and S. Hirota, *Angew. Chem., Int. Ed.*, 2014, **53**, 13817–13820.

72 M. Kampa, M. E. Pandelia, W. Lubitz, M. van Gastel and F. Neese, *J Am Chem Soc*, 2013, **135**, 3915–3925.

73 Y. Ilina, C. Lorent, S. Katz, J. H. Jeoung, S. Shima, M. Horch, I. Zebger and H. Dobbek, *Angew. Chem., Int. Ed.*, 2019, **58**, 18710–18714.

74 M.-E. Pandelia, H. Ogata, L. J. Currell, M. Flores and W. Lubitz, *Biochim Biophys Acta Bioenerg*, 2010, **1797**, 304–313.

75 M.-E. Pandelia, P. Infossi, M. T. Giudici-Orticoni and W. Lubitz, *Biochemistry*, 2010, **49**, 8873–8881.

76 Y. Shomura, K. S. Yoon, H. Nishihara and Y. Higuchi, *Nature*, 2011, **479**, 253–256.

77 N. D. M. Noor, H. Matsuura, K. Nishikawa, H. Tai, S. Hirota, J. Kim, J. Kang, M. Tateno, K. S. Yoon, S. Ogo, S. Kubota, Y. Shomura and Y. Higuchi, *Chem. Comm.*, 2018, **54**, 12385–12388.

78 S. Eguchi, K. S. Yoon and S. Ogo, *J Biosci Bioeng*, 2012, **114**, 479–484.

79 M. M. Roessler, R. M. Evans, R. A. Davies, J. Harmer and F. A. Armstrong, *J Am Chem Soc*, 2012, **134**, 15581–15594.

80 K. Knuettel, K. Schneider, A. Erkens, W. Plass, A. Mueller, E. Bill and A. X. Trautwein, *Bull Pol Acad Sci Chem*, 1995, **42**, 495–511.

81 M.-E. Pandelia, W. Nitschke, P. Infossi, M. T. Giudici-Orticoni, E. Bill and W. Lubitz, *Proc Natl Acad Sci U S A*, 2011, **108**, 6097–6102.

82 M. Asso, B. Guigliarelli, T. Yagi and P. Bertrand, *Biochim. Biophys. Acta - Proteins Proteom*, 1992, **1122**, 50–56.

83 M. Teixeira, I. Moura, A. v Xavier, J. J. Moura, J. LeGall, D. v DerVartanian, H. D. Peck and B. H. Huynh, *J. Biol. Chem.*, 1989, **264**, 16435–16450.

84 Y. Montet, P. Amara, A. Volbeda, X. Vernede, E. Claude Hatchikian, M. J. Field, M. Frey and J. C. Fontecilla-Camps, *Nat. Struct. Biol.*, 1997, **4**, 523–526.

85 J. Kalms, A. Schmidt, S. Frielingsdorf, P. van der Linden, D. von Stetten, O. Lenz, P. Carpentier and P. Scheerer, *Angew. Chem., Int. Ed.*, 2016, **55**, 5586–5590.

86 S. Zacarias, A. Temporão, M. del Barrio, V. Fourmond, C. Léger, P. M. Matias and I. A. C. Pereira, *ACS Catal*, 2019, **9**, 8509–8519.

87 A. M. Escorcia and M. Stein, *Front Chem*, 2018, **6**, 164.

88 A. R. Brasnett, M.Chem. thesis, University of Oxford, 2019.

89 D. Tombolelli and M. A. Mroginski, *J. Phys. Chem. B*, 2019, **123**, 3409–3420.

90 R. M. Evans, P. A. Ash, S. E. Beaton, E. J. Brooke, K. A. Vincent, S. B. Carr and F. A. Armstrong, *J Am Chem Soc*, 2018, **140**, 10208–10220.

91 S. Frielingsdorf, J. Fritsch, A. Schmidt, M. Hammer, J. Löwenstein, E. Siebert, V. Pelmenschikov, T. Jaenicke, J. Kalms, Y. Rippers, F. Lendzian, I. Zebger, C. Teutloff, M. Kaupp, R. Bittl, P. Hildebrandt, B. Friedrich, O. Lenz and P. Scheerer, *Nat. Chem. Bio.*, 2014, **10**, 378–385.

92 K. Trchounian, A. Poladyan, A. Vassilian and A. Trchounian, *Crit Rev Biochem Mol Biol*, 2012, 47, 236–249.

93 A. Volbeda, C. Darnault, A. Parkin, F. Sargent, F. A. Armstrong and J. C. Fontecilla-Camps, *Structure*, 2013, **21**, 184–190.

Chapter 2. Experimental theory and methods

Several different experimental techniques are used and developed throughout this Thesis. In this Chapter, the principles behind each method are explained to give an understanding. Experimental procedures, such as how the enzymes were prepared, and the specifications of the various equipment are also described in detail.

2.1. Infra-red spectroscopy

2.1.1. General principles

Infrared (IR) spectroscopy is an analytical technique used to identify molecules by how they interact with infrared light. When a molecule is exposed to IR radiation, it can absorb specific wavelengths that correspond to spectroscopic transitions from a lower to an upper vibrational energy level. The energy absorbed depends on the structure and environment of the molecule, thus allowing identification of functional groups within a sample.

2.1.1.1. Molecular vibrations

The distance between atoms in a molecule, i.e. the bond length, is not fixed, which allows atoms to vibrate. These vibrations range from the simple motion between two atoms in diatomic molecules to each atom in a polyatomic molecule vibrating simultaneously. The number of degrees of vibrational freedom is subject to the shape of the molecule. Linear molecules possess $3N - 5$ vibrational modes (N = number of atoms in molecule) whereas non-linear molecules have $3N - 6$.

To a first approximation, a diatomic molecule (one vibrational mode, shown in Figure 2.1) can be described as a simple harmonic oscillator that obeys Hooke's Law, similar to two point masses connected by a spring.

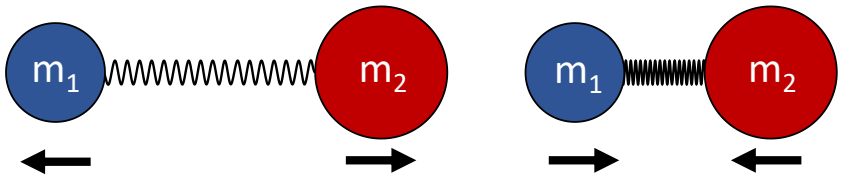


Figure 2.1 Representation of the stretching vibrational mode in a heteronuclear diatomic molecule, such as HCl. The atoms have masses m_1 and m_2, respectively.

As the distance between the two atoms, r, increases beyond the equilibrium bond length, r_e, the energy of the molecule increases as the "spring" acts to pull the atoms together. When $r < r_e$, repulsion between the two positively charged nuclei also causes the energy of the molecule to increase. This interaction can be illustrated by plotting potential energy, V(r), as a function of r (Figure 2.2). For a vibration to occur, the molecule needs to transition from a lower vibrational quantum level to a higher one. The energy of a vibrational level can be represented by Equation [1.1], with vibrational quantum number, v, Planck's constant, h, and vibrational frequency, ν in s^{-1}.

$$E(\mathrm{v}) = \left(\mathrm{v} + \frac{1}{2}\right) h\nu \qquad [2.1]$$

The harmonic oscillator model predicts that the vibrational levels are equally spaced, and that the energy required to transition between vibrational levels is constant. In reality, as the vibrational quantum number increases, the energy between levels decreases, eventually reaching a point where the bond dissociates. Thus, the simple harmonic oscillator approximation only holds at low vibrational levels. Molecular vibrations are more accurately described by a Morse potential, which factors in the molecule's dissociation energy, D_e, and bond force constant at the bottom of the potential well, k_e (Equation [2.2], Figure 2.2)[1]. This accounts for anharmonicity within molecules, such as the fact that vibrational transitions where $\Delta \mathrm{v} > \pm 1$ are observed as weak overtones. As such, the energy of a vibrational level can now be represented by Equation [2.3], where the anharmonicity is accounted for by x_e.

$$V(r) = D_e \left(1 - e^{-\sqrt{\frac{k_e}{2D_e}}(r - r_e)}\right)^2 \qquad [2.2]$$

$$E(\mathrm{v}) = h\nu\left(\mathrm{v} + \tfrac{1}{2}\right) - h\nu x_e \left(\mathrm{v} + \tfrac{1}{2}\right)^2 + \cdots \text{ with } x_e = \frac{\nu}{4D_e} \qquad [2.3]$$

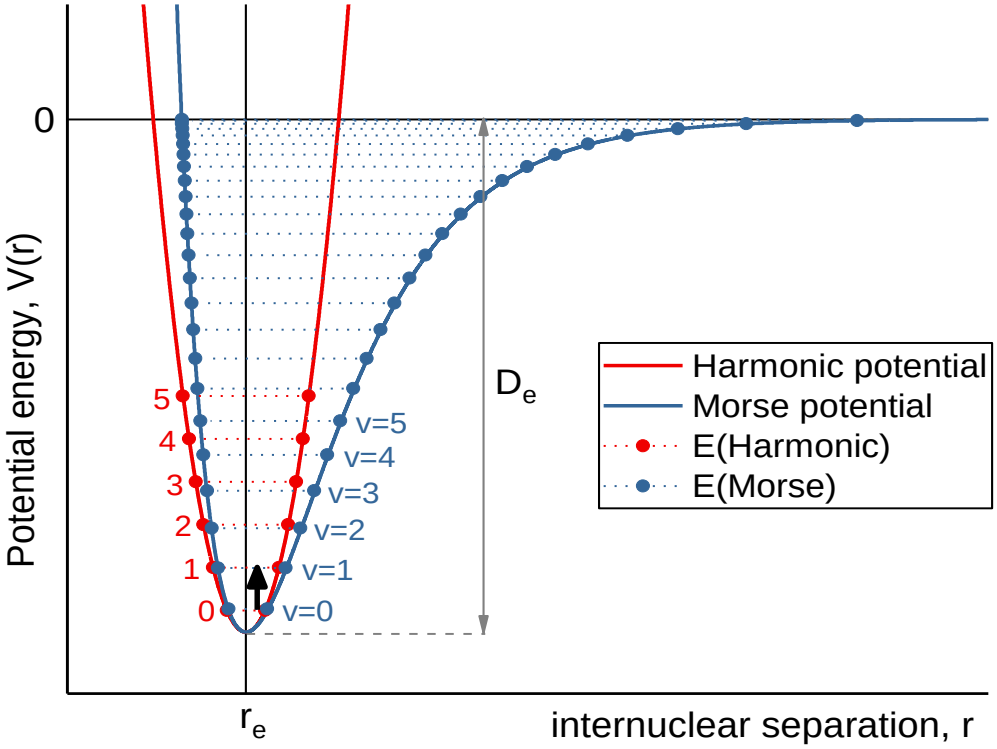


Figure 2.2 Potential energy, V(r), of a diatomic molecule as a function of distance between atoms for a simple harmonic oscillator (red line) and an anharmonic Morse oscillator (blue line). The red and blue dotted lines represent the vibrational energy levels for the harmonic and Morse oscillator respectively. The black arrow shows a possible vibrational transition between the ground vibrational level (v=0) and the first excited vibrational state (v=1). r_e represents equilibrium bond length and D_e represents dissociation energy.

2.1.1.2. Vibrational coupling

Diatomic molecules only have one degree of vibrational freedom, and thus possess one vibrational mode (Figure 2.1). Polyatomic molecules possess a number of vibrational modes which can broadly be separated into stretching and bending vibrations. Stretching vibrations involve the lengthening and compressing of a bond, whereas bending vibrations occur when the bond angles change. Figure 2.3 shows the four vibrational modes of a molecule of carbon dioxide, with the stretching and bending vibrations labelled.

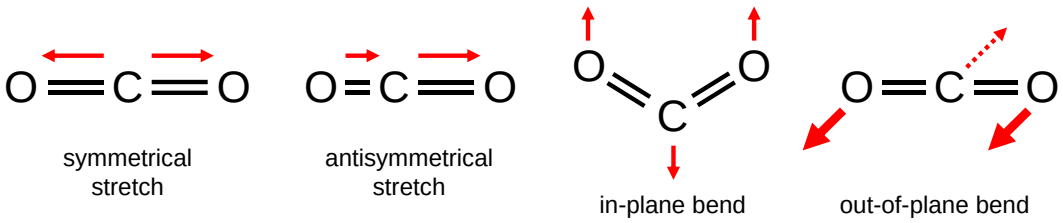


Figure 2.3 Carbon dioxide possesses 4 vibrational modes: one symmetric stretch, one antisymmetric stretch, one in-plane bend and one out-of-plane bend.

The interaction of the two C=O bonds in CO_2 to give the symmetric and antisymmetric stretching modes is known as vibrational coupling. Strong coupling of stretching vibrations occurs when there is a common atom between the two vibrating bonds and is maximised when each bond absorbs a similar frequency.

In this Thesis, only vibrational bands arising from stretching modes are noted as they are more intense and distinct than their bending counterparts.

2.1.1.3. Peak position

For a transition between vibrational levels to occur, a specific amount of energy must be absorbed (Equation [1.1]). The equivalent frequency is calculated using Equation [2.4], where c is the speed of light in cm.s^{-1}, k_f is the force constant in kg.s^{-2} and m_R is the reduced mass in kg.

$$\nu\ (cm^{-1}) = \frac{1}{2\pi c}\sqrt{\frac{k_f}{m_R}} \qquad [2.4]$$

Vibrational frequencies are often referred to in units of wavenumbers, cm^{-1}. Most functional groups have characteristic frequencies that fall within the range of mid-infrared light (4000-400 cm^{-1}), making IR spectroscopy a good technique for measuring the absorptions of molecules.

As the vibrational frequency is proportional to the force constant, the energy of a vibration depends heavily on the strength of the vibrating bond. Stronger bonds result in higher frequencies and thus appear in the higher wavenumber region of an IR spectrum. Stretching vibrational modes have larger force constants than bending modes and so appear at higher frequencies in the IR spectra. Similarly, antisymmetric stretching vibrations usually have higher wavenumbers than symmetric stretches due to the larger amount of energy required to perform an antisymmetric stretch.

The reduced mass of the atoms involved in the bond, however, is inversely proportional to vibrational frequency. Therefore, isotopic substitution can be used to help assign vibrational bands to functional groups as increasing the reduced mass will result in a shift to lower wavenumbers.

2.1.1.4. Peak shape

From Equation [2.4], one would assume that as each functional group has an exact vibrational frequency, it would appear as a single sharp line in an IR spectrum. However, most molecules do not exist on their own and are instead surrounded by other vibrating bands and molecules. Like vibrational coupling, interaction between the molecules and their respective environments occurs, although all in slightly different ways. This means that the frequency at which each molecule vibrates will differ, and thus the line shape observed in the IR spectrum is the sum of that for all the individual molecules.

A classic, albeit extreme, example of the environment affecting the peak shape of a functional group is the O-H stretch in water. Hydrogen bonding between the water molecules influences the frequency at which each individual O-H bond vibrates, and thus the IR band is remarkably broad.

The function that best describes the peak shape also depends on the environment of the vibrating molecules. When a molecule vibrates, it absorbs a quantified amount of energy and is excited from the ground vibrational state to an excited vibrational state (Figure 2.2). There are two components that contribute to the effective lifetime of the vibration, τ: the coherence lifetime τ_c and energy lifetime τ_a. Whichever component results in the fastest decay in the given environment dominates. Upon excitation, all molecules vibrate in unison. However the small differences in vibrational frequency (due to environment interactions) cause the molecules to begin to vibrate asynchronously until there is complete incoherence after a few picoseconds, the lifetime of which is given by τ_c. The relaxation lifetime from the excited state to the ground state, which also is approximately a few picoseconds, is given by τ_a.[2]

As the effective lifetime, τ, decreases, the width of the resulting peak increases. Going back to the example of water, the complex hydrogen-bonding network results in relaxation of the water molecules occurring quickly. Therefore, the shape of the peak is broad.

The state the molecules are in also dictates the dominant decay effect. In the gaseous state, the environment of each vibrating molecule is continuously changing with rapid collisions and rotations of molecules. Thus, $\tau_c \ll \tau_a$ as incoherence is fast. The resulting peak is then best described by a Lorentz function. The opposite is true for molecules in the solid state: a motionless environment means that the molecules relax before incoherence can occur. In this case, a Gaussian profile is more suited as it represents a statistical distribution of environments. A mixture of the two functions is appropriate for molecules in the liquid state, as it represents a mid-point between the two extremes, much like liquid does between solid and gas. A Voigt profile may also be used to describe the line shape of

liquid molecular vibrations. A comparison of the three functions, Gaussian, Lorentz, and Voigt is presented in Figure 2.4.

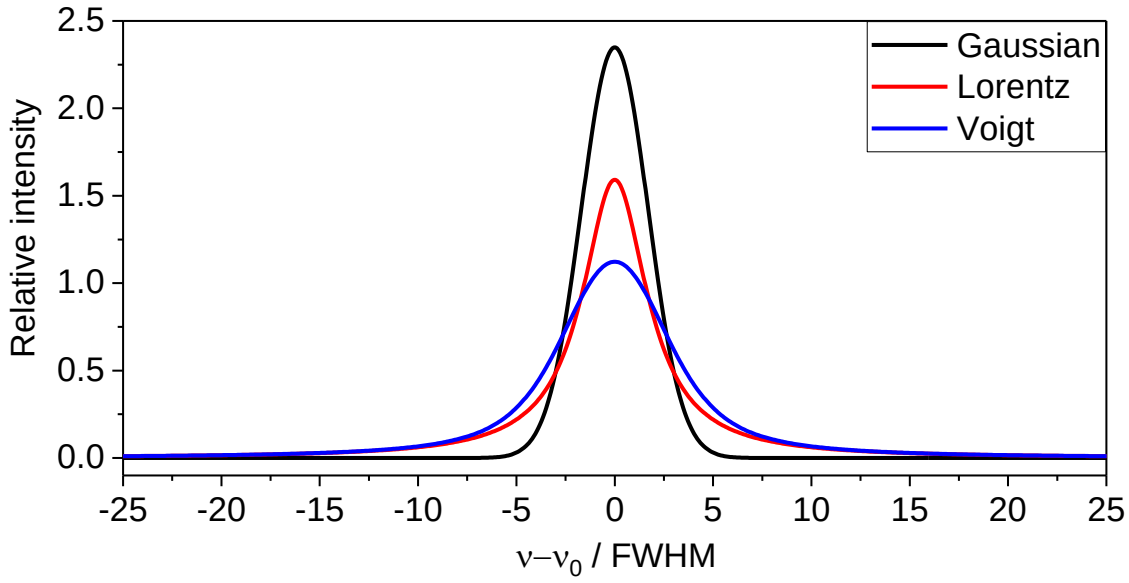


Figure 2.4 A comparison of the three functions used describe the peak shape of the vibrational bands for solid (Gaussian, black), liquid (Voigt, blue), and gaseous (Lorentz, red) samples.

2.1.1.5. Peak height

Absorbances observed in IR spectra are related to the sample concentration and thickness by the Beer-Lambert law (Equation [2.5]), where I is the intensity of light transmitted from the sample, I_0 is the incident light intensity, ε is the molar absorptivity, c is the sample concentration and l is the path length. IR spectra are generally plotted in terms of absorbance, in units of optical density O.D., as a function of vibrational frequency (cm^{-1}).

$$A = -log\frac{I}{I_0} = \varepsilon cl \qquad [2.5]$$

However, not all vibrational transitions result in the absorption of infrared radiation. The gross selection rule that determines whether a molecule or bond is IR active is that there must be a change in the dipole moment during the vibration. This allows interaction of the dipole moment with the alternating electrical component of the IR radiation. Therefore,

molecules such as CO and CN are IR active, but symmetric molecules such as N_2 and O_2, do not absorb IR light and are classed as IR inactive. This is also the case for symmetrical vibrational modes of linear molecules such as the symmetrical stretch of CO_2 (CO_2 has 4 vibrational modes, Figure 2.3, but only 3 are IR active: two bending modes and one antisymmetric stretch).

The molar absorptivity of a molecule is related to its dipole moment by Equation [2.6], where $d\mu$ is the change in dipole moment during a vibration and dx is the change in bond length.[3,4] Thus the intensity of the absorbance bands of a molecule is proportional to the bond dipole moment (Equation [2.7]) and depends on its electronic structure, chemical environment, and how its electronic structure varies during the vibration. Polar functional groups with large dipole moment such as CO and OH will therefore have intense vibrational peaks and as such are usually easily identified in IR spectra.

$$\varepsilon = \left(\frac{d\mu}{dx}\right)^2 \qquad [2.6]$$

$$A \propto \mu \qquad [2.7]$$

Antisymmetric stretching vibrations are generally more intense than the accompanying symmetric stretching vibrations due to their larger $(d\mu/dx)$ term.[5]

2.1.2. Sampling geometries

IR spectrometry is compatible with a range of sample geometries, allowing different sample preparations and methods. Work in this Thesis uses three different geometries: transmission, reflectance-absorption, and attenuated total reflectance.

2.1.2.1. Transmission

The most traditional sampling geometry is transmission (Figure 2.5A). Here, the sample is sandwiched between two IR-transparent windows (often CaF_2 or BaF_2) and mounted into

a holder. The IR beam passes directly through the sample where specific wavelengths are absorbed, and the remaining radiation is transmitted to a detector. This geometry is compatible with solid, liquid, and gaseous samples, and it has been used to study a wide range of proteins in solution.[6–9] The absorbance recorded is directly proportional to the path length of the cell (Beer-Lambert Law, Equation [2.5]) and so the intensity of the IR bands measured can be increased by adjusting the path length. The path length of a typical transmission cell is between 25-100 µm, however a thicker sample often results in complete absorption of the IR radiation. As the IR beam passes through the entire sample, the spectra obtained represent the bulk of the volume sampled. The larger possible path length of transmission compared to other sample geometries makes this geometry ideal for detecting lower concentration species, although a larger volume of solution is required.

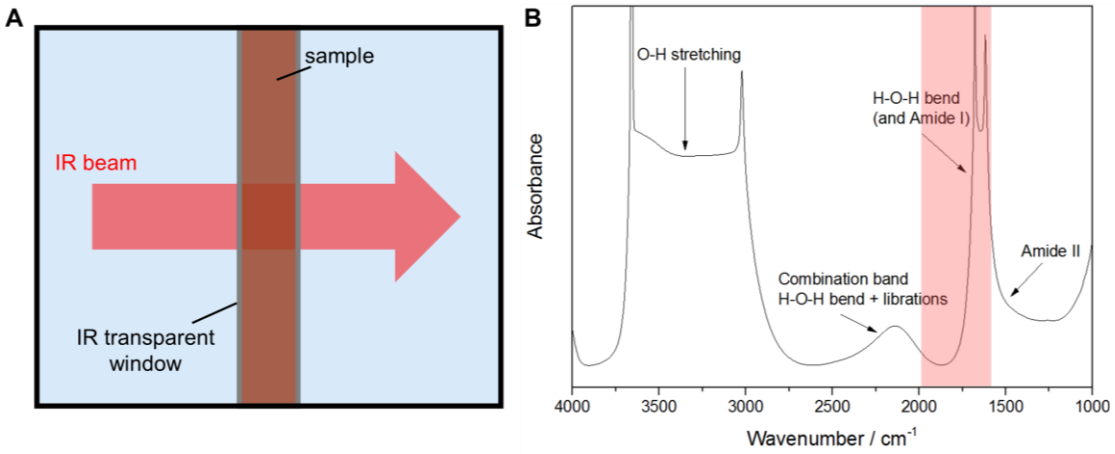


Figure 2.5 A: Transmission IR spectroscopy configuration. The IR beam passes directly through the sample which is held between two IR transparent windows. B: 0.5 mM myoglobin solution in water measured using a transmission IR cell, path length = 38 µm. The vibrational bands due to water are labelled. The red band shows the CO and CN stretching region (~2100 – 1800 cm^{-1}).

The main drawbacks to using a transmission geometry primarily involve sample preparation, particularly when working with proteins. Water is a common solvent used for

biological samples. Despite its relatively low molar coefficient within the mid-IR range,[10] the high concentration of water in aqueous solutions (~55.3 M) results in intense and broad bands that can mask IR signals from the protein. Figure 2.5B shows a 0.5 mM solution of myoglobin in water where the amide I and amide II bands are hidden by the H-O-H bending vibration, and the CO and CN stretching region (2100 – 1800 cm^{-1}) is obscured by the less intense band from the combination of the H-O-H bend and low wavenumber "libration" modes. To overcome this without using isotopically labelled water (which would shift the solvent peaks to lower wavenumbers with the increase in effective mass, see Equation [2.4]), high concentrations of protein e.g. 0.5 mM, are required. This poses some practical issues: low yielding protein preparations require a large initial volume to then concentrate down (for example, a 60 L preparation of WT Hyd-1 from *E.coli* as described in Section 2.3 produces only ~2 mL of 4 µM Hyd-1); highly concentrated protein solutions are viscous and difficult to introduce into the transmission cell; and proteins often aggregate and precipitate when highly concentrated. Recovery of the protein solution is often tricky and achieved by flushing the transmission cell with a large volume of buffer. Furthermore, the presence of any air bubbles in the transmission cell results in scattering which can corrupt an IR spectrum.

A transmission geometry is utilised in the light-induced cryo IR spectroscopy of Hyd-2, as detailed in Chapter 6, due to the requirement of cryo-temperatures and ability to direct visible light onto the sample.

2.1.2.2. Reflectance-Absorption

In reflectance-absorption IR spectroscopy (RAIRS, also known as IR reflectance-absorption spectroscopy, IRRAS), the IR beam passes through a thin sample layer, which absorbs some radiation, before being reflected off an optically dense reflective surface and back

through the sample as shown in Figure 2.6. Due to the nature of this geometry, the IR beam passes through the sample twice, effectively doubling the path length. However, only a small concentration of sample is measured compared to the bulk solvent concentration. As with transmission, this can cause issues, particularly when the bulk contains strongly absorbing components such as water which can mask vibrations from the sample.

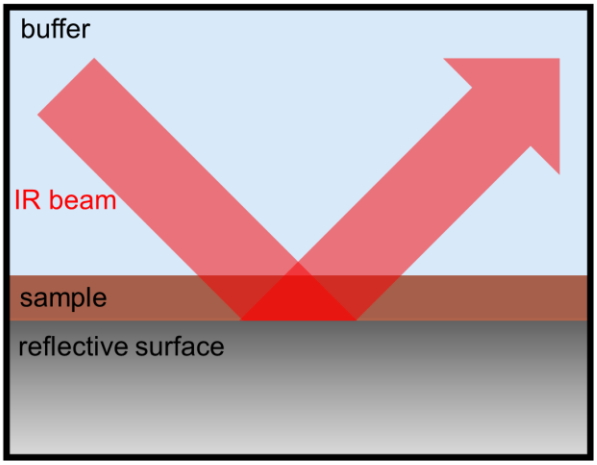


Figure 2.6 Reflectance absorption IR geometry. The IR radiation passes through the sample and is then reflected off the reflective surface, before passing through the sample again and collected at the detector.

A second issue with using a reflectance absorption geometry is the appearance of interference fringes in the IR spectra. Interference fringes can also occur when using transmission IR spectroscopy, however it is more prevalent in reflectance-absorption, particularly with the set-up used in this Thesis. IR reflectance cells often have multiple plane parallel layers of different refractive indices which the IR light must pass through twice (see Figure 2.7). If the distance between each layer is near the wavelength of the IR radiation, multiple internal reflections occur. This causes sinusoidal fringes that superimpose onto the sample IR spectrum and can hinder analysis. The position of the interference fringes is dictated by the sample's thickness and absorption bands.[11,12]

Distinguishing IR bands arising from absorption by the sample from the peaks and troughs of the sinusoidal interference can be challenging. With this set-up, the amplitude of the interference fringes can be minimised by reducing the thickness of the buffer layer between the crystal and the CaF_2 window. There are various methods of processing IR spectra to correct for interference fringes,[11–15] but they are not always reliable, and loss of spectral information can sometimes occur.

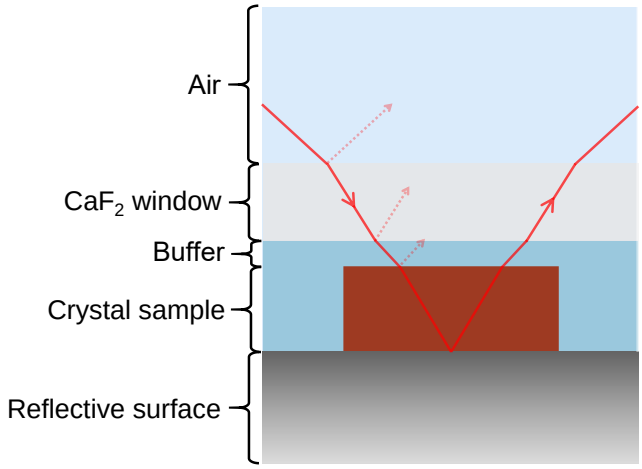


Figure 2.7 Interference fringes due to multiple internal reflection between thin layers in a reflectance cell. A schematic diagram of thin layers present when measuring an IR spectrum of single crystals in the IR microspectroscopic-electrochemical cell described in Chapter 4. The solid red line represents the IR beam, showing refraction at each layer interface, whereas the transparent dotted lines show the internal reflection at each layer interface.

Reflectance absorbance is the primary IR sampling geometry used in this Thesis. The IR microspectroscopic-electrochemical technique described in Chapter 4 uses polished glassy carbon as the reflective surface on which the hydrogenase crystals are sampled.

2.1.2.3. Attenuated Total Reflection

Another common IR sampling technique is attenuated total reflectance (ATR). When light passes from one medium with refractive index, n_1, to another with a lower refractive

index, n_2, at an angle greater than the critical angle, θ_c (Equation [2.8]), the light undergoes total internal reflection (Figure 2.8).

$$\theta_c = \sin^{-1}\frac{n_2}{n_1} \qquad [2.8]$$

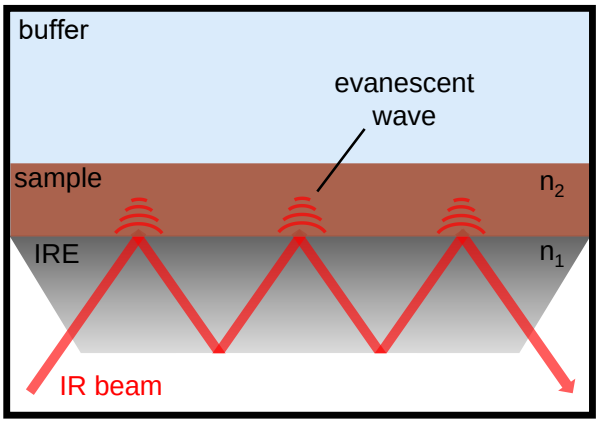


Figure 2.8 Attenuated total reflection IR geometry. The IR beam passes through the internal reflection element (IRE) and is totally reflected at the IRE-sample interface. An evanescent wave penetrates the sample at each reflection.

An optically dense component known as an internal reflection element (IRE) has a high refractive index (n = 3.42 for Si in mid-IR wavelengths,[16]) which makes it ideal for ATR-IR spectroscopy. The sample is placed onto the IRE, through which the IR beam passes and undergoes total internal reflection at the IRE-sample interface. The IR beam does not directly penetrate the sample. Instead, an evanescent wave occurs due to a boundary condition that requires the electric field of the incident light perpendicular to the plane of incidence to be continuous across the IRE-sample interface.[17] This wave decays exponentially into the optically less dense sample with a characteristic penetration depth, d_p, defined as the distance to where the amplitude of the evanescent wave decreases by 1/e, and is dependent on the angle of incidence, θ_i, and the ratio of medium refractive indices as shown by Equation [2.9].

$$d_p = \frac{\lambda}{2\pi n_1 \sqrt{\sin^2 \theta_i - (\frac{n_2}{n_1})^2}} \quad [2.9]$$

The sample absorbs specific wavelengths from the evanescent wave. The resulting attenuated energy is passed back to the totally reflected IR beam and then to the detector.

The effective path length of the ATR cell, l', i.e. the sample thickness that would give in a transmission experiment the same absorbance as in an ATR experiment, depends on the penetration depth and the number of reflections at the IRE-sample interface, *N* (Equation [2.10]).[18]

$$l' \propto N d_p \quad [2.10]$$

By increasing the number of reflections, the effective path length increases, as does the signal-to-noise ratio. The evanescent waves produced at the reflections interact independently, but their absorptions are additive, thus the sensitivity of the IR spectrum can be increased.

The ATR geometry has the benefit of being able to measure a wide range of sample types quickly and easily without the practical limitations of transmission IR. As the sample only interacts with the IR beam at the IRE-sample interface, this method is insensitive to sample thickness and volume. Therefore, only small sample volumes are required, and there is little to no preparation required. Usually when studying protein samples, a protein film is prepared on the IRE and aqueous buffer is placed on top. The thickness of the buffer layer does not impact the collected spectrum and the buffer can be easily exchanged without affecting the film, meaning different experimental conditions can be studied.[9]

Furthermore, as the IR beam does not pass through the sample, the ATR geometry can be coupled with electrochemical methods without using thin-layer electrochemical cells, thus avoiding the constraints they impose on electrochemical sampling. ATR-IR is used in Chapter 3 with the established protein film infra-red electrochemical (PFIRE) technique. Here, this geometry is ideal as it allows the combination of IR spectroscopy and electrochemistry to analyse small quantities of protein.

2.1.3. IR microspectroscopy

IR microspectroscopy is an analytical technique that combines IR spectroscopy and microscopy to obtain spatially resolved chemical information of samples. This, and its non-destructive nature, have allowed it to be used extensively across a wide range of scientific fields, from biomedical research to geology.[19–21] However, when using a traditional thermal (globar) IR source, the smallest aperture size that can be used whilst maintaining an adequate signal-to-noise ratio (as decreasing aperture size reduces the amount of light detected) is ~20 μm.[22,23] This is far above the diffraction limit for mid-infrared light and thus restricts the spatial resolution possible. This limitation is due to the low intrinsic brightness (defined as the photon flux or power emitted per unit area and unit solid angle) of the globar source. Synchrotron radiation, on the other hand, is incredibly bright, 100-1000 times brighter than a globar source. This is not due to an increase in power, rather due to the smaller effective source size and narrower angular range of emitted light.[20] This higher brightness allows diffraction-limited spatial resolutions of 3-8 μm to be achieved, whilst maintaining high signal-to-noise ratios. Figure 2.9 shows IR spectra of the same sample measured using a globar and synchrotron IR source respectively. It is difficult to distinguish sample bands from the spectral noise in the globar source spectrum (Figure 2.9, top), whereas the spectrum collected using synchrotron radiation is much cleaner (Figure 2.9, bottom). Importantly, increased

signal-to-noise ratios mean absorbances from lower concentration samples are more easily detected. Thus, this technique is useful for monitoring small populations of transient intermediates. Further advantages synchrotron radiation has over globar sources are the broad and continuous spectral range; high intensity; it is naturally well collimated; it is pulsed on the picosecond timescale; and possesses a high degree of polarization.[24] IR microspectroscopy can use a number of different sample geometries. Work in this Thesis uses reflectance-absorbance as described in Section 2.1.2.2.

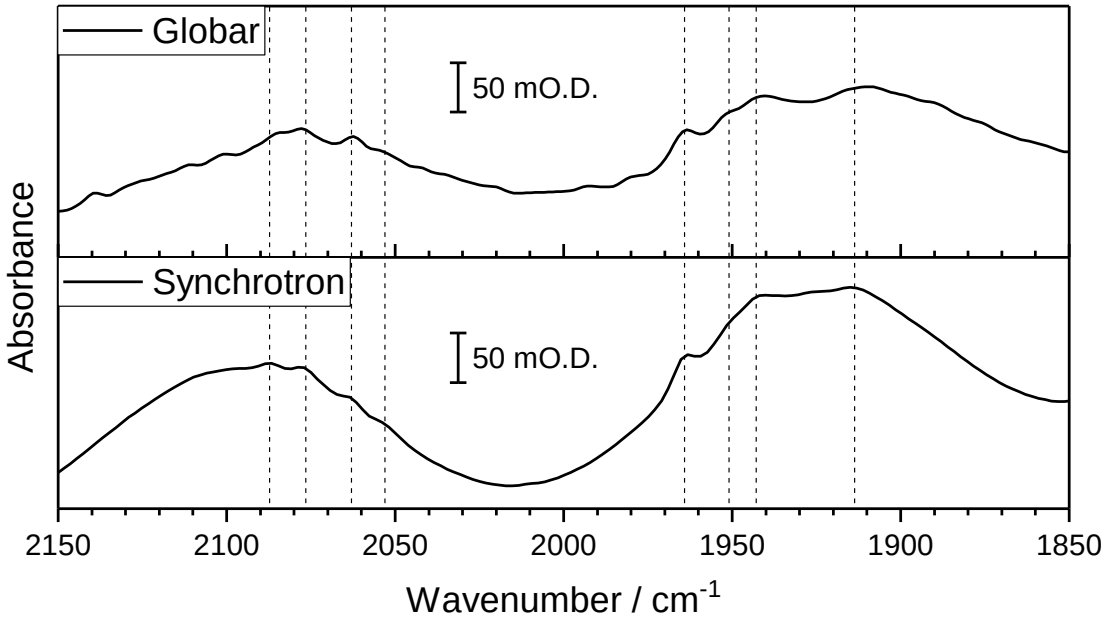


Figure 2.9 Comparison of IR sources and the effect on the quality of IR spectra. Top: Silicon carbide globar source. Bottom: Synchrotron radiation. Dotted lines signify the position of IR peaks as determined by the 2nd derivative spectrum of the synchrotron spectrum. These peaks are almost indistinguishable from the noise in the globar spectrum.

2.1.4. IR spectra of carbonyl and cyanide ligands

Carbonyl (CO) and cyanide (CN^-) ligands are diatomic asymmetric ligands that have distinct, sharp bands in IR spectra between 2100-1800 cm^{-1} and 2250-1950 cm^{-1}, respectively.[25,26] Bonding to a metal centre affects the strength of the C-O/N bond, and

thus the frequency at which it absorbs IR light. Hence, IR spectra of these ligands are useful reporters of the electronic behaviour of the metal they are bonded to.

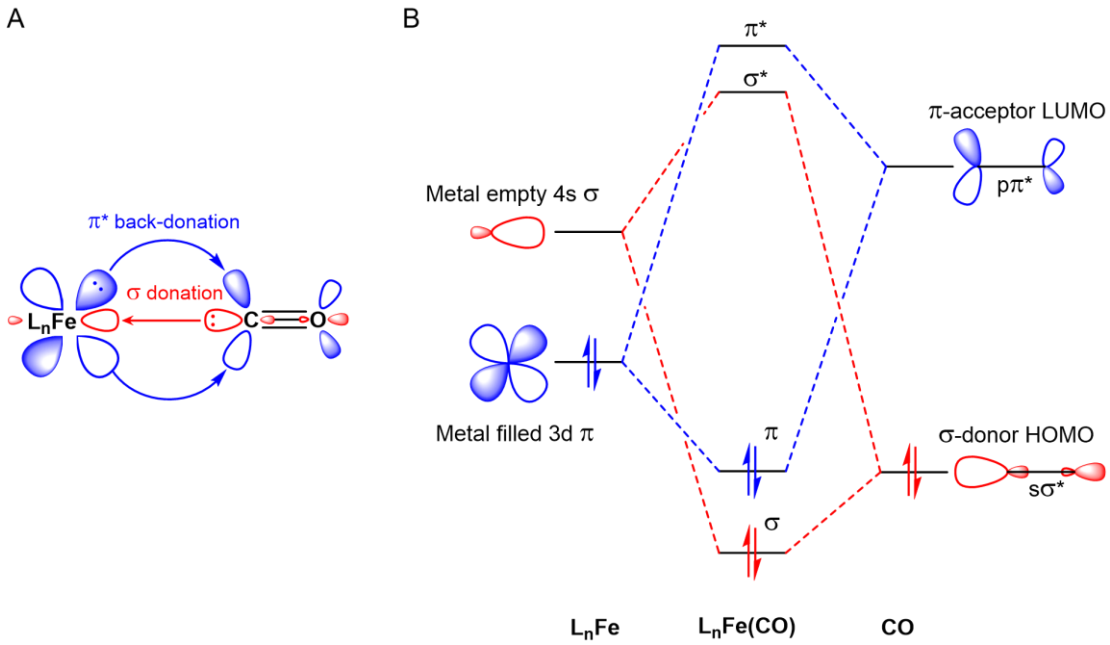


Figure 2.10 A: Synergistic bonding interaction between a transition metal and a π-acid ligand (Fe and CO respectively in this example). A second set of Fe d-orbitals (π symmetry) and CO antibonding orbitals (π* symmetry), not depicted, lie perpendicular to the plane of the page. B: Fragment molecular orbital diagram showing σ-interaction and π-interactions involved in bonding between a metal, Fe, and the π-acid ligand, CO. The resulting $L_nFe(CO)$ complex orbitals are symmetry adapted linear combinations (SALCs) based on a metal in octahedral symmetry.

Due to their ability to accept electrons into an unoccupied π orbital, carbonyl and cyanide ligands are often referred to as π-acid ligands. The bonding between a metal and a π-acid ligand is described as a synergistic σ-donating, π-accepting interaction. The highest occupied molecular orbital (HOMO, σ symmetry) of the π-acid ligand donates electrons to the metal's empty ns orbital (σ symmetry), increasing electron density on the metal. Simultaneously, the lowest unoccupied molecular orbital (LUMO, π* symmetry) on the ligand accepts electron density from the filled nd orbitals (π symmetry) on the metal

centre. Figure 2.10 shows the overall bonding between a metal and a π-acid ligand, along with a fragment molecular orbital diagram.

The degree of π-back bonding between the metal and ligand directly affects the wavenumber position of the ligand's vibrational peaks in the mid-IR. This is clearly observable with CO and CN^- metal complexes. As electrons are accepted into the antibonding π-orbital of the ligand, the C-O/N bond is weakened and becomes more double-bond like in character (Figure 2.11). Thus, the force constant, k_f, decreases, along with the vibrational frequency (Equation [2.4]).

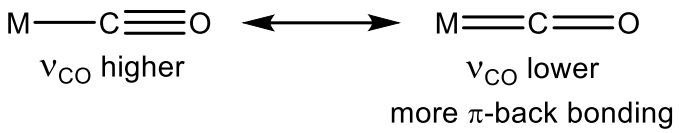


Figure 2.11 The effect of π-back bonding on the character of the C–O bond.

The strength of the π-back bonding interaction depends on the electronic configuration of the metal and the strength of the σ-donation interaction. As the oxidation state of the metal increases, the metal d orbitals are stabilised, bringing them closer in energy to the σ-donor orbitals on the ligand. This improves the σ-donation interaction. At the same time, the degree of π-back bonding decreases as the metal d orbitals are further away in energy from the ligand LUMOs. Therefore, the vibrational frequency of the C-O/N bond increases with metal oxidation state. Table 2.1 shows how the ν(CO) and ν(CN) bands change with oxidation state of iron for homoleptic complexes of these ligands. For both the carbonyl and cyanide complexes, the vibrational frequencies increase as the formal oxidation state of the iron increases.

Table 2.1 Vibrational ν(CO) and ν(CN) frequencies observed in IR spectroscopy of a set of mononuclear iron carbonyl and mononuclear iron hexacyanide complexes.[25,27]

Complex	**Formal oxidation state of iron**	**ν(CO) / cm^{-1}**	**ν(CN) / cm^{-1}**
$[Fe(CO)_4]^{2-}$	2-	1815	-
$[Fe(CO)_5]$	0	2030	-
$[Fe(CO)_6]^{2+}$	2+	2215	-
$[Fe(CN)_6]^{4-}$	2+	-	2098
$[Fe(CN)_6]^{3-}$	3+	-	2135

The main difference between CO and CN^- as ligands is in their ability to act as π-acceptors. Carbonyl ligands are very good π-acceptors, due to the better energy match between their π-antibonding LUMOs and the metal d orbitals. Therefore metal carbonyl complexes usually have ν(CO) values lower than free CO (ν_{CO} = 2155 cm^{-1})[25]. Cyanide, on the other hand, is a much stronger σ-donor due to its negative charge and lower energy 5σ HOMO, and consequently a poorer π-acceptor. Thus, metal cyano complexes have ν(CN) above that of free CN^- (ν_{CN} = 2080 cm^{-1})[25]. Furthermore, factors that affect the degree of π-bonding (such as increasing metal oxidation state) do not impact the shifts in ν(CN) bands as much as their analogous carbonyl complexes.

A second factor that can impact the degree of π-back bonding, and thus the vibrational bands of carbonyl and cyano metal complexes, is the presence of other co-ligands. When a

ligand that is strongly σ-donating is also bonded to a carbonyl complex, the extent of π-back bonding increases. This is due to an increased electron density on the metal from the σ-donating ligands. Table 2.2 demonstrates this principle with molybdenum carbonyl complexes. The ν(CO) bands decrease with increasing substitution of σ-donating $P(OMe)_3$ ligands.[28] The arrangement of the ligands also plays an important role as different stereoisomers have different ν(CO) bands.

Table 2.2 The effect of substitution of a molybdenum hexacarbonyl complex on ν(CO) frequencies observed. L=$P(OMe)_3$ Only the highest ν(CO) band for each complex is given.[28]

Complex	**ν(CO) / cm^{-1}**
$Mo(CO)_6$	2120
$Mo(CO)_5L$	2080
$Mo(CO)_4L_2$	2036
mer-$Mo(CO)_3L_3$	1993
fac- $Mo(CO)_3L_3$	1977
$Mo(CO)_4L_2$	1909
$Mo(CO)L_5$	1844

The intensities of the vibrational bands of metal carbonyl/cyano complexes are also influenced by the π-back bonding interaction. Despite the large difference in electronegativity between C and O, free CO has a net dipole close to zero due to sp hybridisation. However, binding to a metal centre induces polarisation of the C-O bond,

thus increasing the bond dipole. As peak intensities are proportional to dipole moment (Equation [2.7]), ν(CO) bands often have large absorbances. Conversely, the dipole moment of the C-N bond decreases upon binding to a metal centre due to the strong σ-donating and poor π-accepting interactions decreasing electron density on the carbon. Thus, the overall intensities of ν(CN) bands tend to be lower than ν(CO).[29]

[NiFe]-hydrogenases contain one carbonyl and two cyanide ligands bonded to the Fe in their active sites (Figure 1.1C). Each of these ligands are IR active, and the active site gives rise to three distinct bands in the IR spectrum: one CO stretching vibration, two CN stretching vibrations (one symmetric and one antisymmetric due to vibrational coupling). The stretching frequencies of these ligands differ from those found in small molecule systems such as $Fe(CO)_6$ and $[Fe(CN)_6]^{4-}$ due to hydrogen bonding to the surrounding secondary amino acid residues Arg and Ser and the presence of thiolate co-ligands.[30,31] The positions of the CO and CN vibrational bands are sensitive to the electron density and coordination of the active site and hence IR spectroscopy is a useful tool for monitoring active site redox chemistry.

2.1.5. Data processing

The IR data presented throughout this Thesis is processed in order to clearly identify the IR bands in each spectrum. This section will give a detailed walkthrough of how the "raw" IR spectra collected using OPUSv7.1 software is treated, using data collected using the single crystal IR microspectroscopic-electrochemical technique as an example. All data analysis was carried out using OriginPro software (OriginLab Corp., version 9.1).

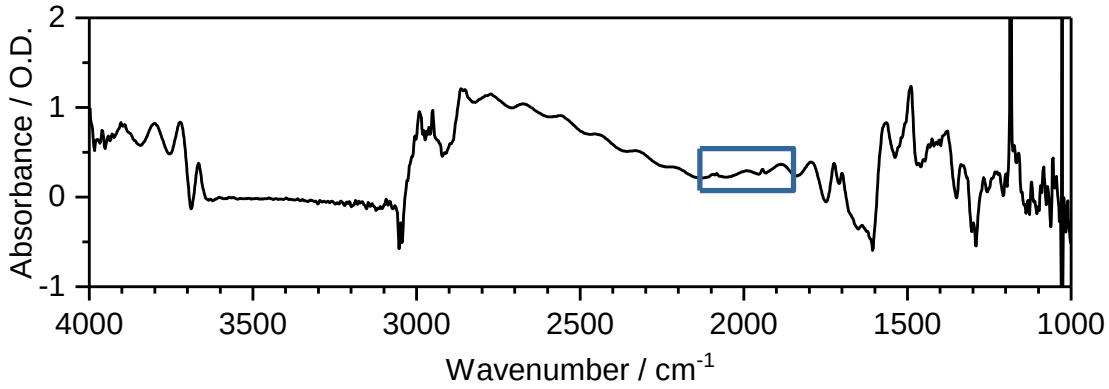


Figure 2.12 Full unprocessed 'absolute' IR spectrum of a single crystal of as-isolated Hyd-1, pH 5.9, at open circuit potential, +205 mV *vs* SHE. The ν_{CO} and ν_{CN} regions (2150 – 1800 cm^{-1}) are highlighted by the blue rectangle.

Figure 2.12 shows an 'absolute' IR spectrum of a single crystal of as-isolated Hyd-1, pH 5.9, at open circuit potential, +205 mV *vs* SHE. The complete 4000-1000 cm^{-1} range is shown. An 'absolute' IR spectrum is one recorded against a background reference spectrum without the sample present. For the IR microspectroscopic-electrochemical experiments, a background measurement is recorded when the IR beam is focused on an empty section of the working electrode approximately 30 µm from the edge of a crystal. As the background spectrum contains the buffer solution, when the absolute sample spectrum is measured, absorption from the buffer is automatically subtracted leaving only the IR peaks from the sample. A low frequency sinusoidal interference pattern is superimposed onto the IR spectrum in Figure 2.12, most noticeably between 2800 – 1800 cm^{-1}. This is due to multiple internal reflections between thin layers in the IR microspectroscopic-electrochemical cell (see Section 2.1.2.2). The reference and sample spectra are recorded on different sections of the cell, with minute difference between the thin layers. These differences lead to the sinusoidal interference. This interference pattern varies between experiment and is ideally minimised by choosing an appropriate background spectrum. It can also change with time, as shown in Figure 2.13. During an

electrochemical redox titration, recorded over a period of approximately 4.2 hours, the sinusoidal interference increases in amplitude whilst undergoing a phase shift. IR spectra collected at the start and end of a redox titration show different interference patterns (red and blue spectra respectively in Figure 2.13). Therefore, each spectrum measured has a different baseline and requires individual processing.

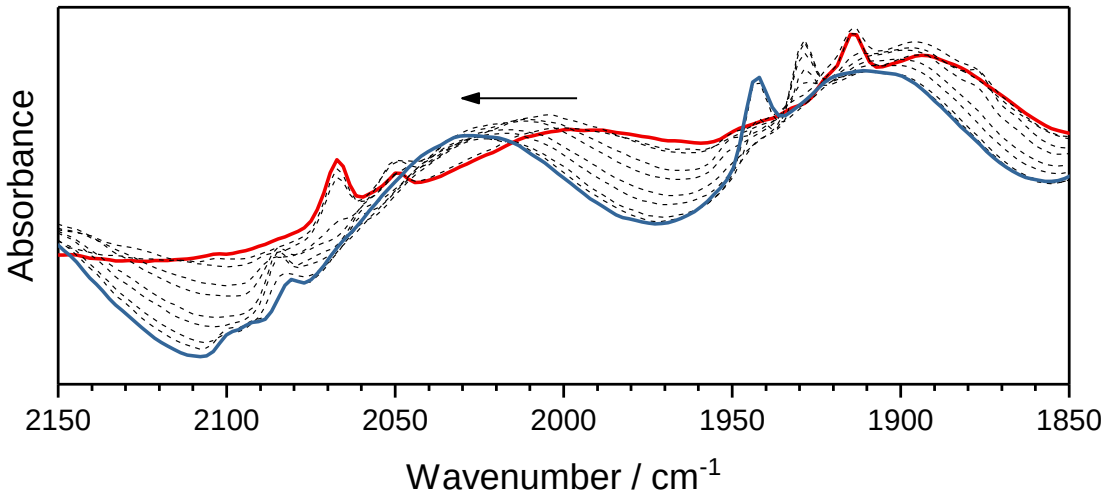


Figure 2.13 The sinusoidal interference present during the IR microspectroscopic-electrochemical experiments changes with time. Over the course of an electrochemical titration, the amplitude of the interference increases, and the phase shifts to higher wavenumbers. Time passed between the first (red spectrum) and the last (blue spectrum) is approximately 4.2 hours. The black dotted lines represent the IR spectra recorded in between the first (red) and last (blue) spectrum of the electrochemical titration. The black arrow indicates the phase shift of the interference.

A baseline is subtracted from each individual spectrum using an interpolated spline function (Figure 2.14A). Corresponding 2nd derivative spectra are used to identify the position of peaks and guide the placement of the baseline anchors (Figure 2.14B). If the bands identified in the 2nd derivative spectrum occur in either the peak or trough of the sinusoid, then baseline anchors need to be placed underneath the bands (as seen by the point around 2085 cm^{-1} in Figure 2.14A) to preserve the true peak absorbances. This is done carefully as it risks distorting peaks.

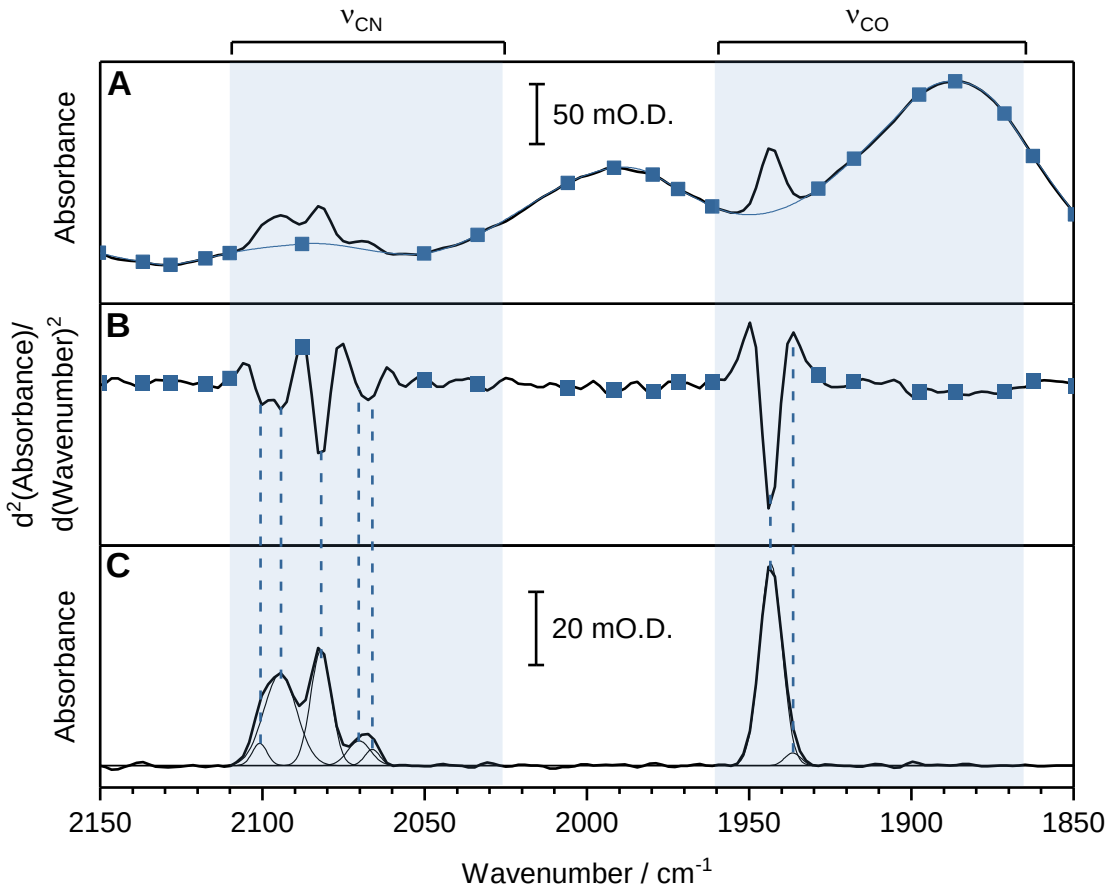


Figure 2.14 Subtracting a baseline from an IR spectrum (example: single crystal of as-isolated of Hyd-1 at pH 5.9, at open circuit potential, OCP, of +209 mV *vs* SHE). A: 'Absolute' IR spectrum with the blue squares marking the baseline points used to subtract the sinusoidal baseline (blue line). B: The 2nd derivative IR spectrum of the spectrum shown in (A). The blue squares mark the baseline points showing that their placement avoids any peak absorption. C: Baseline subtracted IR spectrum. The fitted Gaussian peaks are shown by the thin black lines. Dotted lines between (B) and (C) show that the fitted Gaussian peaks match the peaks identified in the 2nd derivative spectrum. The shaded blue areas mark the ν_{CO} and ν_{CN} regions.

After baseline-subtraction, each spectrum is fitted to Gaussian profiles (Figure 2.14C). Whilst a combination Gaussian-Lorentz profile is traditionally used for fitting peaks in IR data, and it is used in the case for the PFIRE data, a purely Gaussian profile is more appropriate for IR spectra collected on single crystals of protein. This is because the peak shape varies between the solid and liquid state, as explained in Section 2.1.1.4.

As before, the positions of the bands are chosen with reference to the 2nd derivative spectrum. Occasionally, the fitted data do not align well with the baseline-corrected data. This is due to the presence of hidden or overlapping peaks. Figure 2.15 shows an example of unaligned fitting to the baseline-corrected spectra. The blue line represents the cumulative fitted peaks which is shown to overlay the baseline-corrected spectrum (black) poorly in some areas. Adding in extra peaks, in this example at 2100, 2070 and 1938 cm^{-1}, improves the fitting of the peaks to the baseline-subtracted data.

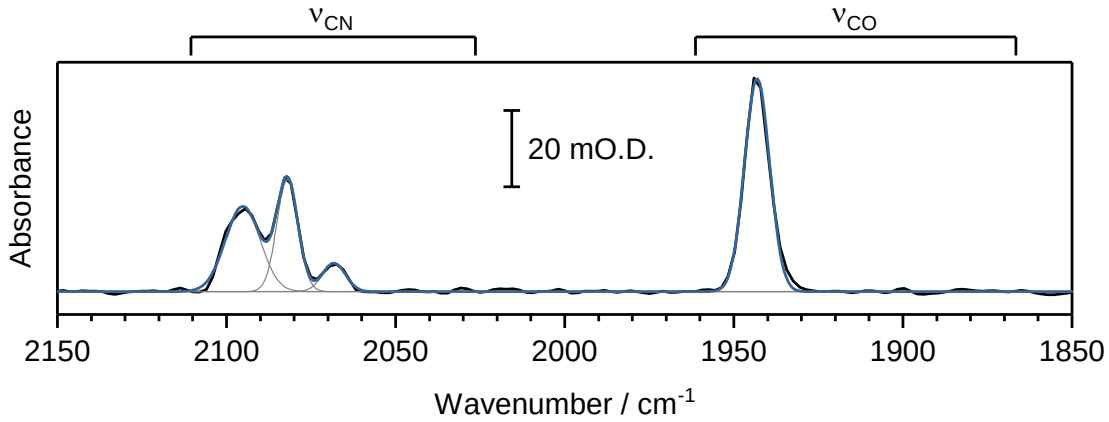


Figure 2.15 Example of poor fitting of the baseline subtracted spectrum to Gaussian profiles. The cumulative fitted peaks are shown by the blue line, which overlays the baseline subtracted spectrum (black line) poorly.

Some data collected on the Diamond synchrotron beam line showed a high frequency sinusoidal interference pattern on top of the persistent low frequency interference fringe. The origin of this interference fringe is unknown and posed a problem in distinguishing active site peaks. IR spectra that contained this noise was digitally filtered using a Savitzky-Golay algorithm[13] as shown in Figure 2.16. A fourth order polynomial fit with 15 data points is used to give the smoothed IR spectrum shown in blue. Parameters were chosen to minimise the high frequency interference pattern whilst maintaining the shape

and amplitude of the peaks from the crystal sample. However, spectral detail of low concentration species may have been filtered out.

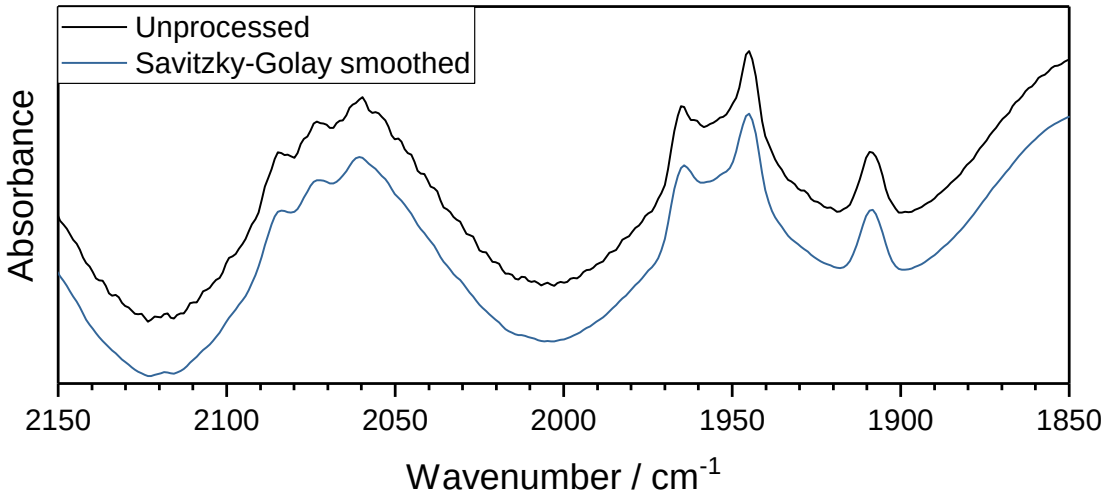


Figure 2.16 Applying a digital filter removes the high frequency interference that appears on some data collected using the IR microspectroscopic-electrochemical cell (shown here, an IR spectrum of single crystals of Hyd-2, pH 5 held at -595 mV *vs* SHE). The unprocessed spectrum is shown in black. A Savitzky-Golay filter was applied using a fourth order polynomial fit with 15 data points to give the smoothed IR spectrum shown in blue.

2.2. Protein film electrochemistry

2.2.1. Redox reactions in enzymes

A redox reaction is a type of chemical reaction that consists of the transfer of electrons from one species, which is subsequently oxidised, to another species, which is thus reduced. This can be represented by Equation [2.11], where *n* represents the number of electrons, *y* and *z* are the stoichiometric coefficients of the oxidised and reduced species in the cell half-reaction.

$$Ox_y + ne^- \rightleftharpoons Red_z \qquad [2.11]$$

Many biological processes involve redox reactions. Thus, electrochemical techniques are ideal for determining the kinetic and thermodynamic properties of these reactions.

The vast majority of work in this Thesis (aside from studies using PFIRE under turnover conditions, as in Chapter 3) involves studying [NiFe]-hydrogenases under electrochemical equilibrium conditions, i.e. when there is no net flux of electrons through the electrode. The potential, *E*, of the redox couple in Equation [2.11] at equilibrium is dependent on the activities of the reduced and oxidised species, as given by the Nernst equation (Equation [2.12]; *n* represents the number of electrons, *R* is the gas constant, *T* is the temperature, *F* is the Faraday constant, *y* and *z* are the stoichiometric coefficients of the oxidised and reduced species in the cell half-reaction, and a_{ox} and a_{red} are their respective activities).

$$E_{red} = E^{\circ}_{red} - \frac{RT}{nF} - \ln\left\{\frac{a^{z}_{red}}{a^{y}_{ox}}\right\} \qquad [2.12]$$

The standard reduction potential, E°_{red}, is different to the measured reduction potential of the redox couple, E_{red}, in that it is a thermodynamic parameter dependent on the Gibbs free energy of the redox process. The reduction potential, E_{red}, is instead the measured potential difference between the electrode where the reaction is occurring and a reference electrode (see Section 2.2.2.2).

When two redox processes are coupled in an electrochemical cell, current flows and a reaction occurs until equilibrium is reached and the potential difference between the electrodes reaches zero. However, with the methods described below, a potentiostat is used to control the potential of a "working electrode", allowing oxidation/reduction to be controlled and measured, and electrocatalytic activity to be initiated.

Proton-coupled electron transfer

When an electron transfer process is accompanied by a proton transfer process, it is referred to as proton-coupled electron transfer (PCET). PCET can occur either concertedly, i.e., the electron and proton transfers take place simultaneously, or via a stepwise

process., where either an electron or proton transfer occurs immediately followed by the other. These processes are integral to the catalytic mechanism of [NiFe]-hydrogenases and there is much debate on how these PCET steps occur, concerted or stepwise, and by which amino acid residues.

For a proton-dependent process, Equation [2.13], the redox couple potential is now given by Equation [2.14]. The involvement of protons within the redox reaction means that the redox potential is dependent on pH (Equation [2.15]).

$$Ox + ne^- + H^+ \rightleftharpoons RedH \quad [2.13]$$

$$E = E^0 - \frac{RT}{nF}\ln\left\{\frac{[RedH]}{[Ox][H^+]}\right\} \quad [2.14]$$

$$E = E^0 - \frac{0.059}{n}\log\left\{\frac{[RedH]}{[Ox]}\right\} - \frac{0.059}{n}pH \quad [2.15]$$

2.2.2. Principles of protein film electrochemistry

The behaviour of a redox centre within a metalloprotein can be studied using protein film electrochemistry (PFE). When a protein is immobilised onto an electrode, the electrode acts as a direct redox partner of the studied enzyme, providing a continuous flow of electrons, back and forth, as the potential is varied. This allows potential control over the enzyme and thus the kinetics and thermodynamics of an enzymatic reaction can be observed. In the absence of substrate, this allows the redox properties of the enzyme to be determined. PFE also allows study of the catalytic properties of the adsorbed enzyme. When substrate is present, the enzyme can undergo steady-state catalysis. In this case, current can be used as a measure of the catalytic activity of the enzyme film. The current, i, is directly proportional to rate, as given by Equation [2.16].[32] Here, k_E represents the potential-dependent turnover frequency of the enzyme, the number of electrons involved

is given by n, A is the electrode surface area, Γ is the electroactive coverage and F is the Faraday constant.

$$i = k_E nA\Gamma F \quad [2.16]$$

However, there are factors that can result in the measured current not truly representing the rate of the redox processes that occur within the adsorbed enzyme.

Faradaic and non-Faradaic currents

There are two components of the current measured during an electrochemical experiment: Faradaic and non-Faradaic. The current arising from charge transfer at the electrode-solvent interface, such as enzyme-electrode redox reactions, are governed by Faraday's law, and thus called Faradaic currents. These are usually the currents of interest. However, when there is a change in potential or solution composition (e.g. addition of an inhibitor), other processes occur, giving rise to non-Faradaic currents. These include the adsorption/desorption on the electrode, and the ionic interaction between the charged electrode and the solvent molecules which rearrange to form an electrical "double layer" at the electrode-solvent interface. Non-Faradaic currents are usually small relative to Faradaic current and decay with time following a change in potential.

Mass transport

An inherent necessity of any electrochemical measurement is the efficient transport of substrate to and removal of product between the enzyme and the bulk solution, i.e. mass transport. If the experiment is mass transport limited, then the current is no longer purely a measure of the catalytic activity of the redox enzyme, as part of the enzyme is not undergoing catalysis. This issue can be overcome by using a rotating ring disk electrode in the standard protein film electrochemical measurement, or by using another method of

stirring the bulk solution, for example, by using a flow cell. Increasing the electrode rotation rate or flow rate of the system will have an effect on the current up to a certain point, at which the experiment is no longer mass transport limited.

Interfacial electron transfer

Efficient interfacial electron transfer, i.e. transfer between the electrode and the enzyme, is essential during an electrochemical experiment. As such, an important factor to consider is the orientation of the enzyme on the electrode, as usually only a certain configuration will lead to electroactive coverage. A variety of different adsorption methods have been developed to ensure this is the case.

2.2.2.1. Adsorption of protein onto an electrode

Fast electron exchange between the protein and the working electrode is necessary for good electrochemical control. Figure 2.17 gives examples of the three ways this can be achieved. The simplest method is direct adsorption of the redox protein onto the working electrode *via* electrostatic attraction between the oppositely charged protein residues and electrode surface (Figure 2.17A). In this case, the redox centres on the protein's surface (the distal FeS cluster for [NiFe]-hydrogenases) are in direct contact with the working electrode, allowing for swift electron transfer. This method is utilised in the protein film infrared electrochemistry technique detailed in Chapter 3. However, it is possible for the protein to adsorb onto the electrode surface in a non-electroactive configuration, i.e. one that doesn't facilitate direct electron transfer. Furthermore, using a metal electrode such as Au or Pt can cause protein unfolding due to strong interactions between thiol groups on the protein surface and the metal.

To overcome this, a variety of methods which protect the protein from the metal electrode surface and immobilise the protein in an electroactive configuration have been

developed (Figure 2.17B).[33] Self-assembled alkanethiol monolayers (SAMs) are commonly used to bind enzymes to gold surfaces.[34–36] The monolayer protects the thiol groups on the enzyme surface from the gold surface whilst also providing a reactive functional group on the electrode surface that induces binding of the protein in an electroactive configuration. An alternative technique involves covalently coupling the electrode surface to the protein by forming peptide bonds. This strategy was utilised by Evans *et al.* where peptide coupling with 1-ethyl-3-(3-dimethylaminopropyl)carbodiimide and N-Hydroxysuccinimide (EDC/NHS) was necessary for immobilising the E28Q variant of *E. coli* hydrogenase-1 onto carbon particles for study by PFIRE/PFE.[37]

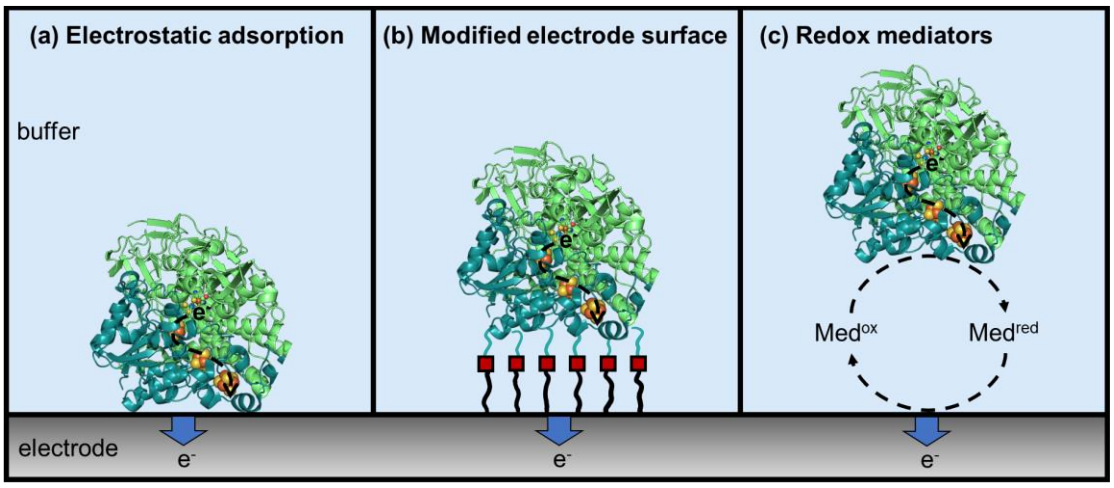


Figure 2.17 Methods of electron transfer between redox protein and an electrode. (A) Adsorption *via* electrostatic attraction to allow direct electron transfer; (B) immobilisation onto a modified electrode surface to facilitate direct electron transfer; (C) redox mediators allow indirect, diffusion-controlled electron transfer.

The above methods, whilst enabling direct electron transfer between the electrode and redox centre of an enzyme, have their limitations. When there is poor electroactive coverage on the electrode, or if the protein remains in solution, an indirect method of electron transfer is required. In these cases, small molecule redox mediators are used to facilitate diffusion-controlled transfer of electrons through the electrolyte (Figure 2.17C).

A wide range of redox mediators, such as viologens, anthraquinones and indigo carmine, have been used to aid the study of the different redox states of [NiFe]-hydrogenase in solution.[7,8,38,39] Mediated electron transfer is also necessary when the protein is crystallised. Diffusion of the mediators through the solvent channels within the crystal enables electron transfer between the electrode and each protein molecule within the entire crystal.[40] There are, however, disadvantages to using mediated electron transfer when studying catalytic reactions. Diffusion-controlled electron transfer *via* redox mediators in solution is likely to become rate limiting, which can result in loss of mechanistic information.

2.2.2.2. Three electrode system

All electrochemical measurements performed in this Thesis use a three-electrode system, consisting of a working electrode (WE), reference electrode (RE) and counter electrode (CE) controlled via a potentiostat, as shown in Figure 2.18. The working electrode is made from an electrochemically inert material and the interface between the electrode surface and the electrolyte solution is where the electrochemical process of interest occurs. The potential of this reaction cannot be measured directly. Instead, the potential difference between the working electrode and reference electrode, which has a known and constant stable potential, is measured, according to Equation [2.17], where $(\phi_E - \phi_S)$ represents the difference in potential between the electrode and the solution. Any changes in *E* are thus solely attributed to potential changes at the working electrode.

$$E = (\phi_E - \phi_S)_{working} - (\phi_E - \phi_S)_{reference} \quad [2.17]$$

A counter electrode is added to complete the circuit and ensure current doesn't flow through the reference electrode, thus affecting its potential. The counter electrode is

usually made from an inert material, such as platinum or carbon, and should have a surface area much greater than that of the working electrode. This is to ensure it is not a limiting factor in the kinetics of the reaction occurring at the working electrode. Furthermore, the counter electrode is ideally placed where it is equidistant from all points on the working electrode, to prevent non-uniform current densities developing across the working electrode surface. Otherwise peak distortions and side reactions may occur.[41]

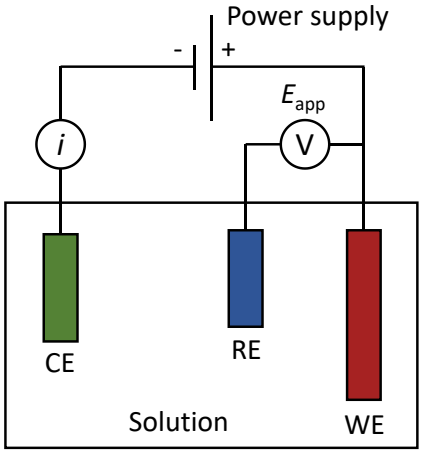


Figure 2.18 Schematic diagram of the set-up of a three-electrode system, with the working electrode (WE), counter electrode (CE) and reference electrode (RE) labelled. The potential difference between the WE and RE, E_{app}, is measured by the potentiostat.

The placement of the reference electrode is also important in a three-electrode system. Ideally, it is positioned as close to the working electrode as possible in order to minimise the uncompensated resistance that arises when current passes through the cell. Uncompensated resistance, R_u, or ohmic drop, is the potential drop that occurs between the working electrode and the reference electrode due to solution resistance and leads to an offset in measured cell potential as represented by Equation [2.18], where i represents the current.[42] The conductivity of the electrolyte solution also impacts the ohmic drop. Solutions with low conductivities have higher ohmic resistance, and thus ohmic drop.

$$E_{measured} = E_{applied} - iR_u \quad [2.18]$$

High uncompensated resistances are often found in thin-layer electrochemical cells, where a small volume of solution (<10 µL) is dispersed in a 2 – 100 µm thin layer at the working electrode. The high resistance of the thin layer leads to a large ohmic drop which needs to be accounted for when using thin-layer electrochemical cells.

In this Thesis, all potentials are reported relative to the standard hydrogen electrode (SHE) which is composed of a platinum wire immersed in aqueous solution at pH 0, 298 K, in equilibrium with 1 bar H_2. Experimentally, a silver-silver chloride, Ag/AgCl electrode is used as the reference electrode. Potentials (E) quoted are thus adjusted to millivolts (mV) *vs* the standard hydrogen electrode (SHE) using the conversion E (mV *vs* SHE) = E (mV *vs* Ag/AgCl) + 201 mV at 20 °C.

A three-electrode system is used to perform two types of electrochemical experiments in this Thesis: potential step chronoamperometry and cyclic voltammetry.

2.2.2.3. Potential step chronoamperometry

Chronoamperometry (CA) is the primary electrochemical technique employed in this Thesis. A constant potential is applied to the working electrode and the resulting current response is recorded as a function of time. The applied potential can then be stepped to a different value, and the subsequent effect on current is observed. With this, the steady state behaviour of a redox species at specific potentials can be monitored to produce a potential titration. In the absence of substrate, no electrocatalytic current is observed, indicative of a lack of catalytic activity. However when the substrate is present, CA allows the study of the catalytic activity of the enzyme, as the current is a direct measure of the enzyme's activity (Equation [2.16]). Ensuring the experiment is not mass transport limited is critical when monitoring the redox states of an enzyme under catalytic conditions. This

is because if mass transport is an issue, then part of the enzyme will not be under electrocatalytic control, and instead reflect the non-catalytic, electrochemical distributions of the redox states.

Chronoamperometry can also be used to study the effect of inhibitors on the catalytic activity of an enzyme, as any changes in current reflect the impact the inhibitor has on the activity of the adsorbed protein.

2.2.2.4. Cyclic Voltammetry

Another invaluable electrochemical technique is cyclic voltammetry (CV). This technique provides a general overview of the enzyme's catalytic properties, such as the onset and rate of electrocatalysis, along with information on the redox potentials of the redox couples within the enzyme. During a CV experiment, the working electrode is swept back and forth between two limiting values, which encompass the potential range at which redox processes occur, and the current response is recorded. The current is then plotted as a function of potential to give a voltammogram.

2.2.3. IR spectroelectrochemistry

As electrochemical and infrared spectroscopic techniques can provide valuable insight into the catalytic properties and structure of proteins, respectively, combining them into a single method allows correlation between the catalytic rate and the molecular species present. IR spectroelectrochemical techniques have been used to investigate a wide range of redox reactions at the electrode surface and in solution.[9,43,44]

There are some factors that need to be considered when combining the two techniques. Firstly, implementing a working electrode into the IR spectroscopic set-up can pose some problems depending on the sample geometry. Both transmission and reflectance-absorbance geometries require thin layer electrochemical cells in order to

minimise masking of sample IR bands by the bulk solution. This can lead to uncompensated resistance and mass transport issues.

Another important aspect is the relative sensitivities of the two techniques. Direct absorption of IR light is a weak effect and requires a high concentration of sample. This is even more prominent when the protein is adsorbed onto an electrode, where only the electrode/protein interface is sampled by IR light (as with reflection-adsorption IR spectroscopy) as opposed to the bulk solution. It may be the case where an electrochemical response is detected, but a spectroscopic one is not. Electroactive coverages of proteins adsorbed on electrodes can be below 1 pmol cm^{-2},[45] and so highly-sensitive spectroscopic approaches are required.

Two different IR spectroelectrochemical techniques are employed in this Thesis: protein film infrared electrochemistry (PFIRE), as developed by Hidalgo *et al.*, for the study of *E. coli* [NiFe] hydrogenase-1 adsorbed onto an electrode in Chapter 3; and an adaptation of single crystal IR microspectroscopic-electrochemistry used to investigate the redox behaviour of multiple preparations *E. coli* [NiFe] hydrogenase-1 and *E. coli* [NiFe] hydrogenase-2 crystals in Chapters 4-7.

2.3. Protein preparations

The protocols used to prepare *Escherichia coli* WT Hyd-1 (wild type hydrogenase-1) and *Escherichia coli* Hyd-2-NOP (native overproduced hydrogenase-2) are those that have been described previously.[46,47] Following Ni-affinity and size exclusion chromatography, purified Hyd-2-NOP was concentrated to 5 mg mL^{-1}, as judged by Bradford assay. For WT Hyd-1, three different preparations were obtained: without the cytochrome *b* subunit (Hyd-1), with the cytochrome *b* subunit (Hyd-1-cyt*b*) and an unpurified 'mixed' Hyd-1, i.e. some Hyd-1 molecules with the cytochrome *b* subunit, and some without it. For the

protein film infrared electrochemistry experiments, the 'mixed' Hyd-1 was used whereas separation of the Hyd-1 and Hyd-1-cyt*b* was necessary for crystallisation. This was obtained by using hydroxyapatite chromatography. Once again, the protein solutions were then concentrated to 5 mg mL^{-1} according to Bradford assays.

DeltaTM (delta transmembrane) Hyd-1 enzyme was prepared from the FTH2014 *E. coli* K-12 strain by Dr Stephen Carr according to the previously published procedure.[48] Solutions were also concentrated to 5 mg mL^{-1} as judged by Bradford assay.

2.4. Crystallisation

2.4.1. Buffer solutions

All buffers in this work were prepared in ultra-high purity water (MilliQ Millipore, 18 MΩ cm) and degassed with N_2 prior to use.

SEC buffer: 20 mM Tris, pH 7.2, 150 mM NaCl, 0.02% (w/v) DDM detergent, 1 mM dithiothreitol

Hydrogenase-1 crystallisation buffer: 100 mM Bis-Tris pH 4.0, 200 mM Li_2SO_4, 150 mM NaCl, PEG 3350 (19-21% w/v) or 100 mM Bis-Tris pH 5.9, 200 mM Li_2SO_4, 150 mM NaCl, PEG 3350 (19-21% w/v) or 100 mM tris.HCl pH 8.0, 200 mM Li_2SO_4, 150 mM NaCl, PEG 3350 (19-21% w/v)

Hydrogenase-2 crystallisation buffer: 100 mM Bis-Tris pH 5.9, 200 mM $MgCl_2$, PEG 3350 (19-22% w/v)

The crystal stabilisation buffers were prepared by adding 23% w/v PEG 3350 to the crystallisation buffer.

2.4.2. Procedure

Prior to crystallisation, protein solutions, prepared according to Section 2.3, were buffer exchanged into SEC buffer. Vivaspin 20 mL, 50 kDa molecular weight cut-off centrifugal concentrators were used to perform repeated spin concentrations and dilutions until a 1500-2000 fold dilution of the previous buffer was achieved. All protein samples were then concentrated to 5 mg mL^{-1} as judged by Bradford assay.

Crystals of Hyd-1 (with and without cyt*b* sub-unit) and Hyd-2-NOP were acquired under the guidance of Dr Stephen Carr, Research Complex at Harwell, according to previously established protocols.[47,48] This was done using the sitting drop vapour diffusion technique, where 1.5 µL of 5 mg mL^{-1} protein solution was mixed with an equal amount of crystallisation buffer followed by streak seeding with old smaller crystals of the appropriate protein. Long rod-shaped crystals appeared within 24 hours of incubation at 293 K in an anaerobic atmosphere (<0.3 ppm O_2). The size and number of crystals varied between wells.

Crystals of deltaTM Hyd-1 were prepared by Dr Stephen Carr and used as received.

For measurements made at pH 4.0, crystals of as-isolated Hyd-1 (grown at pH 5.9) were soaked for 2 – 3 minutes in (Hyd-1 pH 4 stabilisation buffer). Crystals of Hyd-1 were grown at pH 8.0 for measurements.

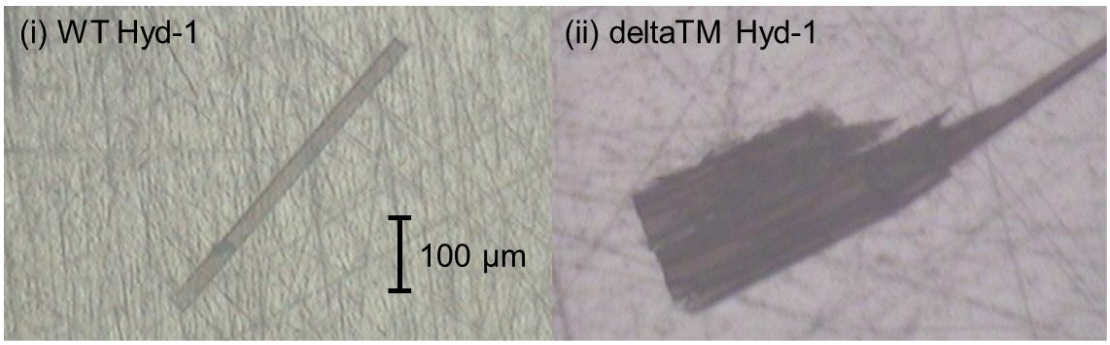


Figure 2.19 Different *E. coli* K-12 strains produced different sized crystals: (i) WT Hyd-1 crystals are long and thin with widths between 15 - 30 µm; (ii) deltaTM Hyd-1 crystals are often much larger, reaching over 100 µm in width and ~250 µm in length. Images are taken at 4× magnification.

Calculation for the number of active sites per unit of crystal volume

Crystals of *E. coli* hydrogenase-1 and hydrogenase-2 are in the space group $P2_12_12_1$ and have approximately the same unit cell volume.[47,49]

Approximate Unit cell volume = 93 x 97 × 183 $Å^3$ = 1.651 × 10^6 $Å^3$

Unit cells / $µm^3$ = 605,700

In Spacegroup $P2_12_12_1$, the unit cell contains 4 asymmetric units.

Thus, hydrogenase molecules / $µm^3$ = 2,423,000

The protein is a dimer, therefore there are 4.846 x 10^6 active sites / $µm^3$

Conversion of number of active sites to effective molarity of active sites

$$molar\ concentration\ of\ active\ site = \frac{number\ of\ active\ sites\ \div Avogadro's\ constant}{volume\ in\ dm^3}$$

$$\frac{4.846 \times 10^6\ \div (6.022 \times 10^{23})}{1 \times 10^{-15}} = \sim 8\ mM\ per\ \mu m^3$$

Thus, the effective concentration of Hyd-1 and Hyd-2 crystals is approximately 8 mM.

An exception to this are the Hyd-1 crystals with the cytochrome B sub-unit still present. The unit cell volume of these crystals is larger, and thus there are fewer active sites per μm^3 resulting in a lower molar concentration of active site states (~3 mM).

2.5. Protein film IR electrochemistry set-up

2.5.1. Reagents and equipment

2.5.1.1. Buffer solutions

Potassium phosphate buffers were prepared by titrating solutions of potassium phosphate dibasic anhydrous (K_2HPO_4, Sigma-Aldrich) and potassium phosphate monobasic anhydrous (KH_2PO_4, Sigma-Aldrich) until the desired pH was reached.

4-Morpholineethanesulfonic acid (MES), 4-(2-Hydroxyethyl)piperazine-1-ethanesulfonic acid (HEPES), N-[Tris(hydroxymethyl)methyl]-3-aminopropanesulfonic acid (TAPS), 2- (Cyclohexylamino)ethanesulfonic acid (CHES) and sodium acetate (CH3COONa) were purchased from Sigma-Aldrich and NaCl, HCl 37% and NaOH were purchased from Fisher Scientific. They were used to prepare mixed buffer solutions at the desired pH values.

All buffers were prepared in ultra-high purity water (MilliQ Millipore, 18 MΩ-cm) and were degassed with N_2 prior to use in experiments.

2.5.1.2. Gases

N_2, Ar, H_2 and CO were purchased from BOC. All these gases were passed through an O_2-removal filter (Restek Super-Clean, gas outlet quality > 99.9999 %) before using them in experiments.

2.5.1.3. Sample preparation

Carbon nanoparticles Black Pearls (BP) 2000 (approximately 1300 $m^2 g^{-1}$) were purchased from Cabot Corp and sonicated in 15 mM potassium phosphate buffer solution, pH 5.8, prior to each experiment to give 20 mg mL^{-1} dispersions.

E. coli hydrogenase-1 solution (5 mg mL^{-1}) was prepared as described in Section 2.3, although further purification to remove the cytochrome *b* sub-unit was not necessary. Hyd-1 modified particles were prepared by adding a 50 µL aliquot of Hyd-1, whose buffer was exchanged for phosphate buffer (15 mM, pH 5.8) using a centrifugal filter unit (Ultracel – 50K membrane), to a 5 µL aliquot of 20 mg mL^{-1} BP 2000 dispersion and left for adsorption overnight at <5° C. The non-absorbed Hyd-1 was then removed by washing with buffer and centrifugation. The resulting Hyd-1 modified particles were concentrated back down to give a 20 mg mL^{-1} dispersion.

2.5.1.4. Sample handling

All studies were carried out in anaerobic glove boxes (Glove Box Technology, < 1 ppm O_2), as the samples used are air/O_2-sensitive. All solution were saturated with N_2 for approximately 2 hours per 100 mL before transfer into the glove box to remove all traces of oxygen.

2.5.1.5. ATR-IR spectroelectrochemical cell

The ATR-IR spectroelectrochemical cell was built in house as previously reported.[50] A 2 mm diameter miniature Ag/AgCl electrode (eDAQ) was used as the reference electrode as opposed to a mini saturated calomel electrode. Pt wire (Surepure Chemetals, 99.99 %, 26 gauge) was used as the counter electrode and the working electrode was made from carbon pencil lead (Pentel 0.9 mm Ain Stein HB lead, WH Smith) connected to a Pt wire by silver-loaded epoxy resin (RS Components). A trapezoidal Si internal reflection element

(IRE) measuring 8.39 x 5 x 1 mm^3, face angle 39° (Crystal GmbH) was thoroughly washed by sonication in concentrated H_2SO_4, oxidation in concentrated HNO_3, rinsed in water, and then left in H_2O prior to cell assembly.

2.5.1.6. Instrumentation

FTIR spectra were recorded using a Bruker Vertex 80 IR-spectrometer with OPUS v.7.4 software. OriginLab Pro software was used to perform baseline corrections and peak fitting of the spectroscopic data. All spectra were recorded at 2 cm^{-1} resolution. Electrochemical measurements were controlled by an AutoLab 128N potentiostat (Metrohm) controlled by Nova 1.10 software.

2.5.2. Experimental procedure

The Si IRE is sealed into the ATR cell baseplate with silicone sealant (Dowsil, SE 9187L Silicone RTV). A background of the baseplate and prism is recorded before continuing the cell assembly. 1 µL of the Hyd-1 modified nanoparticles is drop-cast onto the Si IRE and allowed to partially dry before a rectangle of 110 µm thick carbon paper (approximately 5 x 8 mm^2, Toray, TGP-H-030) is placed on top of the film. The cell body containing the electrodes is then screwed onto the baseplate and 100 µL of mixed buffer solution, pH 6, is added to the cell in order to prevent the Hyd-1 modified particles from drying out.

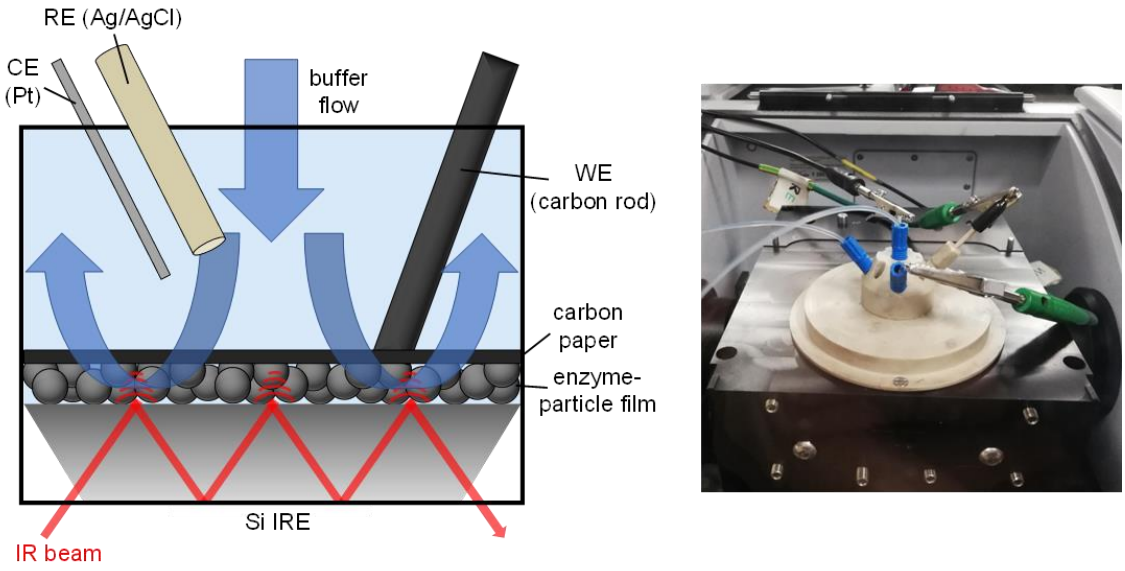


Figure 2.20 ATR-IR cell set-up used for the PFIRE experiments. Left: Schematic diagram. The reference (RE), counter (CE) and working (WE) electrodes are labelled along with the Si internal reflection element (IRE). The red waves represent the evanescent IR waves penetrating the sample. The blue arrows imitate the buffer flow throughout the cell. Right: Photograph of the ATR-IR cell on the ATR accessory within the IR-spectrometer.

The assembled cell is connected to the pump flow system with a peristaltic pump (Watson-Marlow 120U/D1) which provides continuous flow of Ar- or H_2-saturated buffer solutions through the cell at a flow rate of approximately 60 mL min^{-1}. The gases were added to the buffer using a mass flow controller (Brooks) so the concentration and flow rates could be accurately monitored. When switching to a different buffer (for example, if changing the pH of the solution), the new buffer is flowed through the cell for a minimum of 10 minutes to ensure complete buffer exchange.

2.6. IR microspectroscopic-electrochemical set-up

In this section, the materials and chemicals used to build the IR microspectroscopic-electrochemical cell as developed in Chapter 4 and used in Chapters 4-7, are described. A detailed experimental procedure is also given.

2.6.1. Reagents and equipment

2.6.1.1. Hydrogenase crystals and buffers

Crystal samples and buffers used in the IR microspectroscopic-electrochemical experiments described in Chapters 4-7 were prepared as described in Section 2.4 above.

2.6.1.2. Redox mediators

2,6-dichloroindophenol sodium salt (DCPIP), phenazine methosulfate, indigo carmine, anthraquinone-2-sulfonate, and methyl viologen were purchased from Sigma. Each mediator was initially made up to a 100 mM solution (50 mM for indigo carmine and anthraquinone-2-sulfonate due to their slight insolubility at high concentrations) in the appropriate crystal stabilisation buffer. The redox mediator cocktail solution was then prepared by dilution of each mediator solution with the appropriate crystal stabilisation buffer to give a 1 mM final concentration of each redox mediator.

2.6.1.3. Electrode and electrode materials

Working electrode: A 4 mm diameter glassy carbon rod (Alfa Aesar) is sealed into a custom brass connector using silver-loaded epoxy resin (RS Components) and then sealed into the custom Delrin holder with resin (Araldite).

Counter electrode: A graphite ring counter electrode (Goodfellow, 1.6 mm wall thickness, 12.7 mm outer diameter, 9.5 mm inner diameter) is sealed to a Pt wire (Surepure

Chemetals, 99.99 %, 26 gauge) connector with silver-loaded epoxy resin (RS Components) and then also sealed into the Delrin holder with resin (Araldite).

The working and counter electrodes were polished using increasingly fine grades of silicon carbide paper (to 4000 grit, Kemet), and washed by ultrasonication in ultrapure water.

Reference electrode: A 2 mm diameter miniature Ag/AgCl reference electrode was purchased from eDAQ and used as received. Its potential was recorded in reference to a standard calomel electrode before being sealed into the cell using silicone sealant (Dowsil, SE 9187L Silicone RTV).

2.6.1.4. Instrumentation

The IR microspectroscopic experiments presented in this Thesis recorded using a synchrotron IR source were obtained at the MIRIAM beamline, Diamond Light Source, using a Bruker Vertex 80 IR spectrometer and a Hyperion 3000 IR microscope (Bruker) with a high-sensitivity photovoltaic mercury cadmium telluride (MCT) detector cooled to 77 K using liquid N_2. A reflection geometry was used to obtain IR spectra, using a 36×, 0.5 NA Schwarzschild objective and 15×15 μm^2 knife-edge aperture. Each spectrum is recorded as an average of 1024 interferograms at 4 cm^{-1} resolution.

For IR microspectroscopic experiments recorded using the in-house IR microscope at the Inorganic Chemistry Laboratory, Oxford, a Bruker Vertex 80 IR spectrometer and a Hyperion 3000 IR microscope (Bruker) was also used, but with a globar silicon carbide IR source. A reflection geometry was again used to obtain IR spectra, using a 36×, 0.5 NA Schwarzschild objective, however an increased aperture size was employed: 250×150 μm^2. Each spectrum is recorded as an average of 1024 interferograms at 4 cm^{-1} resolution.

All IR data acquisition was performed using Bruker Optik's OPUS software (version 7.5). Electrochemical measurements were acquired using an AutoLab 128N potentiostat (Metrohm) controlled by Nova software (version 1.10). Potentials (E) quoted are adjusted to millivolts (mV) *vs* the standard hydrogen electrode (SHE) using the conversion E (mV *vs* SHE) = E (mV *vs* Ag/AgCl) + 201 mV at 20 °C.

2.6.2. Experimental procedure

2.6.2.1. Assembly of the IR microspectroscopic-electrochemical cell

A 3 µL aliquot of redox mediator cocktail solution is added to a crystallisation plate well of single crystals of the appropriate protein. Each well contains approximately 3 µL of mother liquor and the number and size of crystals can vary from well to well. The crystals are suspended by gentle pipetting whilst ensuring the integrity of the crystals is maintained. The resulting 6 µL mix is deposited onto the glassy carbon working electrode. An additional 12 µL of mediator-containing crystal stabilisation buffer is then pipetted onto the Ag/AgCl reference electrode and graphite counter electrode. A 25 µm PTFE gasket is placed around the three electrodes before an IR-transparent CaF_2 window (30 mm diameter, 1 mm thickness) is carefully placed on top, ensuring no gas bubbles are trapped in the cell, nor the crystal samples move off the working electrode, nor any solution reaches the edge of the PTFE gasket to avoid liquid seeping off the electrodes. The cell is screwed shut as much as possible whilst ensuring the crystals remain intact, in order to minimise the buffer layer between the crystal and the window that can cause interference fringes (see Section 2.1.2.2). Finally, silicone sealant is used to seal the cell and maintain an anaerobic environment. Assembly of the IR microspectroscopy-electrochemical cell is carried out in a N_2-filled glovebox.

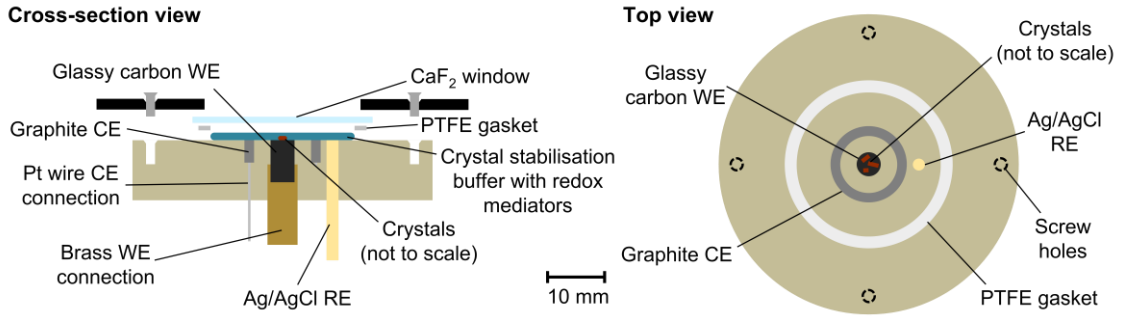


Figure 2.21 Schematic representation of the IR microspectroscopic-electrochemical cell. The placement of the single crystals onto the glassy carbon working electrode (WE) is shown, with the positioning of reference and counter electrodes (RE, CE). The cell is to scale (aside from the crystals) as indicated.

2.6.2.2. Background measurement

The assembled cell is secured to the IR microspectroscope stage, which is then enclosed within an acrylic box, to minimise changes in atmospheric water vapour across the experimental time. A 15×15 μm^2 aperture is used to record the IR spectra (Figure 2.22) when the synchrotron source is used. The IR beam is initially focused on the crystal before a background reference spectrum of an empty section of working electrode approximately 30 µm from the edge of a crystal is recorded at open circuit potential. This is repeated for each cell set up. Absolute spectra are then recorded against this background spectrum. Before electrochemical reduction is applied, an IR spectrum is recorded at the open circuit potential (OCP, ranging between +209 mV and +274 mV *vs* SHE), imposed by the mediator cocktail to ascertain the quality of the crystal.

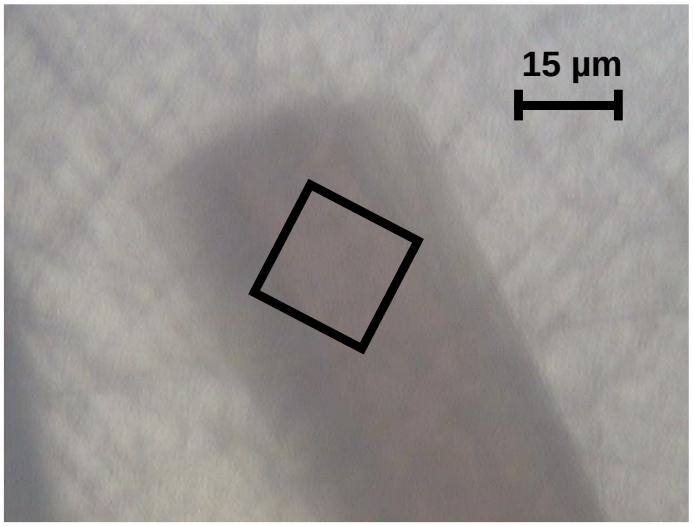


Figure 2.22 Visible image at 36× magnification of a single Hyd-1 crystal on the working electrode of the IR microspectroscopic-electrochemical cell, showing the 15×15 mm^2 sampling area used to collect IR spectra. Fine scratches that remain in the glassy carbon surface following the polishing procedure are also visible.

2.6.2.3. Delta transmembrane Hyd-1 crystals

Some adjustments to the experimental procedure were necessary when studying crystals of deltaTM Hyd-1 due to their larger size. Firstly, a thicker PTFE gasket (50 µm) was required to prevent crushing the larger crystals. Secondly, when the in-house IR microscope was used to record IR spectra, an alternative method of measuring the background reference spectrum was employed. The background IR spectrum was recorded on the unassembled cell. The IR beam is focused on the empty working electrode and a background reference spectrum is measured using a 250×150 $µm^2$ aperture. The cell is then assembled as described in Section 2.6.2.1.

2.7. IR cryo-spectroscopy set-up

2.7.1. Reagents and equipment

2.7.1.1. Sample preparation

Hyd-2-NOP solution (prepared as described in Section 2.3) was first buffer exchanged into SEC buffer (20 mM Tris, pH 7.2, 150 mM NaCl, 0.02% (w/v) DDM detergent, 1 mM dithiothreitol) *via* repeated spin concentrations and dilutions until a 1500-2000 fold dilution of the previous buffer was achieved. The solution was then concentrated down to 0.7 mM.

Initially, aggregation of the solution occurred, and so additional SEC buffer was introduced to give an approximate concentration of 100 µM. The Hyd-2-NOP solution was then exposed to H_2 in an open vial within a sealed H_2 environment for 24.5 hrs to reduce the sample. No subsequent aggregation of the sample occurred, and the sample was visibly reduced after the 24.5 hrs as the reddish-brown colour of the solution had faded.

2.7.1.2. Variable temperature equipment

A sealed, variable temperature (VT) transmission cell (GS20502, Specac Ltd) with CaF_2 windows and a fixed path length of 25 µm was used to hold the enzyme solution when performing the low temperature studies. This was fitted into a VT cell holder (GS21525, Specac Ltd). The liquid-N_2 compartment of the cell holder was purged using a vacuum pump prior to attachment to the IR spectrometer.

2.7.1.3. Instrumentation

FTIR spectra were recorded using a Bruker Vertex 80 IR-spectrometer with OPUS v.7.4 software. OriginLab Pro software was used to perform baseline corrections and peak fitting of the spectroscopic data. All spectra were recorded at 2 cm^{-1} resolution.

2.7.2. Experimental procedure

A 40 µL aliquot of reduced Hyd-2 solution was injected into the transmission cell inside a dry, anaerobic glovebox. The cell was then placed into the VT cell holder within the IR spectrometer. Initial spectra were recorded at room temperature under ambient light. Liquid-N_2 was used to cool the cell holder and thus the Hyd-2 solution. The aim was for the solution to reach a temperature of -195 °C, however the recorded temperature was higher at approximately -170°C.

Aluminium foil was used to block ambient light, providing "dark" conditions, and a 505 nm laser light directed onto the transmission cell was used to provide "light" conditions. IR spectra were recorded in the "dark" followed by under "light". IR spectra were recorded continuously whilst the solution was left in the dark for any illuminated states to relax. The process was then repeated.

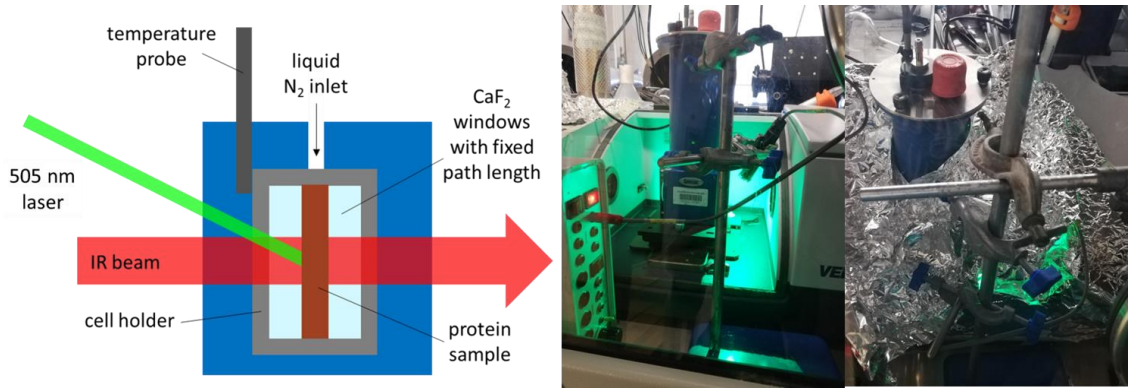


Figure 2.23 IR cryo-spectroscopy set-up. Left: Schematic diagram of temperature-controlled IR transmission cell, showing direction of 505 nm light and IR beam. Right: Photographs of the set-up with and without the aluminium foil used to create "dark" conditions.

2.8. References

1 P. M. Morse, *Physical Review*, 1929, **34**, 57–64.

2 M. Bradley, *Spectroscopy*, 2015, **30**, 42–46.

3 B. C. Smith, *Quantitative Spectroscopy: Theory and Practice*, Elsevier, 2002.

4 J. Michael. Hollas, *Modern Spectroscopy*, Wiley, New York, 4th edn., 2003.

5 K. Nakamoto, *Infrared and Raman Spectra of Inorganic and Coordination Compounds: Part A: Theory and Applications in Inorganic Chemistry: Sixth Edition*, 2008, 1–419.

6 V. A. Lorenz-Fonfria, *Chem Rev*, 2020, 120, 3466–3576.

7 W. Lubitz, H. Ogata, O. Rüdiger and E. Reijerse, *Chem Rev*, 2014, 114, 4081–4148.

8 A. L. de Lacey, V. M. Fernández, M. Rousset and R. Cammack, *Chem Rev*, 2007, 107, 4304–4330.

9 A. Barth, *Biochim Biophys Acta Bioenerg*, 2007, **1767**, 1073–1101.

10 S. Y. Venyaminov and F. G. Prendergast, *Anal Biochem*, 1997, **248**, 234–245.

11 T. G. Mayerhöfer, S. Pahlow, U. Hübner and J. Popp, *Analyst*, 2020, **145**, 3385–3394.

12 C. Lutinski, *Anal Chem*, 1958, **30**, 2071–2072.

13 A. Savitzky and M. J. E. Golay, *Anal Chem*, 1964, **36**, 1627–1639.

14 G. Azarfar, E. Aboualizadeh, N. M. Walter, S. Ratti, C. Olivieri, A. Norici, M. Nasse, A. Kohler, M. Giordano and C. J. Hirschmugl, *Analyst*, 2018, **143**, 4674–4683.

15 F. Neri, G. Saitta and S. Chiofalo, *J Phys E*, 1987, **20**, 894–896.

16 D. F. Edwards and E. Ochoa, *Appl Opt*, 1980, **19**, 4130.

17 D. A. Woods and C. D. Bain, *Soft Matter*, 2014, 10, 1071–1096.

18 J. D. Schuttlefield and V. H. Grassian, *J Chem Educ*, 2008, **85**, 279–281.

19 G. della Ventura, F. Bellatreccia, A. Marcelli, M. Cestelli Guidi, M. Piccinini, A. Cavallo and M. Piochi, *Anal Bioanal Chem*, 2010, 397, 2039–2049.

20 L. M. Miller, G. L. Carr, M. Jackson, P. Dumas and G. P. Williams, *Synchrotron Radiat News*, 2000, **13**, 31–38.

21 K. R. Bambery, B. R. Wood, E. Schültke, B. H. J. Juurlink, T. May and D. McNaughton, *Biomedical Applications of Synchrotron Infrared Microspectroscopy*, Royal Society of Chemistry, Cambridge, 2010.

22 H. A. Bechtel, M. C. Martin, T. E. May and P. Lerch, *Rev. Sci. Instrum.*, 2009, **80**, 126106.

23 P. Dumas and M. J. Tobin, *Spectrosc. Eur.*

24 S. Mobilio, F. Boscherini and C. Meneghini, *Synchrotron radiation: Basics, methods and applications*, Springer Berlin Heidelberg, 2015.

25 K. Nakamoto, *Infrared and Raman Spectra of Inorganic and Coordination Compounds: Part B*, John Wiley & Sons, Inc., Hoboken, NJ, USA, 6th Edn., 2009.

26 T. P. Hanusa, in *Encyclopedia of Inorganic and Bioinorganic Chemistry*, John Wiley & Sons, Ltd, Chichester, UK, 2011.

27 E. Bernhardt, B. Bley, R. Wartchow, H. Willner, E. Bill, P. Kuhn, I. H. T. Sham, M. Bodenbinder, R. Bröchler and F. Aubke, *J Am Chem Soc*, 1999, **121**, 7188–7200.

28 Franz. L. Wimmer, Doctor of Philosophy, University of Adelaide, 1977.

29 S. F. A. Kettle, G. L. Aschero, E. Diana, R. Rossetti and P. L. Stanghellini, *Inorg Chem*, 2006, **45**, 4928–4937.

30 A. Volbeda, E. Garcin, C. Piras, A. L. de Lacey, V. M. Fernandez, E. C. Hatchikian, M. Frey and J. C. Fontecilla-Camps, *J Am Chem Soc*, 1996, **118**, 12989–12996.

31 A. J. Pierik, W. Roseboom, R. P. Happe, K. A. Bagley and S. P. J. Albracht, *J Biol Chem*, 1999, **274**, 3331–7.

32 R. M. Evans and F. A. Armstrong, *Methods Mol. Biol.*, 2014, **1122**, 73–94.

33 N. D. J. Yates, M. A. Fascione and A. Parkin, *Chem. Eur. J.*, 2018, **24**, 12164–12182.

34 S. Song, R. A. Clark, E. F. Bowden and M. J. Tarlov, *J. Phys. Chem.*, 1993, **97**, 6564–6572.

35 D. E. Khoshtariya, T. D. Dolidze, M. Shushanyan and R. van Eldik, *J. Phys. Chem. B*, 2014, **118**, 692–706.

36 P. C. Mondal and C. Fontanesi, *ChemPhysChem*, 2018, **19**, 60–66.

37 R. M. Evans, P. A. Ash, S. E. Beaton, E. J. Brooke, K. A. Vincent, S. B. Carr and F. A. Armstrong, *J Am Chem Soc*, 2018, **140**, 10208–10220.

38 O. Gutiérrez-Sanz, O. Rüdiger and A. L. de Lacey, *Methods Mol. Biol.*, 2014, **1122**, 95–106.

39 C. Fichtner, C. Laurich, E. Bothe and W. Lubitz, *Biochemistry*, 2006, **45**, 9706–9716.

40 P. A. Ash, S. B. Carr, H. A. Reeve, A. Skorupskaite, J. S. Rowbotham, R. Shutt, M. D. Frogley, R. M. Evans, G. Cinque, F. A. Armstrong and K. A. Vincent, *Chem. Comm.*, 2017, **53**, 5858–5861.

41 A. J. Bard and L. R. Faulkner, *Electrochemical methods : fundamentals and applications*, Wiley, 2001.

42 N. Elgrishi, K. J. Rountree, B. D. McCarthy, E. S. Rountree, T. T. Eisenhart and J. L. Dempsey, *J Chem Educ*, 2018, **95**, 197–206.

43 K. Ashley, *Talanta*, 1991, **38**, 1209–1218.

44 D. H. Murgida, *ACS Omega*, 2021, **6**, 3435–3446.

45 P. A. Ash and K. A. Vincent, in *Biophotoelectrochemistry: From Bioelectrochemistry to Biophotovoltaics*, Springer Berlin Heidelberg, 2016, pp. 75–110.

46 M. J. Lukey, A. Parkin, M. M. Roessler, B. J. Murphy, J. Harmer, T. Palmer, F. Sargent and F. A. Armstrong, *J Biol Chem*, 2010, **285**, 3928–38.

47 S. E. Beaton, R. M. Evans, A. J. Finney, C. M. Lamont, F. A. Armstrong, F. Sargent and S. B. Carr, *Biochem J*, 2018, **475**, 1353–1370.

48 R. M. Evans, E. J. Brooke, S. A. M. Wehlin, E. Nomerotskaia, F. Sargent, S. B. Carr, S. E. V. Phillips and F. A. Armstrong, *Nat Chem Biol*, 2016, **12**, 46–50.

49 A. Volbeda, P. Amara, C. Darnault, J. M. Mouesca, A. Parkin, M. M. Roessler, F. A. Armstrong and J. C. Fontecilla-Camps, *Proc. Natl. Acad. Sci.*, 2012, **109**, 5305–5310.

50 R. Hidalgo, P. A. Ash, A. J. Healy and K. A. Vincent, *Angew. Chem., Int. Ed.*, 2015, **54**, 7110–7113.

Chapter 3. Characterisation of Hyd-1 using PFIRE

In this Chapter, protein film infra-red electrochemistry (PFIRE) is employed to study the IR spectroelectrochemical behaviour of *E. coli* hydrogenase-1 when adsorbed onto an electrode and how it compares to previous results.

3.1. IR spectroelectrochemical studies of [NiFe]-hydrogenases

3.1.1. Introduction

IR spectroelectrochemistry is a valuable tool for investigating the redox behaviour of the active site of [NiFe]-hydrogenases and has been used to characterise various standard and O_2-tolerant [NiFe]-hydrogenases.[1–7] The biologically unusual CO and CN ligands bound to Fe are IR active and act as reporters of the redox state of the active site. In the IR spectra of [NiFe]-hydrogenases, each active site redox state has one IR band attributed to the CO ligand, and two CN bands, indicative of the symmetric and antisymmetric stretches from the two CN ligands in the active site. If multiple IR bands are detected within the ν_{CO} region, this usually signals the presence of multiple redox species in the protein sample. Combining IR spectroscopy with *in situ* electrochemical control has allowed a multitude of active site redox states of [NiFe]-hydrogenases to be identified. Figure 3.1 gives an overview of the different active site redox states of [NiFe]-hydrogenases, ordered by redox level. The catalytically inactive states are indicated on the left of the figure, with the catalytically active states on the right.

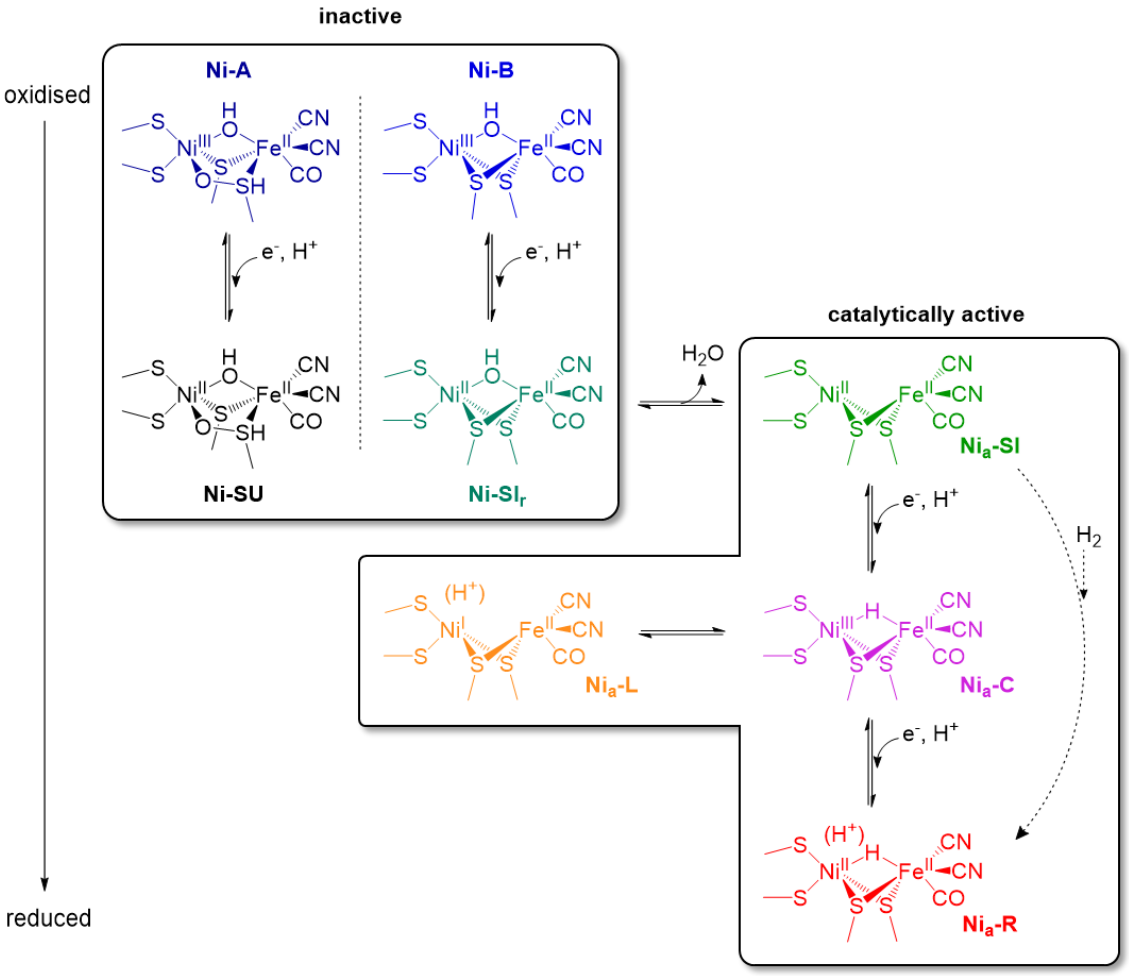


Figure 3.1 Overview of the active site redox states present in [NiFe]-hydrogenases. The states are ordered by redox level, with the most oxidised species at the top and the most reduced species at the bottom of the Figure. Inactive and catalytically active states are separated by two boxes for clarity. The subscript "a" signifies the state is catalytically active, while the subscript "r" represents a "ready" state, i.e., the species is inactive but on the same redox level as an active species which it can be activated into.[1,8–11]

3.1.2. Inactive states

The two most oxidised active site redox states are the catalytically inactive Ni-A and Ni-B species. These species are formed upon exposure to O_2 and possess a paramagnetic $Ni^{III}Fe^{II}$ (S=½) active site. Whilst Ni-B has been confirmed to have a hydroxide bridging ligand,[10] there is still controversy over the identity of the bridging ligand in Ni-A. The most

supported assignment is a hydroxido bridging ligand, similar to Ni-B, alongside an oxygenated bridging cysteine coordinated to the Ni.[10,12,13] Due to their similar structures, it is difficult to distinguish between Ni-A and Ni-B using IR spectroscopy, although they do possess different *g*-tensors in EPR measurements and have vastly different rates of activation. Ni-A requires several hours to be reduced to a catalytically active species, whereas Ni-B can usually be reduced within a few minutes.[1]

One-electron reduction of the Ni-A and Ni-B species leads to the formation of the "unready" Ni-SU and "ready" Ni-SI_r states respectively.[8] These are thought to retain an oxygenic bridging ligand, which prevents the species from being active, but have a diamagnetic $Ni^{II}Fe^{II}$ active site. There is some debate as to whether the formation of the Ni-SI_r state is a concerted or step-wise proton-coupled electron transfer. One mechanism predicts the bridging ligand is protonated to H_2O either by transfer of a proton directly to the active site or through protonation of a Ni-coordinated cysteine.[14] Others suggest the Ni-SI_r species is in an acid-base equilibrium with a protonated version which has a loosely bound H_2O bridging ligand.[3,9,15] Recent DFT analysis has proposed the Ni-SU state has a terminal coordinated water molecule to the Fe atom with a modified coordination of Ni, along with the oxygenated Cys seen in Ni-A.[16] Slow activation of the Ni-SU state leads to the Ni-SI_r species. Subsequent release of a water molecule activates the hydrogenase and forms the catalytically active Ni_a-SI species.

3.1.3. Active states

Four active site species have been shown to be catalytically active and participate in the [NiFe]-hydrogenase catalytic cycle as shown in Figure 3.2: Ni_a-SI, Ni_a-R, Ni_a-C and Ni_a-L (the subscript "a" signifies the state is catalytically active).

The EPR silent Ni_a-SI state has a $Ni^{II}Fe^{II}$ centre and a vacant bridging site which is susceptible to attack by H_2. The high electron density at the active site polarises the H-H bond, with subsequent heterolytic cleavage forming the most reduced active state, Ni_a-R. The identity of the proton acceptor is still debated. High resolution crystal structures and DFT calculations have shown protonation of a Ni-bound cysteine and thus suggest that this cysteine accepts the proton *via* initial side-on binding of H_2 to Ni.[17–19] However, there is no direct experimental evidence of a bound H–H.

Armstrong and co-workers have proposed an alternative mechanism following the observation that substitution of a highly-conserved arginine residue results in decrease in enzyme activity, thus suggesting its role as a proton acceptor. Here, the arginine group acts as a base to polarise the H-H bond, similar to a frustrated-Lewis pair.[20]

These mechanisms do not fully account for the fact that multiple Ni_a-R species have been observed using IR spectroscopic techniques. One interpretation of this is that each Ni_a-R sub-species represents a proton moving further away from the active site: the highest wavenumber species, Ni_a-R_I, has a protonated Ni-coordinated cysteine thiolate, with Ni_a-R_{II} and Ni_a-R_{III} having fully deprotonated active sites.

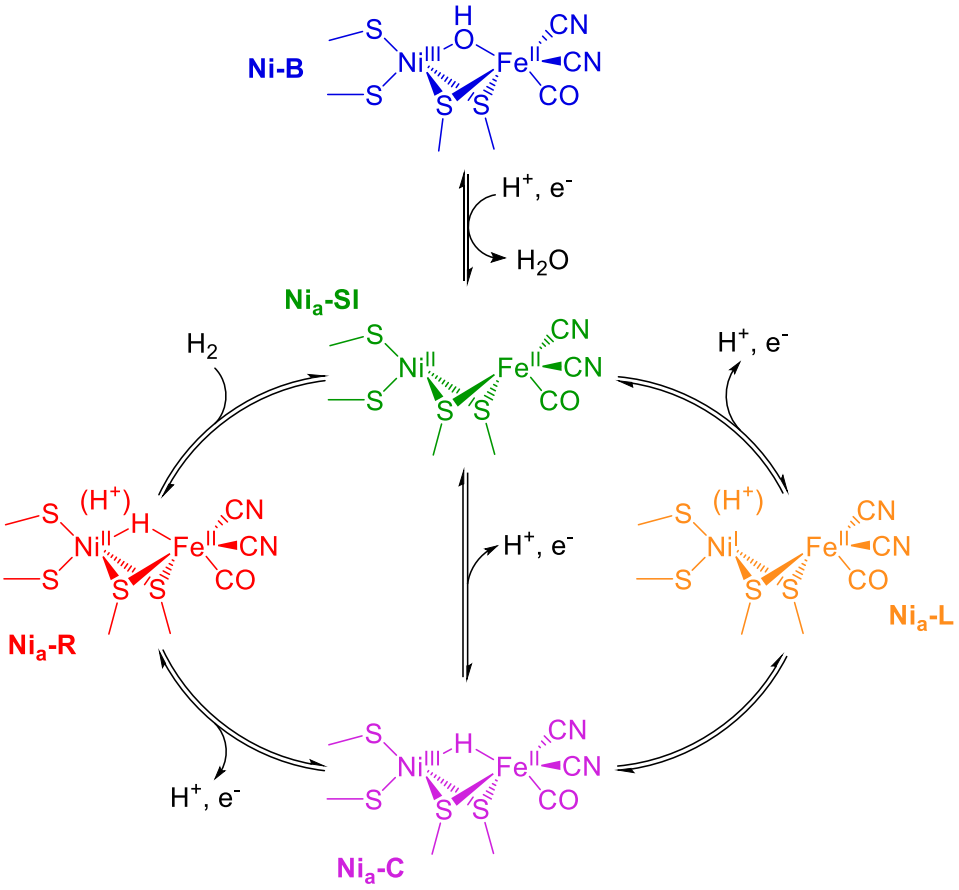


Figure 3.2 Schematic representation of the general [NiFe]-hydrogenase catalytic mechanism. The colours used to represent each active site redox species are those used throughout this Thesis.

A second deprotonation-coupled oxidation of the Ni_a-R species forms Ni_a-C. Here, the Ni^{II} is oxidised to give a $Ni^{III}Fe^{II}$ centre, with the bridging position still occupied by a hydride.[21,22] From the Ni_a-C state, oxidation back to Ni_a-SI can proceed via two pathways: direct loss of a second electron and proton; or, by means of a Ni^{I} -intermediate termed Ni_a-L. Similar to Ni_a-R, multiple Ni_a-L states have been spectroscopically characterised, and are suggested to represent successive transfer of a proton away from the active site. The Ni_a-L species were initially only observed upon illumination of the Ni_a-C state under cryogenic temperatures, and thus presumed to be catalytically insignificant. However, studies of certain hydrogenases under physiologically relevant conditions have shown this not to be the case. Subsequent removal of a proton and an electron from the active site in

Ni_a-L then recovers the Ni_a-SI species thus completing the catalytic cycle. It remains uncertain whether Ni_a-L is a common intermediate in all [NiFe]-hydrogenases.

3.1.4. *E. coli* hydrogenase-1

Escherichia coli hydrogenase-1 (Hyd-1) is a well characterised, group 1, O_2-tolerant [NiFe]-hydrogenase. Its redox behaviour has been studied using different IR spectroelectrochemical techniques. Initial spectroscopic characterisation was performed by Healy, using an *in-situ* ATR-IR spectroelectrochemical cell to study Hyd-1 in solution.[23,24] This work was expanded upon by Hidalgo *et al.* who developed the protein film infra-red electrochemistry (PFIRE) technique which combines protein film electrochemistry with IR spectroscopy to monitor active site species under non-turnover and turnover conditions.[25,26]

Each active site redox state observed in other standard and O_2-tolerant [NiFe]-hydrogenases has been detected in Hyd-1, along with multiple Ni_a-R and Ni_a-L ν_{CO} bands indicating the presence of sub-species. Table 3.1 details the wavenumber positions of the observed ν_{CO} and ν_{CN} vibrational bands. Importantly, Hidalgo *et al.* discovered evidence of reversible Ni_a-L formation under turnover conditions, suggesting its role as a catalytic intermediate.

Table 3.1 Vibrational ν(CO) and ν(CN) frequencies observed in IR spectroscopy of different active site redox species of *E. coli* Hyd-1 as measured in solution by Healy[23] or with the protein film infra-red electrochemistry (PFIRE) technique, collected by Hidalgo[25]. All measurements were performed at pH 6. n.d. signifies that no band was detected.

Redox species	**Wavenumber / cm^{-1}**			
	Solution[23,24]		**Electrode-adsorbed**[25,26]	
	ν(CO)	**ν(CN)**	**ν(CO)**	**ν(CN)**
Ni-B	1943	2099, 2081	1943	2099, 2093[a] 2082
Ni_a-SI	1929	2085, 2076	1929	2085, 2077
Ni_a-C	1951	n.d.	1952	2089, 2079[b]
Ni_a-L_I	n.d.	n.d.	n.d.	n.d.
Ni_a-L_{II}	1877	2051, 2034	1877	2051, 2034
Ni_a-L_{III}	1866	2045, 2029	1868	2028
Ni_a-R_I	n.d.	n.d.	n.d.	n.d.
Ni_a-R_{II}	1922	2070, 2053	1922	n.d.
Ni_a-R_{III}	1914	2066, 2049	1915	2066, 2049

Many other IR spectroscopic investigations into the catalytically relevant redox states of [NiFe]-hydrogenases involve flowing gases such as H_2 or O_2 to induce the reduction and oxidation of the enzyme. However, this does not represent catalytic turnover. In solution, the enzyme becomes rapidly reduced by H_2 and cannot turnover again until it is re-oxidised, and diffusion-controlled oxidation by soluble oxidants cannot keep up with

[a] Additional ν_{CN} band suggested to be due to protonated Ni-B species
[b] Measured at pH 4.0

catalysis. Therefore, electrochemical control is required to mimic catalytic H_2 oxidation. Spectroelectrochemical techniques such as PFIRE allow this.

A significant benefit of utilising the PFIRE technique developed by Hidalgo *et al.* is that it allows direct measurement of the steady-state distributions of the active site redox levels under turnover conditions. This in turn can provide insight into the role of each active site species in the catalytic cycle. It is imperative though that the experiment is not mass transport limited, i.e., the current is purely a measure of the catalytic activity of the redox enzyme. During the PFIRE experiments, a flow system was used to provide a continuous supply of fresh substrate to the particle electrode network. Hidalgo showed that increasing the flow rate above 62 mL min^{-1} had no effect on the catalytic current, indicating it was independent of mass transport.[25] Furthermore, the voltammogram waveshape of Hyd-1 in the presence of H_2 in the PFIRE cell was shown to be similar to that recorded using a traditional rotating disk electrode.[26]

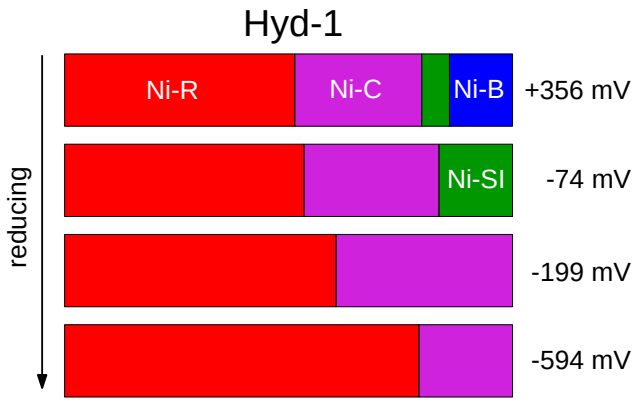


Figure 3.3 Steady-state distributions of active site redox levels of Hyd-1 (100% H_2) at different potentials measured using the PFIRE technique as performed by Hidalgo.[25,26] Each coloured section of a bar represents the proportion of ν(CO) peak absorbances for each active site redox level measured at the given potentials: Ni-R (red), Ni-C and Ni-L (purple), Ni-SI (green), and Ni-B (blue).

Nevertheless, there are some concerns as to whether the measurements recorded by Hidalgo under turnover conditions are completely free of mass transport issues. Namely, whether the observation of Ni_a-SI and Ni-B at high potentials is due to the lack of substrate reaching the entire enzyme film, causing a portion of the enzyme to be under electrochemical rather than electrocatalytic control. Figure 3.3 shows the steady-state distributions of the active site redox levels measured by Hidalgo under 100% H_2 using the PFIRE technique. At -74 mV *vs* SHE, a notable proportion of the Hyd-1 film (16%) is at the Ni_a-SI redox level. Observing the Ni_a-SI redox state at this potential is not unexpected. Referring to the catalytic cycle (Figure 3.2), the formation of Ni_a-SI involves a proton-coupled one-electron oxidation step, and so at higher applied potentials this rate increases. The rate of Ni_a-SI consumption on the other hand is dependent on H_2 concentration which remains constant at all potentials. It is then expected that the steady-state concentration of Ni_a-SI will increase with potential.

In this Chapter, the protein film IR electrochemical experiments performed by Hidalgo on *E. coli* hydrogenase-1 are repeated in order to: a) confirm the results obtained; b) address the query regarding mass transport; and c) provide an overview of the redox characteristics of Hyd-1, including the IR bands of each redox active site state, for comparison with data collected using the developed IR microspectroscopic-electrochemical technique performed on single crystals of Hyd-1, as in Chapter 4. Furthermore, the steady-state distributions of the active site redox levels under turnover conditions of Hyd-1 are compared to its O_2-sensitive counterpart, Hyd-2, providing insight into the differences between the two.

3.2. Results and discussion

All data presented in this Chapter were obtained using the protein film infra-red electrochemistry technique developed by Hidalgo *et al.*.[26,27] The experimental method and equipment are described in Chapter 2, Section 2.5.

3.2.1. Redox states of Hyd-1

3.2.1.1. As-isolated

The initial IR spectrum of as-isolated Hyd-1 at pH 6 and open circuit potential (OCP, +109 mV *vs* SHE) is presented in Figure 3.4 Both the ν_{CO} and ν_{CN} regions are included and labelled.

First of note, the peak absorbances measured are approximately 0.1 – 0.5 mO.D.. These are comparable to those observed by Hidalgo, signifying that a similar amount of [NiFe] active site is being detected.

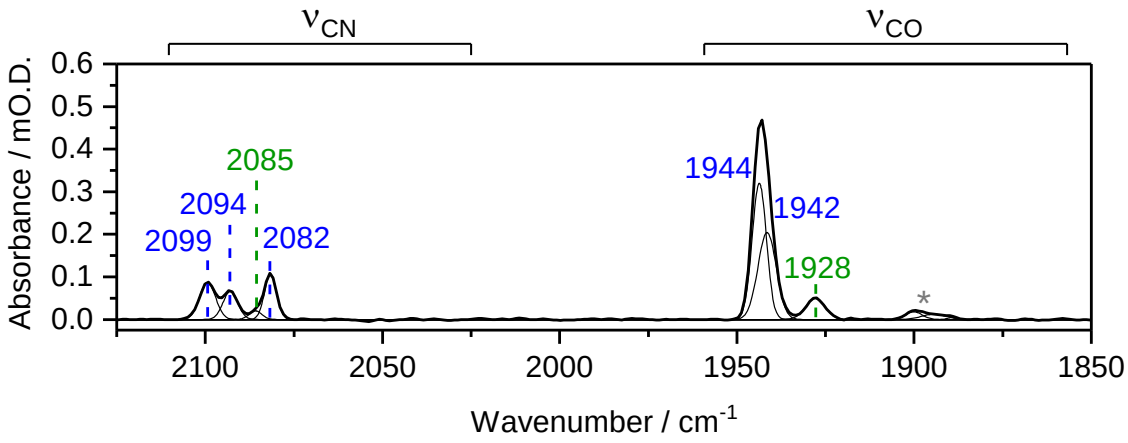


Figure 3.4 Baseline-corrected infrared spectrum of as-isolated Hyd-1 adsorbed onto a carbon particle film at pH 6, open circuit potential +109 mV. Blue represent IR bands assigned to the Ni-B redox level and green represents IR bands assigned to the Ni_a-SI redox level. The grey asterisk represents a group of unassigned, low absorbance IR peaks. Thin grey lines represent Gaussian fitted peaks.

There are two main bands in the ν_{CO} region of the as-isolated IR spectrum, one intense at 1943 cm^{-1} and one smaller band at 1928 cm^{-1}. However, the band at 1943 cm^{-1} is asymmetric, and Gaussian fitting shows it could be deconvoluted to two peaks at 1944 and 1942 cm^{-1}. As the Hyd-1 sample was prepared under aerobic conditions, it is expected that the spectrum would show a mixture of oxidised inactive states. The inactive Ni-B species in Hyd-1 has been previously observed at 1943 cm^{-1}, with 2099, 2093 and 2082 cm^{-1} being the accompanying ν_{CN} bands (Table 3.1). Usually, there are only two ν_{CN} bands for each active site redox species due to the coupled symmetric and antisymmetric ν_{CN} stretches. The additional ν_{CN} band at 2093 cm^{-1} previously assigned to the Ni-B species may either be a protonated form of the inactive Ni-B state, whose ν_{CO} band was hidden by the peak at 1943 cm^{-1}, or a structure with different hydrogen-bonding intermediates between the CN^- ligands and nearby amino acid residues causing differences in the antisymmetric CN stretch.

A higher resolution relative to that used by Hidalgo (2 cm^{-1} cf. 4 cm^{-1}) was used to collect the IR spectra presented in this Chapter. This has allowed the 1943 cm^{-1} band to be resolved into two peaks at 1944 cm^{-1} and 1942 cm^{-1}, suggesting there is an additional ν_{CO} band that was previously hidden. As the difference in wavenumber of these resolved peaks is very small, the active site redox species they represent are likely to be structurally similar. If one of these is the Ni-B species, there are a few possibilities for the identity of the second species:

1) The inactive oxidised Ni-A species: the Ni-A ν_{CO} band is nearly indistinguishable from the Ni-B ν_{CO} band in many [NiFe]-hydrogenases[2,3,13,28]
2) A protonated Ni-B species, where either the bridging hydroxide ligand is protonated to H_2O, or a nearby amino acid residue is protonated.

3) 'Superoxidised' Ni-B, where the proximal [4Fe3S] cluster is superoxidised to $[4Fe3S]^{5+}$ causing a slight change in electron density at the active site.

If 1) is the case, the Ni-A band should not be observed after complete activation, *via* electrochemical reduction, of the sample as it has been reported that activation of as-isolated Hyd-1 and subsequent re-oxidation exclusively forms the Ni-B state.[25,29]

It is expected that the 'protonated Ni-B' species (with a H_2O bridging ligand) would have a higher wavenumber ν_{CO} band. This is due to H_2O being a poorer π-donor ligand than ^{-}OH, thus the amount of π-backbonding from the Fe to the CO ligand decreases. Thus, the 1944 cm^{-1} would be assigned to the Ni-B^{+}, and the 1942 cm^{-1} to the Ni-B species. If there exists an acid-base equilibrium between two Ni-B like species, as with 2), then the behaviour of these species will be affected by pH. This is investigated in Section 3.2.2.

The spectrum presented in Figure 3.4 was measured at open circuit potential, +109 mV, which is close to the potential of the $[4Fe3S]^{5+/4+}$ proximal cluster transition.[30,31] Therefore it may be the case that some of the proximal cluster is superoxidised. If the additional ν_{CO} band is due to a 'superoxidised' Ni-B, its absorbance should increase with potential alongside a decrease in the 'normal' Ni-B species.

A lower intensity ν_{CO} band at 1928 cm^{-1} is also present in the as-isolated Hyd-1 spectrum, alongside a band at 2085 cm^{-1} in the ν_{CN} region. These are similar to those attributed to the active Ni_a-SI species. It was expected that only inactive species would be present in the as-isolated spectra due to Hyd-1 being prepared in the presence of O_2. As there is such a small proportion of the 1928 cm^{-1} species, some of the Hyd-1 may have been reduced upon desorption onto the carbon particles but this is a minor component compared to the inactive species around 1943 cm^{-1}.

There are also a group of low absorbance bands between 1900 – 1887 cm^{-1} observed in the as-isolated IR spectrum, as marked by the grey asterisk in Figure 3.4. These are discussed in Section 3.2.1.2.

After the initial as-isolated spectrum is measured, the Hyd-1 particle film is activated by application of a low potential, -592 mV *vs* SHE, and flow of H_2 saturated buffer, for 12 hours to fully reduce any slowly activating species. The redox behaviour of Hyd-1 can then be investigated under non-turnover (Ar) and turnover (H_2) conditions at four selected potentials: -592, -197, -72 and +358 mV *vs* SHE. These values represent the potentials at which each active site redox species is maximised at pH 6, as observed by Hidalgo.[26]

3.2.1.2. Non-catalytic turnover conditions (Ar)

Figure 3.5A shows the current-time traces of Hyd-1 adsorbed onto a carbon nanoparticle electrode in the ATR spectroelectrochemical cell. The electrode was poised at four different values, representing the potentials at which each active site redox species is maximised at pH 6. The current was measured under an inert (Ar) atmosphere, as represented by the grey line. As expected, lack of substrate results in no electrocatalytic current being measured under Ar at any of the potential steps. Furthermore, no H^+ reduction is detected, consistent with Hyd-1 being a poor H_2 producer at pH 6.[32]

The IR spectra recorded at each potential under Ar are shown in Figure 3.5B. For clarity, only the ν_{CO} region is given. In general, these spectra are analogous to those observed in the previous IR spectroelectrochemical study of Hyd-1 under Ar using the PFIRE technique.[26] At the lowest potential, -592 mV, the most reduced redox species, Ni_a-R, are dominant as shown by the bands at 1922 and 1914 cm^{-1}. These correspond to two sub-species, Ni_a-R_{II} and Ni_a-R_{III} respectively, and are thought to represent different protonation states of the same redox level. The bands at at 1952, 1877 and 1866 cm^{-1}

have also been previously observed and signify the presence of the Ni_a-C and the two Ni_a-L sub-species, Ni_a-L_{II} and Ni_a-L_{III} respectively. Stepping up to higher potentials results in the more oxidised redox states appearing, in line with the order of states in Figure 3.1. The band at 1929 cm^{-1} represents the Ni_a-SI species, with a peak at 1942 cm^{-1} appearing at -72 mV.

However, there are some features currently unaccounted for. Between 1900 – 1887 cm^{-1}, there are a group of low absorbance bands similar to those seen in Figure 3.4, which appear across all potentials and conditions used throughout this Chapter (marked by the grey asterisk in Figure 3.4 and Figure 3.5). The intensities and positions of these features vary unpredictably and are thus unlikely to be due to an active site redox state. It is possible they are due to impurities on the carbon particle surface or incorrect fitting of the subtracted baseline during data processing.

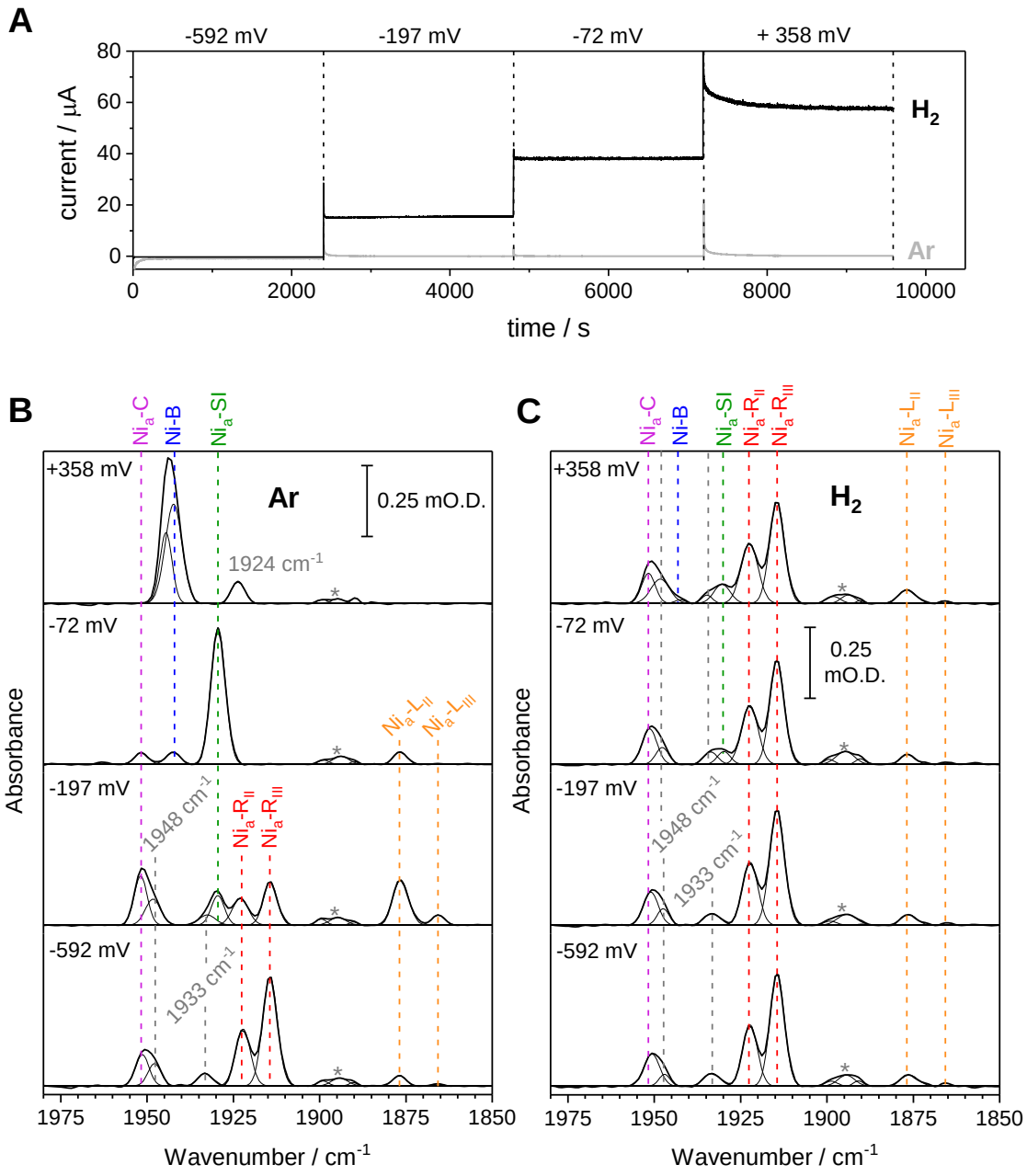


Figure 3.5 (a) Current-time traces of Hyd-1 collected in the ATR-IR cell in Ar-saturated (grey) and H_2-saturated (black) buffer, pH 6; (b),(c) absolute IR spectra showing the ν_{CO} region at each potential of Hyd-1 under Ar (b) and H_2 (c).

Secondly, there are two unassigned ν_{CO} bands at 1948 and 1933 cm^{-1} that are only present at the two lowest potentials, -197 and -592 mV. The 1948 cm^{-1} species is close in wavenumber to the known Ni_a-C band at 1951 cm^{-1} and thus likely also represents a Ni(III) species. In FTIR studies of *Pyrococcus furiosus (Pf)* [NiFe] soluble hydrogenase 1, Greene *et*

al. observed a pH-dependent peak shift of the Ni_a-C state which was suggested to be due to the change in population of two distinct species termed Ni_a-C^+ and Ni_a-C.[33] The behaviour of the 1948 cm^{-1} species with pH is discussed below in Section 3.2.2.

Regarding the 1933 cm^{-1} band, its position and presence at low potentials suggests it may be a Ni_a-R species. Three sub-species of the Ni_a-R state have been detected *via* IR spectroscopy in several [NiFe]-hydrogenases,[2,5,34–37] but no third Ni_a-R IR band has been observed for Hyd-1 before. Each sub-species is purported to represent a successive proton transfer step away from the active site, with the decreasing ν_{CO} wavenumber of Ni_a-R_I to Ni_a-R_{III} reflecting the proton moving further from the active site (and thus influencing the Fe-CO bond less).[11] It has been suggested that the Ni_a-R_I species is not detected in Hyd-1 due to the high potential of the [4Fe3S] proximal cluster hindering the electron transfer required for the Ni_a-R/Ni_a-C transition.[24] This would result in proton transfer continuing to the point where it is furthest from the active site (Ni_a-R_{III}) rather than remaining near the active site (Ni_a-R_I).

Ash *et al.* have shown that the relative ν_{CO} positions of the Ni_a-R states of [NiFe]-hydrogenases with respect to the Ni_a-C state fall into three groupings.[11] The Ni_a-R_{II} and Ni_a-R_{III} bands for Hyd-1 (1922 and 1914 cm^{-1}) are within the expected wavenumber range, with the Ni_a-R_I peak predicted to be between 1942 and 1932 cm^{-1}. The band observed at 1933 cm^{-1} is within this range and, coupled to the fact it only appears at low potentials alongside the assigned Ni_a-R sub-species, it may then be attributed to the previous unobserved Ni_a-R_I species.

Finally, the IR spectrum at the most oxidative potential, +358 mV, contains three ν_{CO} bands, instead of the predicted single Ni-B peak. Similar to the as-isolated spectrum in Figure 3.4, the peak centred around 1943 cm^{-1} is asymmetrical, and Gaussian peak fitting

reveals two individual bands at 1944 and 1942 cm^{-1}. The 1942 cm^{-1} peak first appears at the lower potential, -72 mV, with the higher wavenumber peak only observed at the highest potential.

As the sample has been activated under low potential and H_2, there should not be any of the slowly activating, inactive Ni-A species present. This rules out the first suggested identity of the additional ν_{CO} band noted above in Section 3.2.1.1. The appearance of the 1942 cm^{-1} peak at -72 mV prior to the 1944 cm^{-1} at +358 mV may imply that the 1944 cm^{-1} band belongs to a 'superoxidised' proximal cluster Ni-B species. However a full potential titration is required to confirm this. Furthermore, this does not rule out the other suggestion of a protonated Ni-B with a H_2O bridging ligand.

Alongside the 'Ni-B' peaks, there is a band at 1924 cm^{-1} at high potential. A similar wavenumber band, 1923 cm^{-1}, was observed by Hidalgo in certain as-isolated samples of Hyd-1. This species, however, disappeared upon activation of the sample, and was suggested to be a sulfur containing Ni(II) species. As the spectra shown in Figure 3.5B were collected after activation of the sample, the appearance of this 1924 cm^{-1} band is unexplained.

3.2.1.3. Catalytic turnover conditions (H_2)

Figure 3.5C shows the IR spectra collected at the same 4 potentials as in Figure 3.5B, but now in the presence of 1 bar H_2. At the most reduced potential, -592 mV, the IR spectrum is essentially identical to that collected under an inert atmosphere. Despite the presence of substrate, Hyd-1 is unable to undergo H_2 oxidation catalysis, as shown by the lack of current in Figure 3.5A at -592 mV (the black line represents the measured current under a H_2 atmosphere). Therefore the distribution of the active site redox states is the same as without substrate.

Stepping above the onset potential, (~ -305 mV for Hyd-1, 1 bar H_2, pH 6, 298 K)[38], Hyd-1 engages in electrocatalytic H_2 oxidation resulting in a positive current. The higher the potential, the larger the current measured due to the increased electrochemical driving force for H_2 oxidation (as moving to more positive potentials relative to the onset potential). At +358 mV, following the initial increase, the current decays exponentially for ca. 1000 s before stabilising, consistent with high potential oxidative inactivation and the formation of Ni-B.[39]

When stepping to -197 mV, there are no changes in the steady-state distributions of the active site species: Ni_a-R remains the most dominant, with the proportions of Ni_a-C and Ni_a-L unchanged. Most significantly, no Ni_a-SI is observed, in contrast to the corresponding spectrum measured under an inert atmosphere. This is consistent with the fast attack on Ni_a-SI by H_2 to form Ni_a-R preventing build-up of the Ni_a-SI species (Figure 3.2). The appearance of both the Ni_a-C and Ni_a-L species under catalytic turnover conditions supports their involvement in the catalytic cycle.

It is only when the potential is stepped up to -72 mV that the Ni_a-SI species is first detected, albeit at a significantly smaller concentration than the equivalent spectrum under Ar (4% cf 80%). Formation of Ni_a-SI from either Ni_a-C or Ni_a-L involves an oxidative step (Figure 3.2). Applying a higher potential increases the rate of electron transfer due to the larger driving force. Therefore, moving to more oxidative potentials increases the rate of steps involving electron transfers, whilst not those involving a purely chemical step. The rate of Ni_a-SI consumption only depends on the concentration of H_2, and thus is constant across all potentials. Thus, despite the high turnover frequency of Hyd-1, stepping to -72 mV results in a large enough increase in the rate of Ni_a-SI formation for the steady-state concentration of Ni_a-SI to be detected spectroscopically.

The Ni_a-R redox level remains the majority species at -72 mV but do experience a small decrease in absorbance relative to the lower potentials. This can again be explained by referring to the catalytic cycle in Figure 3.2. Consumption of Ni_a-R involves a proton-coupled one-electron oxidation, whose rate of reaction increases with potential, similar to the formation of Ni_a-SI. Formation of Ni_a-R is independent of potential, so overall the steady-state concentration decreases when more oxidative potentials are applied. The steady-state concentrations of the Ni_a-C/Ni_a-L species on the other hand remain constant.

Finally, at the most oxidising applied potential +358 mV, all active site redox levels are observed under H_2 with once again the most reduced Ni_a-R species dominating the spectrum, although at a lower concentration than before due to the increase in potential. The steady-state concentration of the Ni_a-SI and Ni_a-C / Ni_a-L redox levels, however, increase in proportion upon stepping to +358 mV. Most notably, whilst the inactive Ni-B species at 1942 cm^{-1} is detected at this potential, it is in a drastically small proportion: ~1% of the enzyme sample. The presence of Ni-B is consistent with the initial exponential current decay observed in the current-time graph in Figure 3.5A (black line), as oxidative inactivation of Hyd-1 is linked to the formation of Ni-B.

3.2.1.4. Discussion

Comparison to previous Hyd-1 characterisation using PFIRE

Overall, the data presented in Figure 3.5 are comparable to previous IR spectroelectrochemical studies of Hyd-1. The ν_{CO} bands for each active site redox species are equivalent to those observed by Hidalgo, along with their potential behaviour. As stated above, the absorbances of the ν_{CO} peaks are also within a similar range (0.1 - 0.5 mO.D.) signifying that the amount of [NiFe] active site detected with the PFIRE technique remains approximately constant. Under catalytic turnover conditions (100% H_2,

Figure 3.5C), the most reduced active site species, Ni_a-R, is shown once again to dominate at each potential, whilst the more oxidised species, Ni_a-SI and Ni-B are only detected at high potentials. Importantly, the Ni_a-L species are also observed at potentials outside of the range they are seen under non-turnover conditions. This means the Ni_a-L species can be generated in response to catalytic H_2 oxidation, supporting their inclusion in the [NiFe]-hydrogenase catalytic cycle. In general, the work presented in this Chapter has confirmed the majority of the results previously published.

However, there are some notable differences. A number of additional ν_{CO} bands are observed in Figure 3.5, some of which have been tentatively assigned to active site species: 1933 cm^{-1} (Ni_a-R_I), 1948 cm^{-1} (Ni_a-C like species) and 1944 cm^{-1} (Ni-B like species). The higher resolution of the IR spectra (2 cm^{-1} cf. 4 cm^{-1}) has allowed distinct peaks to be resolved within the Ni-C and Ni-B bands, suggesting protonated and unprotonated states. The behaviour of these peaks with pH may confirm this assignment. Furthermore, a much smaller proportion of the Ni_a-L species relative to that recorded by Hidalgo was observed throughout the experiments. The origin of this is unknown.

The most significant differences between the two set of data were seen when under turnover conditions. At each potential above the onset potential, Hidalgo *et al.* observed significantly larger currents under H_2 compared to the data shown in Figure 3.5. For example, at -74 mV, the current was measured to be ~140 µA,[26] in contrast to ~40 µA shown above (Figure 3.5A). Higher currents are usually indicative of an increase in enzyme coverage on the working electrode (Chapter 2, Equation 2.16)[40]. As the peak absorbances between the two sets of data are comparable (~0.4 mO.D.), the larger sample of enzyme has likely occurred from the use of a thicker film of the enzyme-particle network, rather than from a higher absorption of the enzyme onto the carbon particles.

The disadvantage of a thicker enzyme-loaded particle film is that the H_2 supply may not reach the entire sample, causing mass transport issues, i.e., part of the enzyme film is under electrocatalytic control (as it receives a continuous flow of fresh substrate and removal of product), but the rest is under electrochemical control. Figure 3.6 gives an example of an ATR-IR cell set-up where this problem arises. The IR beam can only detect sample that is within a specific distance from the IRE-sample interface (Section 2.1.2.3), as represented by the transparent red box in Figure 3.6. When the enzyme film is too thick, the buffer flow may not penetrate this portion of the sample. Thus it is possible for the sample that is detected by IR spectroscopy to not be entirely engaging in catalysis. This would mean that the active site redox states detected are not a true representation of the enzyme under catalytic turnover. Instead, they would reflect a portion of the enzyme under non-turnover conditions, similar to those shown in Figure 3.5B.

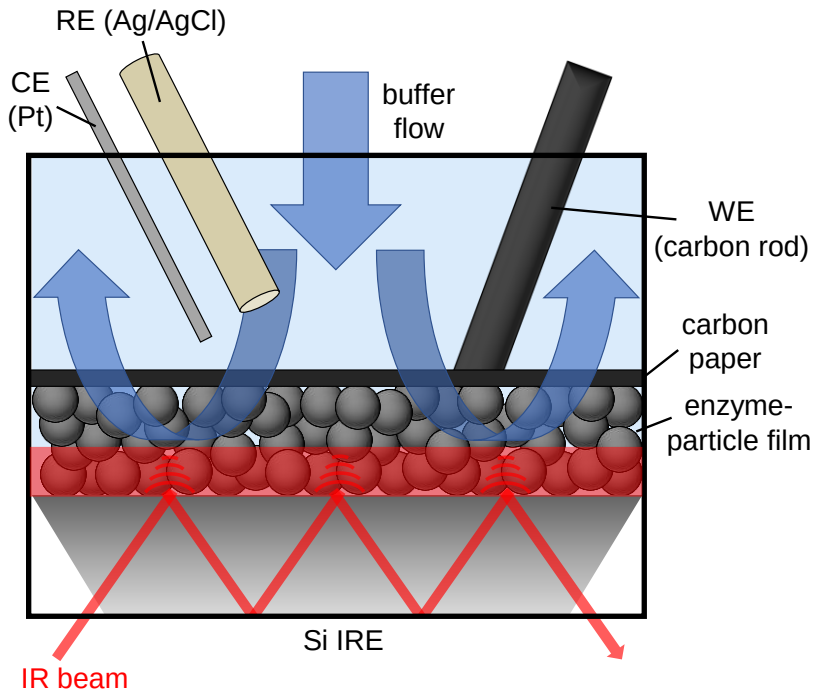


Figure 3.6 Schematic diagram of ATR-IR cell set-up with a thicker enzyme-loaded particle film, compared to the ideal set-up in Figure 2.20. The reference (RE), counter (CE) and working (WE) electrodes are labelled along with the Si internal reflection element (IRE). The transparent red box represents the approximate proportion of the enzyme-particle film detected by the IR beam. The blue arrows imitate the buffer flow through the cell. When the film is too thick, substrate cannot reach enzyme molecules at the bottom of the film.

When comparing the steady-state distributions of the active site redox levels under turnover conditions (H_2) of Hyd-1 as observed by Hidalgo *et al*. (Figure 3.7A) and in this Thesis (Figure 3.7B), there are some inconsistencies which may be due to mass transport limitations in the initial data. At low potential, the distributions are similar, with the Ni_a-R redox level making up the majority. Stepping up to -199 mV, Hidalgo observed an increase in the Ni_a-C / Ni_a-L redox level species accompanying the increase in current. However in Figure 3.7B, there is no detectable change in the relative distributions of the Ni_a-R and the Ni_a-C / Ni_a-L redox levels. Furthermore, at higher potentials, smaller proportions of the more oxidised redox levels, Ni_a-SI and Ni-B, were observed in Figure 3.7B compared to

previously. This is most notable at +356 mV where only 1% of Ni-B was observed compared to 14%. The higher proportion of Ni-B observed by Hidalgo may also be due to the initial larger amount of Ni_a-SI detected, as stepping from -74 mV to +356 mV involved a decrease in Ni_a-SI and increase in Ni-B in Figure 3.7A. This was not observed in the repeated experiments in Figure 3.7B as both the Ni_a-SI and Ni-B redox levels increased in absorbance.

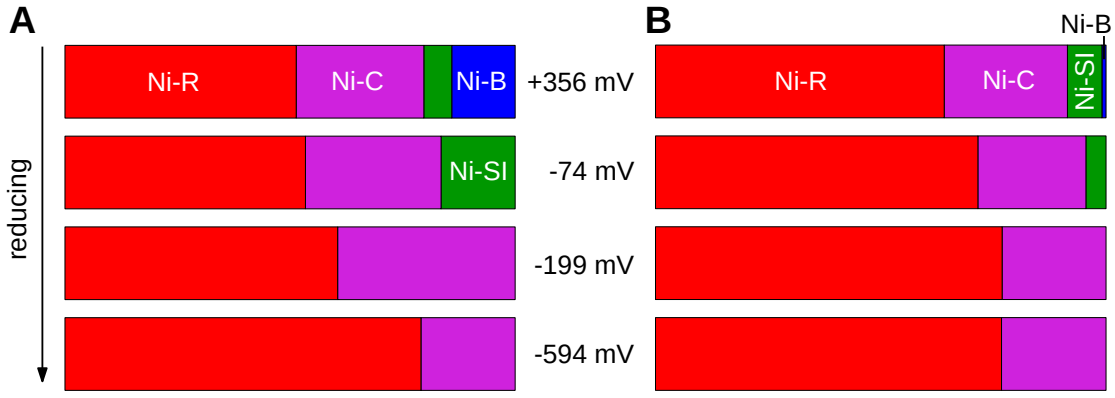


Figure 3.7 A comparison of the steady-state distributions of the active site redox levels under turnover conditions (100% H_2) of Hyd-1 as observed by Hidalgo *et al.*,[26], (A) and in this Thesis (B). The Ni_a-C band includes the Ni_a-L species as they are at the same redox level (-2 relative to Ni-B).

For both experiments, the H_2 concentration in the inlet buffer is far above the Michaelis Menten constant for Hyd-1 (9 µM)[38] throughout. Thus, providing there are no mass transport issues, there is enough substrate for each enzyme molecule to engage in catalysis. The difference between the two data sets suggests that the data obtained by Hidalgo was mass transport limited, likely caused by the thickness of the enzyme-particle film.

Repeating the PFIRE experiments have thus provided a more genuine representation of Hyd-1 under catalytic turnover, which in turn can provide valuable insight into the mechanism and O_2-tolerance of Hyd-1.

In the next section, the effect of pH on the non-turnover and turnover behaviour of Hyd-1 is discussed to investigate whether previous observations were affected by mass transport limitations.

3.2.2. The effect of pH

The activity and speciation of [NiFe]-hydrogenases are widely known to be pH-dependent.[1,11,41,42] For example, below pH 4, *E. coli* Hyd-1 transitions from being heavily biased towards H_2 oxidation to an efficient H_2-producer.[32] Multiple steps within the catalytic cycle involve proton transfers (Figure *3.2*) and are therefore highly sensitive to the protonation environment. In particular, the pH dependent equilibrium between the Ni_a-C and Ni_a-L species is well-documented across a range of [NiFe]-hydrogenases. For Hyd-1, a mixture of EPR and FTIR techniques have demonstrated this relationship whilst also highlighting the catalytic involvement of the Ni_a-L species.[25,41]

Importantly, pH also affects the reduction potentials of the proton-coupled electron transfer steps. For a PCET reaction, Equation [2.13], at 298 K, 1 atm, this relationship is given by the pH-dependent Pourbaix expression, Equation [3.2], as derived from the Nernst equation in Chapter 2.

$$Ox + ne^- + H^+ \rightleftharpoons RedH \qquad [3.1]$$

$$E_{Ox/RedH} = E^{0'}_{Ox/RedH} - \frac{0.059}{n} pH \qquad [3.2]$$

For each PCET step within the [NiFe]-hydrogenase catalytic cycle, n = 1 i.e., one electron transfer per proton transfer. Thus, for Equation [2.13], the reduction potential varies by -59 mV pH^{-1}. This also means that the potentials at which each redox species is maximised will also change with pH.

The PFIRE experiments under non-turnover and turnover conditions were repeated across a range of pH values (4.0, 5.0, 7.0, 8.0), although the data presented in this section focus on the lowest (4.0) and highest (8.0) pH values. Table *3.2* lists the potentials used at each pH, which were obtained with reference to those used by Hidalgo.[25] The potentials at which the Ni_a-R and Ni-B were maximised remained at -592 and +358 mV respectively as those potentials are still far enough removed from the Ni_a-R/Ni_a-C and Ni_a-SI/Ni-B transition redox potentials.

Table 3.2 Redox potentials at which each active site redox level is maximised.

pH	**Potential at which each redox level is maximised / mV**			
	Ni-b	**Ni_a-SI**	**Ni_a-C / Ni_a-L**	**Ni_a-R**
4.0	+358	+96	-102	-592
6.0	+358	-72	-197	-592
8.0	+358	-182	-312	-592

The change in potential between pH 8.0 and pH 6.0 for Ni_a-SI and Ni_aC / Ni_a-L are both within the expected range (∼-113 mV). This is similar to the changes in reduction potential of the redox transitions observed by Hidalgo, implying that the transitions involve a single $1H^+1e^-$ PCET, and that the pK_a of the proton acceptor is not between 6.0 and 8.0.[25] However, at pH 4.0, the change in potential for the Ni_a-C / Ni_a-L redox level is +95 mV, slightly less than expected (1.2 n), whereas the opposite is the case for Ni-SI: a much higher potential was required to obtain maximum Ni_a-SI intensity (+168 mV, 0.7 n).

There are four main observations in the non-turnover IR spectra measured at each pH value:

1) The ν_{CO} peak positions for all the active site redox states shift to higher wavenumbers at pH 4.0 and lower wavenumbers at pH 8.0 relative to pH 6.0.
2) The relative populations of Ni_a-C and total Ni_a-L, and of the individual Ni_a–$L_{II/III}$ sub-states, are pH dependent, however the pK_a for the Ni_a-C/Ni_a-L equilibrium is higher than that observed by Hidalgo.
3) The relative populations of the individual Ni_a–$R_{II/III}$ sub-states, are also pH dependent.
4) The intensities of the redox species with ν_{CO} bands at 1952 cm^{-1} (Ni_a-C^+) and 1933 cm^{-1} (Ni_a-R_I) at pH 6 appear to be pH dependent, but the high potential Ni-B-like species does not.

3.2.2.1. ν_{CO} pH dependency

Table 3.3 gives the ν_{CO} band positions for each active site redox species measured at the three main pH values, 4.0, 6.0 and 8.0. Band positions, reported the nearest 1 cm^{-1}, are derived from Gaussian profiles fitted to baseline-corrected IR spectra at the respective potentials at which the active site species is maximised, as in Table 3.2. The resolution used to record the IR spectra was 2 cm^{-1} and thus the shifts observed from Gaussian fits are not necessarily exact.

Table 3.3 The pH dependence of active site ν_{CO}. Band positions are rounded to 1 cm^{-1} from the fitted parameter and were taken from IR spectra at the potential at which each redox species is maximised.

pH	ν_{CO} band position/ cm^{-1}									
	Ni-B'	**Ni-B**	**Ni_a-SI**	**Ni_a-C^+**	**Ni_a-C**	**Ni_a-L_{II}**	**Ni_a-L_{III}**	**Ni_a-R_I**	**Ni_a-R_{II}**	**Ni_a-R_{III}**
4	1945	1942	1930	1953	1949	1877	1867	1936	1924	1915
6	1944	1942	1929	1952	1948	1876	1866	1933	1922	1914
8	1943	1940	1928	1951	1947	1875	1865	1932	1922	1913

Each active site redox species experiences a shift in ν_{CO} band position of 2-3 cm^{-1} between pH 4.0 and pH 8.0. This includes the additional bands labelled as Ni-B', Ni_a-C^+ and Ni_a-R_I**.** Hidalgo noted that the Ni_a-C species had the largest shift in ν_{CO} between pH 4.0 and 8.0, observing a 6 cm^{-1} increase with decreasing pH.[25] This is equivalent to the difference between the two 'Ni_a-C like' species with the 'Ni_a-C' species ν_{CO} = 1947.0 cm^{-1} at pH 8 and the 'Ni_a-C^+' species ν_{CO} = 1952.9 cm^{-1} at pH 4. This suggests that two active site species were present in the data recorded by Hidalgo, but the lower resolution (4 cm^{-1}) meant that only one peak was resolved.

For each active site ν_{CO} band, an increase in pH leads to a decrease in wavenumber. Typically, a decrease in ν_{CO} results from weakening of the C-O bond. This is often due to an increase in electron density at the metal centre resulting in more π-back bonding (refer to Section 2.1.4). However other factors such as interaction between the ligands and the surrounding coordination environment can also impact the C-O bond.

The CO and CN ligands bound to Fe in the [NiFe] active site participate in hydrogen bonding to the nearby secondary amino acid residues.[13] Changing the pH will alter the

protonation state of the residues, and thus the degree to which they interact with the active site. This in turn will affect the strength of the Fe-ligand bonds, and thus the $\nu_{CO/CN}$.

There are multiple cases of the IR bands of active site redox species shifting upon site-directed mutagenesis of amino acid residues near the active site. Both De Lacey *et al.* and Greene *et al.* observed shifts up to 4 cm^{-1} in the active site IR bands of a number of variants of *D. fructosovorans* [NiFe]-hydrogenase and the E17Q variant of *Pf* SH1 respectively.[43,44] Most recently, PFIRE experiments on the Arg → Lys variant of Hyd-1, R509K, showed minor shifts in active site ν_{CO} bands relative to native Hyd-1.[45] Therefore it can be seen that it is likely the change in the protonation of the surrounding amino acid residues that affects the position of the IR bands of active site species upon a change in pH.

Now that the overall effect of pH has been shown, individual pH-dependent equilibria are discussed.

3.2.2.2. Ni_a-C/Ni_a-L

The Ni_a-C and Ni_a-L redox species are known to be in a pH-dependent tautomeric equilibrium with each other (Figure 3.8).[1,41] The bridging hydride in Ni_a-C is extracted as a proton, leaving 2 electrons to reduce the Ni(III) to Ni(I), forming Ni_a-L. The exact identity of the base (B in Figure 3.8) has yet to be conclusively confirmed, but the presence of multiple Ni_a-L species detected in IR spectra suggest that there are multiple protonation sites within the active site. Nevertheless, studies on selected variants of [NiFe]-hydrogenases have shown that the nearby glutamine residue plays an important role in the subsequent oxidation of Ni_a-C/Ni_a-L to the Ni_a-SI species.[44,46,47]

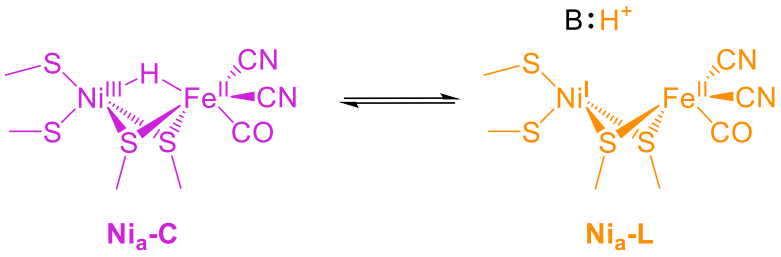


Figure 3.8 Tautomeric equilibrium between the Ni_a-C and Ni_a-L species. B represents a proton acceptor site within the active site region.

Figure 3.9 shows the IR spectra collected at the two extreme pH values (4.0 and 8.0) at the Ni_a-C/Ni_a-L redox level potential. There is a clear pH dependence on the relative intensities of the Ni_a-C and Ni_a-L species: at low pH, the protonated species, Ni_a-C, dominates over the unprotonated species, Ni_a-L, whereas the opposite is true at high pH. This is consistent with the results observed by Hidalgo.[41]

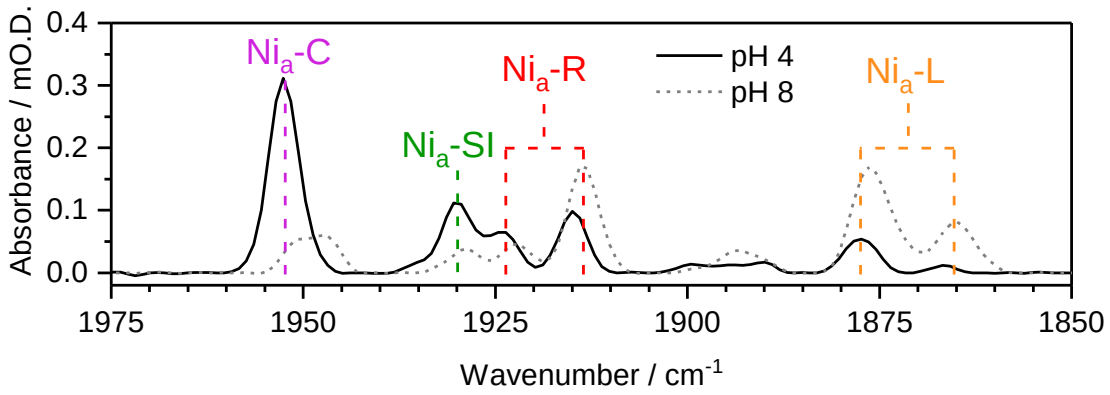


Figure 3.9 Baseline-corrected IR spectra, showing the ν_{CO} region only, recorded at pH 4.0 solid line, -102 mV) and 8.0 (dotted line, -312 mV).

This relationship is clearly observed when the relative areas of the two redox species are plotted as a function of pH (Figure 3.10A). Here, Ni_a-L represents the two sub-species Ni_a-L_{II} and Ni_a-L_{III}, while Ni_a-C includes the two redox species labelled above as Ni_a-C and Ni_a-C^+ (Table 3.3).

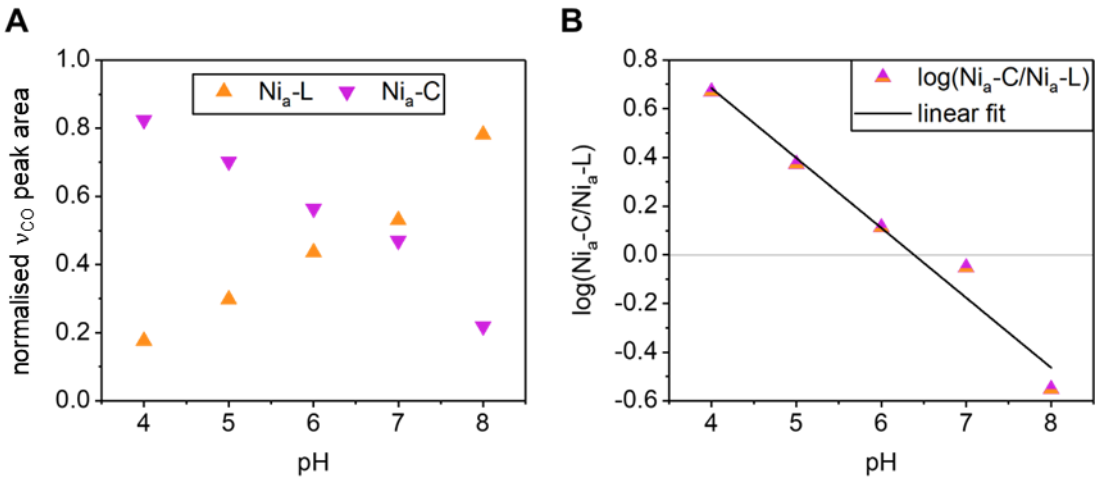


Figure 3.10 A) The relative peak areas of the Ni_a-C and Ni_a-L species as a function of pH. The intensities have been normalised to the sum of the peak areas of the Ni_a-C + Ni_a-L species. B) Henderson-Hasselbalch plot of Ni_a-C/Ni_a-L acid-base equilibrium. The slope of the linear fit is -0.29 and the x-axis intercept, determined from the fit, is 6.38, with an R^2 value of 0.97.

The Henderson-Hasselbalch equation (Equation [3.3]) can be used to predict the pK_a of the acid-base equilibrium. For a one proton transfer, the slope should be -1.

$$\log_{10}\left(\frac{HA}{A^-}\right) = -pH + pK_a \qquad [3.3]$$

Figure 3.10B shows this plot for the Ni_a-C/Ni_a-L acid-base equilibrium. As expected, the slope of the linear fit is not -1 but instead -0.29 ± 0.03, demonstrating that there are multiple protonation sites for this acid-base equilibrium, consistent with the multiple Ni_a-L sub-species and the additional Ni_a-C species. The predicted pK_a of the equilibrium is 6.4 ± 0.2, as determined from the linear fit. This is higher than the pK_a of 5.0 which was previously observed by Hidalgo for Hyd-1. Whilst this is not expected, a difference in the predicted pK_a for the Ni_a-C/Ni_a-L equilibrium in Hyd-1 has been observed before.[41] Murphy *et al.* performed similar pH titrations using EPR spectroscopy on frozen samples of Hyd-1. Their results followed a more traditional single one-proton equilibrium with a pK_a > 6.[41] This discrepancy was rationalised by the difference in sampling states and temperature.

However, this is not the case for the results given in Figure *3.10* as measurements were performed using the PFIRE method, under similar conditions to those obtained previously. One reason for the inconsistency may be that the peak intensities for two Ni_a-C species are used when calculating the proportion of Ni_a-C, and thus across all pH values Ni_a-C is in greater quantities than observed by Hidalgo. Furthermore, the pH range used in this Thesis (4.0 – 8.0) is relatively narrow compared to that studied by Hidalgo (3.0 – 9.0), and so a complete comparison cannot be given.

As noted above, two 'Ni-C' like ν_{CO} bands were detected in the PFIRE spectra across all pH values, contrary to the single species observed by Hidalgo. Possible identities of the two 'sub-species' are a Ni-C^+ species, where an additional proton acceptor within the active site is protonated, and the traditional Ni-C species. If this is the case, it is expected that both species will be pH-dependent.

Despite the Ni_a-C species decreasing overall with an increase in pH, the distinct behaviour of the individual 'sub-species' with pH alludes to an acid-base equilibrium. Performing a Henderson-Hasselbalch analysis reveals the pH dependence of these two species, as shown in Figure *3.11*. At low pH, the higher wavenumber 'Ni_a-C^+' species predominates although it decreases as the pH increases. The lower wavenumber 'Ni_a-C' species on the other hand, increases in concentration with pH. The Henderson-Hasselbalch plot in Figure *3.11*B does not follow that for a single protonation curve, with the slope calculated as -0.39 instead of -1. This is likely due to the influence from the acid-base equilibrium with the Ni_a-L species. Nevertheless, the linear fit predicts a pK_a for the Ni_a-C/Ni_a-C^+ equilibrium of 7.42.

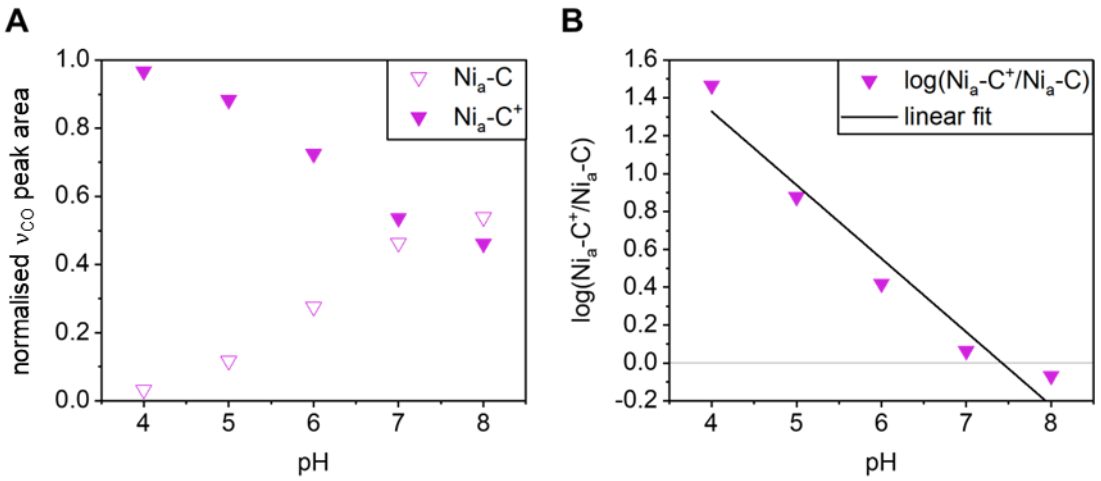


Figure 3.11 A) The relative peak areas of Ni_a-C (1948 cm^{-1} at pH 6) and Ni_a-C^+ (1952 cm^{-1} at pH 6) as a function of pH. The intensities have been normalised to the total peak areas for both species. B) Henderson-Hasselbalch plot of Ni_a-C/Ni_a-C^+ acid-base equilibrium. The slope of the linear fit is -0.39 and the x-axis intercept, determined from the fit, is 7.42, with an R^2 value of 0.92.

The behaviour of these two species with pH is similar to that observed in pH FTIR studies on *Pf* SHI by Greene *et al.*, supporting the hypothesis that there may be a protonated and an unprotonated Ni_a-C species. Formation of the Ni_a-C state from Ni_a-R involves a proton-coupled electron transfer step. It is quite possible that the protonated Ni_a-C^+ species arises following oxidation of the Ni^{II} within Ni_a-R prior to complete removal of the proton from the active site vicinity, i.e. electron transfer occurs before proton transfer. However, the appearance of the Ni_a-R sub-species, in particular the prominence of the Ni_a-R_{III} species over the other two, implies that, at least initially, this is not the case.

3.2.2.3. Ni_a-R

Up to three Ni_a-R species have been observed across a number of [NiFe]-hydrogenases (Section 3.1.3). These are thought to represent different protonation states of the Ni_a-R active site redox level, with each species representing a proton moving further from the [NiFe]-active site, as shown in Figure 3.12.[11] In Hyd-1, two Ni_a-R sub-species have been

conclusively reported: Ni_a-R_{II} and Ni_a-R_{III}. The third species, Ni_a-R_I, was not observed in the solution IR studies performed by Healy nor the PFIRE experiments performed by Hidalgo.[23,26] Nevertheless, as shown in Figure 3.5, a ν_{CO} band at 1933 cm^{-1} at pH 6 was observed at low potentials, hypothesised to be the elusive Ni_a-R_I sub-species.

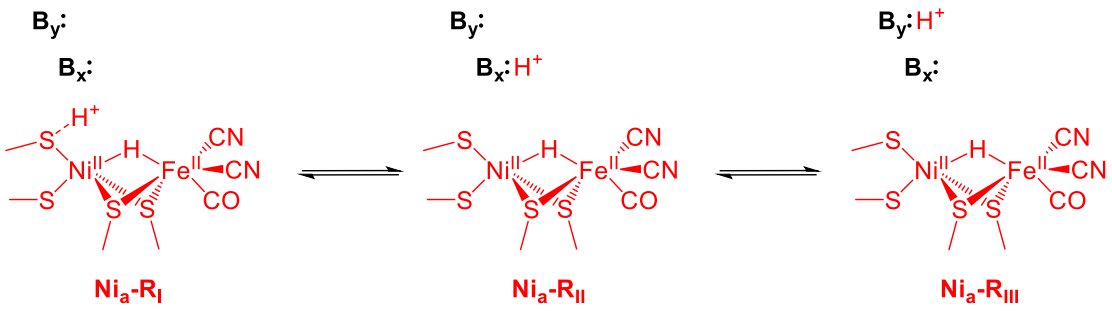


Figure 3.12 Schematic representation of the Ni_a-R sub-species showing proton transfer *via* three different proton acceptors shuttling the abstracted proton from the [NiFe] active site: the terminal Ni cysteine is proposed to be the initial proton acceptor, with B_x and B_y representing the subsequent basic sites.

As the Ni_a-R sub-species are differentiated by the position of a proton, it follows that the equilibrium between the three will be pH-dependent. Figure 3.13 shows how each Ni_a-R species behaves with varying pH. In Figure 3.13A, the ν_{CO} peak areas for each Ni_a-R sub-species (normalised to the total peak areas of all sub-species) are given as a function of pH. It is evident that even though the behaviour of the Ni_a-R species does not follow a traditional Henderson-Hasselbalch acid-base equilibrium, there is a strong correlation with pH. Between pH 4.0 and 6.0, Ni_a-R_{III} decreases alongside an increase in Ni_a-R_{II} and Ni_a-R_I. However, above pH 6.0, the reverse is apparent: Ni_a-R_{III} increases whilst Ni_a-R_{II} and Ni_a-R_I decrease.

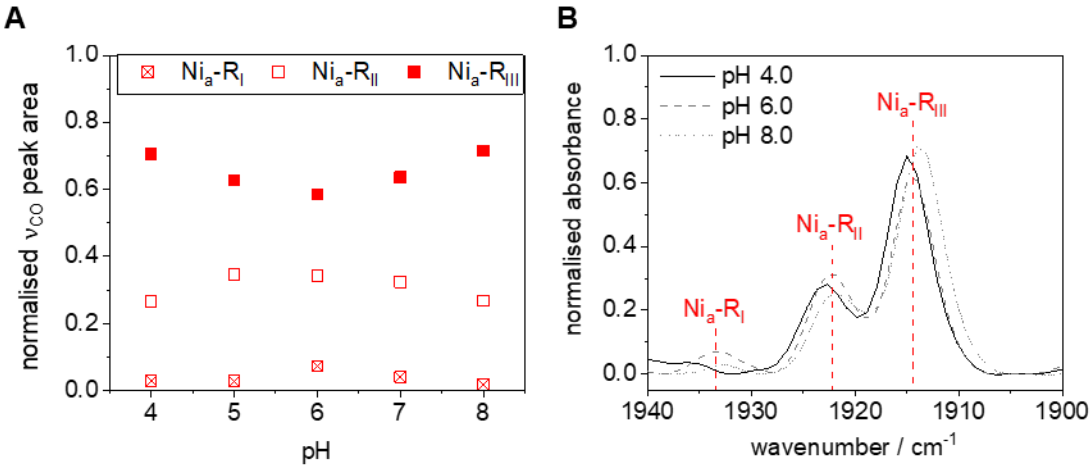


Figure 3.13 A) The relative peak areas of the Ni_a-R_I, Ni_a-R_{II} and Ni_a-R_{III} species as a function of pH. The areas have been normalised to the total peak areas of the Ni_a-R species. B) IR spectra, showing the region where the Ni_a-R ν_{CO} bands are observed, recorded at pH 4.0, 6.0 and 8.0 at -592 mV. The change in wavenumber with pH is apparent.

Overall, the behaviour of the Ni_a-R sub-species with pH is analogous to that observed by Hidalgo. Furthermore, the pH dependency of the 1933 cm^{-1} species in comparison with the other Ni_a-R sub-species strongly suggests that it is in fact a Ni_a-R_I species.

3.2.2.4. Ni-B

At high potentials, two ν_{CO} bands within 3 cm^{-1} of one another were detected across all pH values. In previous IR spectroelectrochemical studies of [NiFe]-hydrogenases, including Hyd-1, only one ν_{CO} band was observed at high potential under non-turnover conditions, assigned as the inactive Ni-B species. The similarity in wavenumber of the two ν_{CO} bands suggests they arise due to similarly structured active site redox species. One hypothesis on the identities of two species (as discussed above in Section 3.2.1.1) is that one belongs to the traditional inactive Ni-B species, whereas the second arises from protonation of the OH bridging ligand to give H_2O. If this were the case, it is expected that the two species would be pH dependent and follow a Henderson-Hasselbalch acid-base equilibrium.

However, there appears to be no correlation between the relative intensities of the two high potential ν_{CO} bands and pH.

Out of the three suggestions on the identity of the additional high potential ν_{CO} band, a 'superoxidised' Ni-B, where the proximal [4Fe3S] cluster is superoxidised to $[4Fe3S]^{5+}$, remains the most likely. However, a detailed high potential redox titration of these two species is required to confirm this, as if the additional ν_{CO} band is due to a 'superoxidised' Ni-B, its absorbance should increase with potential alongside a decrease in the 'normal' Ni-B species.

3.2.3. Comparing O_2-tolerant and O_2-sensitive [NiFe]-hydrogenases under catalytic turnover

3.2.3.1. Hyd-1

When under H_2, the most reduced redox level, Ni_a-R, dominates as the majority species at all applied potentials, alongside a reasonable amount of Ni_a-C and Ni_a-L, as shown in Figure *3.7*B (Ni-C represents the sum of the Ni_a-C and Ni_a-L species). This signifies that for Hyd-1 the kinetic bottleneck is the Ni_a-R species, i.e., consumption of Ni_a-R is rate limiting. Conversion of the Ni_a-R species to the Ni_a-C species involves a proton-coupled electron transfer step (Figure 3.2): Ni^{II} is oxidised to Ni^{III} and a proton is removed from the vicinity of the active site. The exact details of this mechanism, whether it is a concerted or stepwise PCET, and the proton transfer pathway are not yet fully determined.

DFT calculations suggest that the terminal Ni-bound cysteine thiolate is the base that accepts the proton following H_2 cleavage and is thus protonated in the Ni_a-R species.[18,48] In a high-resolution crystal structure of the Ni_a-R state of the [NiFe]-hydrogenase from *D. vulgaris* MF, residual electron density was observed at a terminal cysteine thiolate, which was proposed to be evidence of the protonated cysteine.[17] However due to the

discrepancy between the modelled and theoretical C-S-H bond angle and the known difficulty of resolving protons using X-ray diffraction with their lack of electron density, this assignment is still questioned. The exact protonation environment of the Ni_a-R state is further complicated by the appearance of multiple ν_{CO} bands in the IR spectra. The IR spectrum of the *Dv* MF reduced crystals showed that 78-85% of the sample was in the Ni_a-R_I state, with <18% as Ni_a-R_{II}. Therefore the crystal structure only represents one Ni_a-R sub-species. Three Ni_a-R ν_{CO} bands were observed throughout the PFIRE experiments performed in this Chapter and are posited to represent multiple protonation states of the Ni_a-R species. As the proton moves further from the active site, its influence on the Fe-CO bond decreases and is reflected by a decrease in ν_{CO} wavenumber. This observation also suggests that, at least initially, proton transfer occurs prior to oxidation of the Ni, and thus the Ni_a-R/Ni_a-C transition involves stepwise PCET. During the photoinduced reduction of *P. furiosus* SH1, Dyer and co-workers observed a delay in Ni_a-R_I formation relative to decay of Ni_a-C which suggests there is an intermediate during Ni_a-R/Ni_a-C conversion.[36] As only one Ni_a-R species was observed (Ni_a-R_I, ν_{CO} 1954 cm^{-1}) it is possible that the intermediate is another sub-species of Ni_a-R. In fact, the time dependent formation of Ni_a-R sub-species has already been detected in crystalline Hyd-1. Ash *et al.* distinguished distinct kinetics of formation of two Ni_a-R states following a reductive potential step, further supporting the assignment of the Ni_a-R/Ni_a-C intermediate as another Ni_a-R sub-species.[49]

Assuming the Ni_a-R_I state is the initial state formed after H_2 cleavage, and that it does contain a protonated thiolate, deprotonation would lead to the other Ni_a-R sub-species. Through PFIRE studies on a Hyd-1 variant, E28Q, Evans *et al.* showed that the nearby glutamate residue is not required for transferring protons from the active site between the Ni_a-R and Ni_a-C intermediates, as Ni_a-C was observed in a significant proportion under turnover conditions.[47] This contrasts with previously hypothesised proton pathways

which, based on evidence that proton transfer is slowed at pH values greater than the p*K*a of the glutamate, predict the glutamate residue to be required for deprotonation.[17,36,50] Nevertheless, this does not completely discount the role of the glutamate in proton transfer between Ni_a-R and Ni_a-C. If the glutamate was essential for proton transfer, the E→ Q variants would not show any activity. In many variants, there is still relatively high residual activity implying flexibility of proton transfer within the active site.[51] Thus, during Ni_a-R / Ni_a-C transition, proton transfer *via* the glutamate may be preferred but at least in the E→ Q variant, an alternative pathway is used.

Only a small proportion of the Ni-R level is Ni_a-R_I in Hyd-1 under turnover conditions (<8%). Instead, the two lower wavenumber bands are most prominent, with the Ni_a-R_{III} species at 1914 cm^{-1} making the majority. This implies that proton transfer, at least not the initial transfer away from the active site, is not the limiting step in Ni_a-R/Ni_a-C conversion. Instead, electron transfer must be hindered. The reduction potential of the [4Fe3S] proximal cluster is unusually high in Hyd-1, much higher than the Ni_a-R/Ni_a-C redox couple (+30 mV c.f. -220 mV).[26,41] This means that oxidation of the active site to the Ni_a-C level is hindered as the proximal cluster is already occupied. Therefore, under turnover, the majority of the enzyme remains in the Ni_a-R state.

Table 3.4 Mid-point potentials of the EPR-active Fe-S clusters in O_2-tolerant [NiFe]-hydrogenases

Enzyme	Mid-point potentials / mV *vs* SHE				
	$[4Fe3S]^{5+/4+}$ proximal	$[4Fe3S]^{4+/3+}$ proximal	$[3Fe4S]^{+/0}$ medial	$[3Fe4S]^{+/0}_{app.}$ medial	$[4Fe4S]^{2+/+}$ distal
***Ec* Hyd-1**[31]	+230	+30	+190	+130	n.d.
***Aa* Hase I**[52]	+232	+98	n.d.	+78	-65
***Re* MBH**[53]	+160	n.d.	n.d.	+25	-60

It is important to note that neither under Ar nor H_2 was it possible to completely reduce Hyd-1 to Ni_a-R. There is always a proportion of the enzyme at the Ni-C/Ni-L redox level. This is the case for a number of standard [NiFe]-hydrogenases,[2,4] but not for O_2-tolerant [NiFe]-hydrogenases such as *Aquifex aeolicus* Hase I and *Ralstonia eutropha* H16 MBH.[6,7] The redox potentials of the iron-sulfur clusters of these enzymes are comparable to those of Hyd-1 (Table 3.4), and thus are fully reduced at low potentials. Therefore it is expected Hyd-1 would behave in a similar way upon reduction, i.e., oxidation to the Ni-C/Ni-L redox level is hindered, meaning only Ni_a-R is detected at low potentials under H_2. As this is not the case, there must be another reason why Hyd-1 behaves slightly differently than other O_2-tolerant [NiFe]-hydrogenases. It is possible that Hyd-1 utilises a different proton transfer pathway to remove the proton from the Ni_a-R_{III} sub-species, i.e., the sub-species where the proton is furthest from the active site. Indeed, there appear to be possible alternate pathways as shown by the residual activity in variants of Hyd-1, noted above.[47,51] Alternatively, it may be that small amounts of the active site were at the Ni_a-C/Ni_a-L redox level in *Aa* Hase I and *Re* MBH, but the sensitivities of the techniques used to measure the 'pure' Ni_a-R spectra were not high enough to detect such low concentrations.

Nevertheless, using the PFIRE technique has revealed that the rate limiting step in the catalytic cycle of Hyd-1 is the Ni_a-R / Ni_a-C transition and that this may also be the case for other O_2-tolerant [NiFe]-hydrogenases.

3.2.3.2. Hyd-2

A similar steady-state analysis can be performed on another [NiFe]-hydrogenase studied using the PFIRE technique: *E. coli* hydrogenase-2 (Hyd-2). All data pertaining to Hyd-2 are provided by Min-Wen Chung.[54]

Hyd-2 is a standard Group 1 [NiFe]-hydrogenase which, unlike Hyd-1, is an efficient bidirectional H_2 catalyst and is reversibly inactivated in the presence of O_2. An important difference between Hyd-1 and Hyd-2 is their ability to undergo proton reduction at low potentials. Hyd-1 is a poor H_2 producer under the conditions used throughout the PFIRE experiments, whereas Hyd-2 is shown to produce H_2 when below the H_2/H^+ redox couple (-353 mV, predicted by the Nernst equation under these conditions: 1 bar H_2; pH 6; 298 K).

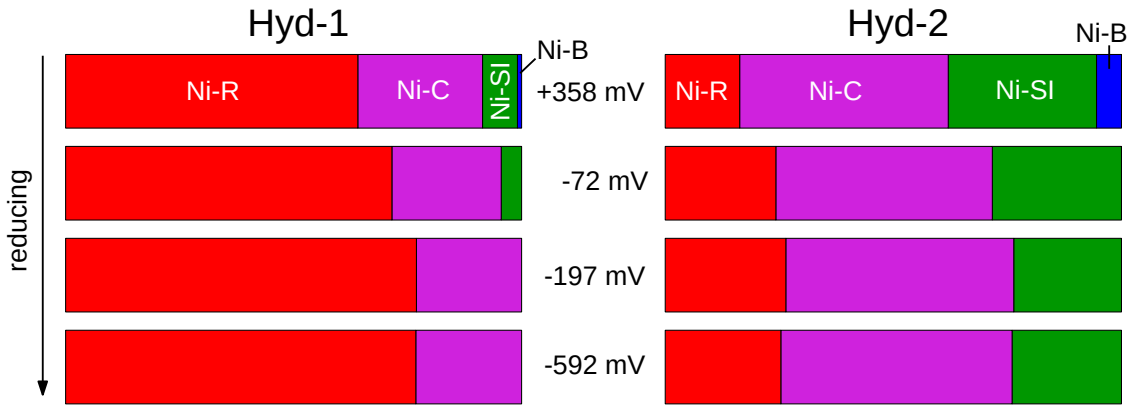


Figure 3.14 Steady-state distributions of active site redox levels of *E. coli* hydrogenase-1 and hydrogenase-2 under turnover conditions (100% H_2) at different potentials. Hyd-2 data was obtained from reference [54]. For Hyd-1, the Ni-C redox level includes absorbances from the Ni-C and Ni-L species, however as no Ni-L was observed by Chung in their Hyd-2 PFIRE experiments, only absorbances from Ni-C are used.

Figure 3.14 gives a side-by-side comparison of the steady-state distributions of the active site species in Hyd-1 and Hyd-2 under turnover conditions. Whilst once again the Ni_a-R and Ni_a-C species are observed at all applied potentials when under H_2 in Hyd-2, the proportions of these species are very different compared to Hyd-1. The Ni_a-C species is now the most dominant, with the Ni_a-R species present, but at a consistently smaller ratio. This implies that the Ni_a-C species is the kinetic bottleneck for Hyd-2, i.e., the Ni_a-C/Ni_a-SI transition is the rate determining step. It is important to note that in the PFIRE studies on Hyd-2, no bands were observed that could be attributed to a Ni_a-L species, and thus the Ni_a-C to Ni_a-SI transition is thought to proceed through a single proton-coupled electron transfer step.[54] Therefore the Ni-C bands (purple) in Figure 3.14 for Hyd-2 only represent the Ni_a-C species.

Most significantly, the Ni_a-SI species is present across all potentials when under H_2. In fact, the distribution of the Ni-R, Ni-C and Ni-SI redox levels remains approximately unchanged upon stepping from -592 mV (below the H_2/H^+ redox couple) to -197 mV (above the H_2/H^+ redox couple). At -592 mV, Hyd-2 catalyses proton reduction (as shown by the negative current in Figure 3.5A), and thus protons react with Ni_a-R to form Ni_a-SI, leading to a high steady-state concentration of Ni_a-SI, even at low potentials. Stepping up to -197 mV, H_2-oxidation now dominates, but Ni_a-SI is still detected. As a standard [NiFe]-hydrogenase, the redox potentials of the iron-sulfur clusters in Hyd-2 are likely to be relatively low, and near the Ni_a-C/Ni_a-SI redox couple. For example, the standard hydrogenase from *Dv*MF has an apparent proximal cluster redox potential of <-300 mV at pH 7.7 and the redox couple for the Ni_a-C/Ni_a-SI transition is -337 mV at pH 7.8.[2,55] This means that at -197 mV, oxidation of Ni_a-C to form Ni_a-SI is not thermodynamically hindered, thus the steady-state concentration of Ni_a-SI is effectively unchanged. The higher concentration of Ni_a-C

compared to Ni_a-SI does, however, imply that this transition is slow relative to other steps within the catalytic cycle.

Similar to Hyd-1, increasing the applied potential further increases the rate of electron transfer, and thus the rate of transitions that involve PCET steps. Therefore, at higher potentials, the steady-state concentration of Ni_a-SI increases and Ni_a-R decreases. At +358 mV, Ni-B is present showing partial inactivation of the enzyme. The concentration of Ni-B detected is higher than that in Hyd-1, likely due to the larger initial amount of Ni_a-SI present under steady-state turnover. The high steady-state concentration of Ni_a-SI during turnover may also explain the sensitivity of Hyd-2 towards O_2, as a significant proportion of the enzyme is in the state that has a vacant bridging site, and thus susceptible to inactivation by O_2 or CO.

As with the PFIRE studies of Hyd-1 performed by Hidalgo, there is a risk that the turnover experiments performed on Hyd-2 by Chung are also partially mass transport limited. Repeating the PFIRE studies on Hyd-2 was beyond the scope of this Thesis, and so it is unclear whether this is the case.

3.2.3.3. Discussion

Under turnover conditions, the primary difference between Hyd-1 and Hyd-2 is which active site redox level has the higher net steady-state distribution. For Hyd-1, the Ni_a-R species are the most dominant by quite a large margin, whereas for Hyd-2 it is the Ni_a-C state. This in turn implies that Hyd-1 and Hyd-2 have different rate determining steps: oxidation of Ni_a-R for Hyd-1, and oxidation of Ni_a-C for Hyd-2.

One explanation for this discrepancy is the differences in each enzymes' iron-sulfur clusters. As a standard [NiFe]-hydrogenase, Hyd-2 contains a [4Fe4S] proximal cluster and the redox potentials of all its iron-sulfur clusters are relatively low. Hyd-1 on the other

hand has a [4Fe3S] proximal cluster, unique to O_2-tolerant [NiFe]-hydrogenases and the redox potentials for the clusters are all unusually high. This means that for Hyd-1, the redox clusters are more likely to be reduced at any point during turnover and unable to accept an electron from the active site. Thus, the catalytic cycle is held up at the first electron transfer step: Ni_a-R to Ni_a-C. This is not the case for Hyd-2, as the lower FeS cluster redox potentials means that they are more likely to be oxidised during turnover and able to accept an electron from the Ni_a-R species.

Instead, the build-up of the Ni_a-C species in Hyd-2 during turnover implies the Ni_a-C / Ni_a-SI transition is hindered. As with oxidation of Ni_a-R, the transition between Ni_a-C and Ni_a-SI requires transfer of a proton and an electron. For Hyd-1 and other O_2-tolerant [NiFe]-hydrogenases, multiple catalytically relevant Ni_a-L species have been observed, hinting at a step-wise Ni_a-C → Ni_a-L → Ni_a-SI transition. However, in standard [NiFe]-hydrogenases like Hyd-2, no catalytically relevant Ni_a-L species have been detected. As the proximal cluster of standard [NiFe]-hydrogenases remain largely oxidised, there is rapid electron transfer to the proximal cluster from Ni_a-L to form Ni_a-SI. Therefore the fast consumption of Ni_a-L means that it is not detected.

Overall, this shows that it is important to consider as wide a range of hydrogenases as possible before drawing any conclusions regarding the general [NiFe]-hydrogenase mechanism as there are subtle but significant differences.

3.2.4. Conclusion

By repeating the IR spectroelectrochemical analysis of Hyd-1 using the protein film IR electrochemical technique, a complete assignment of each active site redox species' ν_{CO} and ν_{CN} bands has been made as shown in Table 3.5. The higher spectral resolution used has also allowed the following additional features to be observed:

1) Ni_a-C^+ – the single ν_{CO} band initially assigned to the Ni_a-C state was found to be composed of two individual peaks, representing a protonated and unprotonated Ni-C species, similar to that observed in another O_2-tolerant [NiFe]-hydrogenase, *Pf* SH1.
2) Ni_a-R_I – a low potential species, whose dependence on potential and pH closely mimicked the Ni_a-R species was observed and assigned as the previously unseen Ni_a-R_I sub-species.
3) Ni-B' – as with the Ni_a-C species, two ν_{CO} bands were observed at high potential, whereas before only one Ni-B band was detected. There was no apparent pH dependency of either band. Assuming one of the bands belongs to the inactive Ni-B species, the identity of the other Ni-B' band is suggested to be due a Ni-B species whose [4Fe3S] cluster is superoxidised to $[4Fe3S]^5$. Further high potential redox titrations are required to confirm this hypothesis.

Furthermore, the results in this Chapter confirm the assignment of the Ni_a-L species as catalytically active in O_2-tolerant Hyd-1, alongside the Ni_a-R, Ni_a-C and Ni_a-SI, as they were observed under H_2 at a potential outside of the potential window where it was seen under non-turnover conditions. However the pK_a of the acid-base equilibrium between the Ni_a-C and Ni_a-L species was determined to be 6.38, closer to that determined from EPR pH titrations rather than from the other PFIRE experiments. The additional Ni_a-C band is likely the cause of this.

Table 3.5 Wavenumber positions of the ν(CO) and ν(CN) bands for each of the identified active site redox species observed by protein film infra-red electrochemistry, measured at pH 6.0. n.d. signifies that no band was detected.

Redox species	**Wavenumber / cm^{-1}**	
	ν(CO)	**ν(CN)**
Ni-B'	1944	n.d., 2093
Ni-B	1942	2099, 2082
Ni_a-SI	1930	2085, 2076
Ni_a-C^+	1952	2090, n.d.
Ni_a-C	1948	2078, n.d.
Ni_a-L_{II}	1877	2051, 2034
Ni_a-L_{III}	1866	2046, 2028
Ni_a-R_I	1933	n.d.
Ni_a-R_{II}	1922	2071, 2053
Ni_a-R_{III}	1914	2067, 2049

Work in this Chapter has also highlighted an inherent difficulty when using the PFIRE technique. As a major characteristic of the technique is its ability to monitor the active site redox species under turnover conditions, it is vital that the entire enzyme sample is under electrocatalytic control. If the enzyme-particle film used is too thick, the PFIRE experiments are mass transport limited, and thus do not give an accurate representation of the active site under turnover conditions. The differences in the data displayed in this Chapter, compared to those presented by Hidalgo, have shown that it is likely the previous PFIRE studies on Hyd-1 under turnover conditions were in fact mass transport limited.

Finally, by comparing the steady-state distributions of the active site redox levels under turnover conditions of Hyd-1 and its oxygen sensitive counterpart, Hyd-2, it is shown that the rate limiting step is not the same across all [NiFe]-hydrogenases. For Hyd-1, the Ni_a-R/Ni_a-C transition is rate limiting, as shown by the predominance of the Ni_a-R species across all applied potentials when under H_2. For the standard Hyd-2, however, the majority of the active site is at the Ni-C redox level under turnover conditions, suggesting that the Ni_a-C/Ni_a-SI PCET step is rate determining. This major difference shows that it may be incorrect to assume that there is a general catalytic mechanism, and that not all [NiFe]-hydrogenases undergo the same elementary proton transfer steps, *via* the same proton acceptor sites, during redox state transitions.

Overall, this Chapter provides a thorough IR spectroelectrochemical analysis of *E. coli* Hyd-1 adsorbed onto an electrode which can then be used to compare the behaviour of Hyd-1 in different forms and preparations. Now a more complete overview of the behaviour of Hyd-1 adsorbed on to an electrode surface has been performed, Chapter 4 will focus on the development of an IR microspectroscopic-electrochemical technique for investigating single crystals of Hyd-1, and whether the crystalline state affects the redox behaviour of the active site.

3.3. References

1 W. Lubitz, H. Ogata, O. Rüdiger and E. Reijerse, *Chem Rev*, 2014, 114, 4081–4148.

2 C. Fichtner, C. Laurich, E. Bothe and W. Lubitz, *Biochemistry*, 2006, **45**, 9706–9716.

3 B. Bleijlevens, F. A. van Broekhuizen, A. L. de Lacey, W. Roseboom, V. M. Fernandez and S. P. J. Albracht, *J. Biol. Inorg. Chem.*, 2004, **9**, 743–52.

4 A. L. de Lacey, E. C. Hatchikian, A. Volbeda, M. Frey, J. C. Fontecilla-Camps and V. M. Fernandez, *J Am Chem Soc*, 1997, **119**, 7181–7189.

5 M. Horch, L. Lauterbach, M. Saggu, P. Hildebrandt, F. Lendzian, R. Bittl, O. Lenz and I. Zebger, *Angew. Chem., Int. Ed.*, 2010, **49**, 8026–8029.

6 M. Saggu, I. Zebger, M. Ludwig, O. Lenz, B. Friedrich, P. Hildebrandt and F. Lendzian, *J. Biol. Chem.*, 2009, **284**, 16264–16276.

7 M. E. Pandelia, V. Fourmond, P. Tron-Infossi, E. Lojou, P. Bertrand, C. Léger, M. T. Giudici-Orticoni and W. Lubitz, *J Am Chem Soc*, 2010, **132**, 6991–7004.

8 M.-E. Pandelia, H. Ogata, L. J. Currell, M. Flores and W. Lubitz, *J. Biol. Inorg. Chem.*, 2009, **14**, 1227–1241.

9 H. Tai, L. Xu, K. Nishikawa, Y. Higuchi and S. Hirota, *Chem. Commun.*, 2017, **53**, 10444–10447.

10 J. L. Barilone, H. Ogata, W. Lubitz, M. van Gastel, A. Pamplona, J. Telser, I. Moura, J. J. G. Moura, B. M. Hoffman and J. C. Fontecilla-Camps, *Phys. Chem. Chem. Phys.*, 2015, **17**, 16204–16212.

11 P. A. Ash, R. Hidalgo and K. A. Vincent, *ACS Catal*, 2017, **7**, 2471–2485.

12 A. Volbeda, L. Martin, E. Barbier, O. Gutiérrez-Sanz, A. L. de Lacey, P.-P. Liebgott, S. Dementin, M. Rousset and J. C. Fontecilla-Camps, *J. Biol. Inorg. Chem.*, 2015, **20**, 11–22.

13 A. Volbeda, E. Garcin, C. Piras, A. L. de Lacey, V. M. Fernandez, E. C. Hatchikian, M. Frey and J. C. Fontecilla-Camps, *J Am Chem Soc*, 1996, **118**, 12989–12996.

14 T. Krämer, M. Kampa, W. Lubitz, M. van Gastel and F. Neese, *ChemBioChem*, 2013, **14**, 1898–1905.

15 A. L. de Lacey, V. M. Fernández, M. Rousset and R. Cammack, *Chem Rev*, 2007, 107, 4304–4330.

16 R. Breglia, C. Greco, P. Fantucci, L. de Gioia and M. Bruschi, *Inorg Chem*, 2019, **58**, 279–293.

17 H. Ogata, K. Nishikawa and W. Lubitz, *Nature*, 2015, **520**, 571–574.

18 H. Ogata, T. Krämer, H. Wang, D. Schilter, V. Pelmenschikov, M. van Gastel, F. Neese, T. B. Rauchfuss, L. B. Gee, A. D. Scott, Y. Yoda, Y. Tanaka, W. Lubitz and S. P. Cramer, *Nat Commun*, 2015, **6**, 1–8.

19 M. Bruschi, M. Tiberti, A. Guerra and L. de Gioia, *J Am Chem Soc*, 2014, **136**, 1803–1814.

20 R. M. Evans, E. J. Brooke, S. A. M. Wehlin, E. Nomerotskaia, F. Sargent, S. B. Carr, S. E. V. Phillips and F. A. Armstrong, *Nat Chem Biol*, 2016, **12**, 46–50.

21 M. Brecht, M. van Gastel, T. Buhrke, B. Friedrich and W. Lubitz, *J Am Chem Soc*, 2003, **125**, 13075–13083.

22 S. Foerster, M. Stein, M. Brecht, H. Ogata, Y. Higuchi and W. Lubitz, *J Am Chem Soc*, 2003, **125**, 83–93.

23 A. J. Healy, D.Phil. thesis, University of Oxford, 2013.

24 P. A. Ash, S. E. T. Kendall-Price, R. M. Evans, S. B. Carr, A. R. Brasnett, S. Morra, J. S. Rowbotham, R. Hidalgo, A. J. Healy, G. Cinque, M. D. Frogley, F. A. Armstrong and K. A. Vincent, *Chem Sci*, 2021, **12**, 12959–12970.

25 R. Hidalgo, D.Phil. thesis, University of Oxford, 2016.

26 R. Hidalgo, P. A. Ash, A. J. Healy and K. A. Vincent, *Angew. Chem., Int. Ed.*, 2015, **54**, 7110–7113.

27 P. A. Ash, R. Hidalgo and K. A. Vincent, *J. Vis. Exp.*, 2017, **2017**, 55858.

28 H. Ogata, P. Kellers and W. Lubitz, *J Mol Biol*, 2010, **402**, 428–444.

29 M. J. Lukey, M. M. Roessler, A. Parkin, R. M. Evans, R. A. Davies, O. Lenz, B. Friedrich, F. Sargent and F. A. Armstrong, *J Am Chem Soc*, 2011, **133**, 16881–16892.

30 H. Adamson, M. Robinson, J. J. Wright, L. A. Flanagan, J. Walton, D. Elton, D. J. Gavaghan, A. M. Bond, M. M. Roessler and A. Parkin, *J Am Chem Soc*, 2017, **139**, 10677–10686.

31 M. M. Roessler, R. M. Evans, R. A. Davies, J. Harmer and F. A. Armstrong, *J Am Chem Soc*, 2012, **134**, 15581–15594.

32 B. J. Murphy, F. Sargent and F. A. Armstrong, in *Energy Environ. Sci.*, Royal Society of Chemistry, 2014, vol. 7, pp. 1426–1433.

33 B. L. Greene, C. H. Wu, G. E. Vansuch, M. W. W. Adams and R. B. Dyer, *Biochemistry*, 2016, **55**, 1813–1825.

34 M. Saggu, I. Zebger, M. Ludwig, O. Lenz, B. Friedrich, P. Hildebrandt and F. Lendzian, *J Biol Chem*, 2009, **284**, 16264–76.

35 P. A. Ash, J. Liu, N. Coutard, N. Heidary, M. Horch, I. Gudim, T. Simler, I. Zebger, O. Lenz and K. A. Vincent, *J. Phys. Chem. B*, 2015, **119**, 13807–13815.

36 B. L. Greene, C. H. Wu, P. M. McTernan, M. W. W. Adams and R. B. Dyer, *J Am Chem Soc*, 2015, **137**, 4558–4566.

37 B. Bleijlevens, F. A. van Broekhuizen, A. L. de Lacey, W. Roseboom, V. M. Fernandez and S. P. J. Albracht, *J. Biol. Inorg. Chem.*, 2004, **9**, 743–752.

38 M. J. Lukey, A. Parkin, M. M. Roessler, B. J. Murphy, J. Harmer, T. Palmer, F. Sargent and F. A. Armstrong, *J Biol Chem*, 2010, **285**, 3928–38.

39 K. A. Vincent, A. Parkin and F. A. Armstrong, *Chem Rev*, 2007, **107**, 4366–4413.

40 R. M. Evans and F. A. Armstrong, *Methods Mol. Biol.*, 2014, **1122**, 73–94.

41 B. J. Murphy, R. Hidalgo, M. M. Roessler, R. M. Evans, P. A. Ash, W. K. Myers, K. A. Vincent and F. A. Armstrong, *J Am Chem Soc*, 2015, **137**, 8484–8489.

42 S. Dementin, B. Burlat, A. L. de Lacey, A. Pardo, G. Adryanczyk-Perrier, B. Guigliarelli, V. M. Fernandez and M. Rousset, *J. Biol. Chem.*, 2004, **279**, 10508–13.

43 A. L. DeLacey, V. M. Fernandez, M. Rousset, C. Cavazza and E. C. Hatchikian, *J. Biol. Inorg. Chem.*, 2003, **8**, 129–134.

44 B. L. Greene, G. E. Vansuch, C.-H. Wu, M. W. W. Adams and R. B. Dyer, *J Am Chem Soc*, 2016, **138**, 13013–13021.

45 A. R. Brasnett, M.Chem. thesis, University of Oxford, 2019.

46 S. Dementin, B. Burlat, A. L. de Lacey, A. Pardo, G. Adryanczyk-Perrier, B. Guigliarelli, V. M. Fernandez and M. Rousset, *J. Biol. Chem.*, 2004, **279**, 10508–10513.

47 R. M. Evans, P. A. Ash, S. E. Beaton, E. J. Brooke, K. A. Vincent, S. B. Carr and F. A. Armstrong, *J Am Chem Soc*, 2018, **140**, 10208–10220.

48 T. Krämer, M. Kampa, W. Lubitz, M. van Gastel and F. Neese, *ChemBioChem*, 2013, **14**, 1898–1905.

49 P. A. Ash, S. B. Carr, H. A. Reeve, A. Skorupskaite, J. S. Rowbotham, R. Shutt, M. D. Frogley, R. M. Evans, G. Cinque, F. A. Armstrong and K. A. Vincent, *Chem. Comm.*, 2017, **53**, 5858–5861.

50 B. L. Greene, G. E. Vansuch, B. C. Chica, M. W. W. Adams and R. B. Dyer, *Acc Chem Res*, 2017, **50**, 2718–2726.

51 P. A. Ash, S. E. T. Kendall-Price and K. A. Vincent, *Acc Chem Res*, 2019, **52**, 3120–3131.

52 M.-E. Pandelia, W. Nitschke, P. Infossi, M. T. Giudici-Orticoni, E. Bill and W. Lubitz, *Proc Natl Acad Sci U S A*, 2011, **108**, 6097–6102.

53 K. Knuettel, K. Schneider, A. Erkens, W. Plass, A. Mueller, E. Bill and A. X. Trautwein, *Bull Pol Acad Sci Chem*, 1995, **42**, 495–511.

54 M.-W. Chung, D.Phil. thesis, University of Oxford, 2015.

55 M. Asso, B. Guigliarelli, T. Yagi and P. Bertrand, *Biochim. Biophys. Acta - Proteins Proteom*, 1992, **1122**, 50–56.

Chapter 4. Single crystal IR microspectroscopic-electrochemistry

This Chapter focuses on developing a technique to provide electrochemical control over single crystals of hydrogenase and how this could be linked to structure determination of well-defined redox states.

4.1. Introduction

X-ray crystallography is an essential tool for obtaining structural information of metalloproteins. Importantly, viewing the structure of functionally-relevant redox states can help improve understanding of the protein's mechanism. Current methods of generating protein crystals in specific redox states include equilibrating the protein solution to the desired redox state prior to crystallisation;[1,2] introducing a substrate or inhibitor to the crystal medium;[3,4] and infusing crystals with oxidants or reductants in solution.[5,6] However, these methods can result in a range of similar redox states being present in the crystals. Thus, the crystallographic structure obtained represents the average of the mixture and is not a true depiction of a single state. A complementary spectroscopic technique is required to provide better control over the redox state within the crystal and to verify the generated redox states before and after diffraction.

Ash *et al.* have shown that it is possible to generate and verify well-defined redox states in single crystals of [NiFe] hydrogenase by combining electrochemical control with *in situ* synchrotron infrared microspectroscopic imaging.[7] With this technique, reversible and uniform electrochemical reduction from the inactive, oxidised level of the hydrogenase to the fully reduced state is observed. Moreover, the preliminary results suggested that the slowed kinetics of chemical steps in the crystalline state enables resolution of the kinetics of transitions between redox states. Ash *et al.* observed the separate time dependent formation of two Ni_a-R states, Ni_a-R_{II} and Ni_a-R_{III} in single crystals of *E. coli* hydrogenase-1 (Hyd-1). They suggested that upon further study, additional detail about proton-coupled electron transfer and the role of the multiple Ni_a-R and Ni_a-L species observed in the [NiFe] hydrogenase catalytic cycle (Figure 1.3) could be possible.

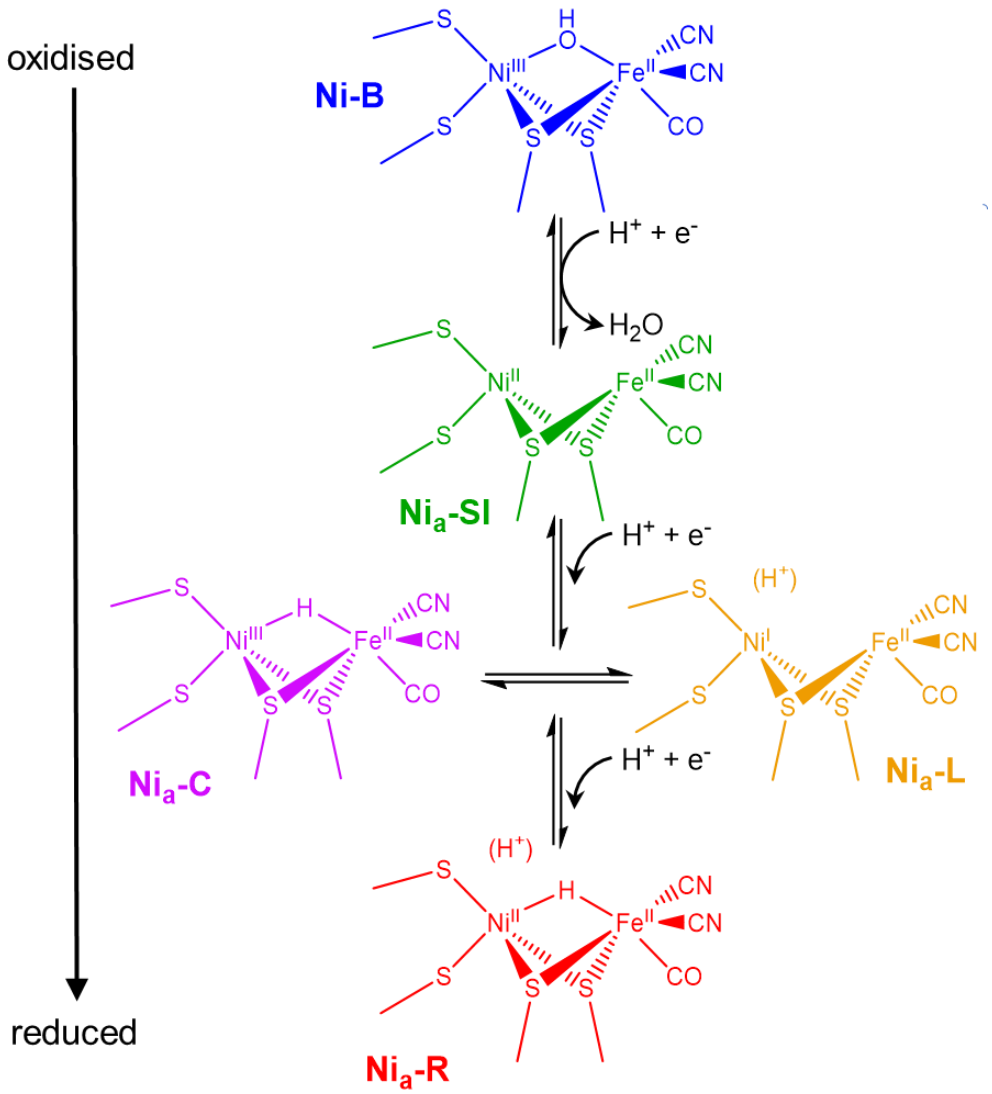


Figure 4.1 Skeletal structure of the active site redox states for [NiFe] hydrogenases ordered by redox level. Catalytically active states are labelled "Ni_a-X", where X=Si, C, L or R. Colours used to represent each species (blue for Ni-B; green for Ni_a-SI; purple for Ni_a-C; yellow for Ni_a-L; and red for Ni_a-R) are consistent with those used throughout this Thesis.

In this Chapter, the IR microspectroscopic-electrochemical technique developed by Ash *et al.* is refined in order to perform an in-depth IR characterisation of single crystals of *E. coli* hydrogenase-1 (Hyd-1). The first section details the improvements made on the established technique and the changes to the experimental procedure. Next, a detailed redox titration is performed to determine whether the full range of active site redox states

observed in solution (Figure 4.1) can also be obtained in the crystalline state. This is important in establishing whether the behaviour of Hyd-1 *in crystallo* is analogous to that observed in previous studies, and also catalytically relevant.

In Section 4.4, IR spectra recorded during the equilibration periods of the electrochemical redox titration are examined to determine whether the kinetics of the transitions can be observed. In particular, spectra from an oxidative step between Ni_a-C/L and Ni_a-SI are analysed to clarify the roles of the Ni_a-L sub-species as catalytic intermediates.

Hyd-1 was chosen as the model metalloprotein for these experiments as it has a well-characterised IR profile to reference and can form large, well-diffracting crystals which facilitates acquisition of spectra.

4.2. Method development

4.2.1. Previous designs and limitations

The first IR microspectroscopic measurements under electrochemical control of hydrogenase crystals were performed by Ash *et al.*[7] in the experimental set-up shown in Figure 4.2.

The electrochemical cell is composed of a 1 mm diameter glassy carbon working electrode, on which the single crystals of Hyd-1 are deposited via a cryo-loop, a homemade 2 mm diameter saturated calomel reference electrode, and a removable Pt wire counter electrode which circles the working electrode in a 1 mm wide groove. A 12 µm PTFE gasket separates the electrodes and the CaF_2 window, providing an effective oxygen-tight seal.

The IR microspectroscopic cell uses a reflection-absorption geometry. The IR beam is directed onto the glassy carbon surface, which acts as a reflective surface, reflecting the

unabsorbed IR light back to the detector. The IR beam thus passes through the crystal sample twice, effectively doubling the absorption pathlength.

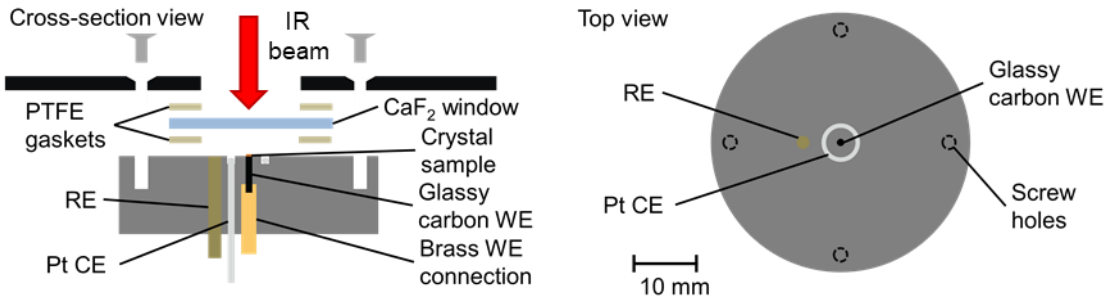


Figure 4.2 Schematic representation of the IR microspectroscopic-electrochemical cell used by Ash *et al.*, showing the positioning of the glassy carbon working electrode (WE), reference and counter electrodes (RE, CE). Approximately to scale as indicated. Red arrow represents the direction of the incoming IR light. This is reflected off the glassy carbon working electrode back to the IR detector.

However, there are several practical issues and limitations to this cell design. Firstly, use of a 12 µm gasket limits the size of protein crystals that can be studied. Crystal with a dimension greater than 12 µm are crushed by the CaF_2 window when the cell is sealed. The crystal used in experiments by Ash *et al.* were approximately 10×22 µm^2 in cross-section, and as such a 12 µm gasket was appropriate. However, the size of the crystals used in this work varies, and so the gasket size must be changed accordingly. Secondly, it was found that often upon sealing the cell, not all of the crystals remained on the working electrode and thus could not be studied. This would often require reassembly of the cell and loss of crystal samples. Furthermore, using a Pt wire counter electrode results in crystals falling into the counter electrode groove when the cell is sealed, and air bubbles becoming trapped under the Pt wire which could cause loss of electrical connection.

Therefore, the new cell must be designed to overcome these limitations whilst still performing to the same standard as before.

4.2.2. Cell design

This section will detail the modifications made to the IR microspectroscopic-electrochemical cell designed by Ash *et al.* shown in Figure 4.2. The new cell design is shown in Figure 4.3.

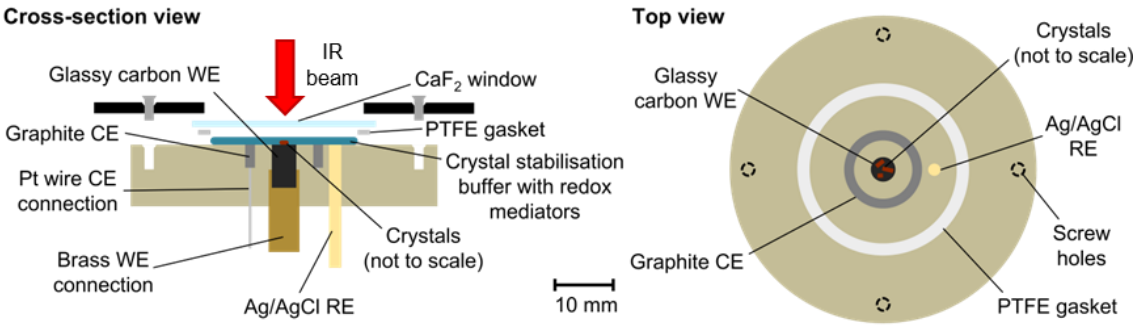


Figure 4.3 Schematic representation of the improved IR microspectroscopic-electrochemical cell. The placement of the single crystals onto the glassy carbon working electrode (WE) is shown, with the positioning of reference and counter electrodes (RE, CE). The cell is to scale (aside from the crystals) as indicated. Red arrow represents the direction of the incoming IR light. This is reflected off the glassy carbon working electrode back to the IR detector.

The working electrode remains as the reflective surface for the IR reflection geometry but has now been changed to a 4 mm diameter glassy carbon rod, sealed into a brass connector with silver loaded epoxy resin. By increasing the diameter of the working electrode, multiple crystals can be pipetted directly on to the working electrode instead of using a cryo-loop, increasing the likelihood of crystals remaining on the surface when the cell is sealed. The counter electrode was also redesigned. The surface area of the counter electrode with respect to the working electrode is important in an electrochemical cell, as it must be large enough to support the current generated at the working electrode. In the

new layout, a graphite ring is used as the counter electrode and circles the working electrode. Using a graphite ring as opposed to Pt wire removes the need for a counter electrode groove, while allowing easier cleaning of the electrode, and maintaining a high surface area. The graphite ring is sealed to a Pt wire connector with silver epoxy resin. Both the working and counter electrodes are then sealed with resin into a custom-built PEEK holder. Use of PEEK as the cell body material compared to Delrin improves the chemical compatibility of the cell. The glassy carbon and graphite ring were polished to a mirror finish using successive grades of silicon carbide paper (up to 4000 grit) and then washed by ultrasonication in ultrapure water. This process was repeated prior to crystal loading and subsequent assembly of the cell to remove contaminants and maintain the mirror finish of the working electrode. A 2 mm diameter miniature Ag/AgCl reference electrode is placed 5.35 mm from the working electrode, sufficiently close to minimise uncompensated resistance. The reference electrode is sealed into the cell using silicone sealant as opposed to resin so that it is easily removable when the working electrode requires polishing. Depending on the size of the crystals, either a 25 µm or 50 µm thick PTFE gasket is used as the spacer between the electrodes and the IR-transparent CaF_2 window. As before, a 30 mm diameter, 1 mm thickness CaF_2 window was used.

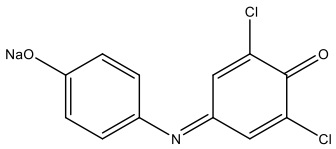
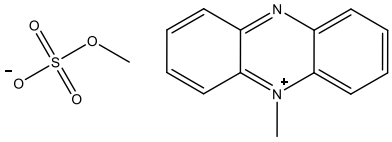
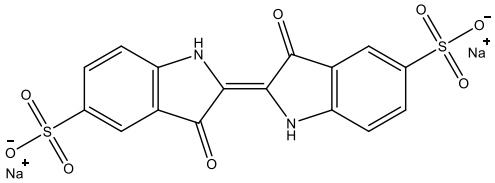
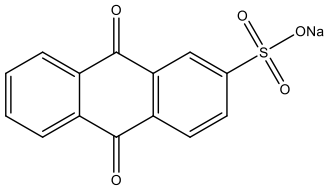
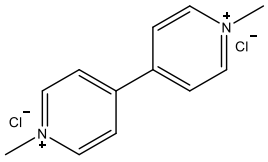
4.2.3. Redox mediators

Redox mediators are required to provide good electrochemical control over the crystalline sample. Ash *et al.* employed a meditator cocktail consisting of methylene blue, methyl viologen and 2-hydroxy-1,4-naphthoquinone when performing IR spectroelectrochemical studies on single crystals of Hyd-1[7]. However, using this selection of mediators presents a few issues. Firstly, the potential range covered doesn't extend to high enough potentials. Thus, electron transfer may be hindered when applying potentials above +50 mV. Furthermore, it is important to have good electrochemical control over the potentials

where the redox transitions of the active site of Hyd-1 occur. The mid-point potential of the Ni_a-C(L)/Ni_a-SI redox couple for Hyd-1 is -148 mV[8] thus using a mediator whose mid-point potential is close to this value is important. Secondly, 2-hydroxy-1,4-naphthoquinone is insoluble at 1 mM in the Hyd-1 crystal stabilisation buffer and its voltammetry shows a large peak-to-peak separation, so an alternative redox mediator would be beneficial. Finally, methylene blue was found to be difficult to completely wash out from the IR microspectroscopic-electrochemical cell between each set-up.

When choosing a new selection of mediators for the single crystal IR microspectroscopic-electrochemical experiments, the following specification was used: easy to dissolve in crystal stabilisation buffer; mutual compatibility; compatible with protein crystals; lack of functional groups that would appear in the IR range of study 2200–1800 cm^{-1}; and redox potentials within the potential range, -600 to +300 mV *vs* SHE. The following redox mediators were chosen, as shown in Table 4.1: 2,6-dichloroindophenol, phenazine methosulfate, indigo carmine, anthraquinone-2-sulfonate, and methyl viologen. Each mediator was studied in solution by cyclic voltammetry to confirm their redox potentials in the crystal stabilisation buffer and to ensure the potentials were not altered when mixed into a mediator cocktail (Figure 4.4).

Table 4.1 Mid-point potentials (E_m) and peak-to-peak separations (ΔE_p) of redox mediators, measured in the infrared microspectroscopic-electrochemical cell described in Figure 4.3. The measured values of E_m are extracted from the black cyclic voltammogram shown in Figure 4.4, which was recorded with the redox mediator cocktail specified in Section 2.6.1.2. Literature values of E_m are provided for comparison.

Redox mediator	**Molecular structure**	**Literature E_m / V**	**Measured E_m / V[c]**	**ΔE_p / V**
2,6-dichloro-indophenol sodium salt (DCPIP)		+217[d]	+316	39
phenazine methosulfate		+80[d]	+132	62
indigo carmine		-125[e]	-35	115
anthraquinone -2-sulfonate		-169[f]	-150	115
methyl viologen		-446[g]	-422	49

[c] Measured at pH 6, 20°C, in hydrogenase-1 stabilisation buffer
[d] Reported at pH 7, 30°C, Ref: [25,26]
[e] Reported at pH 7, 23°C, Ref: [25,27]
[f] Reported at pH 6, 25°C, Ref: [28,29]
[g] Reported at pH 7, 25°C, Ref: [27,30]

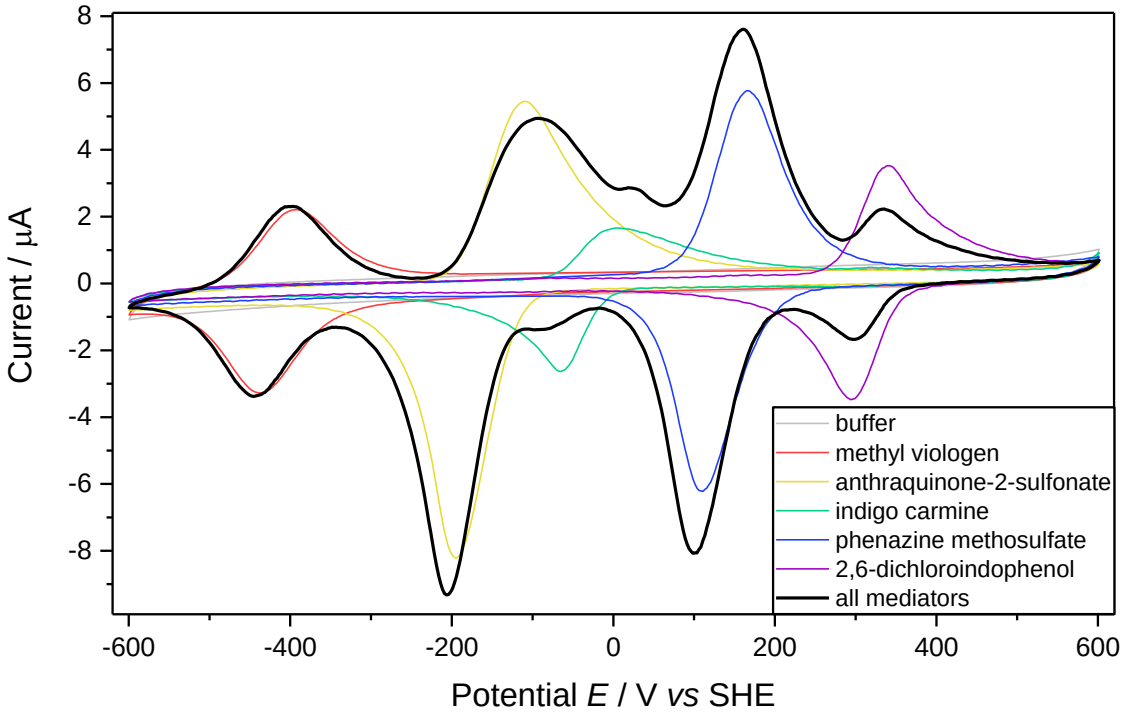


Figure 4.4 Cyclic voltammogram demonstrating electrochemical control within the IR microspectroscopic-electrochemical cell. Recorded at a scan rate of 10 mV s^{-1}, with a background electrolyte of hydrogenase stabilisation buffer (100 mM Bis-Tris pH 5.9, 200 mM Li_2SO_4, 150 mM NaCl, 23% w/v PEG 3350) additionally containing the redox mediators methyl viologen, anthraquinone-2-sulfonate, indigo carmine, phenazine methosulfate and 2,6-dichloroindophenol (1 mM each).

Figure 4.4 shows the cyclic voltammograms of each individual redox mediator in hydrogenase-1 crystal stabilisation buffer. The black voltammogram represents the mediator cocktail, composed of methyl viologen, anthraquinone-2-sulfonate, indigo carmine, phenazine methosulfate and 2,6-dichloroindophenol, all at 1 mM concentration. Table 4.1 shows that the mid-point potentials of the chosen mediators in the crystal stabilisation buffer are similar to those in the literature when accounting for variance in temperature and pH. The peak-to-peak separations for each mediator are greater than the expected Nernstian value for a two-electron process (29 mV). This is likely due to

uncompensated resistance in the thin-layer electrochemical cell, although the cause of the larger peak-to-peak separations of indigo carmine and anthraquinone-2-sulfonate is unclear. Crucially, the redox potentials of the mediators cover the targeted potential range, which will facilitate electron transfer across the redox titrations.

To be effective, the redox mediators must be able to diffuse rapidly throughout the crystal to enable electronic contact between the distal FeS cluster and the working electrode. Figure 4.5 shows that the solvent channels within the hydrogenase crystal (radii of 5.4-6.6 Å for Hyd-1[9]) are large enough for the redox mediators to diffuse through. Diffusion of the mediators occurs quickly, and prolonged exposure has been shown not to affect the diffraction quality of the crystals. All x-ray diffraction data were collected by Stephen B. Carr.

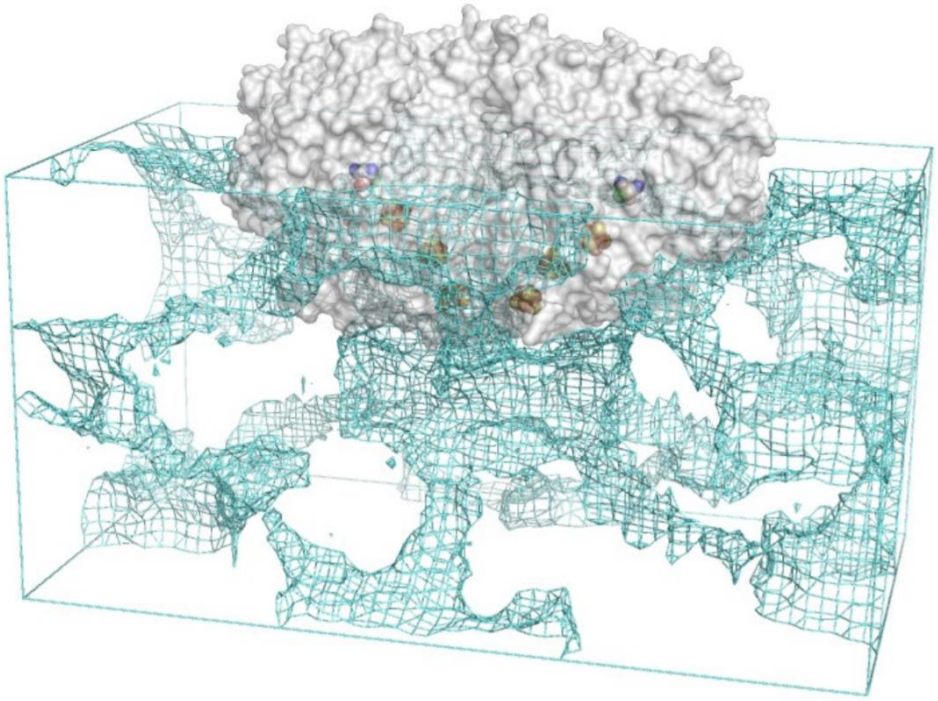


Figure 4.5 Illustration of the solvent channels within a crystal of Hyd-1. Turquoise mesh represents the solvent channels (radii of 5.4-6.6 Å) between each dimer of heterodimers of Hyd-1 within the crystal lattice. All data were collected on the I23 beamline at Diamond Light Source by Dr Stephen B. Carr. Figure prepared by Dr Stephen Carr, used with permission from the authors.[10]

4.2.4. Experimental procedure

The experimental method used in this Thesis is adapted from the method employed by Ash *et al*.[7], and is detailed in Chapter 2. The main improvement to the method involves how the crystals are transferred to the working electrode. Instead of using a cryo-loop to place an individual crystal onto the working electrode, a small amount of redox mediator cocktail solution is added to a crystallisation plate well of single crystals (whose number and size varies). The resulting solution is then pipetted onto the working electrode, whose larger surface area facilitates this. This adaptation increases the ease of the method, whilst also improving the chances of being able to study a single crystal that, when the cell is sealed, remains on the working electrode and is in contact with the redox mediators.

4.3. Spectroelectrochemical characterisation of Hyd-1 crystals

The data presented in this section were collected using the synchrotron IR source unless otherwise stated. Furthermore, all measurements were made on single crystals of *E. coli* WT Hyd-1 prepared without the cytochrome *b* sub-unit. Where appropriate, assignment of the IR bands to the [NiFe] active site redox states is made based on the results presented in Chapter 3 and other IR spectroelectrochemical studies of Hyd-1.[10,11]

4.3.1. Initial characterisation

4.3.1.1 As-isolated

Figure 4.6A shows the ν_{CO} and ν_{CN} regions of an IR spectrum of a single crystal of as-isolated Hyd-1, in in the IR microspectroscopic-electrochemical cell. There is no applied potential (open circuit potential, OCP, +209 mV *vs* SHE), and the solution inside the cell is hydrogenase-1 stabilisation buffer, pH 5.9, with the mediator cocktail as specified in Section 2.6.1.2.

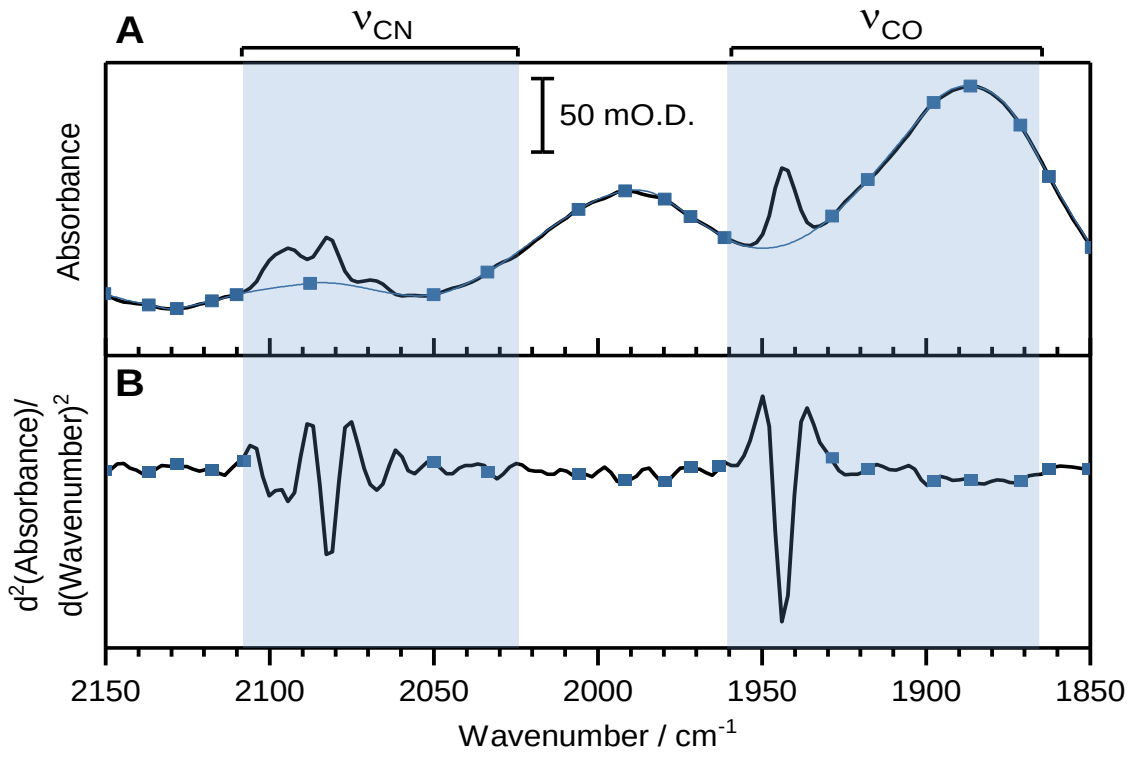


Figure 4.6 A: IR spectrum of a single crystal of as-isolated of Hyd-1 at pH 5.9, at open circuit potential, OCP, of +209 mV *vs* SHE. The shaded blue areas mark the ν_{CO} and ν_{CN} regions, with the blue squares marking the baseline points used to subtract the sinusoidal baseline (blue line). B: The 2nd derivative IR spectrum of the as-isolated Hyd-1 spectrum shown in (A). The blue squares mark the baseline points showing that their placement avoids any peak absorption.

The blue squares represent the baseline points which are connected by a spline function (blue line). The positions of the points are chosen with reference to the 2nd derivative spectrum (Figure 4.6B) so that the sinusoidal baseline is removed whilst leaving the predicted ν_{CO} and ν_{CN} regions (as shown by the light blue shading). Some points are present within these regions as required to remove the baseline. The baseline is then subtracted to give the baseline corrected spectrum, Figure 4.7.

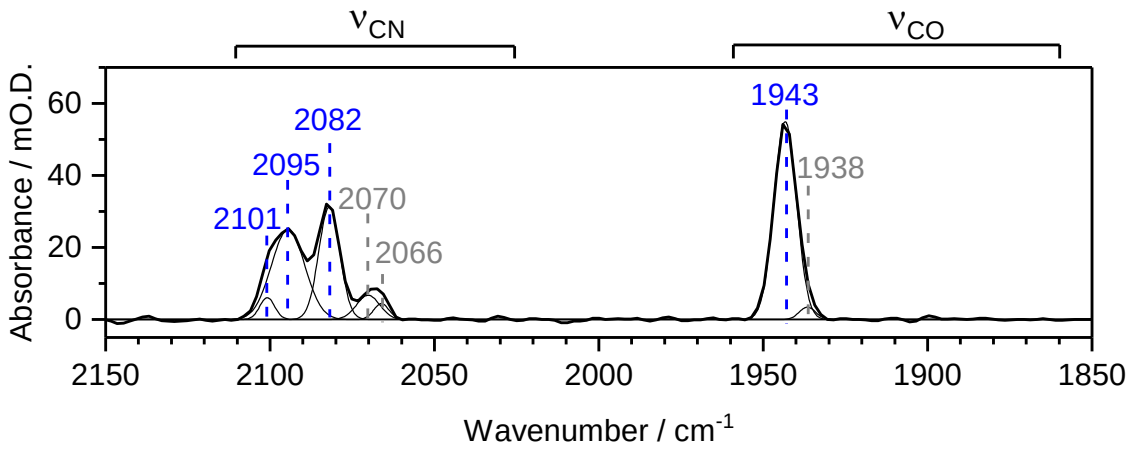


Figure 4.7 Baseline corrected IR spectrum of a single crystal of as-isolated of Hyd-1 at pH 5.9, at open circuit potential, OCP, +209 mV *vs* SHE. Bands marked in blue represent the Ni-B species, whereas those in grey are unassigned. The fitted Gaussian peaks are shown by the thin coloured curves.

The spectrum shows two peaks in the ν_{CO} region, one very intense peak at 1943 cm^{-1} and a smaller one at 1938 cm^{-1}. In the ν_{CN} region, there are 5 bands present of varying intensity at 2066, 2070, 2082, 2095 and 2101 cm^{-1}. As this sample was purified in the presence of air, the IR spectrum is expected to represent a mixture of inactive oxidised species. The appearance of two peaks in the ν_{CO} region, alongside five peaks in the ν_{CN} region, suggests that there are at least two inactive species present. Peaks at 1943, 2082, 2095 and 2101 cm^{-1} are consistent with those assigned as Ni-B in Chapter 3 and by Hidalgo *et al.*[11]. As discussed in Section 3.2.1, the additional ν_{CN} peak is likely associated with a "protonated" Ni-B species or 'superoxidised' Ni-B' species whose ν_{CO} band and second ν_{CN} band are hidden.

The broadness of the 2095 cm^{-1} band (full width half maximum (FWHM) = 11 compared to 6.8 for other fitted peaks) suggests the presence of a hidden peak, which could also be associated with the hidden "protonated Ni-B". However, a band was not distinguishable in the 2nd derivative spectrum and adding an additional peak to the region resulted in poor fitting of the Gaussian functions to the baseline-corrected spectrum.

Apparent in the crystal IR spectra are a set of peaks at 1938, 2070 and 2066 cm^{-1} which are not observed in the PFIRE spectra of as-isolated Hyd-1. Occasionally, IR spectra of as-isolated [NiFe] hydrogenases have shown additional IR bands that have been assigned to a readily activated "Ni-SI like" species.[12,13] The identity of these additional bands will be discussed later (Section 4.3.1.3).

When using the IR microspectroscopic-electrochemical technique, much larger absorbances are observed compared with solution spectra, giving high signal-to-noise ratios. For example, the 1943 cm^{-1} Ni-B peak shown in Figure 4.7 has an absorbance of ~55 mO.D., approximately 100 times greater than the equivalent Ni-B peak measured using the PFIRE technique (Abs~0.5 mO.D; Figure 3.4). This is due to the higher effective concentration of the protein in the crystal (~8 mM of active site, Section 2.4.2) compared to in solution or adsorbed onto the extended carbon electrode, and the increased effective IR pathlength (~30-50 μm) as a result of the reflection-adsorption geometry of the cell. Another factor may be that the nature of the crystalline state naturally promotes a higher population of the alternate inactive species. The increase in intensity of peaks in the crystal IR spectra also could reveal low intensity inactive species which are not observed by PFIRE.

The 'as-isolated' spectrum of each Hyd-1 crystal was recorded prior to any electrochemical manipulation. Figure 4.8 shows the IR spectrum of a single crystal of as-isolated Hyd-1 from a different IR microspectroscopic-electrochemical cell set-up under the same conditions (OCP +213 mV *vs* SHE, pH 5.9). Peaks assigned to the Ni-B species are again observed, as are the unassigned 1938 and 2071 cm^{-1} peaks. This shows there is consistency between each set-up of the IR microspectroscopic-electrochemical cell and

between crystals, with the only differences between the being the overall intensities of the peaks, which in turn is dependent on the quality and size of the crystal.

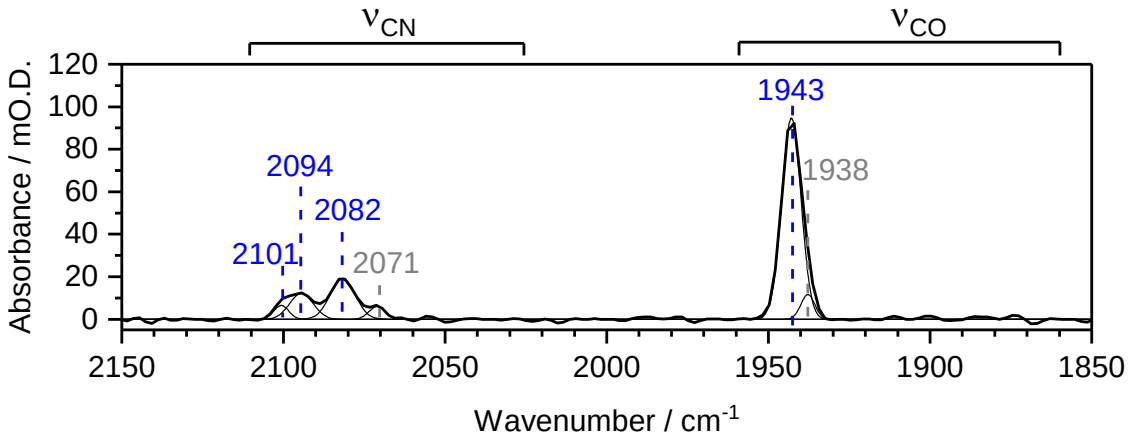


Figure 4.8 Baseline corrected IR spectrum of a single crystal of as-isolated of Hyd-1 at pH 5.9, at open circuit potential, OCP, of +213 mV *vs* SHE in a secondary set-up of the IR microspectroscopic-electrochemical cell. Peaks marked in blue represent the Ni-B species, whereas those in grey are unassigned. The fitted Gaussian peaks are shown by the thin black curves.

4.3.1.2 Electrochemical reduction

Reduction of the as-isolated WT Hyd-1 crystal to a potential of -435 mV *vs* SHE results in the following spectrum, Figure 4.9. Spectra were recorded during application of the reductive potential to monitor the activation of the crystal. It was determined that a minimum of 80 minutes was required to ensure that any slowly activating species, such as Ni-A, are fully reduced, as observed by the decrease of IR bands present at high potential and in the as-isolated spectra.

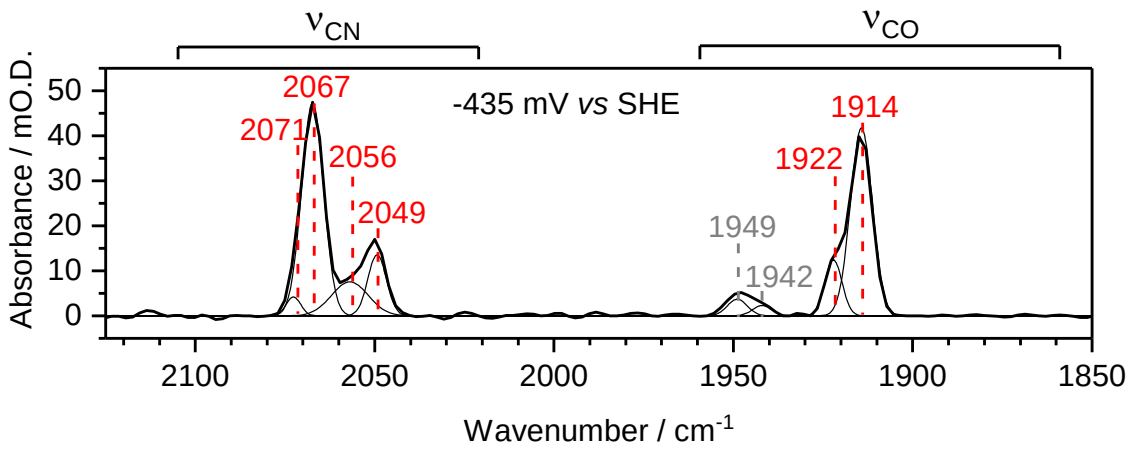


Figure 4.9 IR spectrum of a single crystal of Hyd-1 at pH 5.9, at -435 mV *vs* SHE recorded after the potential was applied for 80 minutes to ensure complete reduction of the crystal sample. The fitted Gaussian peaks are shown by the thin coloured curves. Bands marked in red represent the Ni_a-R species, whereas those in grey are unassigned. The fitted Gaussian peaks are shown by the thin black curves.

The IR spectrum of the reduced Hyd-1 crystal shows multiple ν_{CO} peaks representing multiple active site species. The most reduced species, Ni_a-R, are present with ν_{CO} peaks at 1922 and 1914 cm^{-1}. As with the PFIRE experiments, two sub-species of Ni-R (Ni_a-R_{II}, 1922 cm^{-1} and Ni_a-R_{III}, 1914 cm^{-1}) are observed. Figure 4.9 also shows that four ν_{CN} bands are present at this potential. Two of these, 2067 and 2049 cm^{-1}, have been previously assigned to the Ni_a-R_{III} species. Based on their relative positions and intensities, the other two ν_{CN} peaks (2071 and 2056 cm^{-1}) are consistent with the Ni_a-R_{II} species.

Two other small peaks within the ν_{CO} region are detected at 1949 and 1942 cm^{-1}. Similar peaks were observed in the IR spectra of electrode-adsorbed Hyd-1 as studied using PFIRE (Figure 3.5, 1948 and 1933 cm^{-1}) and were assigned as the Ni_a-C and Ni_a-R_I species respectively. The 9 cm^{-1} difference in the position of the Ni_a-R_I band is discussed in Section 4.3.2.1.

4.3.1.3 Re-oxidation

Applying a potential of +203 mV *vs* SHE electrochemically oxidises the previously reduced Hyd-1 crystals, giving the IR spectrum depicted in Figure 4.10.

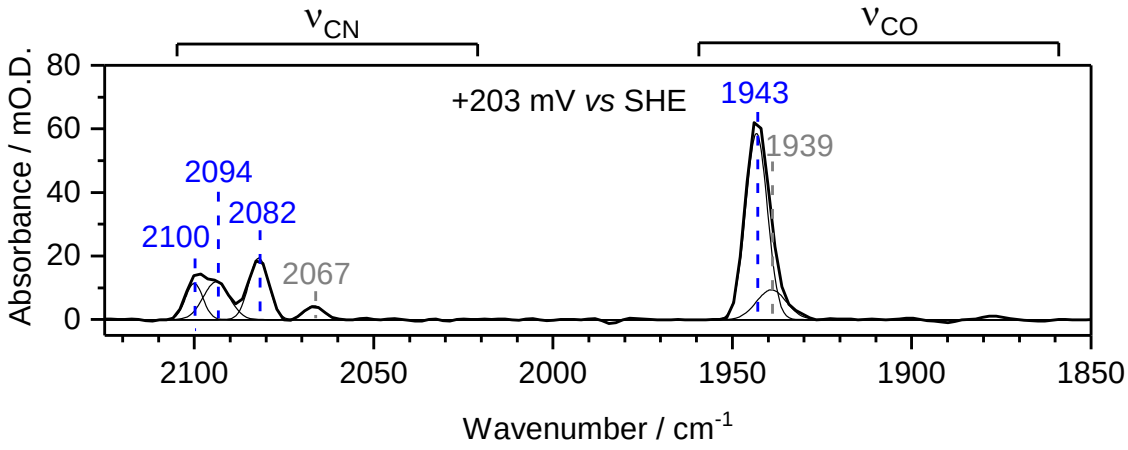


Figure 4.10 IR spectrum of a single crystal of Hyd-1 at pH 5.9, at an applied potential of +203 mV *vs* SHE, after electrochemical reduction. Peaks marked in blue represent the Ni-B species, whereas those in grey are unassigned. The fitted Gaussian peaks are shown by the thin black curves.

This spectrum is very similar to that of Figure 4.7. All of the ν_{CO} and ν_{CN} bands associated with the inactive Ni-B level (1943, 2100, 2094, 2082 cm^{-1}) are present, whilst bands pertaining to the Ni_a-R species are no longer present. This shows that the Hyd-1 crystals have undergone full electrochemical re-oxidation.

The unidentified ν_{CO} and ν_{CN} peaks at 1939 and 2067 cm^{-1} are similar to the unknown bands in the as-isolated spectrum (Figure 4.7). In PFIRE experiments of Hyd-1, re-oxidation of the sample produced IR spectra where any anomalous bands that were initially present did not reappear upon oxidation (Section 3.2.1.2). As these unknown bands reappear after reducing and then re-oxidising the crystal sample, it suggests they are due to other inactive active site species that have not been previously observed. The potential dependence of these bands is discussed in Section 4.3.2.3. It is worth noting that in the

PFIRE IR spectra of Hyd-1, the Ni-B band centred at 1943 cm^{-1} was asymmetric and deconvolution resulted in two bands at 1944 and 1942 cm^{-1}, assigned to a Ni-B' and Ni-B species respectively (Figure 3.4, Section 3.2.1.2). This is not apparent in the IR spectra of the Hyd-1 single crystal, and instead the band at 1939 cm^{-1} is assigned to a Ni-X species (Section 4.3.2.3).

Importantly though, Figure 4.10 shows that Hyd-1 crystals respond to an applied potential in the adapted IR microspectroscopic-electrochemical cell and give results similar to those seen by Ash *et al.*.[7] Now that this is established, a more detailed investigation into the redox behaviour of Hyd-1 crystals can be performed for the first time.

4.3.2. Detailed redox titrations

Initial characterisation of the Hyd-1 crystals has shown that their IR spectroelectrochemical behaviour is consistent with that observed in Chapter 3, albeit with more detail obtained. The fine potential control available with the IR microspectroscopic-electrochemical technique allows an in-depth investigation into the potential dependence of the active site species of Hyd-1.

4.3.2.1 Oxidative titration

Following electrochemical reduction of the Hyd-1 crystals, small successive oxidative potential steps (25 – 100 mV) are applied to the sample. IR spectra are continuously recorded (2 mins per spectrum) whilst the crystal equilibrates with the applied potential until either no spectroscopic changes are observed, or a minimum of 8.5 minutes has passed. Figure 4.11 shows a series of baseline-corrected IR spectra from the first detailed electrochemical oxidative titration from -597 to +203 mV of single crystals of Hyd-1 at pH 5.9. Both the ν_{CO} and ν_{CN} regions are shown. The spacing between each IR spectrum approximately represents how large the potential step is. Smaller steps (25 mV) were

applied when approaching the potentials where it was estimated that the maximum intensity of certain active site species would occur (-222 mV, Ni_a-C / Ni_a-L; -122 mV, Ni_a-SI).

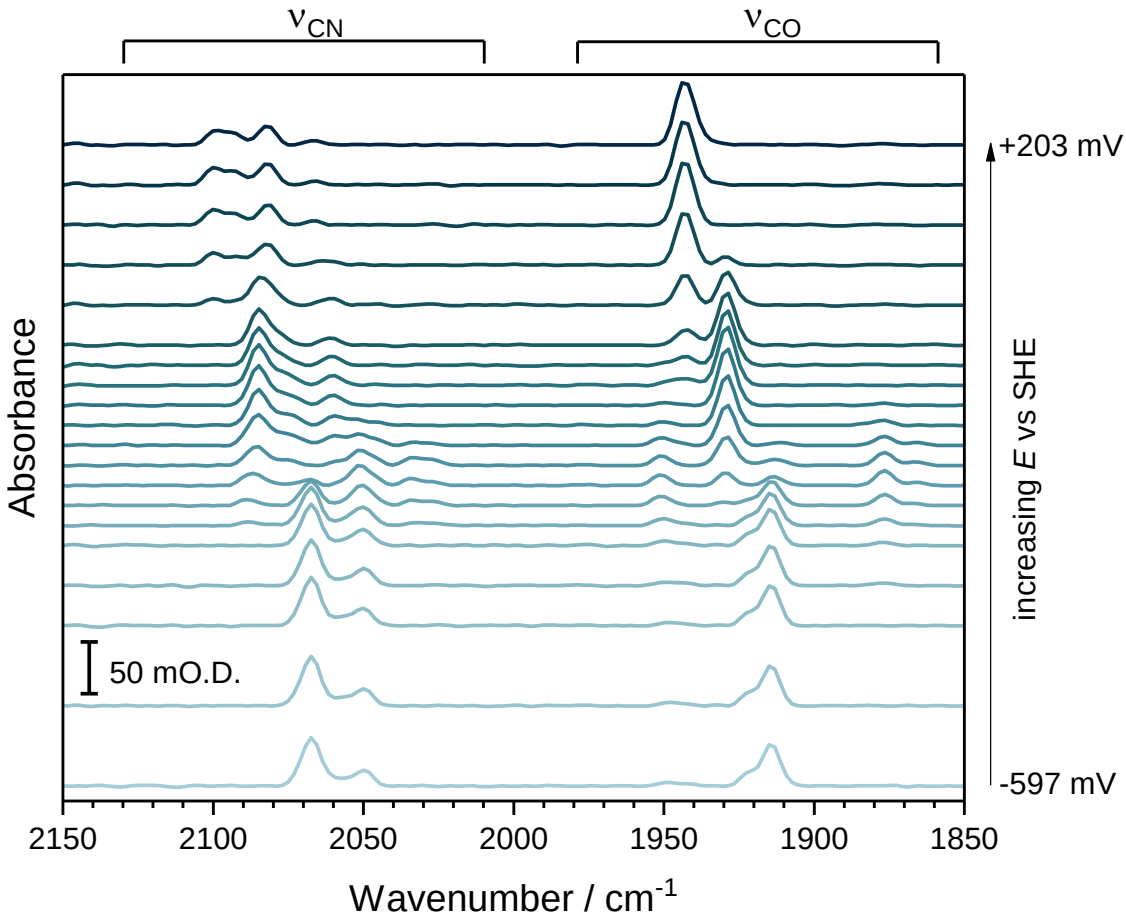


Figure 4.11 Baseline corrected IR spectra of a single crystal of Hyd-1, pH 5.9, following an electrochemical oxidative titration from -597 to +203 mV *vs* SHE. The regions corresponding to ν_{CO} and ν_{CN} bands are labelled.

It is clear that as the potential is increased from -597 mV *vs* SHE (the bottom spectrum in Figure 4.11), a number of IR bands disappear and appear across the titration, representing the oxidation of various active site species. Furthermore, multiple peaks in the ν_{CO} region are present in several individual spectra showing multiple active site species can be present in the crystal at once. This means that it would be challenging to obtain a specific, pure redox state by only adding reductant to the crystals.

This data can also be represented by heatmap plots, as shown in Figure 4.12 (ν_{CO} region, 1975-1850 cm^{-1}) and Figure 4.13 (ν_{CN} region, 2125-2000 cm^{-1}). The absorbance measured for each wavenumber is shown by the change in colour intensity according to the scale on the right of the Figures.

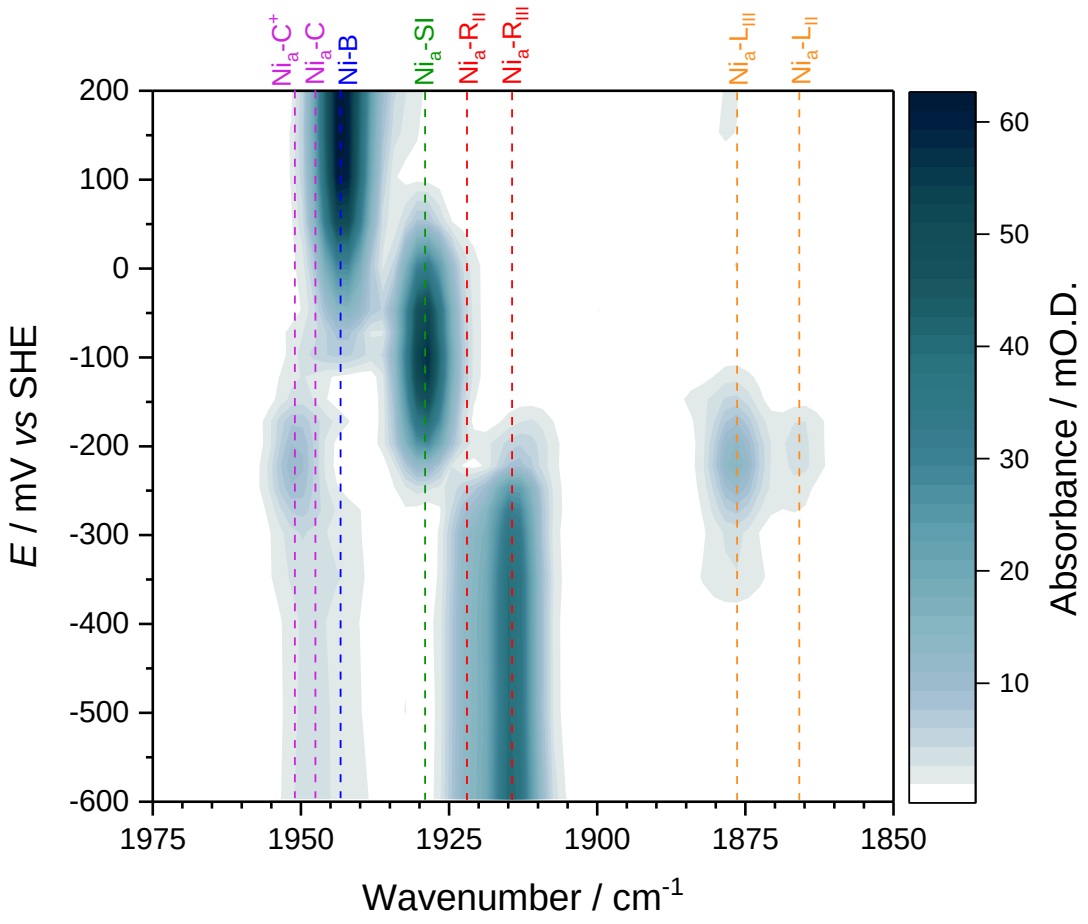


Figure 4.12 Heatmap plot showing the change in absorbance of IR bands with potential following an electrochemical oxidative titration of a single crystal of Hyd1 at pH 5.9. Changes in absorbance are shown by the change in colour intensity as indicated by the scale on the right. Shown is the ν_{CO} region of the IR spectra, with the wavenumbers that represent each active site species (as measured using PFIRE, Chapter 3) labelled by coloured dotted lines (Ni_a-C^+ – 1952 cm^{-1}, Ni_a-C – 1948 cm^{-1} purple; Ni-B – 1943 cm^{-1}, blue; Ni_a-SI – 1929 cm^{-1}, green; Ni_a-R – 1922 and 1915 cm^{-1}, red; Ni_a-L – 1877 and 1868 cm^{-1} yellow).

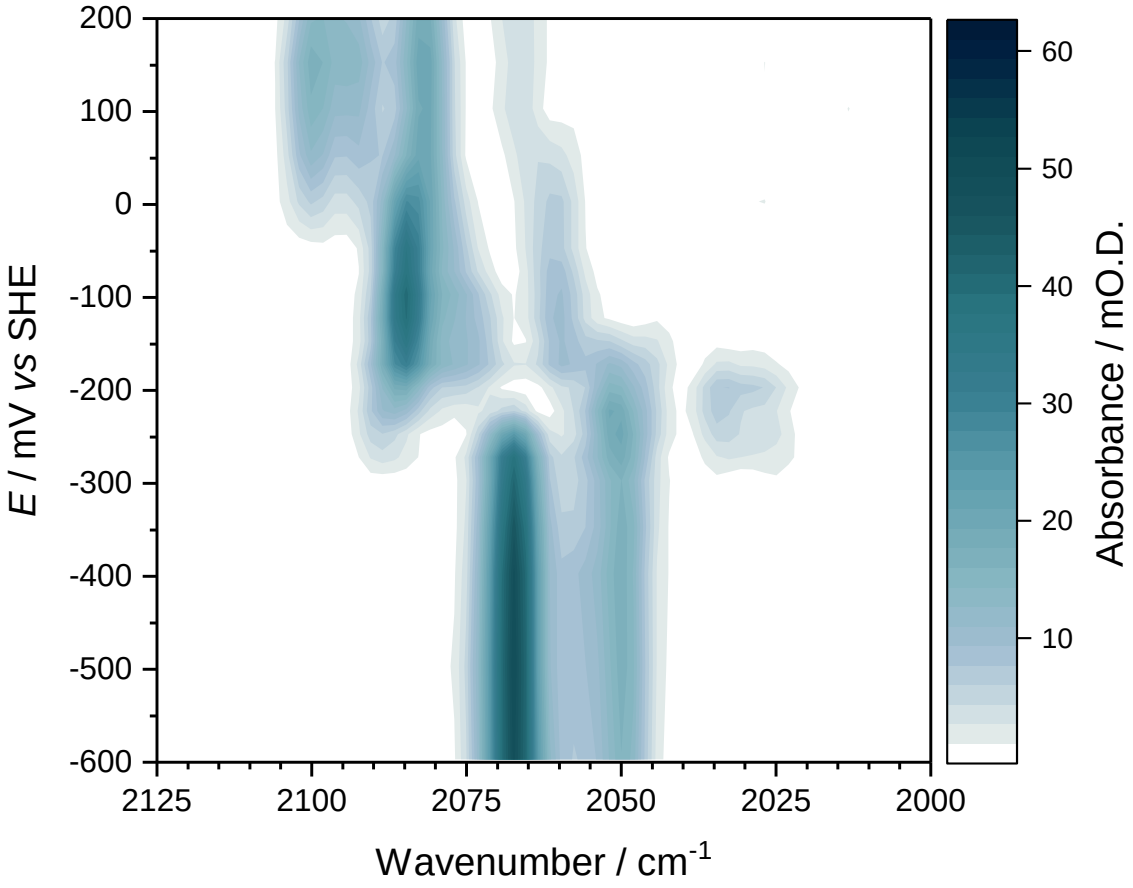


Figure 4.13 Heatmap plot showing the change in absorbance of IR bands with potential following an electrochemical oxidative titration of a single crystal of Hyd1 at pH 5.9. Changes in absorbance are shown by the change in colour intensity as indicated by the scale on the right. Shown is the ν_{CN} region of the IR spectra.

Displaying the data from the IR spectra as a heatmap plot gives a clearer representation of the rise and fall of each active site redox species. In Figure 4.11, it is difficult to accurately track peaks with low absorbances, particularly when determining the potential they first appear. This is the case for several of the peaks within the ν_{CN} region of the IR spectra. In Figures 1.12 and 1.13 however, it is easier to distinguish the potential at which each band appears.

The wavenumbers that correspond to the ν_{CO} band of each active site species (as measured using the PFIRE method in Chapter 3) are marked by coloured dotted lines in

Figure 4.12: purple for Ni_a-C^+ and Ni_a-C (1952 and 1948 cm^{-1}), blue for Ni-B (1943 cm^{-1}), green for Ni_a-SI (1929 cm^{-1}), red for the two sub-species of Ni_a-R (1922 and 1915 cm^{-1}), and yellow for the two sub-species of Ni_a-L (1877 and 1868 cm^{-1}). Each line overlaps with positive absorbances in the heatmap plot of the oxidative titration, suggesting that each species can be attained within the crystal. Furthermore, Figure 4.12 shows that the order in which each active site species appears across the potential range coincides with Figure 4.1 – Ni_a-R at low potentials (-597 to -247 mV); Ni_a-C and Ni_a-L appearing next at the same potential region (-247 to -147 mV); Ni_a-SI (-147 to +3 mV); and finally the inactive Ni-B species at the highest potentials (+3 to +203 mV). From this, the potential at which each active site species is maximised can also be extracted for analysis.

As discussed in Section 4.3.1.2, a peak at 1942 cm^{-1} appears at low potentials in the crystal IR spectra. In Chapter 3, a ν_{CO} band at 1933 cm^{-1} was assigned to the Ni_a-R_I sub-species in Hyd-1. This is not observed in the crystal spectra, however the 1942 cm^{-1} species at low potential may also represent this Ni_a-R_I species. Figure 4.12 shows that absorbances at this wavenumber are dependent on potential, with no peak present between -247 and -122 mV *vs* SHE. This suggests that there are two species, with ν_{CO} bands close in wavenumber (1943 cm^{-1} Ni-B and 1942 cm^{1} Ni_a-R_I). Furthermore, Figure 4.13 shows that there are no Ni-B ν_{CN} bands at low potentials, confirming no Ni-B is present.

One disadvantage of viewing the IR spectra as heatmap plots is that it shows the data as areas of absorbance instead of individual peaks. Broad areas of absorbance may be due to the combination of multiple hidden peaks. Therefore, each spectrum needs to be individually analysed.

4.3.2.2 Maximising the intensity of each redox species

In this section, the IR spectra for the potentials at which the intensity of each redox species is maximised are analysed in detail.

Ni_a-R (-597 mV vs SHE)

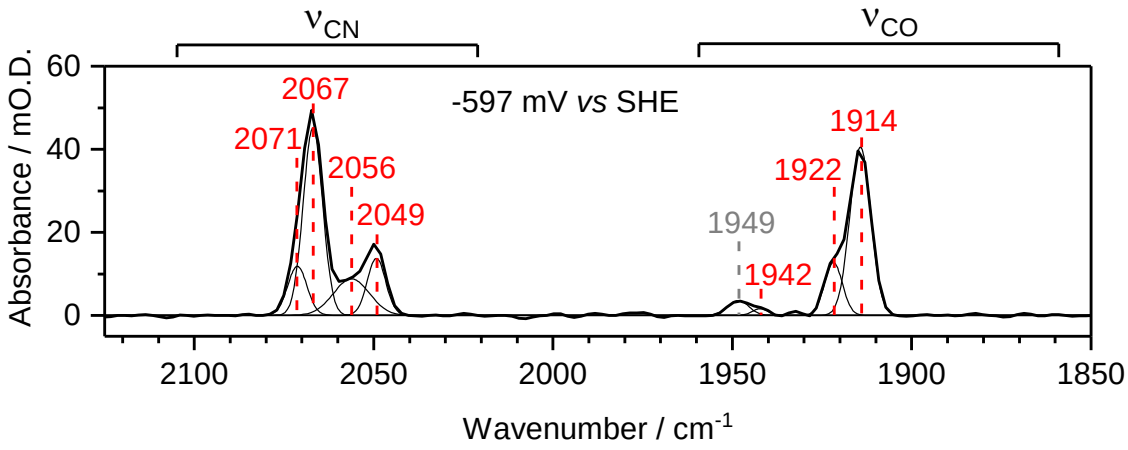


Figure 4.14 IR spectrum of a single crystal of Hyd-1 at pH 5.9, at -597 mV *vs* SHE. Bands marked in red represent the Ni_a-R species, whereas those in grey are unassigned. The fitted Gaussian peaks are shown by the thin black curves.

As expected, the Ni_a-R species are maximised at the most reductive potential, -597 mV *vs* SHE as shown above in Figure 4.14. All three Ni_a-R sub-species are present: Ni_a-R_I (1942 cm^{-1}), Ni_a-R_{II} (1922, 2071, 2056 cm^{-1}) and Ni_a-R_{III} (1914, 2067, 2049 cm^{-1}). This spectrum shows a striking similarity to that shown in Figure 4.9, showing that the Ni_a-R species dominates over a wide potential range. The Ni_a-C ν_{CO} band at 1949 cm^{-1} is also still present within the spectrum.

Ni_a-C/Ni_a-L (-222 mV vs SHE)

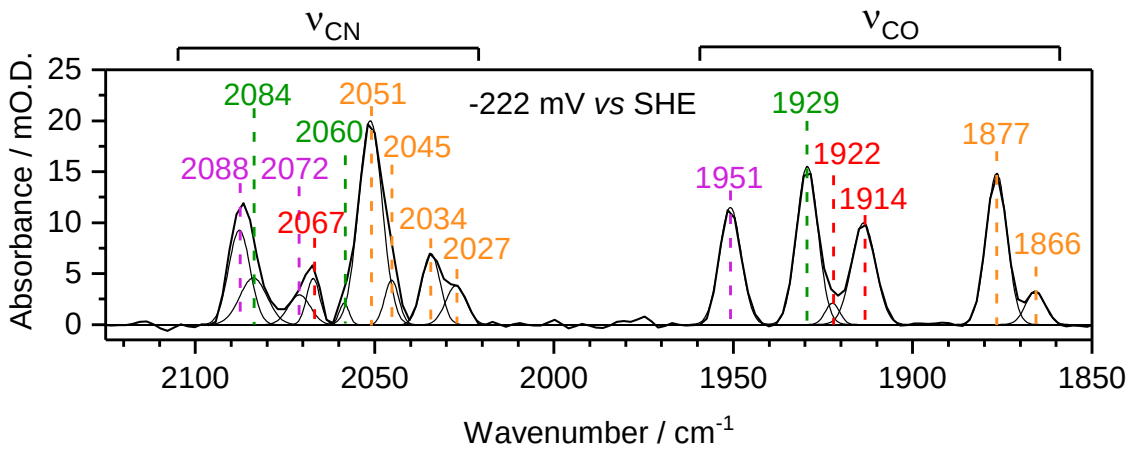


Figure 4.15 IR spectrum of a single crystal of Hyd-1 at pH 5.9, at -222 mV *vs* SHE. Bands marked in red, purple, yellow and green represent the Ni_a-R, Ni_a-C, Ni_a-L and Ni_a-SI species respectively. Fitted Gaussian peaks are shown by thin black lines.

At -222 mV *vs* SHE, there are many ν_{CO} and ν_{CN} peaks in the IR spectrum as shown in Figure 4.15. In the ν_{CO} region, there are 6 peaks at 1951, 1929, 1922, 1914, 1877 and 1866 cm^{-1} representing 6 different active species. The Ni_a-R_{III} species is still present in the crystal sample as shown by its distinctive 1914 cm^{-1} band, with one of its respective ν_{CN} bands at 2067 cm^{-1}. However the intensity of this peak has decreased significantly, ~75% less compared to at -597 mV ($Abs_{-597\ mV} \approx 40$ mO.D.; $Abs_{-222\ mV} \approx 10$ mO.D). There does remain a minor proportion of the Ni_a-R_{II} species at 1922 cm^{-1} but there is no sign of the Ni_a-R_I sub-species. Overall this suggests that the majority of the Ni_a-R species has been oxidised as is expected when applying a more positive potential.

A new band at 1951 cm^{-1} is observed which can be assigned to the Ni_a-C^+ species. The unprotonated Ni_a-C species with ν_{CO} = 1949 cm^{-1} is no longer present. Simultaneously, species at the same redox level, Ni_a-L, are observed at 1877 and 1866 cm^{-1}. As seen in the PFIRE spectra of Hyd-1 at this potential, two sub-species of Ni_a-L are detected, each

representing a different protonation state of the surrounding active site: Ni_a-L_{III} (1877 cm^{-1}) and Ni_a-L_{II} (1866 cm^{-1}). Finally, the remaining ν_{CO} band at 1929 cm^{-1} signifies the presence of the Ni_a-SI species.

In the ν_{CN} region there are a total of 9 bands, some of which are initially hidden. Analysis of the 2nd derivative spectrum shows the hidden peaks and allows good fitting of the Gaussian bands to the baseline-corrected spectrum.

There are 4 low wavenumber peaks (relative to the other ν_{CN} bands) at 2051, 2045, 2034 and 2027 cm^{-1}. Hidalgo *et al.* previously observed the 2051 and 2027 cm^{-1} bands and assigned them to the Ni_a-L_{III} species.[11] However, due to their relative intensities, the 2051 and 2034 cm^{-1} peaks are likely to be the matching ν_{CN} bands of the Ni_a-L_{II} species, whereas the Ni_a-L_{III} ν_{CN} bands would be the 2045 and 2027 cm^{-1} peaks.

Table 4.2 Difference between a redox species' ν_{CN} bands in cm^{-1}

Redox state	**$\Delta\nu_{CN}$ / cm^{-1}**
Ni-B	18 (2100, 2082)
Ni_a-SI	8 (2085, 2077)
Ni_a-C/Ni_a-C^+	16 (2088, 2072)
Ni_a-L_{II}	17 (2051, 2034)
Ni_a-L_{III}	18 (2045, 2027)
Ni_a-R_{II}	15 (2071, 2056)
Ni_a-R_{III}	18 (2067, 2049)

Bands at 2088 and 2084 cm^{-1} were also observed in the PFIRE spectra and are assigned to the Ni_a-C and Ni_a-SI species respectively. The remaining peaks at 2072 and 2060 cm^{-1}

however are unprecedented at this potential for Hyd-1. Table 4.2 shows that the difference between the ν_{CN} bands is approximately consistent for each redox species ($\sim 16 \pm 4$ cm^{-1}) Using this information, and observing how the peaks vary with potential, the 2072 cm^{-1} peak may be assigned to the Ni_a-C species. The identity of the 2060 cm^{-1}, however, is unknown. Later evidence allows this to be assigned to the Ni_a-SI redox level (Chapter 6, Section 6.2.3).

Ni_a-SI (-122 mV vs SHE)

When single crystals of Hyd-1 are exposed to higher potentials, the Ni_a-SI species increases in intensity with the other more reduced species decreasing in population. Figure 4.16 shows the IR spectrum of the Hyd-1 crystals at -122 mV *vs* SHE. A ν_{CO} peak representing Ni_a-L_{II} species (1877 cm^{-1}) is still visible in the spectrum but in a very low proportion. Similarly, there is a low intensity band at 1950 cm^{-1}, suggesting the presence of both the Ni_a-C^+ and Ni_a-C species. Peak fitting was unable to resolve two peaks, although the shift in wavenumber suggests this. In contrast, the Ni_a-SI species at 1929 cm^{-1} dominates. This effect is also apparent in the ν_{CN} region. 4 bands are observed, with those at 2085 and 2077 cm^{-1} matching those seen in the PFIRE spectra for the Ni_a-SI species. The low intensity peak at 2072 cm^{-1} shows the minimal contribution from the Ni_a-C species.

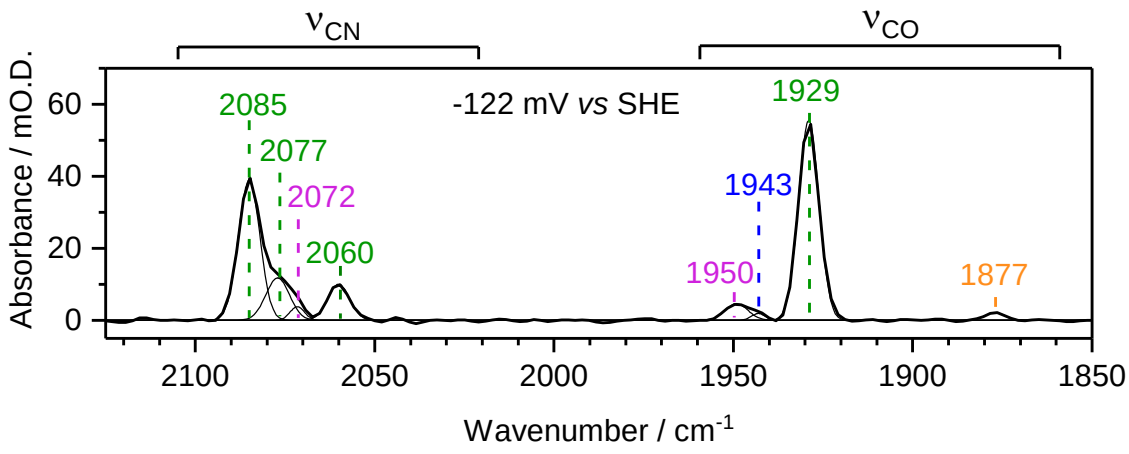


Figure 4.16 IR spectrum of a single crystal of Hyd-1 at pH 5.9, at -122 mV *vs* SHE. Bands marked in purple, yellow, green and blue represent the Ni_a-C, Ni_a-L, Ni_a-SI and Ni-B species respectively. Fitted Gaussian peaks are shown in black.

Another feature of this spectrum is that the 2060 cm^{-1} peak is still present and has increased in absorbance simultaneously with the Ni_a-SI species. This suggests that it is associated with an unknown species at the same redox level as Ni_a-SI. No secondary ν_{CO} band, which would accompany the 2060 cm^{-1} peak, is visible in the IR spectrum, but this may be due to an overlap with the 1929 cm^{-1} peak. Finally, a small band at 1943 cm^{-1} signifies the presence of the inactive Ni-B species which is now present as a minority species in the crystal sample.

Ni-B (+103 mV vs SHE)

At +103 mV *vs* SHE, the inactive Ni-B species at 1943 cm^{-1} is maximised, as shown in Figure 4.17. The IR spectrum measured at this potential is similar to the re-oxidised spectrum in Figure 4.10 which was recorded at an applied potential of +203 mV. Again, peaks attributed to the Ni-B species are all present (1943, 2100, 2094, 2082 cm^{-1}) with the unassigned 1939 and 2067 cm^{-1} bands also appearing in the spectrum.

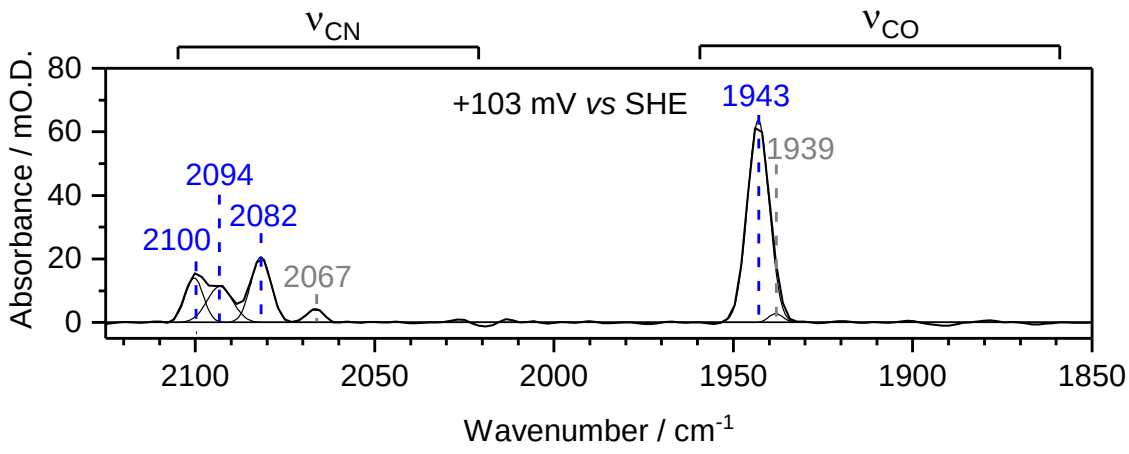


Figure 4.17 IR spectrum of a single crystal of Hyd-1 at pH 5.9, at +103 mV *vs* SHE. Bands marked in blue represent the Ni-B species. Fitted peaks are shown in grey.

Figures 1.10 and 1.17 differ in the relative intensities of the two ν_{CO} bands. The 1943 cm^{-1} band decreases as the potential is increased to +203 mV, whilst the 1939 cm^{-1} band increases in intensity at the higher potential. This suggests that the Ni-B species is oxidised at higher potentials, giving rise to the 1939 cm^{-1} species, similar to the lower wavenumber species at 1942 cm^{-1} observed at high potential when using the PFIRE method in Chapter 3. To understand this further, the behaviour of each IR band with potential needs to be examined.

4.3.2.3 Redox speciation curves

Fitting the ν_{CO} peaks to Gaussian band profiles and extracting the fitted peak absorbances allows for plotting of titration curves of each active site state as a function of potential. Figure 4.18 shows the speciation curves for the ν_{CO} bands observed in an oxidative titration of Hyd-1 crystals at pH 5.9.

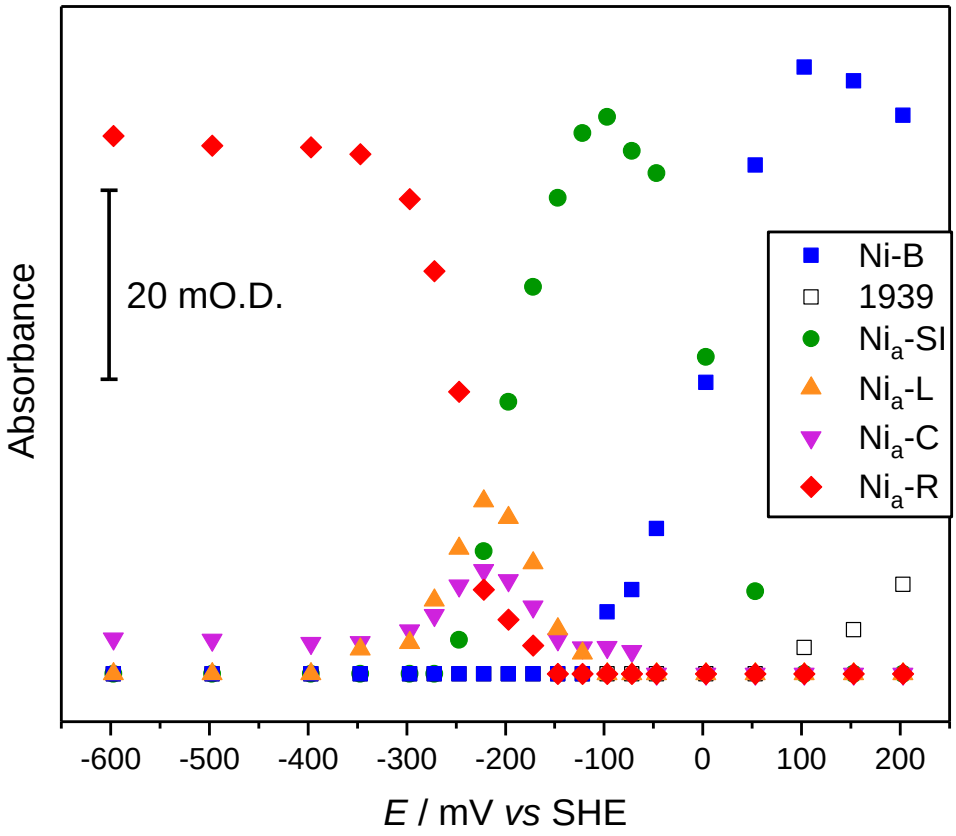


Figure 4.18 Redox speciation curves from an oxidative titration of single crystals of Hyd-1 at pH 5.9 measured using the fitted peak areas for each species. Active site species are labelled in accordance with the colours assigned throughout this Thesis. The unassigned 1939 cm^{-1} peak is included and marked by empty black squares.

For clarity, the absorbances arising from the Ni_a-R_I, Ni_a-R_{II} and Ni_a-R_{III} sub-species have been summed and are represented collectively as Ni_a-R. This is also the case for the Ni_a-L_{II} and Ni_a-L_{III} sub-species, which are represented collectively by Ni_a-L.

Displaying the data as speciation curves clearly shows the potential dependence of each active site species. Across the potential range, the active site speciation is consistent with the redox level of the various states (Figure 4.1): Ni_a-R at low potentials; the tautomers Ni_a-C and Ni_a-L appearing together between -300 and -100 mV *vs* SHE; Ni_a-SI at middle potentials; and the inactive Ni-B species at high potentials. The speciation data for the unassigned 1939 cm^{-1} ν_{CO} peak that appears at high potential is also present in Figure 4.18.

Above +100 mV *vs* SHE the 1939 cm^{-1} band increases in absorbance in conjunction with the Ni-B band decreasing in intensity. This was not observed in the PFIRE experiments by Hidalgo *et al.*, where no additional ν_{CO} band was detected above +100 mV, and the Ni-B species remained constant between +200 and +350 mV.[11] Summing together the absorbances from the Ni-B and 1939 cm^{-1} peak in the crystal spectra results in a similar speciation curve.

Performing the same analysis on IR bands within the ν_{CN} region allows us to confirm the assignments of the ν_{CN} bands to each active site species as they will have the same potential dependency as the assigned ν_{CO} bands. Figures 1.19 to 1.25 show the redox speciation curves for the ν_{CO} and ν_{CN} peaks for each individual active site species observed in the crystal IR spectra. For the majority of the active site species, the ν_{CN} bands mimic the potential dependency of the equivalent ν_{CO} bands. There is slight variation in the potentials at which each band appears in the IR spectra which can be attributed to their relative absorbances. This is clearly seen in Figure 4.19: the ν_{CO} 1914 cm^{-1} band remains until -150 mV, whereas the ν_{CN} bands at 2049 cm^{-1} and 2067 cm^{-1} are no longer detected at potentials -275 mV and -200 mV respectively, consistent with their lower intensity.

The potential dependence of the ν_{CN} bands for the Ni_a-R_{II} species (Figure 4.20, 2056 cm^{-1} and 2071 cm^{-1}) does not accurately follow that of the 1922 cm^{-1} ν_{CO} band. However, as the two ν_{CN} bands generally decrease in absorbance with the 1922 cm^{-1} band, it can be assumed that they are the accompanying ν_{CN} bands for the Ni_a-R_{II} species. The fluctuation of their absorbances may be due to spectral processing as both the 2056 and 2071 cm^{-1} bands are hidden peaks within the IR spectra.

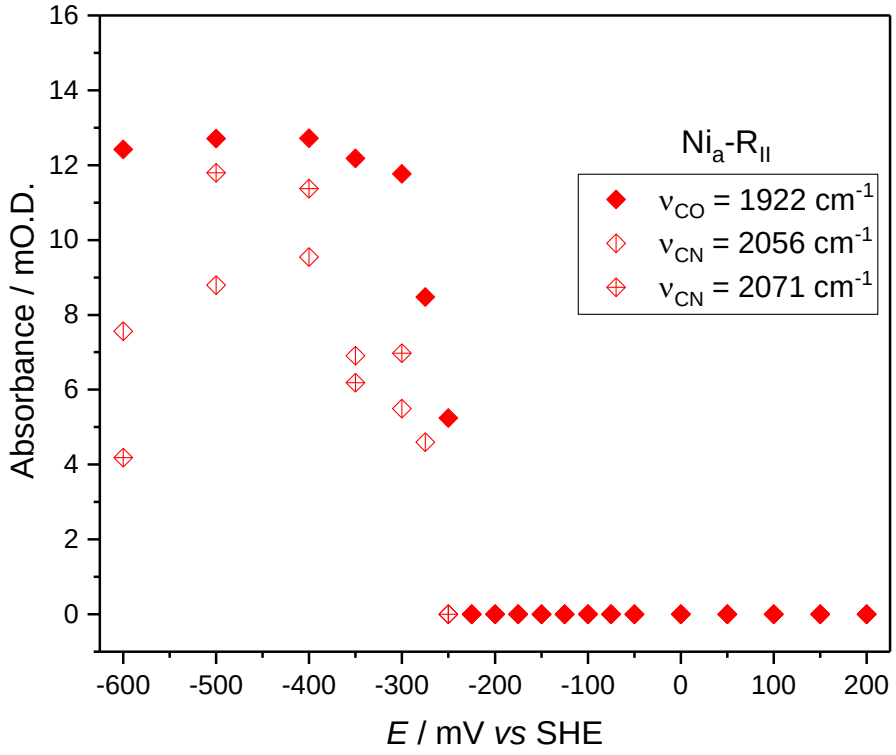


Figure 4.19 Speciation curves for the Ni_a-R_{II} species: ν_{CO} (1922 cm^{-1}) solid red diamonds; ν_{CN} (2056 and 2071 cm^{-1}) hollow red diamonds.

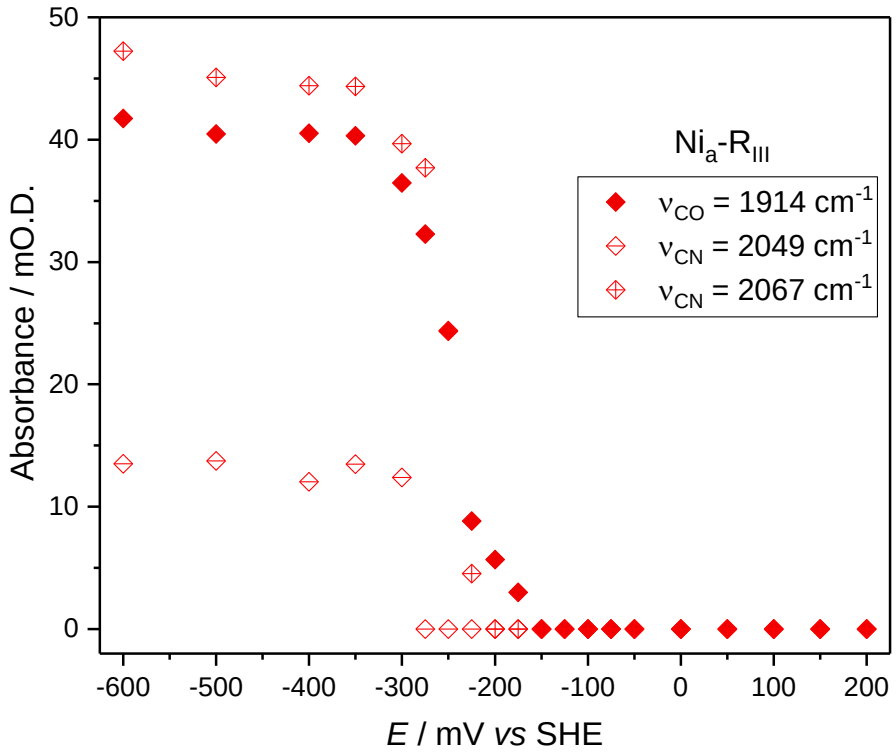


Figure 4.20 Speciation curves for the Ni_a-R_{III} species: ν_{CO} (1914 cm^{-1}) solid red diamonds; ν_{CN} (2049 and 2067 cm^{-1}) hollow red diamonds

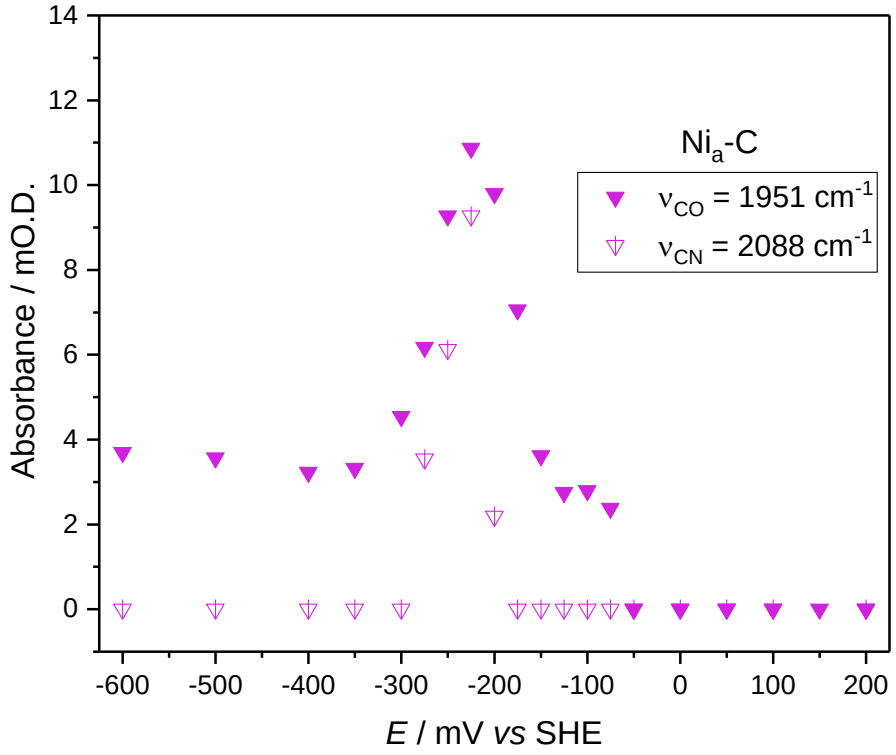


Figure 4.21 Speciation curves for the Ni_a-C redox level (summation of the Ni_a-C^+ and Ni_a-C species): ν_{CO} (1951 cm^{-1}) solid purple triangles; ν_{CN} (2049 and 2067 cm^{-1}) hollow purple triangles.

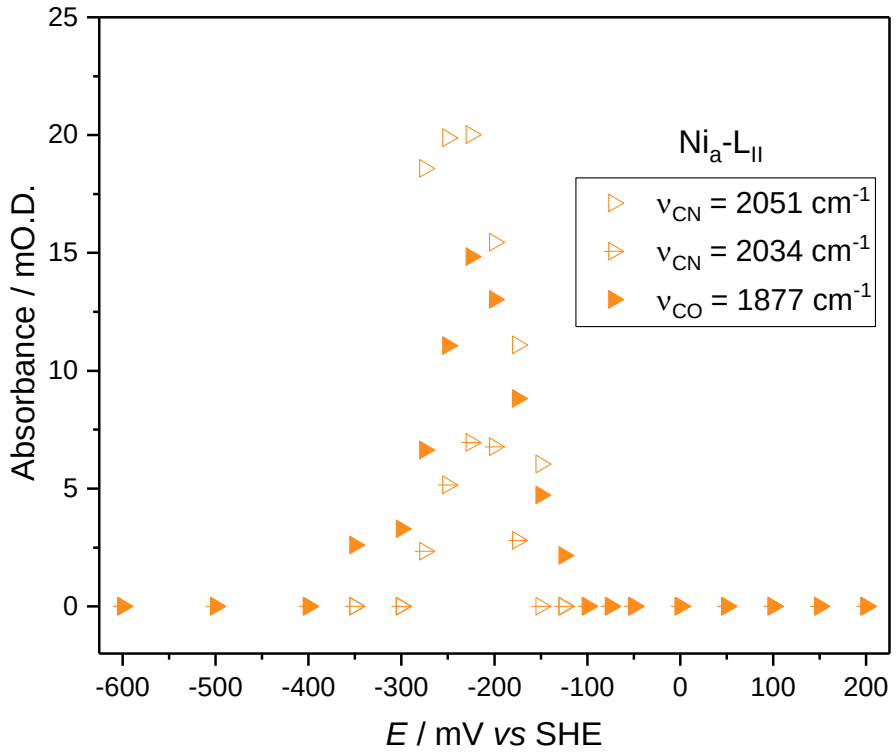


Figure 4.22 Speciation curves for the Ni_a-L_{II} species: ν_{CO} (1877 cm^{-1}) solid yellow triangles; ν_{CN} (2034 and 2051 cm^{-1}) hollow yellow triangles.

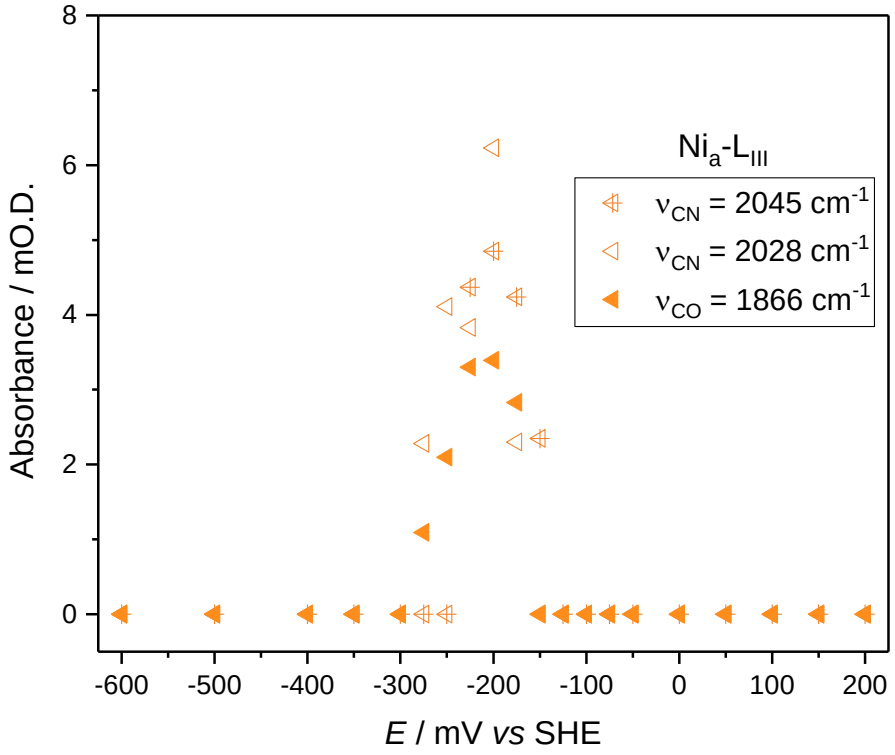


Figure 4.23 Speciation curves for the Ni_a-L_{III} species: ν_{CO} (1866 cm^{-1}) solid yellow triangles; ν_{CN} (2028 and 2045 cm^{-1}) hollow yellow triangles.

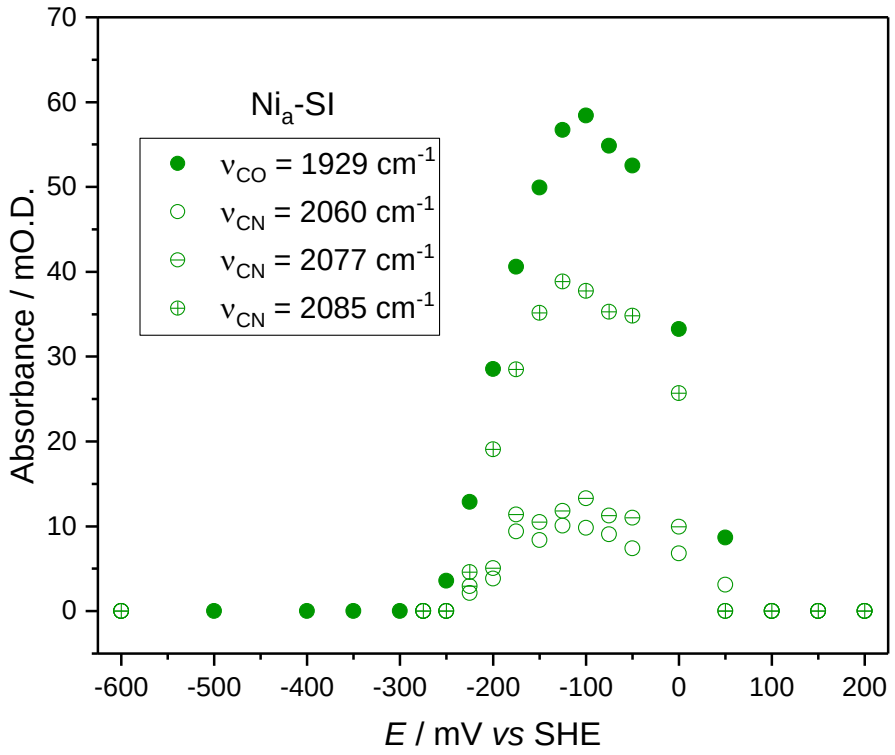


Figure 4.24 Speciation curves for the Ni_a-SI species: ν_{CO} (1929 cm^{-1}) solid green circles; ν_{CN} (2060, 2085 and 2077 cm^{-1}) hollow green circles.

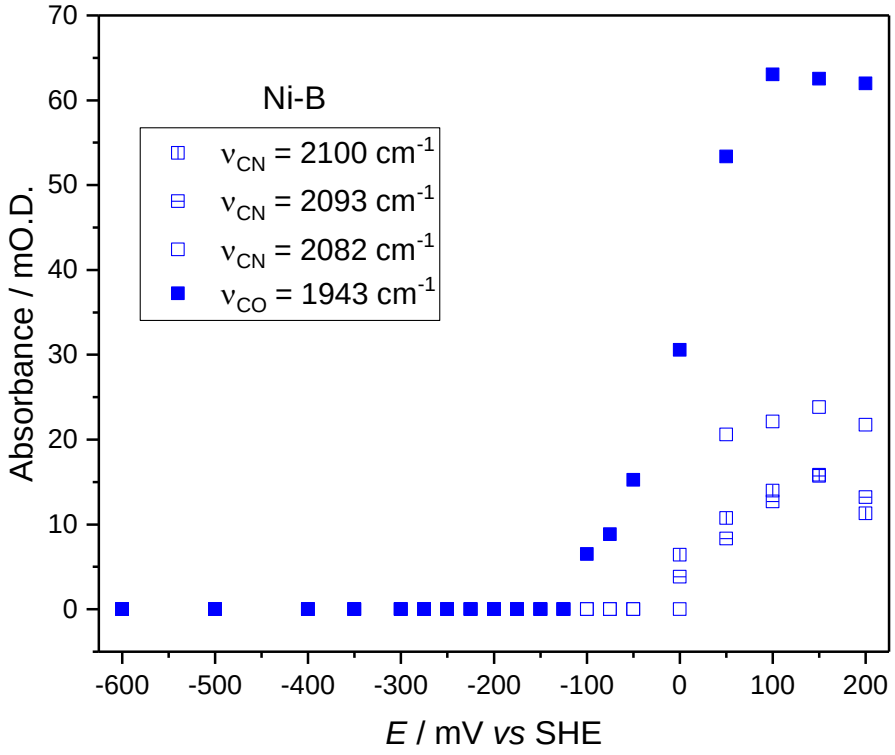


Figure 4.25 Speciation curves for the Ni-B species: ν_{CO} (1943 cm^{-1}) solid blue squares; ν_{CN} (2082, 2093 and 2100 cm^{-1}) hollow blue squares.

Overall, Figures 1.19 to 1.25 corroborate the assignment of each ν_{CN} band to their respective active site species.

Effect of potential on the relative populations of the Ni$_a$-R and Ni$_a$-L sub-species

It is expected that each sub-species will display the same behaviour with potential as they represent active site species at the same redox level. Figure 4.26 shows the redox speciation curves for the ν_{CO} bands of the three Ni$_a$-R sub-species. All three sub-species have the same potential dependence, with the only differences being the potential at which they are no longer detected in the IR spectra. This is likely due to their relative intensities, with the least populated sub-species, Ni$_a$-R$_I$, becoming undetectable first at -247 mV; Ni$_a$-R$_{II}$ is disappearing at -222 mV; whilst Ni$_a$-R$_{III}$ remains until -147 mV.

Overall, the Ni_a-R sub-species are isopotential, appear across the same potential window, and the ratio between them remains constant with potential change. This confirms that these three bands correspond to the same redox level, Ni_a-R.

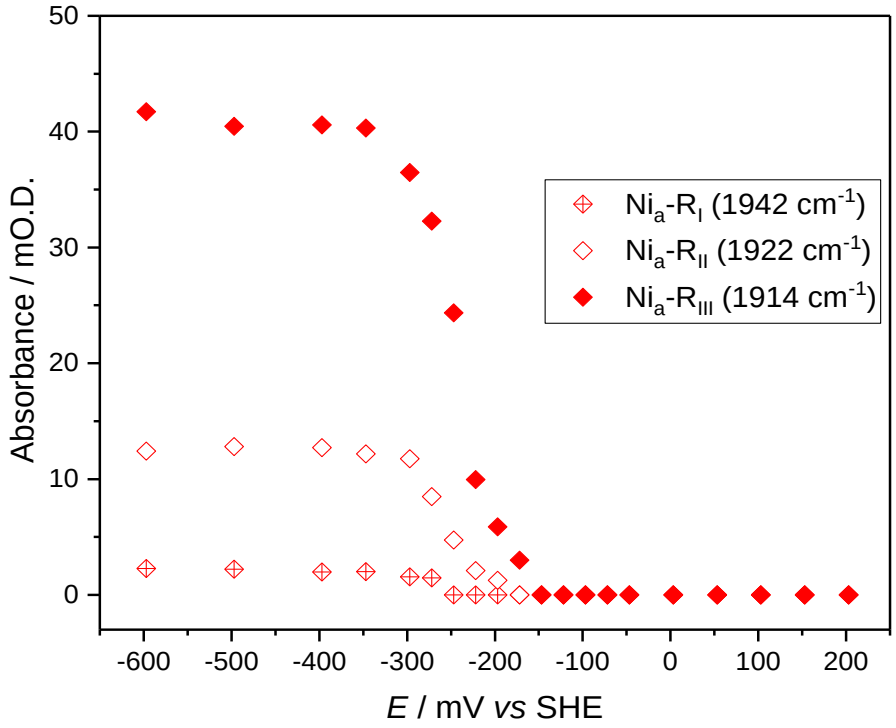


Figure 4.26 Redox speciation curves for the ν_{CO} band of each Ni_a-R sub-species (Ni_a-R_I – 1942 cm^{-1}; Ni_a-R_{II} – 1922 cm^{-1}; Ni_a-R_{III} – 1914 cm^{-1}) measured during an oxidative titration of single crystals of Hyd-1 at pH 5.9.

Figure 4.27 presents the change in ν_{CO} band absorbance with potential of the Ni_a-C (1951 cm^{-1}) and Ni_a-L species (1877 and 1866 cm^{-1}). As observed in other studies of [NiFe] hydrogenases, including Hyd-1, the Ni_a-C and Ni_a-L states have similar potential dependencies. Both species are maximised at -222 mV and then are oxidised at higher potentials. The ratio between the two Ni_a-L sub-species is approximately constant across all potentials, showing that they do correspond to the same redox level. However, the Ni_a-L species is not detected at low potentials in contrast to the Ni_a-C species which is observed at a constant intensity below -347 mV *vs* SHE.

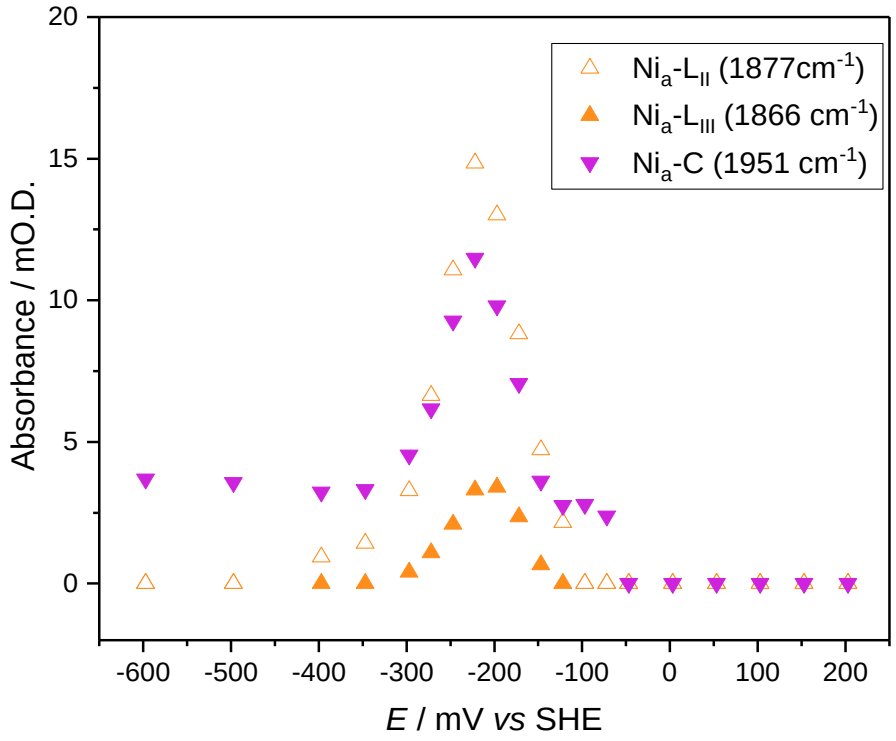


Figure 4.27 Redox speciation curves for the ν_{CO} bands of the Ni_a-C and Ni_a-L sub-species (Ni_a-C – 1951 cm^{-1}; Ni_a-L_{II} – 1877 cm^{-1}; Ni_a-L_{III} – 1866 cm^{-1}) measured during an oxidative titration of single crystals of Hyd-1 at pH 5.9.

Previous studies have demonstrated a pH-dependent tautomeric equilibrium between the Ni_a-C and Ni_a-L states.[11,14] This relationship in the crystalline state is investigated in Chapter 5, where electrochemical redox titrations of single crystals of Hyd-1 are performed at different pH values.

4.3.3. Comparison to other IR spectroelectrochemical techniques

When studying Hyd-1 *in crystallo*, one query is whether the observed spectroscopic behaviour could be translated to the behaviour of Hyd-1 in solution. As detailed above, all of the established active site redox states for Hyd-1 can be attained in the crystalline form, including the Ni_a-L and Ni_a-R sub-species. Furthermore, Table 4.3 shows that the ν_{CO} and ν_{CN} bands observed for each species are congruous with those seen *via* electrode-adsorbed IR spectroscopy. Alongside this, previously hidden redox species are

revealed in the crystal IR spectra. This may be a result of the higher effective concentration of protein present in the crystal compared to when adsorbed onto the extended carbon electrode or in solution, or that the nature of the crystalline form naturally promotes a higher population of certain species as opposed to in solution.

Table 4.3 Comparing the active site species of *E. coli* Hyd-1 at pH 6. The relative ν_{CO} and ν_{CN} band positions of each active site species, to the nearest cm^{-1}, at pH 6 observed for Hyd-1 in crystallo, adsorbed on an electrode (PFIRE) or in solution.

Redox species	Wavenumber / cm^{-1}			
	In crystallo[h]		**Electrode-adsorbed**[i]	
	ν(CO)	**ν(CN)**	**ν(CO)**	**ν(CN)**
Ni-X	1939	2067, 2070	n.d.	n.d.
Ni-B	1943	2100, 2094, 2082	1943	2099, 2082
Ni_a-SI	1929	2085, 2077, 2060	1930	2085, 2076
Ni_a-C^+	1951	2088, 2072	1952	2090, n.d.
Ni_a-C	1949	n.d.	1948	2078, n.d.
Ni_a-L_{II}	1877	2051, 2034	1877	2051, 2034
Ni_a-L_{III}	1866	2045, 2027	1866	2046, 2028
Ni_a-R_I	1942	n.d.	1933	n.d.
Ni_a-R_{II}	1922	2071, 2056	1922	2071, 2053
Ni_a-R_{III}	1914	2067, 2049	1914	2067, 2049

As the crystal IR microspectroscopic-electrochemical experiments are performed under an inert atmosphere and Hyd-1 is a poor H_2 producer at pH 5.9,[15] the IR spectra recorded

[h] This Chapter
[i] See Chapter 3 of this work

effectively show the non-turnover behaviour of the [NiFe] active site. Thus, we can compare the redox titrations of the crystal to other IR spectroelectrochemical techniques that also study Hyd-1 under non-turnover conditions.

Figure 4.28 shows a direct comparison of the redox speciation curves of crystalline Hyd-1 (as depicted in Figure 4.18) with those for electrode-absorbed[11] and solution Hyd-1[10]. Not only are these potential curves remarkably alike, but the approximate ratios of each redox species and the potentials at which the maximum intensity for each redox species is observed are consistent throughout. There are minor differences between the crystal speciation curves and other methods, such as the behaviour of the Ni-B peak above +100 mV and the lack of Ni_a-L below -350 mV, but overall it appears that that the dynamic behaviour around the active site of Hyd-1 crystals is maintained. Therefore observations made in the crystalline state of Hyd-1 are mechanistically relevant to the enzyme in solution, and to PFE studies of enzyme activity.

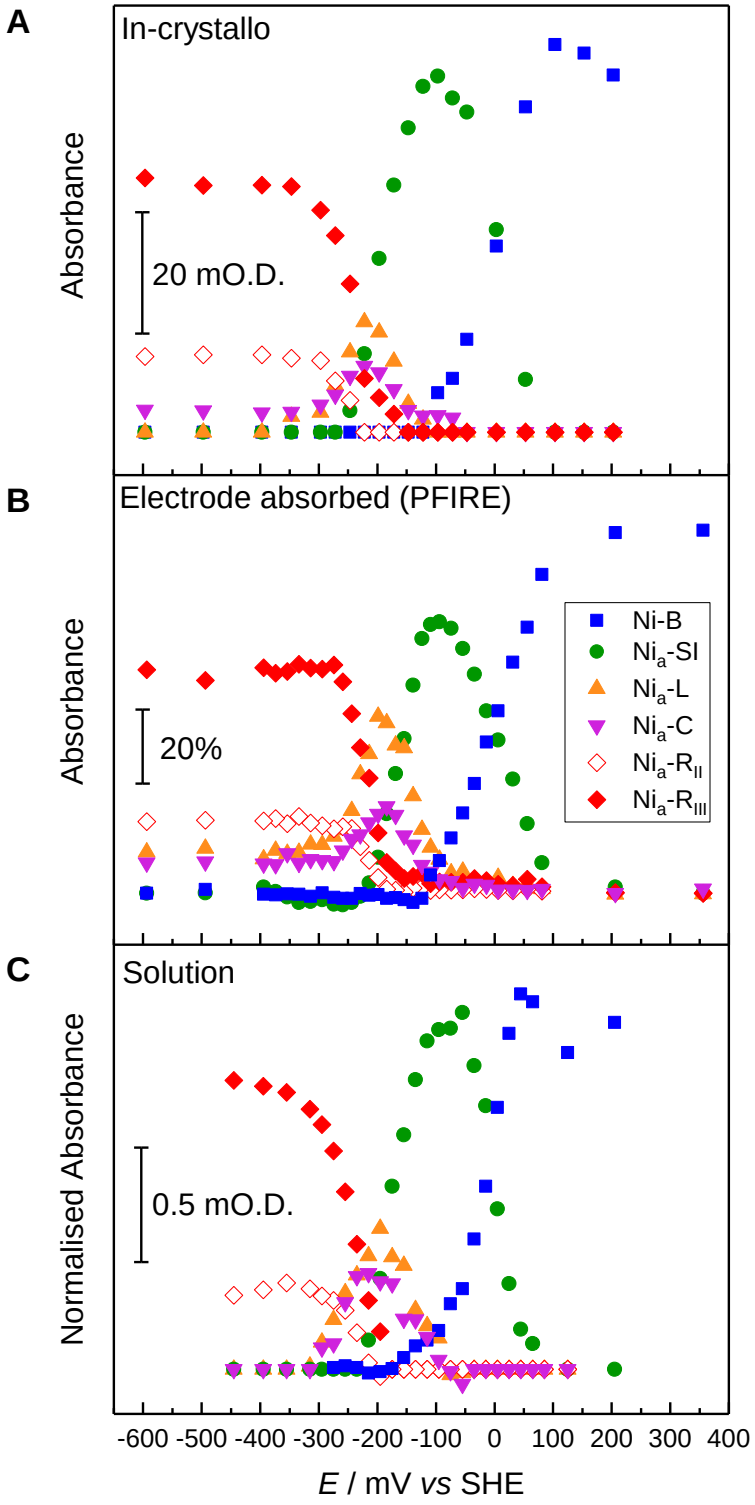


Figure 4.28 Comparison of redox speciation curves (from oxidative titrations) of Hyd-1 at pH 5.9 by three IR spectroscopic-electrochemical methods: (A) single crystal IR microspectroscopic electrochemistry/in crystallo; (B) PFIRE/electrode adsorbed, collected by Hidalgo[11], and (C) in solution, collected by Healy[10]. For clarity the intensities arising from the Ni_a–L_{II} and Ni_a–L_{III} species have been summed and are represented collectively as Ni_a–L.

4.4. Time-resolved experiments

4.4.1. Time-resolved IR spectroelectrochemistry of [NiFe] hydrogenases

Due to the fast catalytic rates of [NiFe] hydrogenases (in the order of 1000 s^{-1}), steady-state IR spectroelectrochemical methods such as PFIRE are not able to fully resolve each step within the catalytic cycle. Therefore techniques with sub-turnover frequency time resolution are necessary to provide insight into the multiple electron and proton transfer steps that occur during catalysis and determine any transient intermediates. Such methods usually involve triggering transitions between active site states *via* photolysis or the release of caged electrons and using IR spectroscopy to monitor changes. Performing photolysis experiments at low temperatures has also been shown to trap transient intermediates.[16]

Dyer and co-workers have developed time-resolved IR methods to probe the active site chemistry of the [NiFe] hydrogenase *Pyrococcus furiosus* SH1. They have shown that the Ni_a-R, Ni_a-C and Ni_a-SI species are able to interconvert faster than the turnover frequency of the hydrogenase giving evidence towards their catalytic relevance.[17] Additionally, time-resolved photolysis experiments have helped elucidate the proton and electron transfer steps in the Ni_a-C to Ni_a-SI transition, showing that the Ni_a-L species acts as an intermediate.[18]

IR microspectroscopic-electrochemical studies of crystalline Hyd-1 performed by Ash *et al.* revealed time-dependent formation of two Ni_a-R sub-states following a reductive potential step.[7] This suggests that redox transitions that involve chemical steps such as proton transfer may be retarded in the crystalline state. Therefore using this technique on single crystals of hydrogenase provides a method to probe the redox chemistry of the [NiFe] active site without the need for fast time resolution.

During the electrochemical redox titration performed in Section 4.3, each potential step is applied until the sample has completely equilibrated to the applied potential, as shown by no further change in the intensity of the ν_{CO} and ν_{CN} bands. By continuously recording IR spectra during the equilibration period, the time-dependence of these spectral changes can be monitored.

4.4.2. Ni_a-L as a precursor to Ni_a-SI

Figure 4.29 shows the successive IR spectra of a single crystal of Hyd-1 at pH 5.9, recorded during an oxidative potential step from -197 mV to -172 mV. Thirteen IR spectra were recorded over a period of 13.4 minutes, after which no change in the absorbances of the ν_{CO} and ν_{CN} bands were visible, signifying the crystal had equilibrated to the applied potential. The black dashed line represents the IR spectrum recorded at -197 mV, i.e. prior to the oxidative step.

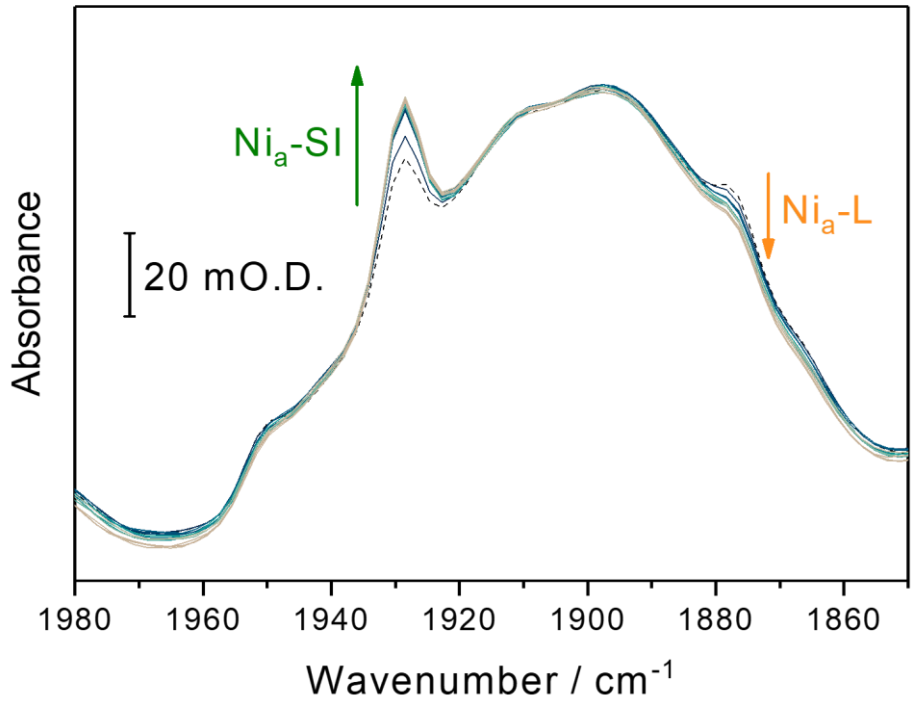


Figure 4.29 Unprocessed 'absolute' IR spectra (ν_{CO} region) of a single crystal of Hyd-1 at pH 5.9 following an oxidative potential step from -197 mV to -172 mV. The black dotted line represents the IR spectrum recorded at -197 mV, prior to the oxidative step.

Two changes in peak intensities are immediately visible: increase of Ni_a-SI (1929 cm^{-1}) and decrease of the two Ni_a-L sub-species (1877 and 1866 cm^{-1}). When represented as difference IR spectra, further spectral changes can be distinguished. In Figure 4.30A, each IR spectrum is presented in reference to the -197 mV spectrum, i.e. -172 mV *minus* -197 mV, to accurately show changes in peak intensity due to the potential step. Five ν_{CO} bands are present, each denoting an active site species: Ni_a-C (1951 cm^{-1}), Ni_a-SI (1929 cm^{-1}), Ni_a-R_{III} (1914 cm^{-1}), Ni_a-L_{II} (1877 cm^{-1}), and Ni_a-L_{III} (1866 cm^{-1}). Initially, all five redox species experience a change in their relative intensities upon oxidation to -172 mV, as shown by the first spectrum in Figure 4.30A (black line). However, subsequent spectra during equilibration show that only the Ni_a-L and Ni_a-SI species experience a further change in absorbance, with the Ni_a-R_{II} and Ni_a-C species remaining approximately constant (Figure 4.30B). Complete equilibration of the crystal with the applied potential then occurs.

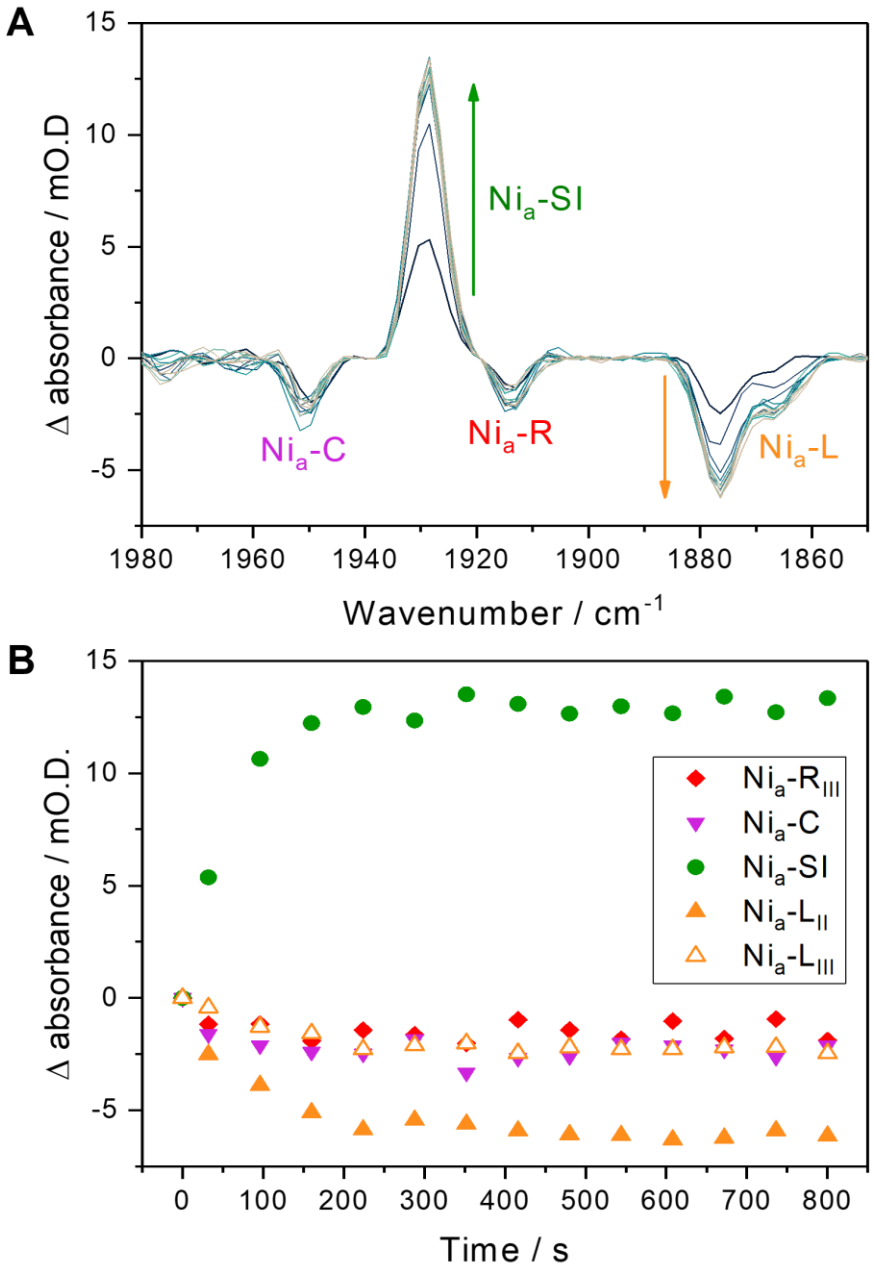


Figure 4.30 Ni_a-L to Ni_a-SI transition in single crystals of Hyd-1, pH 5.9 following an oxidative potential step from -197 mV to -172 mV *vs* SHE. Each IR spectrum was recorded over a period of 64 s, with the resulting ν_{CO} peak absorbance representing the average during that time period. (A) Difference IR spectra (ν_{CO} region) following the potential step showing the increase in Ni_a-SI and decrease in Ni_a-L species over time. The difference spectra are presented as -172 mV *minus* -197 mV. (B) Time dependence of the change in absorbance of active site redox species following the potential step.

4.4.3. Discussion

The involvement of the Ni_a-L sub-species as an on-pathway intermediate in the Ni_a-C / Ni_a-SI transition, as opposed to a single proton-coupled electron transfer (PCET) step, has been a topic of various IR spectroscopic studies.[11,19] Due to the overall transition occurring over reaction times orders of magnitude faster than enzyme turnover, rapid kinetic methods such as pump-probe photolysis have so far been necessary to pick out further details in the kinetic steps. Here, however, using the IR microspectroscopic-electrochemical technique on crystalline protein also allows access to similar information.

Figure 4.30B shows that the Ni_a-R and Ni_a-C species equilibrate to the applied potential faster than the Ni_a-L and Ni_a-SI species. Transition between the Ni_a-R and Ni_a-C species involves an electron transfer and the removal of a proton from the active site vicinity (Figure 4.1). As previously discussed, the presence of multiple sub-species of Ni_a-R has been posited to represent sequential proton movement from the [NiFe] active site, with decreasing wavenumber of the ν_{CO} stretch representing the proton moving further away. A common representation of the Ni_a-R_I species has a protonated terminal cysteine-S that is coordinated to the Ni(II), signifying the base which is hypothesised to initially accept the proton.[20,21] Thus, it is expected that transition between the Ni_a-R_I and Ni_a-C states will involve a proton transfer step, i.e. the deprotonation of the cysteine-thiolate, and an electron transfer step. In Hyd-1, however, Ni_a-R_{III} is the most predominant sub-species, i.e. when the proton is furthest from the active site, and it is the only Ni_a-R species present during the potential step examined in Figure 4.30 (ν_{CO} = 1914 cm^{-1}). If the cysteine-S is also protonated in the Ni_a-$R_{II/III}$ species, it is expected that a vibrational band arising from the S-H stretch would be detected in the IR spectra around 2580 – 2525 cm^{-1}.[22] When examining the difference IR spectra of the Hyd-1 crystal at the potentials where each

redox state is maximised, there is no evidence of any change in cysteine-S protonation during either a Ni_a-R / Ni_a-C nor Ni_a-L / Ni_a-SI transition. This is shown by the lack of S-H bands in the difference IR spectra in Figure 4.31. This means that either the cysteine-S is protonated across all redox states, or in none of them.

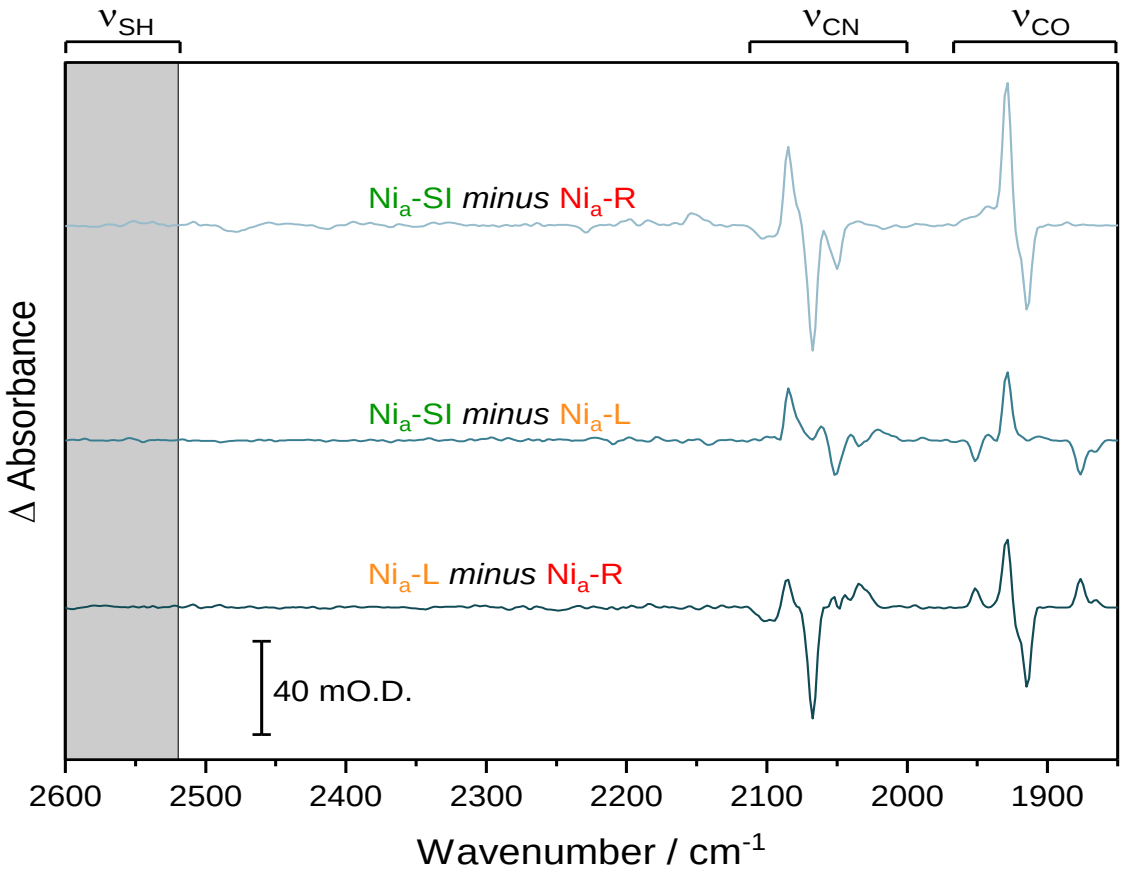


Figure 4.31 Difference IR spectra of single crystals of Hyd-1 at pH 5.9 show no evidence of cysteine-S protonation in the Ni_a-$R_{II/III}$ and Ni_a-$L_{II/III}$ sub-species, as given by the lack of S-H stretch in the IR spectra. The potentials used for each species are as follows: -97 mV for Ni_a-SI, -197 mV for Ni_a-C/Ni_a-L, and -497 mV. The approximate S-H stretching region (ν_{SH}) is shaded in grey.

Tai *et al.* observed that the terminal cysteine-thiolate is not protonated in either the Ni_a-SI nor Ni_a-C species of *Dv*MF,[23] and so it is expected to be the case for Hyd-1 also. This, coupled with the faster rate of transition indicates that the transition between the Ni_a-R_{III} and Ni_a-C species involves only a single electron transfer in Hyd-1. On the other hand, the

comparatively slower rate of the Ni_a-L / Ni_a-SI transition implies that both an electron and proton transfer are required.

Studies by Hirota and Dyer have shown that for Ni_a-C / Ni_a-SI transition to occur *via* a Ni_a-L intermediate, the proximal iron-sulphur cluster must be oxidised in order to able to accept an electron from the [NiFe] active site.[16,18] For O_2-sensitive [NiFe] hydrogenases, the proximal cluster is a standard cubane $[4Fe4S]^{2+/+}$, whose reduction potential is lower than the Ni_a-C / Ni_a-SI redox couple. As such, it can receive an electron from the [NiFe] active site to form Ni_a-SI at potentials around the Ni_a-C / Ni_a-SI couple. However this is not the case for most O_2-tolerant [NiFe] hydrogenases. Hyd-1 in particular has a unique $[4Fe3S]^{5+/4+/3+}$ proximal cluster which has unusually high reduction potential: +3 mV for the 4+/3+ transition and +203 mV for the 5+/4+ transition.[24] Therefore at potentials such as those applied in Section 4.4.2, the proximal cluster remains reduced at equilibrium. This results in oxidation of the active site to the Ni_a-SI level becoming hindered as the proximal cluster is already occupied. This could be the reason why the Ni_a-L_I sub-species is not observed in Hyd-1: with electron transfer delayed, the proton is able to move further from the active site, resulting in the two lower wavenumber Ni_a-L species. Consequently, there are two possible mechanisms by which the Ni_a-L / Ni_a-SI transition can occur, depending on the proximal cluster (Figure 4.32). Firstly, as reported by Dyer and co-workers on the O_2-sensitive [NiFe] hydrogenase, *P. furiosus* SH1, the Ni_a-L converts to Ni_a-SI *via* a concerted proton and electron transfer, with a conserved glutamate residue close to the Ni-bound terminal cysteine thiolates theorised to be the proton acceptor.[18] A second mechanism involves proton transfer prior to the electron transfer step. The identities of the proton acceptor sites are undetermined, but the proton transfer itself is thought to be unaffected due to the conserved nature of the active site and surrounding amino acids.

The limiting effect of the reduced [4Fe3S] proximal cluster on electron transfer means that a proton can leave the active site before oxidation to the Ni_a-SI state.

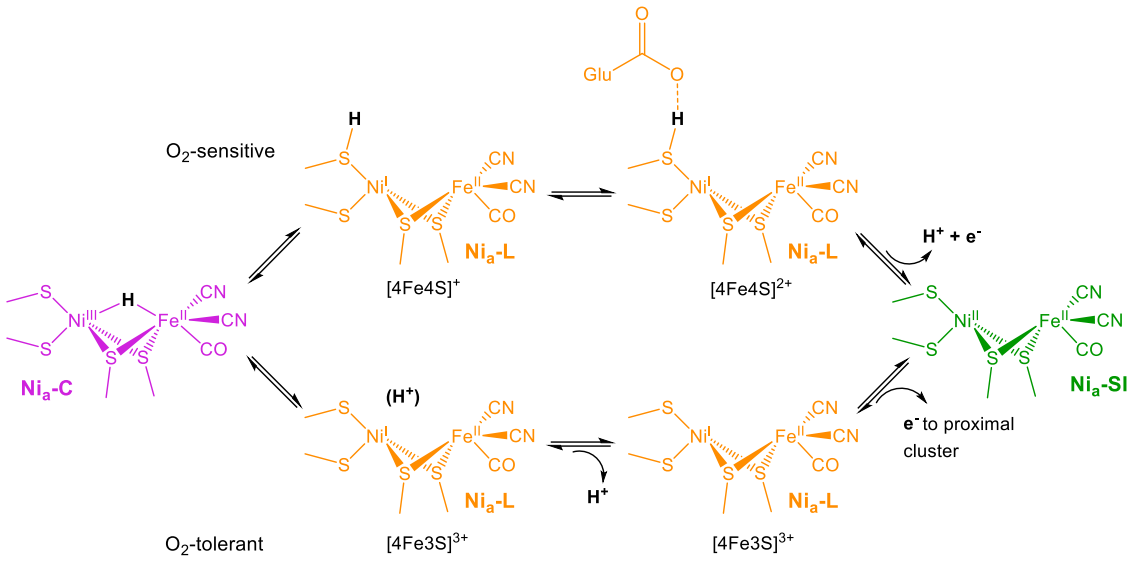


Figure 4.32 Two possible mechanisms of proton-electron transfer during a Ni_a-C / Ni_a-SI transition at potentials around -200 mV *vs* SHE. For O_2-sensitive [NiFe] hydrogenases, the proximal [4Fe4S] cluster is oxidised and conversion to the Ni_a-SI species can occur via a concerted proton-electron transfer step. For O_2-tolerant [NiFe] hydrogenases, the proximal [4Fe3S] cluster remains reduced, hindering electron transfer, thus sequential proton then electron transfers occur.

4.5. Summary

In this Chapter, an improved IR microspectroscopic-electrochemical method for studying proteins in their crystalline state has been developed and used to perform the first in-depth electrochemical oxidative titration on single crystals of Hyd-1. The results show that each active site redox species detected by established IR spectroelectrochemical methods can indeed be obtained within the crystal. Furthermore, the behaviour of each species with respect to potential reflects that previously seen, showing that the [NiFe] active site of Hyd-1 retains its redox chemistry in the crystalline state. This opens the

possibility of directly linking structural information obtained via x-ray diffraction with spectroscopic characterisation.

The high signal-to-noise ratio afforded by the high protein concentration in the crystalline state helps the assignment of each ν_{CO} band to an active site species. This has also allowed previously unseen IR bands to be detected in the crystal IR spectra, suggesting the presence of new active site species. The identities of these new IR bands have been proposed, but further study under varying experimental conditions is required for their confirmation.

This Chapter has also highlighted a significant feature of the IR microspectroscopic-electrochemical technique: the ability to resolve reaction steps without needing sub-turnover frequency time resolution. The crystalline state has been shown to retard proton transfer steps relative to electron transfer, resulting in new information regarding the Ni_a-L / Ni_a-SI transition in Hyd-1 to be obtained. Rather than a concerted proton-electron transfer step as observed in O_2-sensitive [NiFe] hydrogenases, the results above suggest sequential proton then electron transfer steps occur for Hyd-1.

Overall, this Chapter has shown that the IR microspectroscopic-electrochemical technique is a useful tool in investigating the behaviour of redox metalloproteins such as *E. coli* Hyd-1. The next step is to determine if the proton transfer equilibria remain unperturbed in the crystalline state. This is of particular importance when studying redox proteins such as Hyd-1, where proton transfer is an intrinsic part of the catalytic process. This can be achieved by performing similar electrochemical redox titrations on single crystals of Hyd-1 in buffer solutions of varying pH. The IR microspectroscopic-electrochemical method can then be extended to other redox metalloproteins.

4.6. References

1 H. Ogata, S. Hirota, A. Nakahara, H. Komori, N. Shibata, T. Kato, K. Kano and Y. Higuchi, *Structure*, 2005, **13**, 1635–1642.

2 S. E. Beaton, R. M. Evans, A. J. Finney, C. M. Lamont, F. A. Armstrong, F. Sargent and S. B. Carr, *Biochem J*, 2018, **475**, 1353–1370.

3 M. A. Hough, S. v. Antonyuk, R. W. Strange, R. R. Eady and S. S. Hasnain, *J Mol Biol*, 2008, **378**, 353–361.

4 G. Kachalova, K. Decker, A. Holt and H. D. Bartunik, *Proc Natl Acad Sci*, 2011, **108**, 4800–4805.

5 J.-H. Jeoung and H. Dobbek, *J Am Chem Soc*, 2009, **131**, 9922–9923.

6 D. Sippel, M. Rohde, J. Netzer, C. Trncik, J. Gies, K. Grunau, I. Djurdjevic, L. Decamps, S. L. A. Andrade and O. Einsle, *Science (1979)*, 2018, **359**, 1484–1489.

7 P. A. Ash, S. B. Carr, H. A. Reeve, A. Skorupskaite, J. S. Rowbotham, R. Shutt, M. D. Frogley, R. M. Evans, G. Cinque, F. A. Armstrong and K. A. Vincent, *Chem. Comm.*, 2017, **53**, 5858–5861.

8 R. Hidalgo, D.Phil. thesis, University of Oxford, 2016.

9 D. H. Juers and J. Ruffin, *J Appl Crystallogr*, 2014, **47**, 2105–2108.

10 P. A. Ash, S. E. T. Kendall-Price, R. M. Evans, S. B. Carr, A. R. Brasnett, S. Morra, J. S. Rowbotham, R. Hidalgo, A. J. Healy, G. Cinque, M. D. Frogley, F. A. Armstrong and K. A. Vincent, *Chem Sci*, 2021, **12**, 12959–12970.

11 R. Hidalgo, P. A. Ash, A. J. Healy and K. A. Vincent, *Angew. Chem., Int. Ed.*, 2015, **54**, 7110–7113.

12 P. A. Ash, R. Hidalgo and K. A. Vincent, *ACS Catal*, 2017, **7**, 2471–2485.

13 W. Lubitz, H. Ogata, O. Rüdiger and E. Reijerse, *Chem Rev*, 2014, 114, 4081–4148.

14 B. J. Murphy, R. Hidalgo, M. M. Roessler, R. M. Evans, P. A. Ash, W. K. Myers, K. A. Vincent and F. A. Armstrong, *J Am Chem Soc*, 2015, **137**, 8484–8489.

15 M. J. Lukey, A. Parkin, M. M. Roessler, B. J. Murphy, J. Harmer, T. Palmer, F. Sargent and F. A. Armstrong, *J Biol Chem*, 2010, **285**, 3928–38.

16 H. Tai, K. Nishikawa, M. Suzuki, Y. Higuchi and S. Hirota, *Angew. Chem., Int. Ed.*, 2014, **53**, 13817–13820.

17 B. L. Greene, C. H. Wu, P. M. McTernan, M. W. W. Adams and R. B. Dyer, *J Am Chem Soc*, 2015, **137**, 4558–4566.

18 B. L. Greene, C. H. Wu, G. E. Vansuch, M. W. W. Adams and R. B. Dyer, *Biochemistry*, 2016, **55**, 1813–1825.

19 H. Tai, K. Nishikawa, S. Inoue, Y. Higuchi and S. Hirota, *J Phys Chem B*, 2015, **119**, 13668–13674.

20 T. Krämer, M. Kampa, W. Lubitz, M. van Gastel and F. Neese, *ChemBioChem*, 2013, **14**, 1898–1905.

21 H. Ogata, K. Nishikawa and W. Lubitz, *Nature*, 2015, **520**, 571–574.

22 H. Kandori, N. Kinoshita, Y. Shichida, A. Maeda, R. Needleman and J. K. Lanyi, *J Am Chem Soc*, 1998, **120**, 5828–5829.

23 H. Tai, K. Nishikawa, Y. Higuchi, Z. Mao and S. Hirota, *Angew. Chem.*, 2019, **131**, 13419–13424.

24 M. M. Roessler, R. M. Evans, R. A. Davies, J. Harmer and F. A. Armstrong, *J Am Chem Soc*, 2012, **134**, 15581–15594.

25 W. Clark, *Oxidation-reduction potentials of organic systems*, Williams & Wilkins, Baltimore, 1960.

26 O. S. Ksenzhek, S. A. Petrova and M. v. Kolodyazhny, *Bioelectrochem Bioenerg*, 1977, **4**, 346–357.

27 P. G. Tratnyek, T. E. Reilkoff, A. W. Lemon, M. M. Scherer, B. A. Balko, L. M. Feik and B. D. Henegar, 2001, **6**, 172–179.

28 J. B. Conant, H. M. Kahn, L. F. Fieser and S. S. Kurtz Jr, *J. Am. Chem. Soc*, 1922, **44**, 1382–1396.

29 C. Batchelor-McAuley, Q. Li, S. M. Dapin and R. G. Compton, *J. Phys. Chem. B*, 2010, **114**, 4094–4100.

30 C. L. Bird and A. T. Kuhn, *Chem Soc Rev*, 1981, **10**, 49.

Chapter 5. Proton transfer equilibria within single crystals of Hyd-1

Following characterisation of crystalline Hyd-1 at pH 6 using the IR microspectroscopic-electrochemical technique, the redox behaviour under varying pH conditions is investigated to determine whether proton transfer equilibria is perturbed *in crystallo*.

5.1. Introduction

Proton transfers are an integral part of hydrogenase catalysis.[1–4] Several steps within the catalytic cycle involve proton-coupled electron transfers (Figure 5.1) and are therefore highly sensitive to the protonation environment. As demonstrated in Chapter 3, the pH-dependence of the distribution of certain active site redox states is well-established for *E. coli* Hyd-1. Of note is the acid-base equilibrium between the tautomeric Ni_a-C and Ni_a-L species. At high pH values, the Ni_a-L species are favoured whereas under low pH conditions, Ni_a-C is dominant. The predicted pK_a for the Ni_a-C/Ni_a-L equilibrium was calculated to be higher than that previously recorded for electrode-adsorbed Hyd-1, likely due to the inclusion of the additional protonated Ni_a-C^+ species observed in the PFIRE spectra. The presence of a protonated and unprotonated Ni_a-C species within electrode-adsorbed Hyd-1 implies a greater deal of complexity regarding the Ni_a-C to Ni_a-SI transition.

Regarding the PCET steps within the catalytic cycle, multiple Ni_a-R and Ni_a-L sub-species have been detected in many [NiFe]-hydrogenases. These are thought to represent the transfer of a proton from the active site vicinity, with each sub-species signifying the 'removed' proton on a different amino acid along the proton transfer pathway. Once again, Chapter 3 corroborated the pH-dependence of the Ni_a-R sub-species in electrode-adsorbed Hyd-1. Although not a traditional Henderson-Hasselbalch acid-base equilibrium, a strong correlation with pH was indicated.

The protonation environment can also have a significant impact on the catalytic properties of [NiFe]-hydrogenases. At neutral pH, *E. coli* Hyd-1 is an irreversible catalyst, only functioning as an H_2 oxidiser and appearing inactive at potentials below -300 mV.

However, when the pH is lowered, Hyd-1 not only becomes an efficient H^+ reducer, but the overpotential requirement for H_2 oxidation decreases.[5]

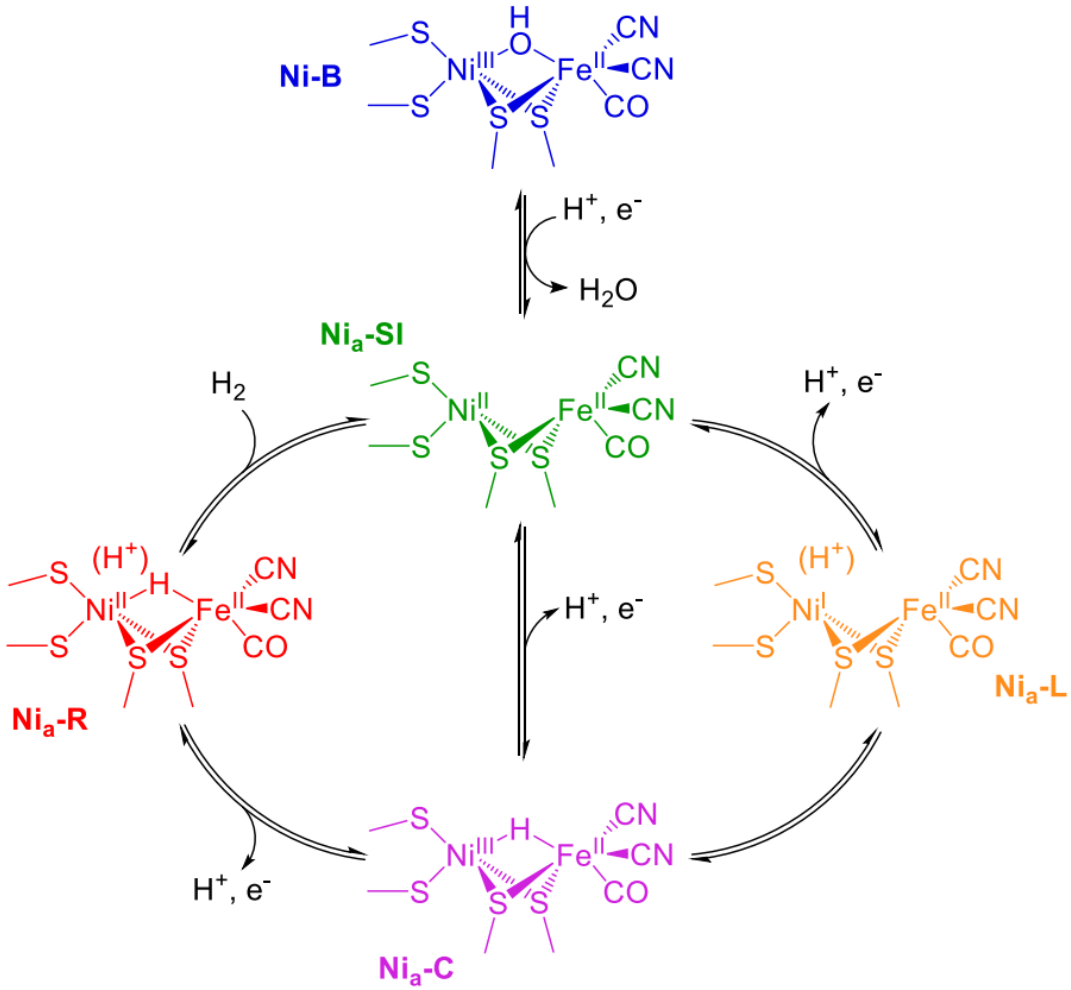


Figure 5.1 The [NiFe]-hydrogenase catalytic cycle involves several proton-coupled electron transfer steps. The Ni_a-R and Ni_a-L species are composed of up to three sub-species where a proton, represented by (H^+), are at different points along the proton pathway away from the active site.

The electrochemical redox titration of single crystals of Hyd-1 performed in Chapter 4 were conducted at pH 5.9. It was established that the potential behaviour of the [NiFe] active site of single crystals of *E. coli* Hyd-1 was consistent with that observed in solution and electrode-adsorbed. The multiple Ni_a-R and Ni_a-L sub-species were retained and a shift in the Ni_a-C ν_{CO} band with potential suggested the presence of two Ni_a-C active site

species. Therefore, it is important to verify that the behaviour of the pH-dependent active site redox states, as observed in Chapter 3 with electrode-adsorbed Hyd-1, is maintained within the crystalline state, and that crystallisation does not perturb proton transfer equilibria within the [NiFe] active site. Furthermore, if the distributions of the active site redox states within the crystal can be influenced to enrich a specific redox state in certain pH environments, this could help in isolating single crystals of specific redox species for structural analysis *via* x-ray crystallography.

Hyd-1 can be crystallised at a variety of pH values and is stable over a reasonably wide pH range.[6] In this Chapter, single crystals of Hyd-1 are studied using the IR microspectroscopic-electrochemical technique at high (8.0) and low (4.0) pH to investigate whether all aspects of proton transfer are retained within the crystalline state with varying pH.

5.2. Results and discussion

Data were collected using the synchrotron IR source and measurements were made on single crystals of *E. coli* WT Hyd-1 prepared without the cytochrome *b* sub-unit as described in Section 2.3.

5.2.1. High pH

A detailed electrochemical oxidative titration was performed on single crystals of Hyd-1 at pH 8.0. Figure 5.2 presents the baseline-corrected IR spectra recorded at specific potentials corresponding to those at which each active site redox species is maximised. As with pH 5.9, all active site redox species are detected in their respective potential windows during the redox titration, including the Ni_a-R and Ni_a-L sub-states. At low potential, the two Ni_a-R sub-species with ν_{CO} at 1921 and 1913 cm^{-1} are the most dominant. There is a minor contribution from a redox species with ν_{CO} at 1938 cm^{-1} (grey

asterisk, Figure 5.2) which may represent the Ni_a-R_I sub-species, similar to that observed in the single crystal Hyd-1 IR spectra at pH 5.9 (Figure 4.9).

Two Ni_a-L sub-states are present at -299 mV *vs* SHE (ν_{CO} 1876 and 1864 cm^{-1}) in greater proportion than their accompanying tautomer Ni_a-C, as expected at the higher pH value (*vide infra*). Once again, two high wavenumber ν_{CO} bands are observed, thought to represent the protonated and unprotonated Ni_a-C^+ species. The behaviour of these species, along with the Ni_a-L sub-states, with potential is discussed later in this Chapter.

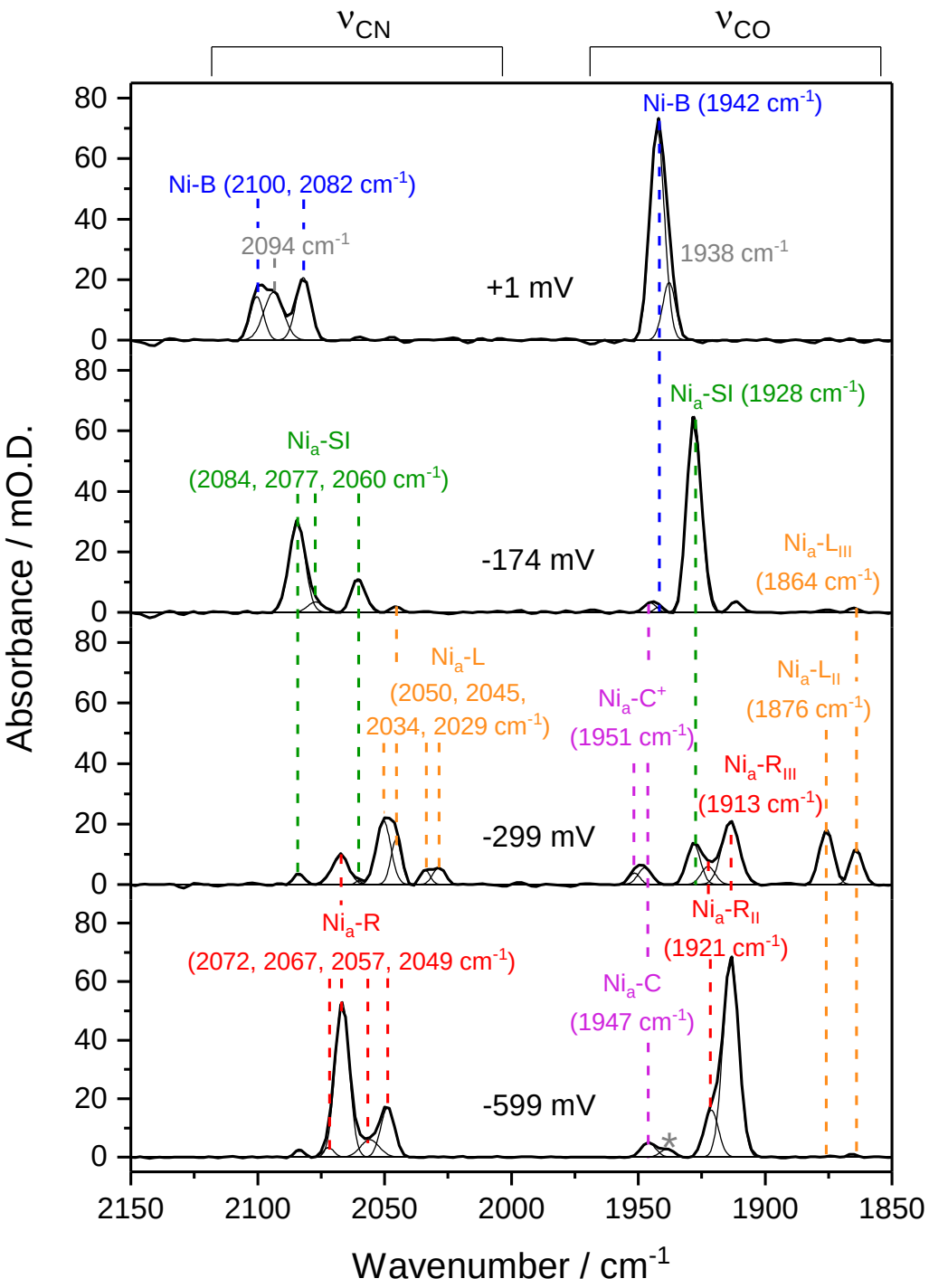


Figure 5.2 Baseline-corrected IR spectra of a single crystal of Hyd-1 at pH 8.0, poised at selected potentials which reflect those at which maximum intensity for each active site redox species is observed during the redox titration (Figure 5.3). Dashed lines mark the wavenumber positions of the intrinsic ν_{CO} and ν_{CN} bands of the Hyd-1 active site redox states. Bands in grey are unassigned, with the peak marked by the asterisk at 1938 cm^{-1} suggested to be a high wavenumber Ni_a-R sub-species. Fitted Gaussian peaks are shown by the thin black curves.

Three ν_{CN} bands are again detected at the Ni_a-SI redox level alongside the single ν_{CO} band at 1928 cm^{-1}, hinting at the presence of a second redox species, whose ν_{CO} band is obscured. Finally, at high potential, the inactive Ni-B species forms alongside a second high potential redox species with ν_{CO} at 1938 cm^{-1}. Potential speciation curves suggest that the ν_{CN} band at 2094 cm^{-1} is, in fact, due to the unassigned high potential redox species rather than a Ni-B ν_{CN} band (*vide infra*) and thus is not labelled as a Ni-B species in Figure 5.2.

Table 5.1 gives the ν_{CO} band positions for each active site redox species measured at pH 5.9 and 8.0. Band positions, reported the nearest 1 cm^{-1}, are derived from Gaussian profiles fitted to baseline-corrected IR spectra at the respective potentials where the active site species is maximised. As expected, for each active site ν_{CO} band, an increase in pH generally leads to a decrease in wavenumber. This is consistent with the results observed in Chapter 3 concerning electrode-adsorbed Hyd-1 (Table 3.3). A change in pH affects the protonation state of the amino acid residues surrounding the active site, and thus the degree to which they interact with the Fe-bound CO and CN ligands. The shift in ν_{CO} band with pH indicates that even within the crystal the protonation state of amino acids can be influenced.

Table 5.1 The pH dependence of active site ν_{CO}. Band positions are rounded to 1 cm^{-1} from the fitted parameter and were taken from IR spectra at the potential where each redox species is maximised.

pH	**ν_{CO} band position/ cm^{-1}**								
	Ni-B	**Ni-X**	**Ni_a-SI**	**Ni_a-C^+**	**Ni_a-C**	**Ni_a-L_{II}**	**Ni_a-L_{III}**	**Ni_a-R_{II}**	**Ni_a-R_{III}**
5.9	1943	1939	1929	1951	1947	1877	1866	1922	1914
8.0	1942	1938	1928	1951	1947	1875	1864	1921	1913

The redox speciation plot illustrating the potential dependence of each active site state, including the unassigned species with ν_{CO} at 1938 cm^{-1}, is displayed in Figure 5.3A. The individual sub-species of Ni_a-L are summated, along with the protonated and unprotonated forms of Ni_a-C.

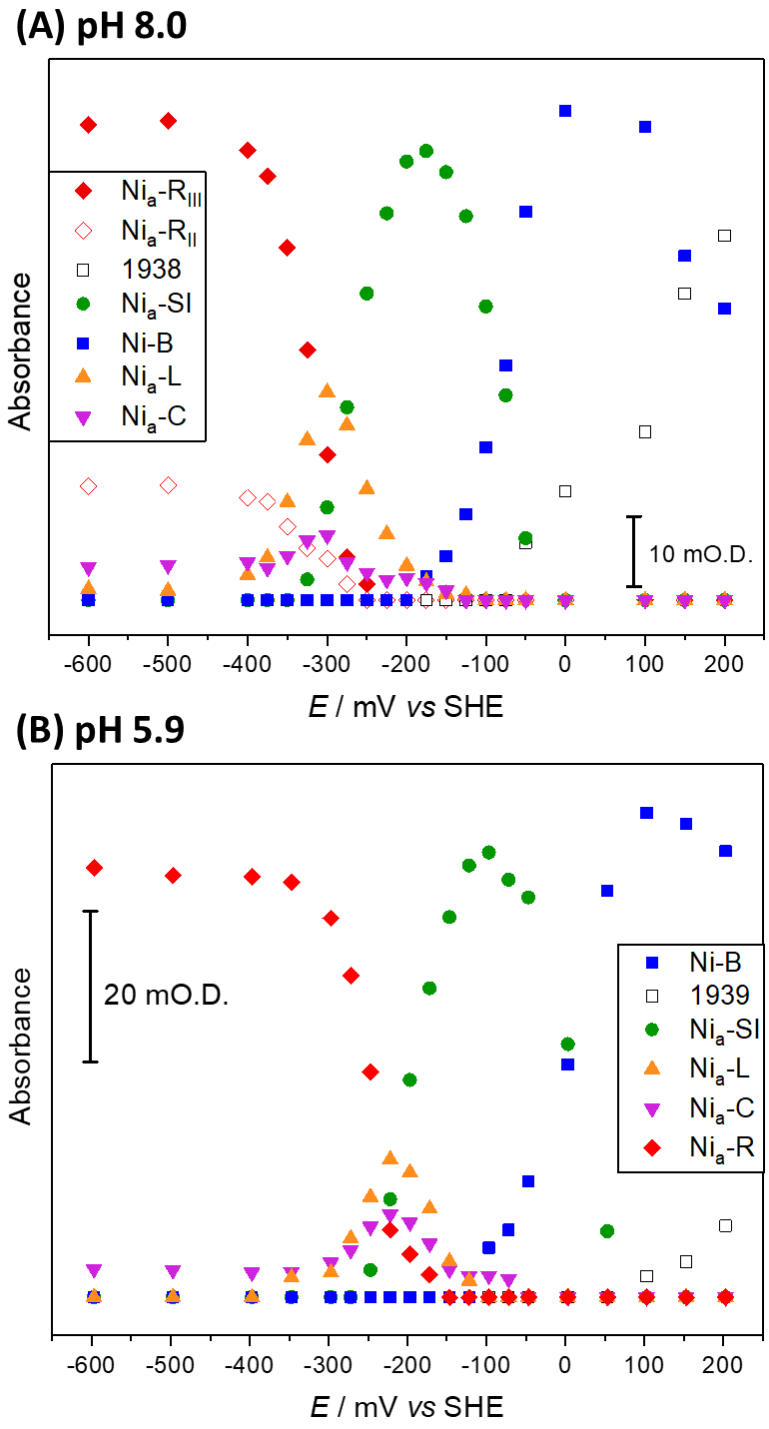


Figure 5.3 (A) Redox speciation curves from an oxidative titration of single crystals of Hyd-1 at pH 8.0 measured using the IR spectroscopic-electrochemical cell. The unassigned 1938 cm^{-1} peak is included and marked by empty black squares. Ni_a-L represents the total absorbance of the Ni_a-L_{II} and Ni_a-L_{III} sub-species and Ni_a-C represents the sum absorbance of the protonated Ni_a-C^+ and unprotonated Ni_a-C species. No data points are available at +50 mV *vs* SHE. (B) Similar redox speciation curve measured at pH 5.9 as previously shown in Chapter 4 (Figure 4.18).

Overall each active site redox species behaves as expected with potential at the higher pH value. The equilibrium midpoint potentials for transitions between each redox level shift to more negative potentials relative to pH 5.9, consistent with the transitions involving PCET processes (Equation 3.2). The shift in the acid-base equilibrium between the Ni_a-L and Ni_a-C redox states is also evident with the Ni_a-L species predominantly more populated than the Ni_a-C species at pH 8 (Figure 5.3A). This is in contrast to the relatively equal distribution observed at pH 5.9 (Figure 5.3B). The pH-dependent tautomeric equilibrium has been established in for Hyd-1 both in solution,[7] and when adsorbed onto an electrode (Section 3.2.2.2)[8]. The fact that it is also maintained within the crystal is extremely important, as it demonstrates that proton transfer equilibria near the [NiFe] active site are not perturbed in the crystalline state. This, coupled with the unperturbed electron transfer redox equilibria demonstrated in Chapter 4, implies that redox processes that occur within the crystal are near analogous to those in solution. Therefore any new information revealed by studying Hyd-1 within the crystalline state are also likely to be present in solution.

A more detailed, direct comparison of the Ni_a-C and Ni_a-L distributions at pH 5.9 and 8.0 is provided in Figure 5.4. Alongside the Ni_a-C/Ni_a-L equilibrium, it is clear that the relative distributions of the Ni_a-L sub-species are also affected by pH. At pH 5.9, only a small proportion of Ni_a-L_{III} is present compared to Ni_a-L_{II}. Increasing the pH to 8.0 shows an accompanying increase in the Ni_a-L_{III} species, without an apparent change in the proportion of the Ni_a-L_{II} species. This behaviour was also observed in PFIRE studies of electrode-adsorbed Hyd-1, where the relative proportion of the Ni_a-L_{II} species remained constant at pH values above 6.0, but a steady increase in the Ni_a-L_{III} species was observed.[8]

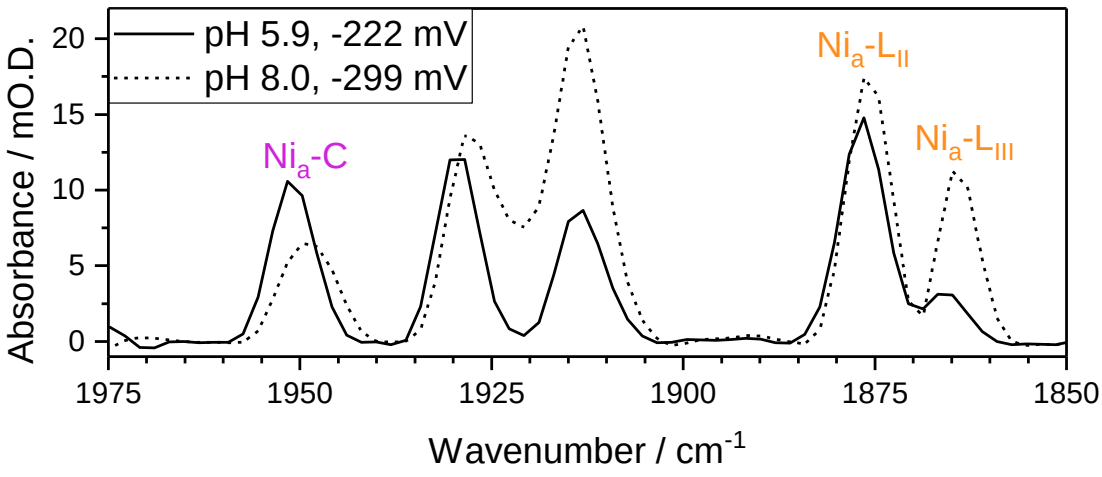


Figure 5.4 Baseline-corrected IR spectra showing the ν_{CO} region of Hyd1 crystals, recorded at pH 8.0 (dotted line,-299 mV) and pH 5.9 (solid line, -222 mV).

The Ni_a-L sub-states are thought to represent sequential proton transfer to and from the [NiFe] active site during the Ni_a-C / Ni_a-SI transition.[9–11] In particular, the low wavenumber species, Ni_a-L_{III}, is suggested to be the state where the proton is furthest from the active site, and thus immediately preceding the Ni_a-SI species during the oxidative Ni_a-C / Ni_a-SI transition. Recent light-triggered FTIR experiments have shown evidence of a Ni-bound cysteine S-H bond in the Ni_a-L_I species of the [NiFe]-hydrogenase from *Dv*MF, implying it is the first base in the proton transfer pathway.[12] It is also widely recognized that the nearby glutamate residue plays an important role in the Ni_a-C / Ni_a-SI transition. For the soluble hydrogenase 1 of *Pyrococcus furiosus*, the apparent pK_a of a proton acceptor during this transition is approximately 7 and proposed to be the conserved glutamate.[1,2] The increase in Ni_a-L_{III} at pH 8 implies that the glutamate is deprotonated in the Ni_a-L_{III} species. The apparent pK_a of the Ni_a-L_{II} species, on the other hand, is ~5, suggesting that deprotonation of the glutamate is not required for formation of the Ni_a-L_{II}, at least in Hyd-1.[13] Altogether, this can suggest the differences in the position of the 'removed' proton within the Ni_a-L sub-species (Figure 5.5).

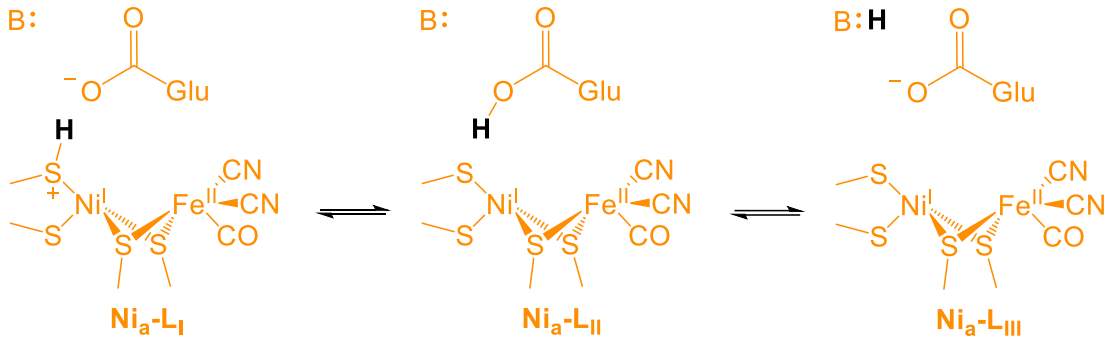


Figure 5.5 Possible movement of the proton (black **H**) between the three Ni_a-L sub-species. The identity of the proton acceptor, B, is unknown.

In Chapter 3, the relative distributions of the two Ni_a-C species were shown to change with pH, with the lower wavenumber ν_{CO} band more prominent at high pH compared to low pH. This is again apparent in single crystals of Hyd-1. Figure 5.6 presents a more detailed redox speciation plot which includes the two Ni_a-L sub-states and the protonated and unprotonated forms of Ni_a-C. Greene *et al.* proposed that the protonation/deprotonation of the glutamate residue caused the appearance of the two Ni_a-C species.[11] The change in distribution of the Ni_a-C^+/Ni_a-C species with pH is analogous to that observed for Ni_a-L_{II}/Ni_a-L_{III}: the lower wavenumber species is more prominent at high pH, possibly due to the deprotonation of the glutamate residue.

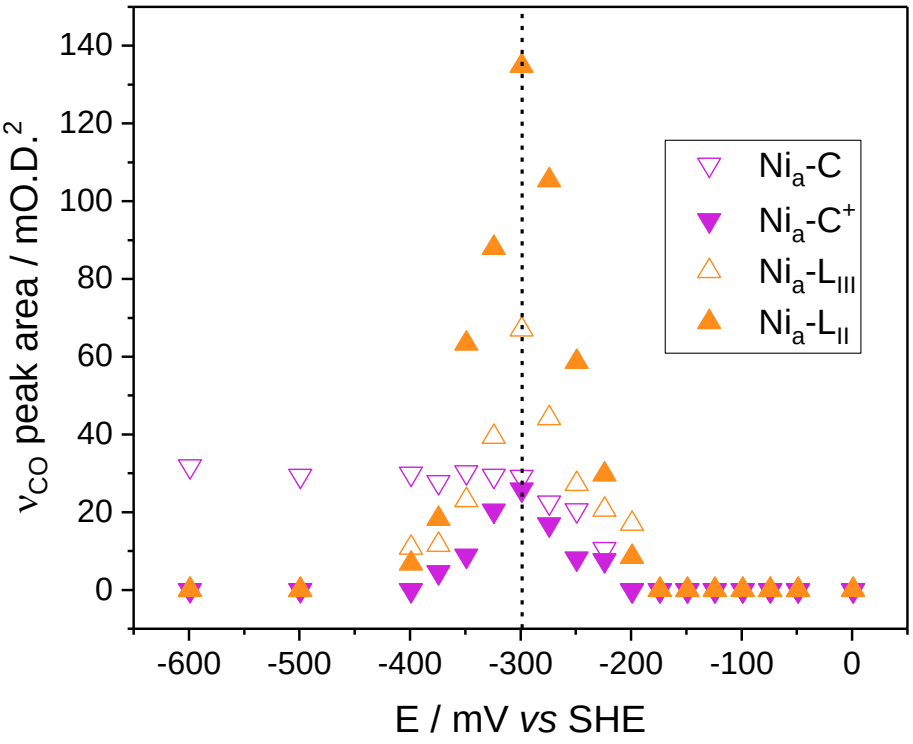


Figure 5.6 Redox speciation curves for the ν_{CO} bands of the Ni_a-L sub-species (Ni_a-L_{II} – 1877 cm^{-1}; Ni_a-L_{III} – 1866 cm^{-1}) and the two Ni_a-C species (Ni_a-C^+ – 1951 cm^{-1}; Ni_a-C – 1947 cm^{-1}) measured during an oxidative titration of single crystals of Hyd-1 at pH 8.0. Dotted line signifies the potential at which the Ni_a-C and Ni_a-L species are maximised (-299 mV).

Another significant detail revealed in Figure 5.3 is the behaviour of the Ni-B and '1938' redox species at high potential. Figure 5.7 presents the redox speciation plots for the known Ni-B ν_{CO} and ν_{CN} bands (A) and the unknown species with ν_{CO} band at 1938 cm^{-1}, named here Ni-X (B). Between -175 and 0 mV, the proportion of Ni-B within Hyd-1 increases, consistent with high potential inactivation. However at potentials above 0 mV, a loss of Ni-B is observed, as shown by the decrease in the ν_{CO} and ν_{CN} bands at 1942 cm^{-1} and 2082, 2100 cm^{-1} respectively. Accompanying this is the apparent increase in a species with ν_{CO} at 1938 cm^{-1}. A high potential Ni-B like species was observed in both PFIRE measurements of Hyd-1 (Chapter 3) and in crystalline Hyd-1 at pH 5.9 (Figure 4.10). Whereas in those cases, only a small proportion of the Hyd-1 active site resided in the

"unknown" state, here, a significant proportion is transformed into the new 'Ni-X' species at high potential. Furthermore, the ν_{CN} band at 2094 cm^{-1} is also demonstrative of the 'Ni-X' species as opposed to the Ni-B species, as its intensity clearly increases at high potential compared to the decrease of the ν_{CN} bands at 2082 and 2100 cm^{-1}. The potential dependence of this 'Ni-X' species is similar to that of the $[4Fe3S]^{5+/4+}$ proximal cluster transition.[14,15] Thus, one possible identity of the high potentials redox species is a 'superoxidised' Ni-B, where the proximal [4Fe3S] cluster is superoxidised to $[4Fe3S]^{5+}$.[13] A method of confirming this theory would be isolating crystals of Hyd-1 at pH 8 at +200 mV for structural determination by x-ray crystallography and EPR measurements to observe the oxidation of the proximal cluster to $[4Fe3S]^{5+}$.

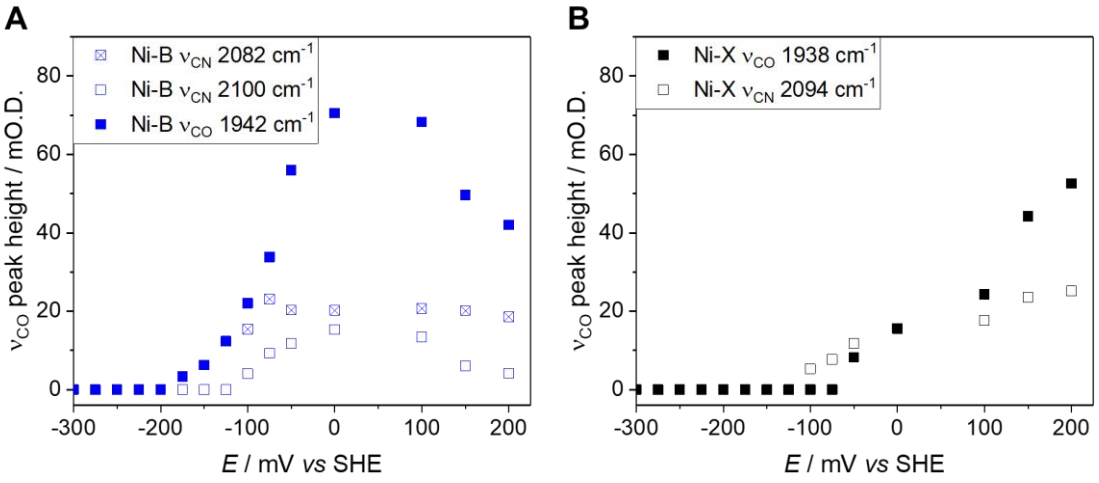


Figure 5.7 Potential dependence of the Ni-B (A) and Ni-X (B) active site redox species. Solid squares represent the ν_{CO} bands (A: 1942 cm^{-1}, B: 1938 cm^{-1}); hollow squares represent the ν_{CN} bands (A: 2082, 2100 cm^{-1}, B: 2094 cm^{-1}).

5.2.2. Low pH

As the pH is lowered below neutral conditions, Hyd-1 becomes a reversible catalyst, which means that at potentials below the H_2/H^+ couple, Hyd-1 catalyses H_2 production.[5] This could pose a slight issue with the IR microspectroscopic-electrochemical technique, as the

accumulation of H_2 gas at low potentials can cause bubbles to appear within the cell, disrupting the electrochemical connection and possibly shifting the crystals away from the IR beam. For the measurements detailed in this Section, negligible current (< 0.1 μA) was observed at low potentials along with little to no visible H_2 production, suggesting minimal H^+ reductive activity.

Relatively low signal intensities were observed for the pH 4 Hyd-1 crystals. Thus, a larger aperture, 20×20 μm, was used throughout the IR measurements in an attempt to increase the peak absorbances. Overall, the measured absorbances are approximately five times lower than those observed for other Hyd-1 single crystal IR spectra.

Figure 5.8 presents the initial characterisation of Hyd-1 crystals at pH 4. The IR spectrum of as-isolated Hyd-1 at pH 4, OCP +262 mV *vs* SHE, contains a number of ν_{CO} bands suggesting that, once again, multiple active site redox species are present. In total, five ν_{CO} bands are observed at 1956, 1945, 1936, 1926 and 1912 cm^{-1}. The peak centred at 1945 cm^{-1} has a full width half maximum nearly twice as large as the other fitted peaks in the spectrum. This suggests it has contributions from at least two unresolved bands, most likely from the inactive Ni-B and Ni-A species, whose ν_{CO} bands are known to be of a similar wavenumber. As the crystals were grown from as-isolated Hyd-1, the remaining ν_{CO} bands also likely represent a mixture of inactive redox species.

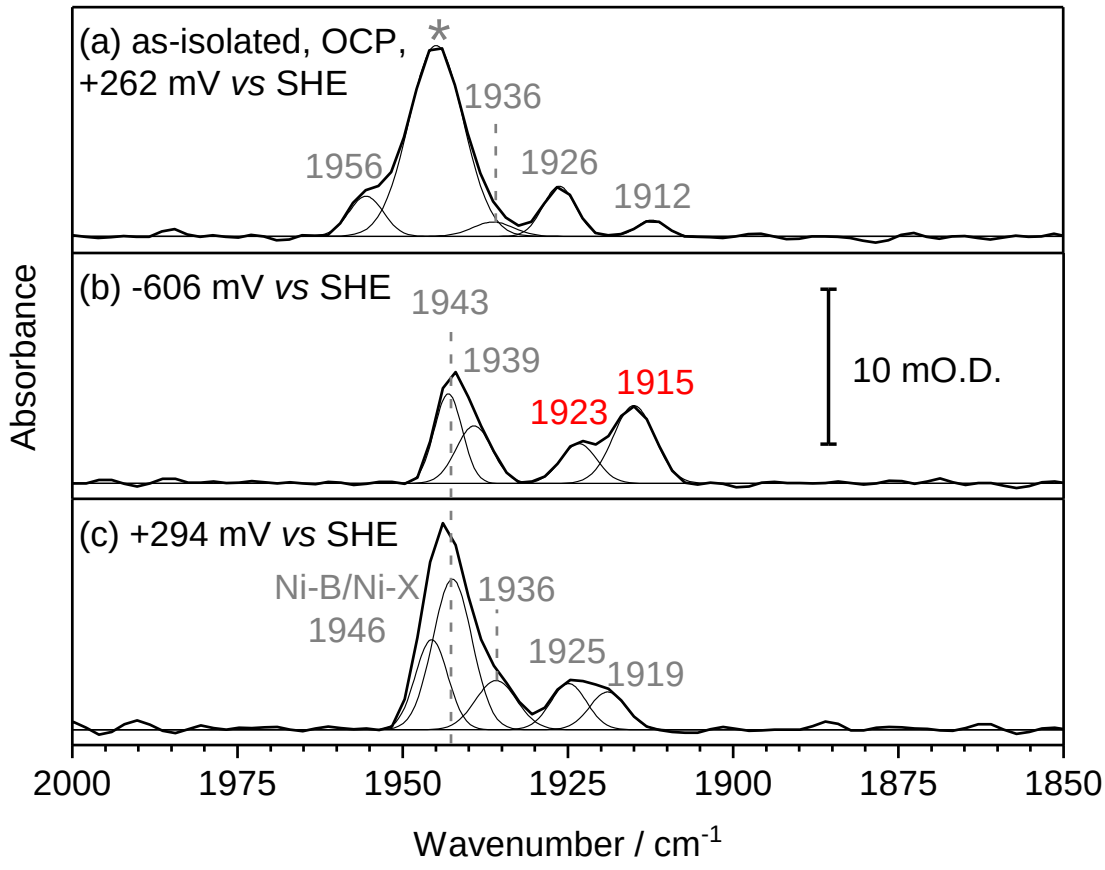


Figure 5.8 The ν_{CO} region of baseline-corrected IR spectra of single crystals of Hyd-1 at pH 4 collected at: (A) open circuit potential +262 mV *vs* SHE: (B) -606 mV *vs* SHE and; (C) +294 mV *vs* SHE.

Electrochemical reduction of the crystal sample usually results in the reduction of any inactive active site species (Section 4.3.1.2 and Figure 5.2). The ν_{CO} bands at 1923 and 1915 cm^{-1} in Figure 5.8B show that reduction to the Ni_a-R species has occurred. However, the two other ν_{CO} bands in the IR spectrum at 1943 and 1939 cm^{-1} suggest that there are still some inactive redox species present. Further electrochemical reduction by poising the crystals at -606 mV did not result in these bands disappearing, suggesting that they are due to damaged active site. By taking the difference between the IR spectra of the 'reduced' and 'as-isolated' crystals, it is clear that reduction was partially successful, as a peak at 1946 cm^{-1} decreases alongside the increase of the Ni_a-R_{III} band at 1915 cm^{-1} (Figure 5.9A). Furthermore, applying a high potential results in re-oxidation of the Hyd-1 crystal

sample, accompanied by an increase in the 1946 cm^{-1} band and a decrease in the Ni_a-R_{III} species (Figure 5.9B). This suggests that the 1946 cm^{-1} band represents a high-potential inactive species, although whether it is Ni-B or 'superoxidised' Ni-X is difficult to tell without a more detailed redox titration. Figure 5.8C reveals that re-oxidation also introduces a number of additional ν_{CO} bands in the IR spectrum, some of which were present in the 'as-isolated' spectrum (Figure 5.8A), suggesting that there are more high-potential inactive species present in the pH 4 Hyd-1 crystals.

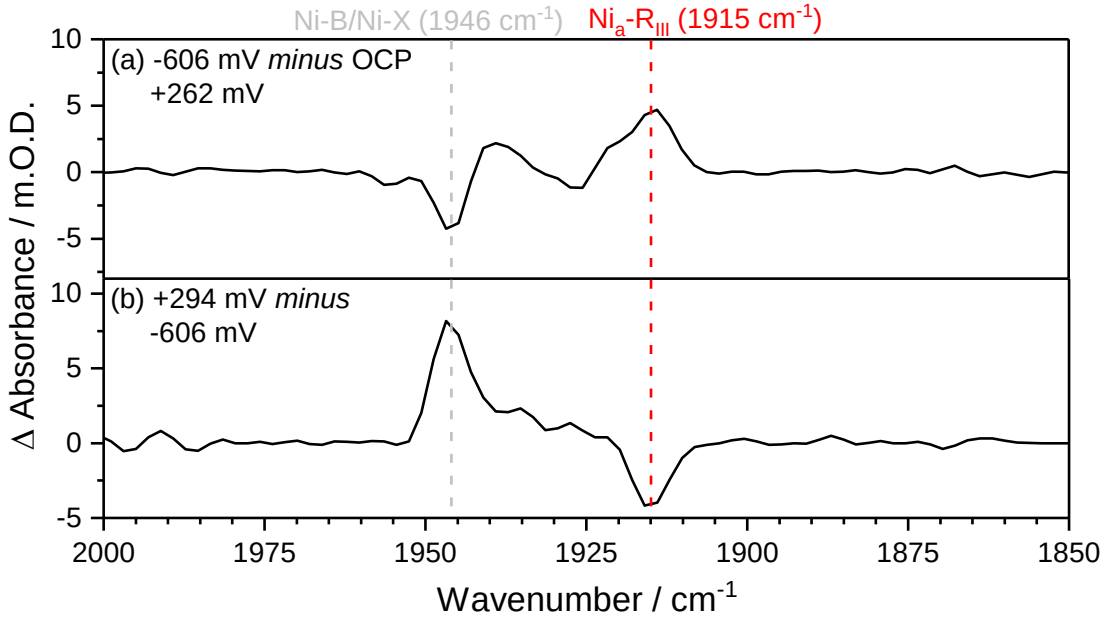


Figure 5.9 IR difference spectra of single crystals of Hyd-1 at pH 4. A) Electrochemically reduced (-606 mV) *minus* as-isolated (OCP = +262 mV). B) Oxidised (+294 mV) *minus* reduced (-606 mV).

Unfortunately no further measurements on the pH 4 Hyd-1 crystals were performed as the crystals began to slowly dissolve in the stabilisation buffer within the IR microspectroscopic-electrochemical cell, showing that Hyd-1 crystals are not stable at pH 4 for long periods of time.

5.3. Summary

In this Chapter, the IR microspectroscopic-electrochemical technique was used to investigate the redox behaviour of single crystals of Hyd-1 under different pH conditions, resulting in two main conclusions.

Firstly, manipulation of the pH of the single crystals of Hyd-1 is possible and all aspects of proton transfer are maintained in the crystalline state: a predicted shift in ν_{CO} band wavenumber is observed; the equilibrium midpoint potentials for the PCET transitions are more negative at high pH; and Ni_a-C/Ni_a-L tautomerism is observed.

Secondly, by manipulating the pH of Hyd-1 single crystals, specific redox species can be enriched at specific potentials. This is most obvious with the Ni_a-C/Ni_a-L tautomerism, with the Ni_a-L species more prominent at high pH. More subtle, however, is the effect of pH on the relative distributions of the Ni_a-R sub-species. At pH 8, the population of the Ni_a-R_{III} sub-species relative to the Ni_a-R_{II} increases to 82% $\pm$ 1.0% compared to 76% $\pm$ 0.6% at pH 6. Thus, it is expected that the x-ray structure of Hyd-1 crystals prepared at high pH will more strongly represent the Ni_a-R_{III} species. By comparing crystal structures measured at a range of pH values, further evidence towards the differences between the sub-species may become apparent.

Overall, the IR microspectroscopic-electrochemical technique has shown that both electron transfer and proton transfer equilibria are not perturbed within the crystalline state of *E. coli* Hyd-1. However, the preparation of Hyd-1 used to prepare the crystals used within this Chapter and Chapter 4 do not completely represent Hyd-1 *in vivo*, as the cytochrome *b* redox partner was removed prior to crystallisation. To ensure this does not have an impact, similar redox titrations on different preparations of Hyd-1 are performed next.

5.4. References

1 B. L. Greene, G. E. Vansuch, C.-H. Wu, M. W. W. Adams and R. B. Dyer, *J Am Chem Soc*, 2016, **138**, 13013–13021.

2 B. L. Greene, C. H. Wu, P. M. McTernan, M. W. W. Adams and R. B. Dyer, *J Am Chem Soc*, 2015, **137**, 4558–4566.

3 P. A. Ash, R. Hidalgo and K. A. Vincent, *ACS Catal*, 2017, **7**, 2471–2485.

4 D. Tombolelli and M. A. Mroginski, *J. Phys. Chem. B*, 2019, **123**, 3409–3420.

5 B. J. Murphy, F. Sargent and F. A. Armstrong, in *Energy Environ. Sci.*, Royal Society of Chemistry, 2014, vol. 7, pp. 1426–1433.

6 R. M. Evans, P. A. Ash, S. E. Beaton, E. J. Brooke, K. A. Vincent, S. B. Carr and F. A. Armstrong, *J Am Chem Soc*, 2018, **140**, 10208–10220.

7 A. J. Healy, D.Phil. thesis, University of Oxford, 2013.

8 B. J. Murphy, R. Hidalgo, M. M. Roessler, R. M. Evans, P. A. Ash, W. K. Myers, K. A. Vincent and F. A. Armstrong, *J Am Chem Soc*, 2015, **137**, 8484–8489.

9 H. Tai, K. Nishikawa, M. Suzuki, Y. Higuchi and S. Hirota, *Angew. Chem., Int. Ed.*, 2014, **53**, 13817–13820.

10 H. Tai, K. Nishikawa, S. Inoue, Y. Higuchi and S. Hirota, *J Phys Chem B*, 2015, **119**, 13668–13674.

11 B. L. Greene, C. H. Wu, G. E. Vansuch, M. W. W. Adams and R. B. Dyer, *Biochemistry*, 2016, **55**, 1813–1825.

12 H. Tai, K. Nishikawa, Y. Higuchi, Z. Mao and S. Hirota, *Angew. Chem.*, 2019, **131**, 13419–13424.

13 P. A. Ash, S. E. T. Kendall-Price, R. M. Evans, S. B. Carr, A. R. Brasnett, S. Morra, J. S. Rowbotham, R. Hidalgo, A. J. Healy, G. Cinque, M. D. Frogley, F. A. Armstrong and K. A. Vincent, *Chem Sci*, 2021, **12**, 12959–12970.

14 M. M. Roessler, R. M. Evans, R. A. Davies, J. Harmer and F. A. Armstrong, *J Am Chem Soc*, 2012, **134**, 15581–15594.

15 H. Adamson, M. Robinson, J. J. Wright, L. A. Flanagan, J. Walton, D. Elton, D. J. Gavaghan, A. M. Bond, M. M. Roessler and A. Parkin, *J Am Chem Soc*, 2017, **139**, 10677–10686.

Chapter 6. Comparing different preparations of Hyd-1 crystals

In vivo, *E. coli* hydrogenase-1 possesses two additional sub-units that are thought to not affect the [NiFe] active site redox chemistry. In this Chapter, single crystals of Hyd-1 with different sub-unit compositions, including addition of the redox partner cytochrome *b*, are studied using the IR microspectroscopic-electrochemical technique to determine whether this is the case.

6.1. Introduction

A key aim of performing IR microspectroscopy on single crystals is to link solution spectroscopic measurements of redox proteins and structural-based techniques such as x-ray crystallography. When the x-ray diffraction pattern of a protein crystal is measured, the average positions of atoms in the crystal can be determined from the electron density image. If the sample contains a mixture of redox species, the crystal structure will either represent the highest concentration redox species or a combination of them all. Structures that are thought to represent a single redox species may, in fact, be averages of multiple species, and thus not a true depiction of the active site at a specific redox level. The single crystal IR microspectroscopic-electrochemistry technique provides a complementary method of measuring the active site redox states present within a protein crystal. This could then be used to confirm whether the structure obtained by x-ray crystallography is a single, or mixture of redox species.

Several crystal structures of *E. coli* hydrogenase-1 (Hyd-1) have been published. The first, by Volbeda *et al.*, reported the structures of Hyd-1 in its as-isolated, H_2-reduced, and chemically oxidised forms.[1] Whilst the structure of the two main units of Hyd-1 (HyaB – large subunit containing the NiFe active site; HyaA – small subunit containing the three iron-sulfur redox clusters) were reported, they do not give a complete picture of Hyd-1. *In vivo*, Hyd-1 is anchored to the periplasmic side of the cytoplasmic membrane by a C-terminal transmembrane alpha helix attached to the small subunit (HyaA) and a transmembrane cytochrome *b* subunit (HyaC) (Figure 6.1). The crystal structures reported by Volbeda *et al.* were obtained from enzyme that did not include the cytochrome *b* redox protein.[1] Furthermore, even though present, the HyaA transmembrane alpha helices could not be fitted from the electron density maps due to their disorder.

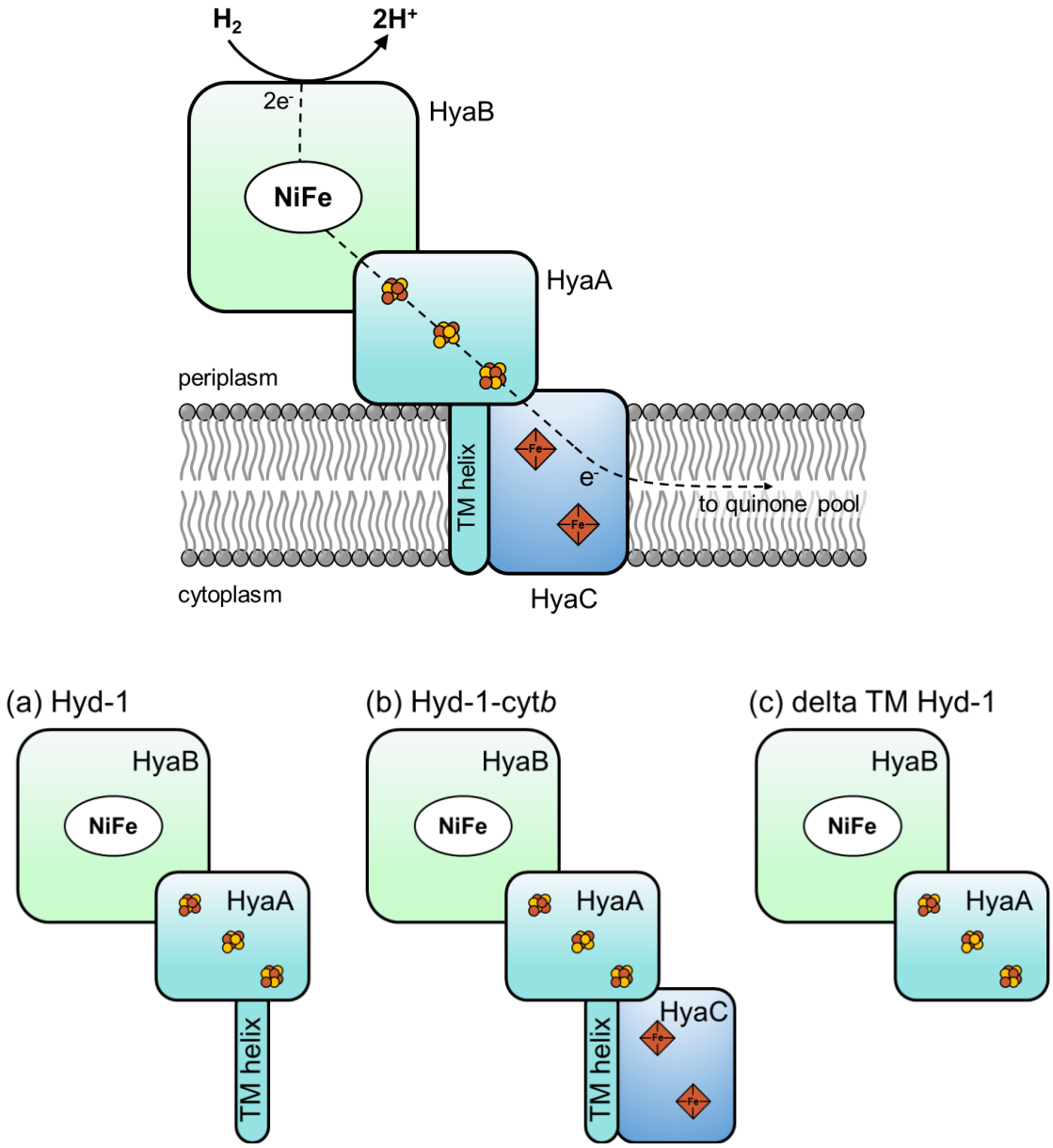


Figure 6.1 Cartoon representation of the subunit composition and cofactors of *E. coli* Hyd-1. Each subunit is labelled: HyaB – the large subunit which contains the [NiFe] active site; HyaA – the small subunit that contains the FeS cluster co-factors and a C-terminal transmembrane alpha helix region (TM helix); and HyaC – the cytochrome *b* redox partner. FeS clusters in HyaA are represented by the groups of circles and the two heme groups in the cytochrome *b* subunit are represented by diamonds. *In vivo*, there are two HyaAB units per cytochrome unit. The subunits present in each of the various preparations of Hyd-1 are also displayed.

The first crystal structure of *E. coli* hydrogenase-1 with its cytochrome *b* redox partner was reported in 2013 by Volbeda *et al.* revealing one cytochrome *b* subunit in its reduced form per Hyd-1 dimer.[2] The data also allowed resolution of the C-terminal transmembrane anchor of the small subunit, which were found to pack against opposite sides of the cytochrome *b*. Importantly, no differences were noted between the active sites of the as-isolated Hyd-1 with the cytochrome *b* and without, suggesting the inclusion of the cytochrome *b* may have little impact on the protein's spectroscopic characteristics. This has been directly shown with other O_2-tolerant [NiFe]-hydrogenases. The membrane bound hydrogenases (MBH) of *Ralstonia eutropha* H16 and *Aquifex aeolicus* have also been isolated with and without the cytochrome *b* electron transfer protein.[3–5] Potentiometric titrations on solutions of *A. aeolicus* Hase I with the cyt*b* were near identical to those obtained without the cyt*b*, suggesting the spectroscopic properties are independent of the presence of the cytochrome subunit.

This is an important detail to clarify for *E. coli* Hyd-1, as some IR spectroelectrochemical experiments, including those using PFIRE in Chapter 3, use samples containing a mixture of Hyd-1 with and without cyt*b*. So far, the *E. coli* Hyd-1 crystals studied using the IR microspectroscopic-electrochemical technique were grown from the *E. coli* K-12 FTH004 strain, which does not include the cytochrome *b* subunit. Therefore it is important to establish whether the cyt*b* has any influence on the active site of Hyd-1, particularly as the crystal structures suggest no difference.

Another crystal structure of as-isolated Hyd-1 has been published by Evans *et al.* using a different *E. coli* K-12 strain, namely FTH2014.[6] This strain, referred to as delta TM, produces enzyme which does not include the transmembrane domain within the small subunit (TM helix, Figure 6.1), nor the cytochrome subunit (HyaC, Figure 6.1) and is thus

not anchored to the membrane.[7] The crystal structure is shown to be very similar to the previously published structure of as-isolated Hyd-1 from the FTH004 strain, as reported by Volbeda *et al.*[1], suggesting the exclusion of the transmembrane domain does not interfere with the active site and surrounding canopy structure. Biochemical assays and electrochemical data also show that the catalytic properties of delta TM Hyd-1 are also not affected. However, no spectroscopic information has been published to confirm this. Delta TM Hyd-1 crystals grow to larger sizes than crystals grown from the FTH004 strain (Figure 2.21), and thus are ideal samples for studying in the IR microspectroscopic-electrochemical cell, particularly with a lab-based globar source which require larger apertures.

In Chapters 4-5, only crystals of Hyd-1 that are prepared without the cytochrome *b* subunit have been studied *via* the IR microspectroscopic-electrochemical technique. In this Chapter, similar spectroscopic characterisations of Hyd-1 crystals with the cytochrome *b* subunit (Hyd-1-cyt*b*), and without the small subunit transmembrane domain (delta TM Hyd-1), are performed to confirm the spectroscopic and electrochemical integrity of the *E. coli* Hyd-1 active site and surrounding amino acid coordination sphere. It is anticipated that these comparative data will be valuable for future studies performed on different preparations of the enzyme.

6.2. The impact of the cytochrome *b* subunit

During the purification procedure of WT Hyd-1, protein without the cytochrome *b* (cyt*b*) subunit is separated from that with the subunit using a hydroxyapatite column (Section 2.3). This is to ensure that the sample used for crystallisation is homogeneous. However, this does not reflect the enzyme *in vivo* as the cytochrome subunit is required to act as a redox partner to shuttle electrons from the distal FeS cluster across the membrane whilst

also anchoring the hydrogenase to the membrane. Therefore it is important to verify whether the addition of the cyt*b* subunit affects the spectroscopic and electrochemical behaviour of the [NiFe] active site. In this section, the IR microspectroscopic-electrochemical technique is used to characterise single crystals of Hyd-1 with the cyt*b* subunit (Hyd-1-cyt*b*). All data presented in this section were collected using the synchrotron IR source.

6.2.1. Initial characterisation

Figure 6.2 shows the IR spectrum of a single crystal of as-isolated Hyd-1-cyt*b* at pH 5.9, open circuit potential +288 mV *vs* SHE. There are three peaks in the ν_{CO} region at 1943, 1922 and 1911 cm^{-1} signifying the presence of at least three active site species. The most intense peak, 1943 cm^{-1}, can be assigned as the inactive Ni-B species, similar to that seen in Chapter 4. Four bands are observed in the ν_{CN} region: 2068, 2081, 2094, 2101 cm^{-1}. These, again, are consistent with ν_{CN} bands observed in the fully oxidised IR spectrum of the Hyd-1 crystals without the cyt*b* subunit present (Chapter 4, Figure 4.10). All but the 2068 cm^{-1} peak are assigned to the inactive Ni-B redox level, likely in two very slightly different substrates with overlapping ν_{CO} and partly overlapping ν_{CN}.

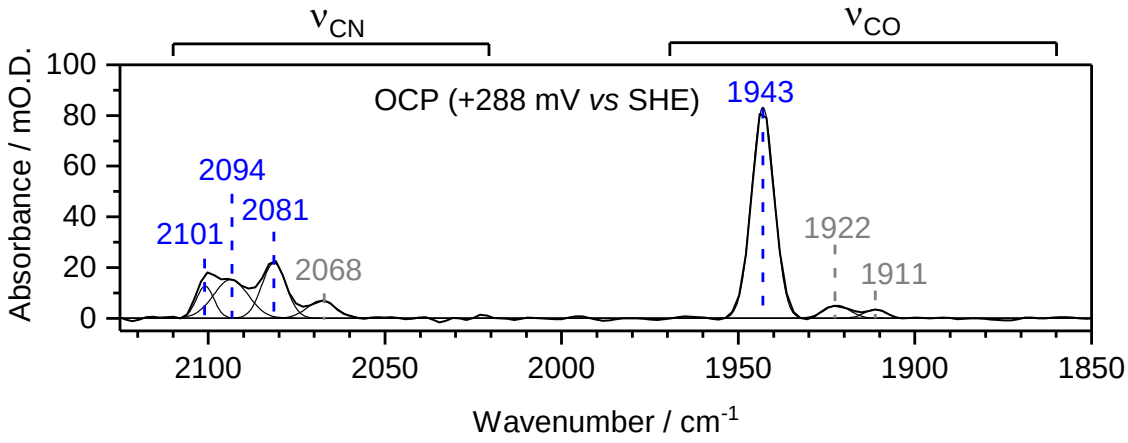


Figure 6.2 Baseline-corrected IR spectrum of a single crystal of as-isolated Hyd-1-cyt*b*, at pH 5.9, at open circuit potential, OCP, +288 mV vs SHE. Bands marked in blue represent the Ni-B level, whereas those in grey are unassigned. The fitted Gaussian peaks are shown by the thin black curves.

The additional features observed in the ν_{CO} region of Figure 6.2 are strikingly similar to the 1923 and 1910 cm^{-1} bands occasionally observed by Hidalgo in certain as-isolated samples of WT Hyd-1 when using the PFIRE method.[8] In those cases, activation of the sample with H_2 and application of a low potential resulted in a spectrum identical to the reduced IR spectrum of a Hyd-1 sample that did not initially include the extra features. Re-oxidation of the sample to high potentials, +356 mV, showed that the 1923 and 1910 cm^{-1} peaks did not return. Similar observations were made during IR spectroelectrochemical studies of *Allochromatium vinosum* MBH. An EPR-silent active site species (ν_{CO}: 1909 cm^{-1}, ν_{CN}: 2066, 2057 cm^{-1}) was detected in as-isolated preparations, and upon activation under H_2, did not reappear.[9]

As shown by Figure 6.3, reduction and re-oxidation of as-isolated Hyd-1-cyt*b* crystals also results in the disappearance of the additional ν_{CO} bands. Application of -592 mV *vs* SHE results in complete reduction of the crystal sample, with IR bands associated with the three Ni_a-R sub-species (ν_{CO}: 1942 cm^{-1} (Ni_a-R_I), 1922 cm^{-1} (Ni_a-R_{II}), 1915 cm^{-1} (Ni_a-R_{III}); ν_{CN}: 2068, 2050 cm^{-1} (Ni_a-R_{III}), 2058 cm^{-1} (Ni_a-R_{II})) along with the initial Ni_a-C species (ν_{CO}:

1949 cm^{-1}), being detected (Figure 6.3B). Subsequent oxidation results in a spectrum similar to that shown in Figure 4.10, with only the Ni-B species and the high-potential 1938 cm^{-1} species present (Figure 6.3C).

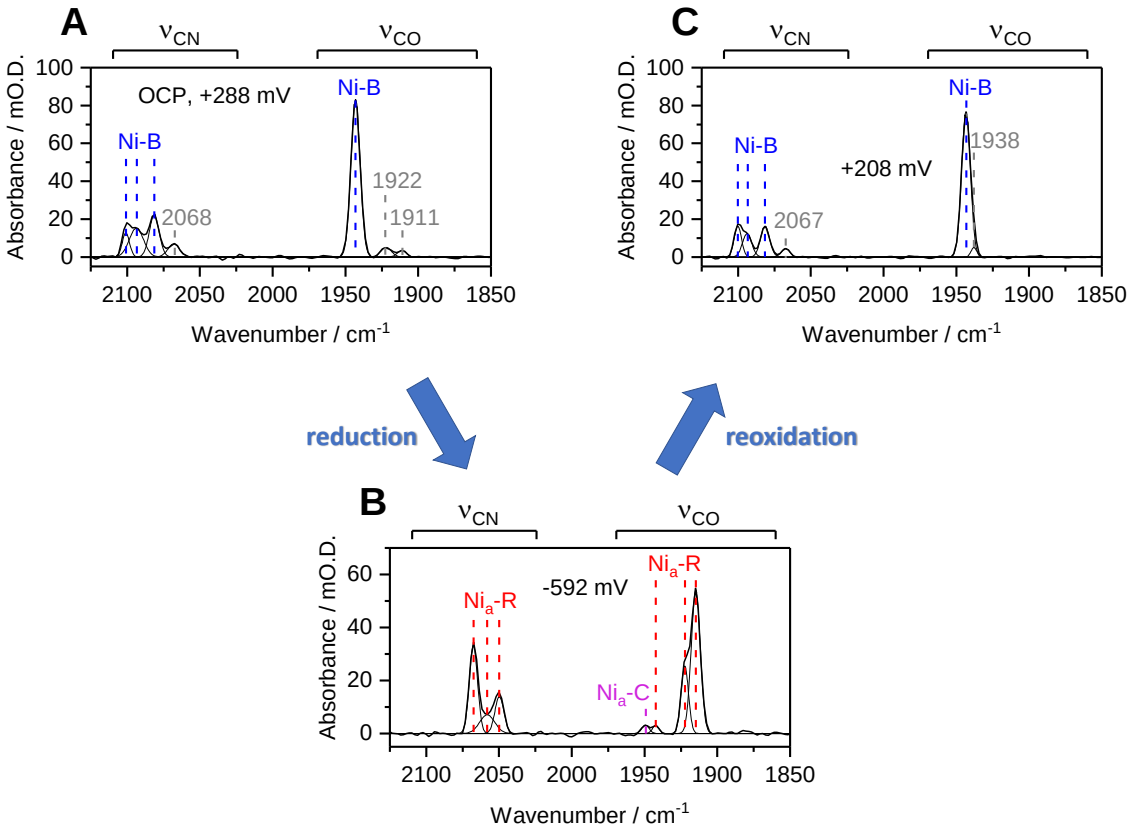


Figure 6.3 Electrochemical reduction and subsequent oxidation of single crystals of *Hyd-1-cyt*b results in the removal of the additional ν_{CO} features (1922, 1911 cm^{-1}) observed in as-isolated samples. A: As-isolated IR spectrum, OCP +288 mV *vs* SHE. B: Reduction to -592 mV *vs* SHE shows the appearance of Ni_a-R and Ni_a-C bands. C: Re-oxidation to +208 mV *vs* SHE leads to the return of Ni-B, with the additional features at 1922 cm^{-1} and 1911 cm^{-1} not reappearing.

6.2.2. Oxidative titration

A full and detailed electrochemical oxidative titration was performed on single crystals of Hyd-1-cyt*b* at pH 5.9 to directly compare to crystals of Hyd-1 without the cyt*b* subunit (Section 4.3.2). The resulting baseline-subtracted IR spectra are displayed in Figure 6.4.

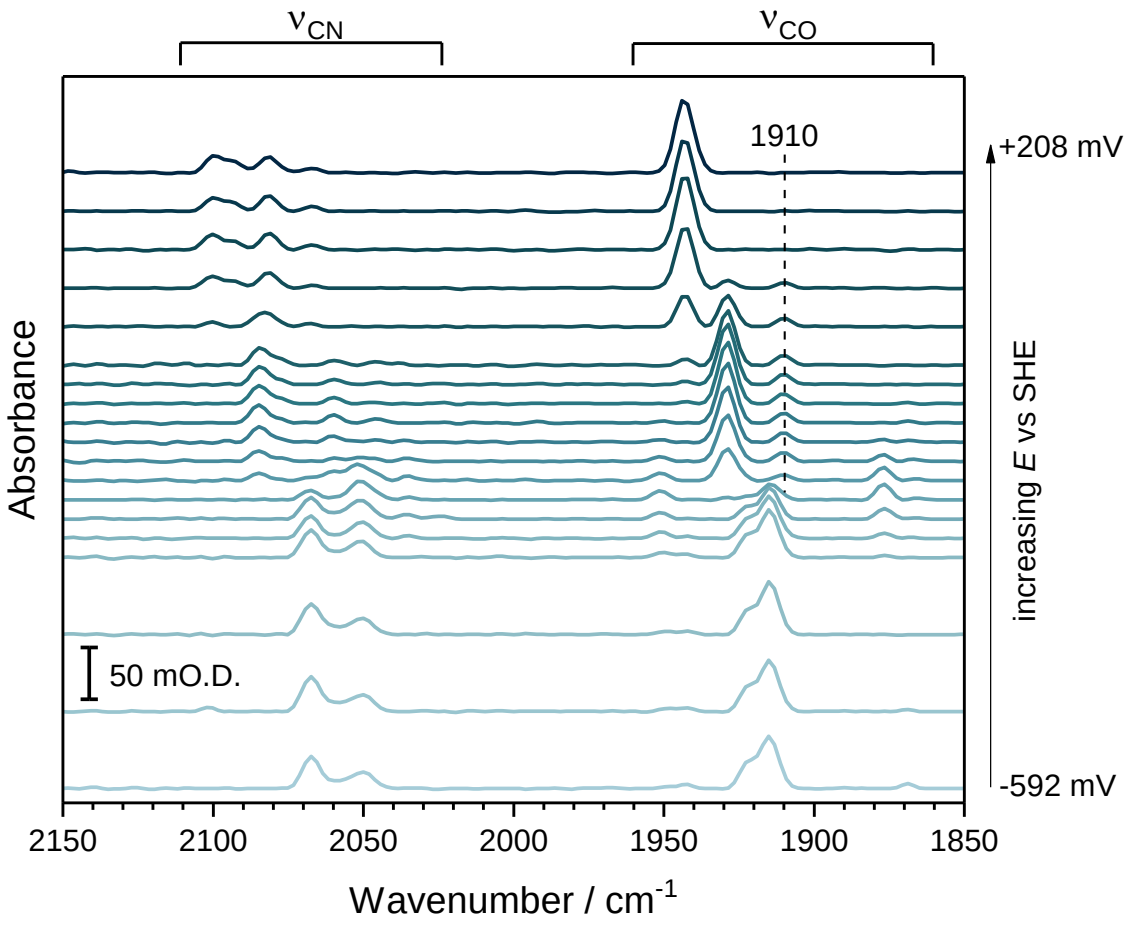


Figure 6.4 Baseline-corrected IR spectra of a single crystal of Hyd-1-cyt*b*, pH 5.9, following an electrochemical oxidative titration from -592 to +208 mV *vs* SHE. The regions corresponding to ν_{CO} and ν_{CN} bands are labelled. An additional ν_{CO} band at 1910 cm^{-1} not present in the redox titrations of Hyd-1 without cyt*b*, as shown in Figure 4.11, is indicated by the dashed black line.

Overall, the IR spectra collected are similar to Figure 4.11, with each active site redox species detected in the Hyd-1 crystals without cyt*b* (Table 4.3) also observed for the Hyd-1-cyt*b* data. Importantly, the positions of the ν_{CO} and ν_{CN} bands for each species do not change with addition of the cyt*b* subunit, suggesting the subunit has no influence on the structure of the [NiFe] active site across each redox state. This is further supported by a comparison of the redox speciation curves of the Hyd-1 and Hyd-1-cyt*b* crystals (Figure 6.5) The behaviour with potential of each active site species is consistent between the two samples.

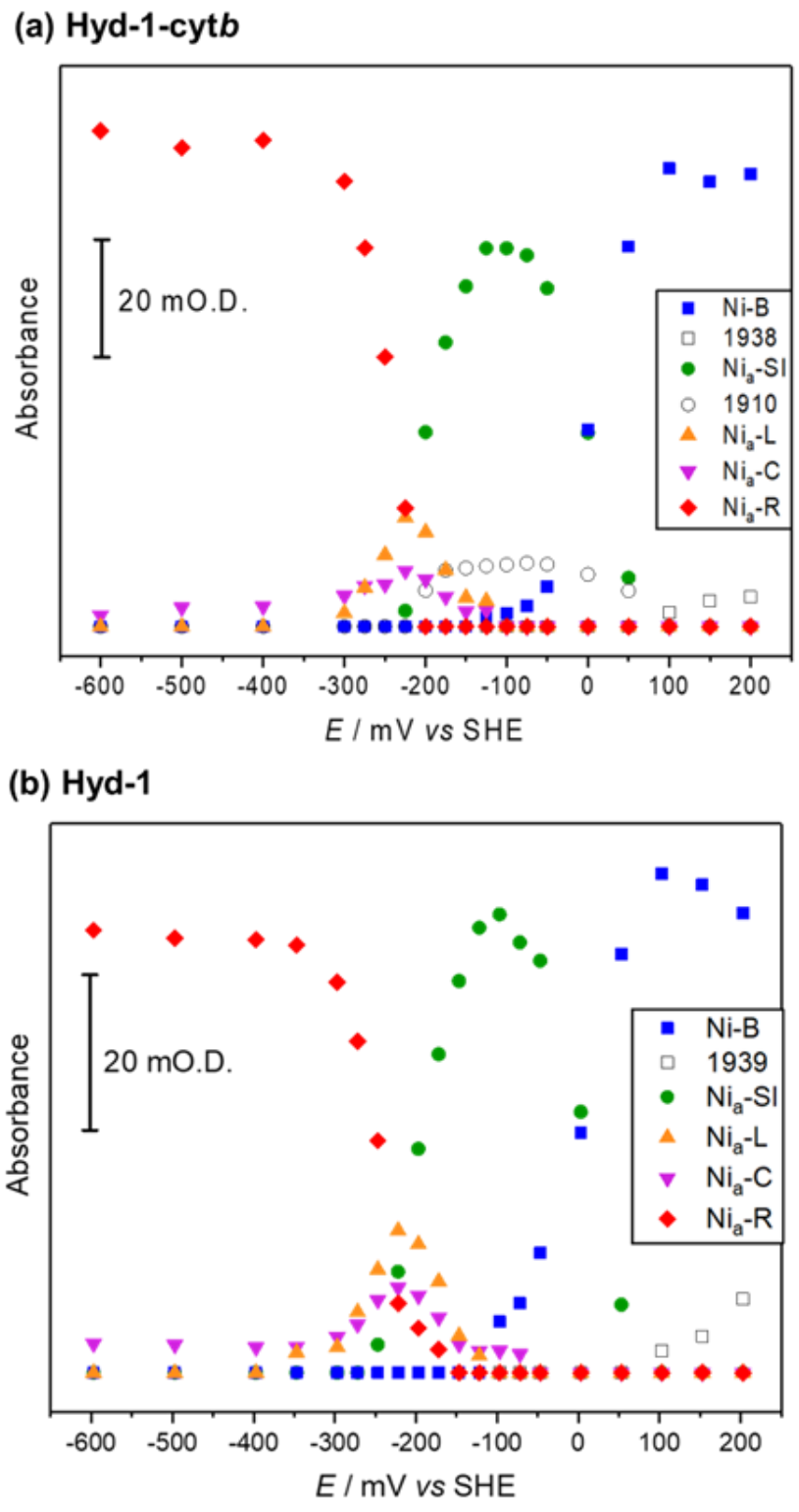


Figure 6.5 Potentiometric redox speciation curves from an oxidative titration of single crystals of Hyd-1-cyt*b* (A) and Hyd-1 (B) at pH 5.9 measured using the IR microspectroscopic-electrochemical cell. Active site species are labelled in accordance with the colours assigned throughout this Thesis. The unassigned 1910 cm^{-1} peak is included and marked by empty black circles.

There is one noticeable difference in the Hyd-1-cyt*b* spectra: an additional band at 1910 cm^{-1} between -192 and +58 mV. This peak is clearly shown in the IR spectrum measured at -117 mV *vs* SHE, i.e. when the Ni_a-SI species at 1929 cm^{-1} is maximised (Figure 6.6). Peak fitting suggests that this species accounts for 13% ± 1.5% of the sample.

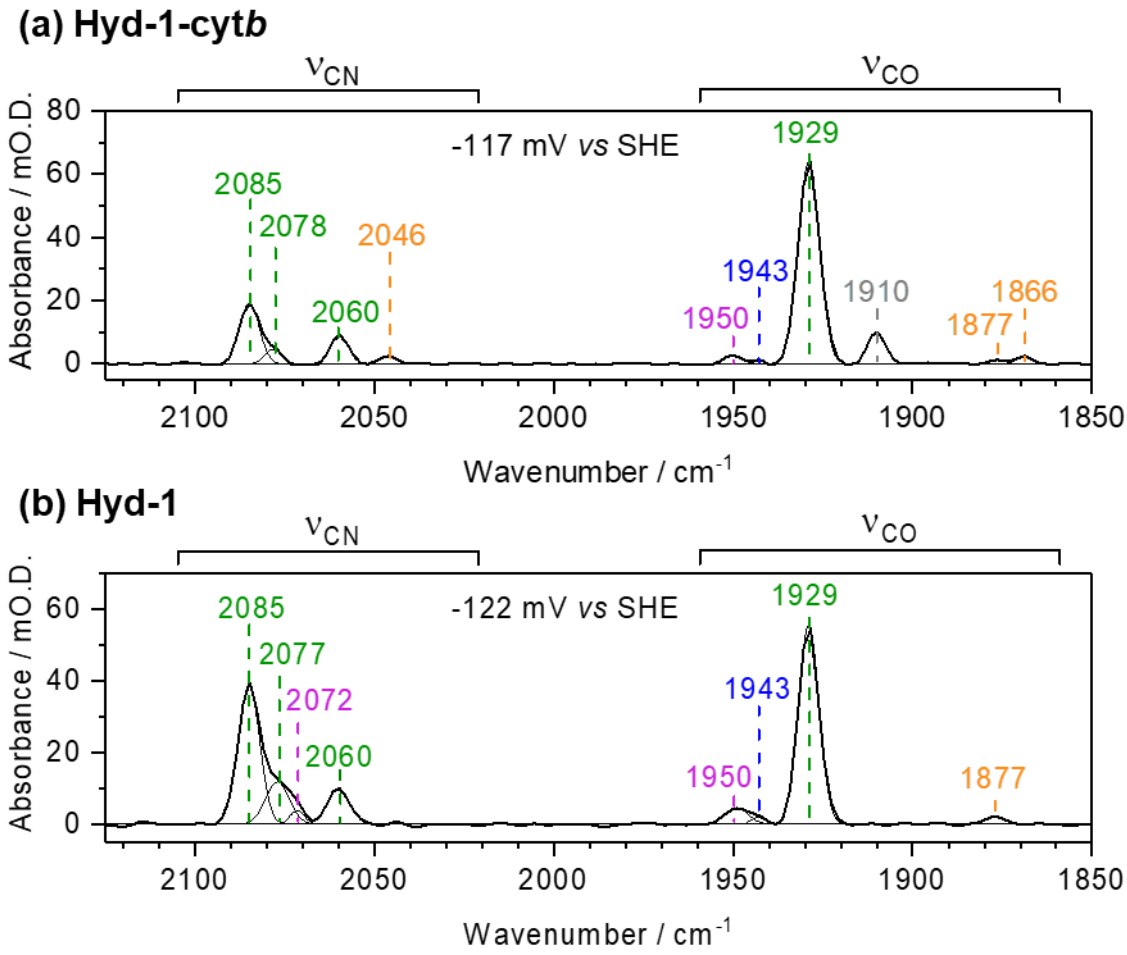


Figure 6.6 (A) IR spectrum of a single crystal of Hyd-1-cyt*b* at pH 5.9, at -117 mV *vs* SHE. Bands marked in purple, blue, green and yellow represent the Ni_a-C, Ni-B, Ni_a-SI and Ni_a-L species respectively. The grey band at 1910 cm^{-1} is unassigned. Fitted Gaussian peaks are shown in black. (B) The equivalent IR spectrum of a single crystal of Hyd-1 without the cytochrome *b* sub-unit at pH 5.9. There is no band detected at 1910 cm^{-1}.

Six ν_{CO} bands are observed in the spectrum: 1950 cm^{-1} (Ni_a-C), 1943 cm^{-1} (Ni-B), 1929 cm^{-1} (Ni_a-SI), 1910 cm^{-1} (unassigned), 1877 cm^{-1} (Ni_a-L_{II}) and 1866 cm^{-1} (Ni_a-L_{III}). Similar to the

Hyd-1 without cyt*b* IR spectrum (Figure 4.16), the Ni-B species is present at -117 mV showing oxidation to the inactive state, alongside minor contributions from the Ni_a-C and Ni_a-L species. The three ν_{CN} bands at 2085 and 2078 cm^{-1} were previously assigned to ν_{CN} of the Ni_a-SI species, with the additional ν_{CN} at 2060 cm^{-1} posited to represent a secondary active site species at the Ni_a-SI redox level. The new ν_{CO} band at 1910 cm^{-1} may be the ν_{CO} of this secondary species.

Of particular interest is the potential dependence of the new 1910 cm^{-1} species compared to the Ni_a-SI species, which is shown in Figure 6.7. The 1910 cm^{-1} band is first detected at -192 mV and sharply increases in absorbance to a slight plateau before decreasing in intensity alongside the 1929 cm^{-1} band, finally disappearing at +108 mV.

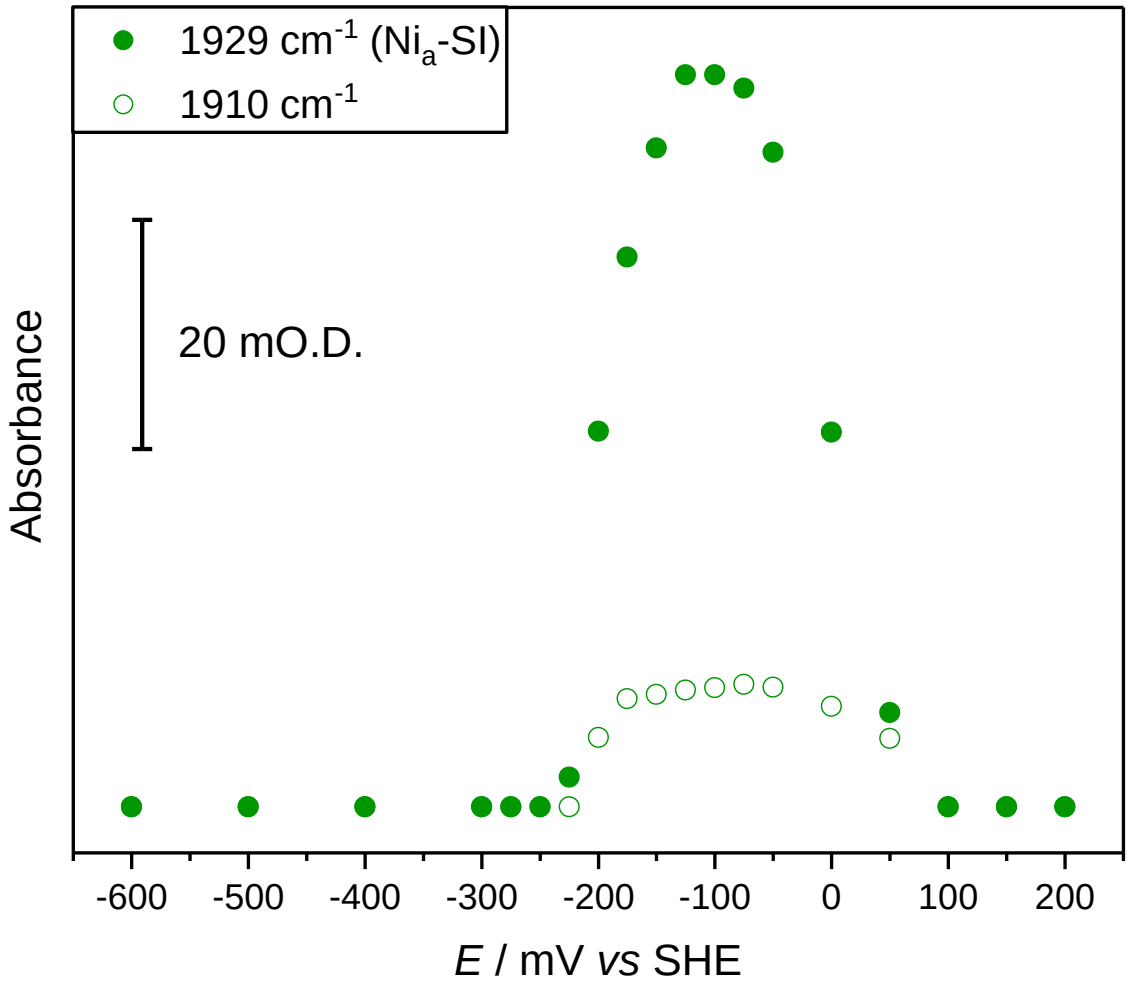


Figure 6.7 Potentiometric speciation curves for the Ni_a-SI species (ν_{CO} = 1929 cm^{-1}, solid green circles) and the 1910 cm^{-1} species (empty green circles).

The potential behaviour of the 1910 cm^{-1} species closely correlates with the Ni_a-SI species. This suggests that the two states are at the same redox level, i.e. the net number of electrons in the active site is the same in both species.

6.2.3. Discussion

Whilst the overall spectroelectrochemical behaviour of the Hyd-1-cyt*b* crystals shows little deviation to Hyd-1 without the cyt*b* subunit, there are a couple of key new features observed.

In the IR spectrum of as-isolated Hyd-1-cyt*b*, two additional low wavenumber bands at 1911 and 1922 cm^{-1} were observed which did not reappear upon reduction and re-oxidation of the crystal sample. Hidalgo hypothesised that the 1910 cm^{-1} ν_{CO} peak (ν_{CN} = 2069, 2060 cm^{-1}) detected in the as-isolated PFIRE spectra of Hyd-1 belonged to an inactive Ni(II) species named Ni-'S_{ox}', which has a persulfide group in one of the terminal cysteines and a vacant bridging position (Figure 6.8).[8] This was based on a comparison to similarly behaving species observed in the [NiFe]-hydrogenases of the sulfur-metabolising bacteria *A. vinosum* and *Desulfovibrio* fructosovorans.[9,10] Observation of a comparable IR band (ν_{CO} = 1911 cm^{-1}) in the as-isolated IR spectrum of Hyd-1-cyt*b* suggests that the Ni-'S_{ox}' species may also present in the crystalline state.

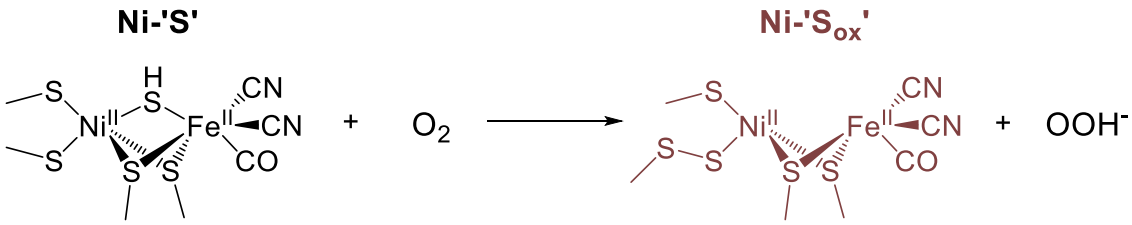


Figure 6.8 Aerobic oxidation of an inactive species Ni-'S', which contains a bridging SH ligand, forms the Ni-'S_{ox}' species, as proposed by Volbeda *et al.*[10]

The other additional band in the spectrum of as-isolated Hyd-1-cyt*b* is at 1922 cm^{-1}. The wavenumber of this band, and the fact it also does not reappear upon reduction and subsequent oxidation, suggests it may also be due to a sulfur containing Ni(II) species such as Ni-'S' (Figure 6.8). However there is no direct evidence to support this theory. A similar wavenumber band at 1924 cm^{-1} was present in the re-oxidised PFIRE spectrum of Hyd-1 (Figure 3.5B, +358 mV). The preparation of Hyd-1 for the PFIRE experiments contained a mixture of Hyd-1 with and without cytochrome *b*, so it is unclear whether the cyt*b* subunit is related to the appearance of the 1924 cm^{-1} band.

Another new feature in the Hyd-1-cyt*b* IR spectroelectrochemical data is the additional ν_{CO} peak at 1910 cm^{-1} observed between -192 mV and +58 mV in the electrochemical oxidative titration (Figure 6.6). Due to the potential correlation between this 1910 cm^{-1} band and the 1929 cm^{-1} Ni_a-SI species (Figure 6.7), it is likely they represent two species at the same redox level, i.e. the 1910 cm^{-1} band is a 'Ni-SI' like species. At first glance, the similarity in wavenumber suggests the 1910 cm^{-1} band detected at mid-range potentials and the 1911 cm^{-1} band observed in the as-isolated spectra (Figure 6.2) may be the same redox species. However comparable features have been observed in other [NiFe]-hydrogenases where two different active site species were distinguished. An IR spectroelectrochemical study of *A. vinosum* MBH also showed the presence of two different active site species whose ν_{CO} bands are close in wavenumber: an inactive species at 1909 cm^{-1} (ν_{CN} 2057, 2066 cm^{-1}) and an inactive Ni-SI species, named Ni-SI_r, at 1910 cm^{-1} (ν_{CN} 2052, 2067 cm^{-1}).[9] From the data shown above, it seems that this is also the case for Hyd-1-cyt*b*.

The Ni-SI_r species has been detected in a number of [NiFe]-hydrogenases,[9,11–15] and is posited to represent an inactive, 'ready' intermediate (i.e. quickly activated in the presence of reducing conditions, as denoted by the 'r' subscript) between the inactive, ready Ni-B and active Ni_a-SI species. A one electron reduction of Ni-B leads to the Ni-SI_r species, as shown in Figure 6.9. Subsequent protonation of the NiFe active site leads to the Ni_a-SI species, which exists at an acid-base equilibrium with Ni-SI_r. The exact mechanism by which this occurs is currently debated. Some suggest the Ni-SI_r retains the hydroxido bridging ligand from Ni-B is in an acid-base equilibrium with a protonated version where there is a loosely bound H_2O bridging ligand.[9,16,17] A second mechanism predicts that a proton is transferred to the active site either directly or *via* protonation of a Ni-coordinated cysteine to form a H_2O bridging ligand in Ni-SI_r.[18] It is, however, widely

agreed that an oxygenic ligand is bound to the active site of Ni-SI$_r$ which prevents it from being active.

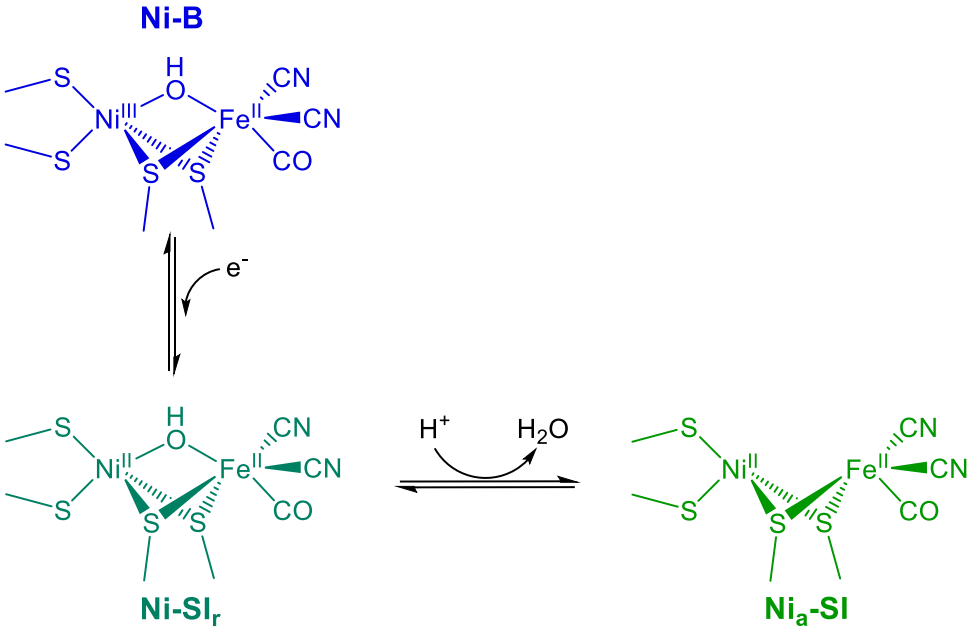


Figure 6.9 One electron reduction of the Ni-B state gives the intermediate Ni-SI$_r$ species which exists in an acid-base equilibrium with the active Ni$_a$-SI species.

The Ni-SI$_r$ species has been observed alongside Ni$_a$-SI in IR spectra at potentials where the Ni$_a$-SI species dominates.[11,12] A similar observation in the Hyd-1-cyt*b* spectra (Figure 6.6 and Figure 6.7) supports the hypothesis that the 1910 cm^{-1} species is indeed due to Ni-SI$_r$.

In Section 4.3.2.2 it was hypothesised that the additional ν_{CN} band at 2060 cm^{-1} seen for Hyd-1 (without cyt*b*) was indicative of an active site species at the same redox level as Ni$_a$-SI, whose ν_{CO} peak was hidden by the large 1929 cm^{-1} band. A 2060 cm^{-1} ν_{CN} band is also observed here with good correlation with the potential dependence of the 1910 cm^{-1} ν_{CO} (Figure 6.10). Therefore the 2060 cm^{-1} ν_{CN} band is likely from the Ni-SI$_r$ species.

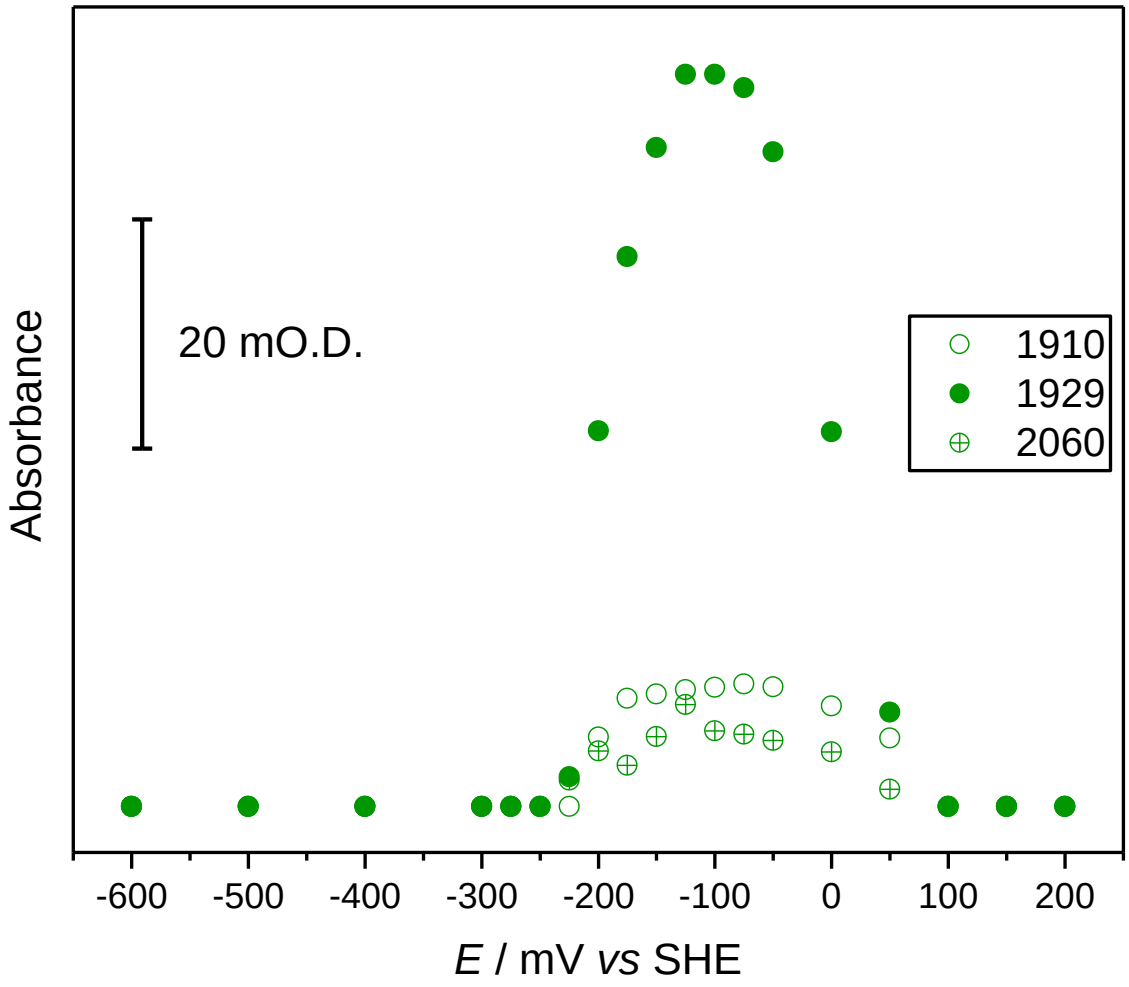


Figure 6.10 Potentiometric speciation curves for the Ni_a-SI species (ν_{CO} = 1929 cm^{-1}, solid green circles) and the Ni-SI_r species (ν_{CO} = 1910 cm^{-1}, empty green circles, ν_{CN} = 2060, crossed green circles).

As the Ni-SI_r and Ni_a-SI species exist in an acid-base equilibrium (Figure 6.9), their relative concentrations should change with pH, much like the acid-base equilibrium between the Ni_a-C and Ni_a-L species. Therefore, repeating the single crystal redox titrations at different pH values and observing whether this is the case is necessary to further support the assignment of the 1910 cm^{-1} band.

From the data presented in this Chapter on single crystals of Hyd-1-cyt*b*, it appears that the addition of the cytochrome *b* subunit in the Hyd-1 crystals stabilises the Ni-SI_r species, allowing it to be detected in higher concentrations. *In vivo*, cyt*b* acts as an electron transfer protein, shuttling electrons across the membrane from the quinone pool to the

distal FeS cluster on the surface of the Hyd-1 protein (Figure 6.1). In the crystal, a similar effect may be occurring. The IR microspectroscopic-electrochemical method utilises redox mediators to ensure fast electron exchange between the electrode and the protein crystals. Including an additional redox protein that is directly connected to the distal FeS cluster may be improving electron transfer between the working electrode and the active site.

Importantly though, these single crystal redox titrations have shown that the Hyd-1 and Hyd-1-cyt*b* crystals do not behave exactly the same spectroscopically with potential, despite their similar crystal structures. As the spectroscopic differences between the two forms of Hyd-1 only occur when the active site is at a specific redox level, namely the Ni-SI redox level, differences may also be present structurally. So far, only crystal structures showing oxidised and chemically reduced Hyd-1 and Hyd-1-cyt*b* have been reported. For Hyd-1-cyt*b* it may prove possible to trap a crystal enriched in Ni-SI_r.

6.3. Delta transmembrane Hyd-1

Delta TM Hyd-1 has been used as a 'native' comparison to variants of Hyd-1 due to its similar crystal structure and electrochemical behaviour to wild type Hyd-1.[6] A major benefit of studying crystals grown from delta TM Hyd-1 is that they are over 6 times larger than those grown from the FTH004 strain (Figure 2.21). Larger crystals means that a larger sampling aperture can be used to measure IR spectra using the IR microscope. This overcomes one of the limitations of using a globar IR source as the increased aperture size results in IR spectra with an improved signal-to-noise ratio. The delta TM Hyd-1 IR spectra presented in this section were collected using the in-house IR microscope using the globar IR source, with an aperture size of 250×150 µm.

6.3.1. Initial characterisation

Figure 6.11 shows the IR spectrum of a single crystal of as-isolated delta TM Hyd-1 measured at pH 5.9, open circuit potential +192 mV *vs* SHE. As with other preparations of as-isolated Hyd-1, the ν_{CO} and ν_{CN} peaks which correspond to the Ni-B level are present at 1943 cm^{-1} and 2099, 2091, 2082 cm^{-1} respectively, alongside the high potential 1939 cm^{-1} species and the unassigned ν_{CN} band at 2066 cm^{-1}. There are also several other ν_{CO} bands observed in Figure 6.11, suggesting a mixture of inactive redox species. Bands at 1921 and 1910 cm^{-1} are similar to those observed in the as-isolated Hyd-1-cyt*b* IR spectrum (Figure *6.2*) and are expected to also disappear upon electrochemical reduction and not reappear following subsequent reoxidation.

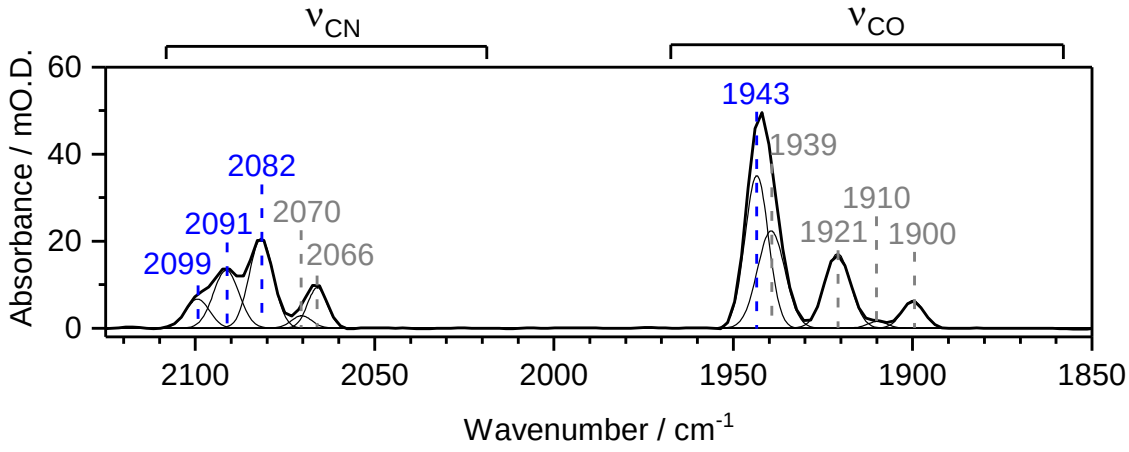


Figure 6.11 Baseline-corrected IR spectrum of a single crystal of as-isolated delta TM Hyd-1, at pH 5.9, at open circuit potential, OCP, +192 mV vs SHE. Bands marked in blue represent the Ni-B level, whereas those in grey are unassigned. The fitted Gaussian peaks are shown by the thin black curves.

Reduction of the delta TM Hyd-1 crystals by application of a low potential, -592 mV, for 6 hours results in the IR spectrum given in Figure *6.12*. A longer reduction period was used as activation of the crystal sample was slow, as observed through the decrease of the Ni-B ν_{CO} band at 1943 cm^{-1}. When there was no visible change in the 1943 cm^{-1} band, the low

potential was held for a further hour to attempt to fully reduce the sample, after which there was still no change.

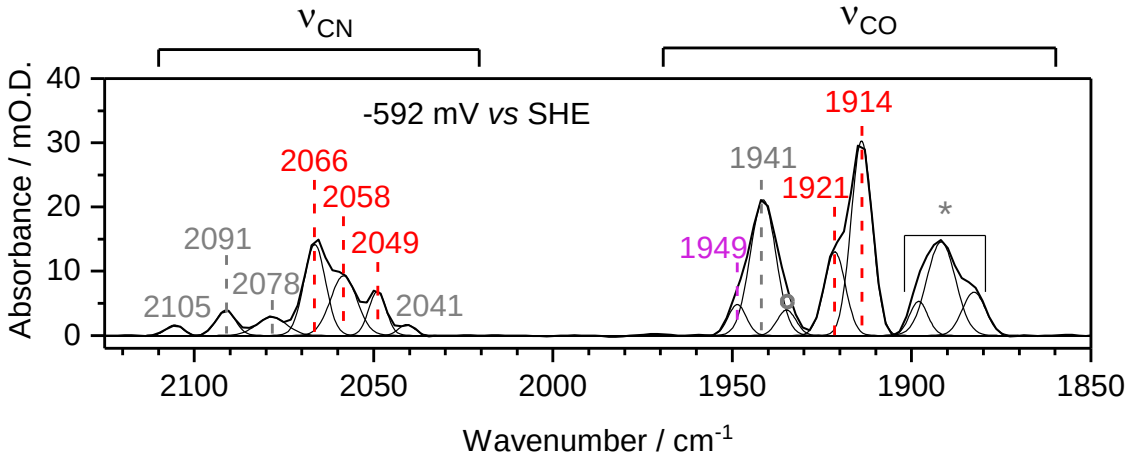


Figure 6.12 Baseline-corrected IR spectrum of a single crystal of delta TM Hyd-1, at pH 5.9, at -592 mV vs SHE. Bands marked in red and purple represent the Ni-R and Ni-C species respectively. The red circle marks the position of the Ni_a-R_I band at 1934 cm^{-1}. Bands in grey are unassigned. The peaks marked by the asterisk are at 1900, 1892 and 1883 cm^{-1}. The fitted Gaussian peaks are shown by the thin black curves.

Bands which correspond to the most reduced active site species, Ni_a-R, are now visible in the IR spectrum (Ni_a-R_{III} ν_{CO} = 1914 cm^{-1}, ν_{CN} = 2066, 2049 cm^{-1}; Ni_a-R_{II} ν_{CO} = 1922 cm^{-1}, ν_{CN} = 2058 cm^{-1}; Ni_a-R_I ν_{CO} = 1934 cm^{-1}), along with a small proportion of a Ni_a-C species at 1949 cm^{-1}. However, there are also several other bands present in both the ν_{CO} and ν_{CN} regions of the spectrum. Most noticeable is the peak at 1941 cm^{-1}. It is difficult to ascertain whether the 1939 cm^{-1} band in Figure *6.11* and the 1941 cm^{-1} band in Figure *6.12* are the same species. On the one hand, the similarity in wavenumber and absorbance (~20 mO.D.) and the fact that a much longer electrochemical reduction was required suggest that they are due to the same redox species, likely the slowly activating Ni-A. On the other hand, there is evidence of two different redox species having remarkably similar

wavenumber IR bands, [9] most noticeably the inactive 1911 cm^{-1} and Ni-SI_r species observed in the IR spectra of Hyd-1-cyt*b* crystals (*vide supra*).

Regarding other changes in the IR spectrum upon reduction, the low wavenumber species at 1900 cm^{-1} is still present at low potential, along with two new peaks at 1892 and 1883 cm^{-1}. In the PFIRE spectra of Hyd-1 adsorbed onto carbon particles there were a group of low absorbance bands between 1900 – 1880 cm^{-1}, whose intensities and positions varied unpredictably across the measurements. As such, they were suggested to not be due to any active site redox species, and more likely caused by impurities on the carbon particle surface. Here, however, peak fitting predicts that the three low wavenumber species in Figure *6.12* account for nearly 30 % of the sample. This, along with the apparent potential dependency of the 1892 and 1883 cm^{-1} peaks (*vide infra*) suggests that they represent previously unknown active site redox species.

Subsequent reoxidation of the delta TM Hyd-1 crystals, by applying a potential of +208 mV *vs* SHE, results in Figure 6.13. In other preparations of Hyd-1, only the IR bands corresponding to the Ni-B level were present at high potential following reduction (Figure 6.3). However, this is clearly not the case with delta TM Hyd-1. IR bands at 1921, 1913 and 1910 cm^{-1} are once again observed alongside the Ni-B bands. As the band at 1900 cm^{-1} is still present after electrochemical reduction and reoxidation, and has not changed in absorbance nor position, it may be representative of damaged active site. The other two unidentified peaks at 1921 and 1910 cm^{-1}, on the other hand, may not have been present at low potentials, but this is difficult to tell due to the large Ni_a-R ν_{CO} bands at 1922 and 1914 cm^{-1}. A more detailed electrochemical redox titration is required to see whether the 1921 and 1913 cm^{-1} species are responsive to potential.

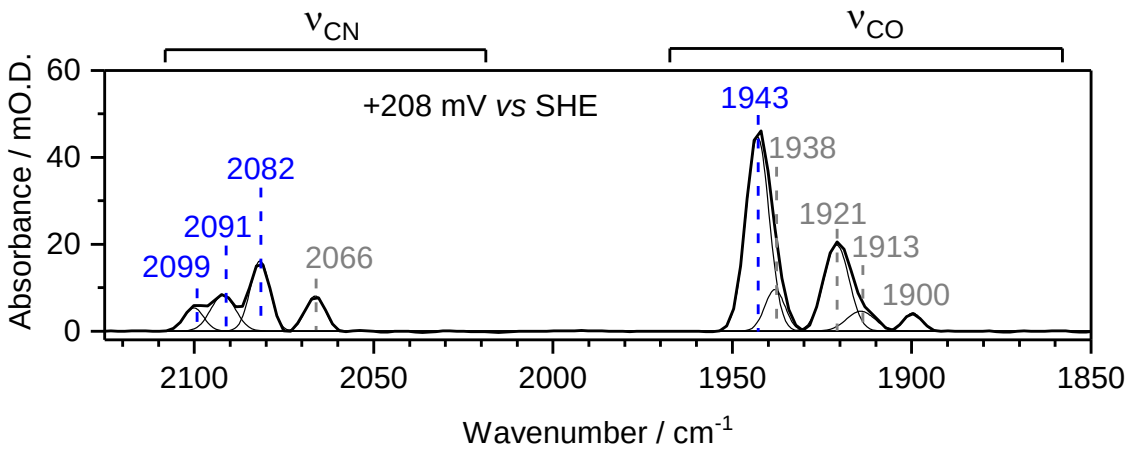


Figure 6.13 Baseline-corrected IR spectrum of a single crystal of re-oxidised delta TM Hyd-1, at pH 5.9, at +208 mV vs SHE. Bands marked in blue represent the Ni-B level, whereas those in grey are unassigned. The fitted Gaussian peaks are shown by the thin black curves.

6.3.2. Electrochemical oxidation

A full electrochemical oxidative titration was performed on single crystals of delta TM Hyd-1 at pH 5.9 to ascertain whether the newly observed IR bands were dependent on potential. The resulting baseline-subtracted IR spectra are displayed in Figure 6.14.

The general redox behaviour of the delta TM Hyd-1 crystals is similar to that of full length Hyd-1 (Figure 4.11) and Hyd-1-cyt*b* (Figure 6.4): IR bands corresponding to the Ni_a-R appear at low potentials, Ni_a-SI (ν_{CO} = 1928 cm^{-1}) at mid-potentials and the inactive Ni-B at high potentials. However, there are also several other ν_{CO} and ν_{CN} bands across the potential range which have not been assigned to a particular active site redox species before.

With so many overlapping IR bands close in wavenumber present in the IR spectra, fitting to Gaussian peaks is challenging. Nevertheless, it is clear that some of the newly observed bands are dependent on potential. For example, the low wavenumber peaks at 1892 and 1883 cm^{-1} only appear upon reduction to -592 mV, and increasing the potential causes

these peak to decrease in absorbance until they are no longer detected at -67 mV. Likewise, Figure 6.14 shows that the new band at 1921 cm^{-1}, observed initially in the as-isolated and high potential IR spectra, is only detected between -67 and +208 mV.

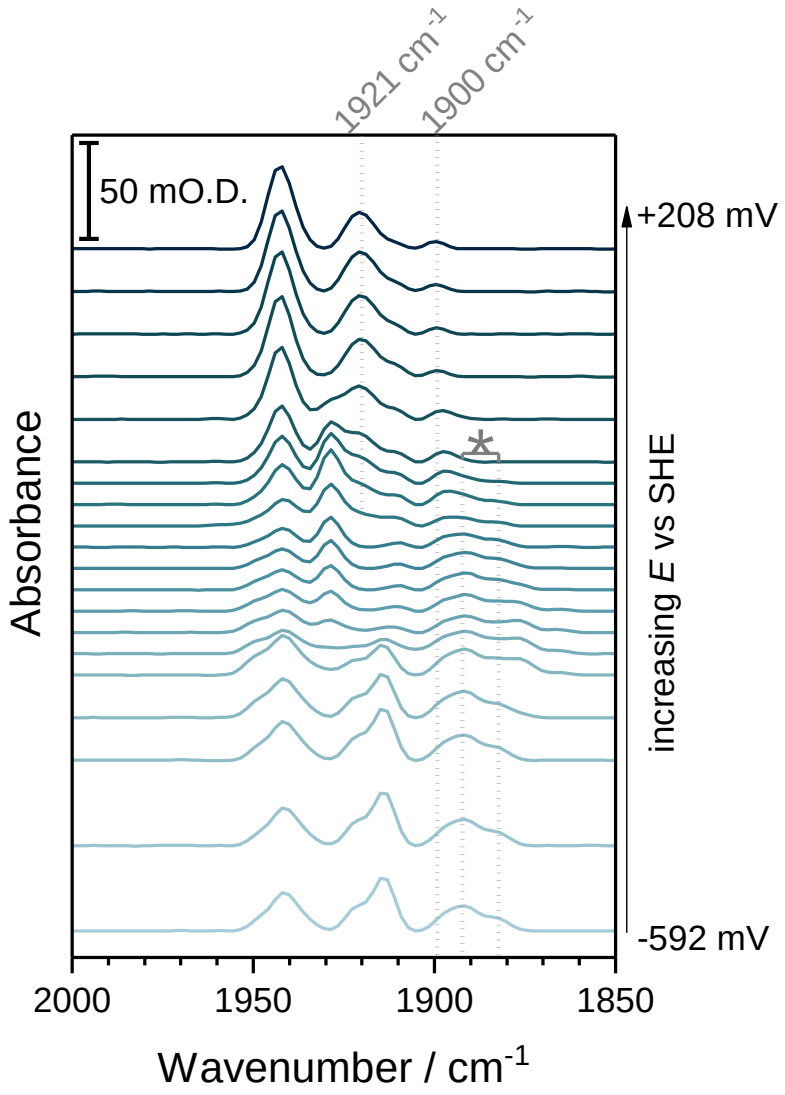


Figure 6.14 Baseline-corrected IR spectra of a single crystal of delta TM Hyd-1, pH 5.9, following an electrochemical oxidative titration from -592 to +208 mV vs SHE. Only the ν_{CO} region is displayed. The grey asterisk marks the position of the 1892 and 1883 cm^{-1} peaks.

6.3.3. Discussion

The general redox behaviour of Hyd-1 is mirrored in the IR spectroelectrochemical titration of delta TM Hyd-1, i.e., the known active site redox species appear at similar

wavenumber positions and at the expected potentials. However, there are also a number of new ν_{CO} and ν_{CN} bands that are present across the potential range. Of note, the 1941 cm^{-1} band at low potential, which overlaps with the Ni_a-C species, is similar to that of Ni-B (ν_{CO} = 1943 cm^{-1}), initially suggesting that the delta TM crystals are still partially inactivated.

Evans *et al.* found that in the crystal structure of as-isolated delta TM Hyd-1, approximately 75% of molecules contained oxygenation of the C79 sulfur (Figure 6.15).[6] This was attributed to the preparation and crystallisation of the samples under aerobic conditions, and the extended length of time between the end of crystal growth and freezing the crystals. A similar oxidative crystal structure of the [NiFe]-hydrogenase from *Desulfovibrio fructosovorans* was described by Volbeda and assigned to the 'unready', inactive Ni-A active site species.[10]

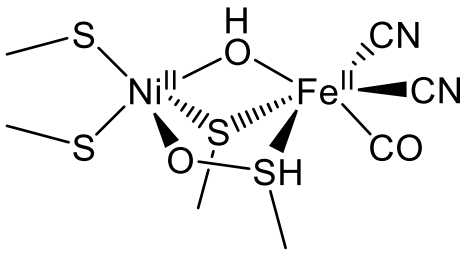


Figure 6.15 Oxidation of C79 to sulfenic acid was observed at the active site of as-isolated delta TM Hyd-1.

The delta TM crystals used in this Thesis were obtained by the same procedure used by Evans *et al.* and were stored frozen prior to thawing for measurement in the IR microspectroscopic-electrochemical cell. Therefore, it is possible that a proportion of the active site was also oxygenated at the C79 sulfur or oxygen-damaged in some way. Usually, reduction of the active site leads to reactivation of any unready states, including Ni-A, although this process is slow. If reduction of the delta TM Hyd-1 crystals was not

complete, then the additional IR bands observed may be a result of oxygen-damaged active site species reacting to the potential changes. Overall the redox behaviour of delta TM Hyd-1 is more complicated than expected, and further study is required to understand.

6.4. Summary

It has been widely assumed that all different preparations of Hyd-1 have the same spectroscopic and electrochemical behaviour. This is because according to the crystal structures, the active site and surrounding amino acid residues are the same, no matter whether the cytochrome *b* subunit or the small subunit transmembrane α-helices are incorporated. However, investigating the spectroscopic properties using the IR microspectroscopic-electrochemical technique has shown that there are minor but significant differences between the various preparations of Hyd-1.

Whilst the majority of the redox behaviour remains the same, addition of the cyt*b* subunit results in the inclusion of an extra active site species at the same redox level as the Ni_a-SI state, dubbed Ni_a-SI_r (ν_{CO} = 1910 cm^{-1}). This species has been detected in other [NiFe]-hydrogenases, but not in Hyd-1 until now. The Ni-SI_r species is suggested to be an intermediate in the activation of the inactive Ni-B state to the 'ready' Ni_a-SI species (Figure 6.9), and so being able to access it within the crystal hints at the possibility of monitoring this transition in finer detail.

Studies on the delta TM Hyd-1 single crystals have shown that there are many more active site species present at all potentials compared to full length Hyd-1, some of which may be due to oxygenation of the active site. Interestingly, most of the 'new' ν_{CO} appear to be potential dependent, and thus may be due to previously unobserved redox species.

However, the overlapping of IR bands means it is difficult to accurately track the absorbances of each peak with potential.

Overall, data presented in this Chapter show the necessity of having a second method to confirm the active site redox state of the protein crystals, as relying solely on x-ray diffraction to provide the crystal structure, and thus assignment of the redox states present, is flawed.

In the next Chapter, the IR microspectroscopic-electrochemical technique is used on a different [NiFe]-hydrogenase from *E. coli*, the O_2-sensitive Hydrogenase-2, to demonstrate that this method is applicable to more than one redox enzyme.

6.5. References

1 A. Volbeda, P. Amara, C. Darnault, J.-M. Mouesca, A. Parkin, M. M. Roessler, F. A. Armstrong and J. C. Fontecilla-Camps, *Proc Natl Acad Sci U S A*, 2012, **109**, 5305–10.

2 A. Volbeda, C. Darnault, A. Parkin, F. Sargent, F. A. Armstrong and J. C. Fontecilla-Camps, *Structure*, 2013, **21**, 184–190.

3 S. Frielingsdorf, T. Schubert, A. Pohlmann, O. Lenz and B. Friedrich, *Biochemistry*, 2011, **50**, 10836–10843.

4 M. Brugna-Guiral, P. Tron, W. Nitschke, K.-O. Stetter, B. B. Burlat, B. Guigliarelli, M. Bruschi, M.-T. T. Giudici-Orticoni, B. Mireille and M.-T. T. Giudici-Orticoni, *Extremophiles*, 2003, **7**, 145–157.

5 M. E. Pandelia, V. Fourmond, P. Tron-Infossi, E. Lojou, P. Bertrand, C. Léger, M. T. Giudici-Orticoni and W. Lubitz, *J Am Chem Soc*, 2010, **132**, 6991–7004.

6 R. M. Evans, E. J. Brooke, S. A. M. Wehlin, E. Nomerotskaia, F. Sargent, S. B. Carr, S. E. V. Phillips and F. A. Armstrong, *Nat Chem Biol*, 2016, **12**, 46–50.

7 K. Hatzixanthis, T. Palmer and F. Sargent, *Mol Microbiol*, 2003, **49**, 1377–1390.

8 R. Hidalgo, D.Phil. thesis, University of Oxford, 2016.

9 B. Bleijlevens, F. A. van Broekhuizen, A. L. de Lacey, W. Roseboom, V. M. Fernandez and S. P. J. Albracht, *J. Biol. Inorg. Chem.*, 2004, **9**, 743–52.

10 A. Volbeda, L. Martin, E. Barbier, O. Gutiérrez-Sanz, A. L. de Lacey, P.-P. Liebgott, S. Dementin, M. Rousset and J. C. Fontecilla-Camps, *J. Biol. Inorg. Chem.*, 2015, **20**, 11–22.

11 C. Fichtner, C. Laurich, E. Bothe and W. Lubitz, *Biochemistry*, 2006, **45**, 9706–9716.

12 P. A. Ash, J. Liu, N. Coutard, N. Heidary, M. Horch, I. Gudim, T. Simler, I. Zebger, O. Lenz and K. A. Vincent, *J. Phys. Chem. B*, 2015, **119**, 13807–13815.

13 M. Saggu, I. Zebger, M. Ludwig, O. Lenz, B. Friedrich, P. Hildebrandt and F. Lendzian, *J. Biol. Chem.*, 2009, **284**, 16264–16276.

14 G. Davidson, S. B. Choudhury, G. Zhijie, K. Bose, W. Roseboom, S. P. J. Albracht and M. J. Maroney, *Biochemistry*, 2000, **39**, 7468–7479.

15 A. L. de Lacey, E. C. Hatchikian, A. Volbeda, M. Frey, J. C. Fontecilla-Camps and V. M. Fernandez, *J Am Chem Soc*, 1997, **119**, 7181–7189.

16 H. Tai, L. Xu, K. Nishikawa, Y. Higuchi and S. Hirota, *Chem. Commun.*, 2017, **53**, 10444–10447.

17 A. L. de Lacey, V. M. Fernández, M. Rousset and R. Cammack, *Chem Rev*, 2007, 107, 4304–4330.

18 T. Krämer, M. Kampa, W. Lubitz, M. van Gastel and F. Neese, *ChemBioChem*, 2013, **14**, 1898–1905.

Chapter 7. Redox characterisation of O_2-sensitive Hyd-2

Following development of the IR microspectroscopic-electrochemical technique and its use in characterising single crystals of *E. coli* hydrogenase-1, this Chapter delves into the IR spectroelectrochemical study of crystals of a different [NiFe]-hydrogenase: O_2-sensitive *E. coli* hydrogenase-2.

7.1. Introduction

Escherichia coli synthesises two periplasmic membrane-bound [NiFe]-hydrogenases: Hyd-1 and Hyd-2. The redox behaviour of the O_2-tolerant Hyd-1 has been thoroughly described using IR spectroelectrochemical methods as demonstrated in Chapters 3-6 of this Thesis, in addition to other studies.[1–3] Hyd-2 has been independently characterised by IR spectroscopy[4,5] and protein film infrared electrochemistry.[6] Due to its ease of crystallisation, coupled with its previous spectroscopic characterisation, Hyd-2 is a convenient second metalloenzyme to investigate using the single crystal IR microspectroscopic-electrochemical technique.

The main differences between Hyd-1 and Hyd-2 lie in their sensitivity towards O_2 and their directional bias. Hyd-2 is a standard [NiFe]-hydrogenase which is reversibly inactivated in the presence of O_2. Furthermore, it can catalyse H^+ reduction under physiological conditions at potentials below the H_2/H^+ redox couple (-353 mV *vs* SHE at pH 6, 298 K). As such, the distribution of the active site redox states present at low potentials under catalytic turnover conditions in Hyd-2 is very different to those found in Hyd-1 (Chapter 3, Section 3.2.3).

Chung performed the first in depth IR spectroelectrochemical characterisation of Hyd-2 using the PFIRE technique.[6] Not only were multiple active site redox states identified for Hyd-2, along with their characteristic ν_{CO} and ν_{CN} bands (Table 7.1), but confirmation of the catalytic relevance of each redox state was provided. However, one noticeable missing feature from the spectra was evidence of the Ni_a-L species. This is in sharp contrast to Hyd-1, where multiple Ni_a-L species are observed under non-turnover and turnover conditions in conjunction with its tautomer Ni_a-C. Nevertheless, this is not unexpected as

detecting Ni_a-L under ambient conditions in [NiFe]-hydrogenases is rare, with *E. coli* Hyd-1, *R. eutropha* RH and a R → K mutant of *P. furiosus* SH1 being the known exceptions.[7,8]

Table 7.1 Previously observed ν(CO) and ν(CN) IR bands for the various active site redox species of *E. coli* Hyd-2, as measured by PFIRE and IR spectroscopy under different gases.

Redox species	**Wavenumber / cm^{-1}**			
	PFIRE[j] (Chung)[6,9]		**FTIR[k] (Senger *et al*)[5]**	
	ν(CO)	**ν(CN)**	**ν(CO)**	**ν(CN)**
Ni-B	1957	2092, 2081	1957	2092, 2082
Ni-SI_r	1937[l]	n.d.	n.d.	n.d.
Ni_a-SI	1946	2086, 2075	1945	2084, 2070
Ni-SCO	1944, 2055[m]	2083, 2073	1944, 2054[m]	2084, 2073
Ni_a-C	1964	n.d.	1966	2088, 2078
Ni_a-L	n.d.	n.d.	1911	2062, 2052
Ni_a-R_I	1954	2060, n.d.	1950	2076, 2062
Ni_a-R_{II}	n.d.	n.d.	1936	2068, 2053
Ni_a-R_{III}	n.d.	n.d.	1927	2063, 2047

Hyd-2 has also been analysed by *in situ* FTIR spectroscopy in the presence of different gases.[5] As shown in Table 7.1, the majority of the ν_{CO} and ν_{CN} IR bands observed by Stripp and co-workers align with those recorded using PFIRE. Previously unseen IR bands were also detected, thought to represent Ni_a-R sub-species as they appeared upon treating as-isolated enzyme solution with H_2. When Hyd-2 was treated with O_2, the inactive Ni-B

[j] Measured at pH 6
[k] Measured at pH 8
[l] Observed in redox-triggered difference spectra measured at pH 7
[m] 2055 and 2054 cm^{-1} bands correspond to the bridging CO

species was observed. Notably, subtracting the IR spectrum of as-isolated Hyd-2 from this oxygenated spectrum, not only demonstrated the expected loss of Ni_a-C and Ni_a-SI, but also loss of a very low absorbance, low wavenumber ν_{CO} band at 1911 cm^{-1}. Based on the frequency of this band, they hypothesised that it represented the Ni_a-L state. This is the only case where the 1911 cm^{-1} Ni_a-L species is detected in this study. IR spectra recorded under other gas-treated conditions did not show its presence, even when the Ni_a-C species was. Thus a more rigorous analysis of Hyd-2 is required to confirm the identity of the low frequency species.

In this Chapter the single crystal IR microspectroscopic-electrochemical technique developed in Chapter 4 is used to probe the redox chemistry of crystalline Hyd-2. Subsequently, low temperature transmission IR spectroscopy is performed on a frozen solution of reduced Hyd-2 under light and dark conditions to see whether illumination of the Ni_a-C state in Hyd-2 results in the formation of Ni_a-L.

7.2. Single crystal IR spectroelectrochemical characterisation

Figure 7.1 presents the baseline-corrected IR spectra of a single crystal of Hyd-2 at pH 5.9 recorded at specific potentials corresponding to those at which each active site redox species is maximised. As with previous data analysis, peak assignment was aided by reference to the 2nd derivative spectra. For the data presented in Figure 7.1, only the ν_{CN} bands that were easily distinguishable in the 2nd derivative spectra are labelled.

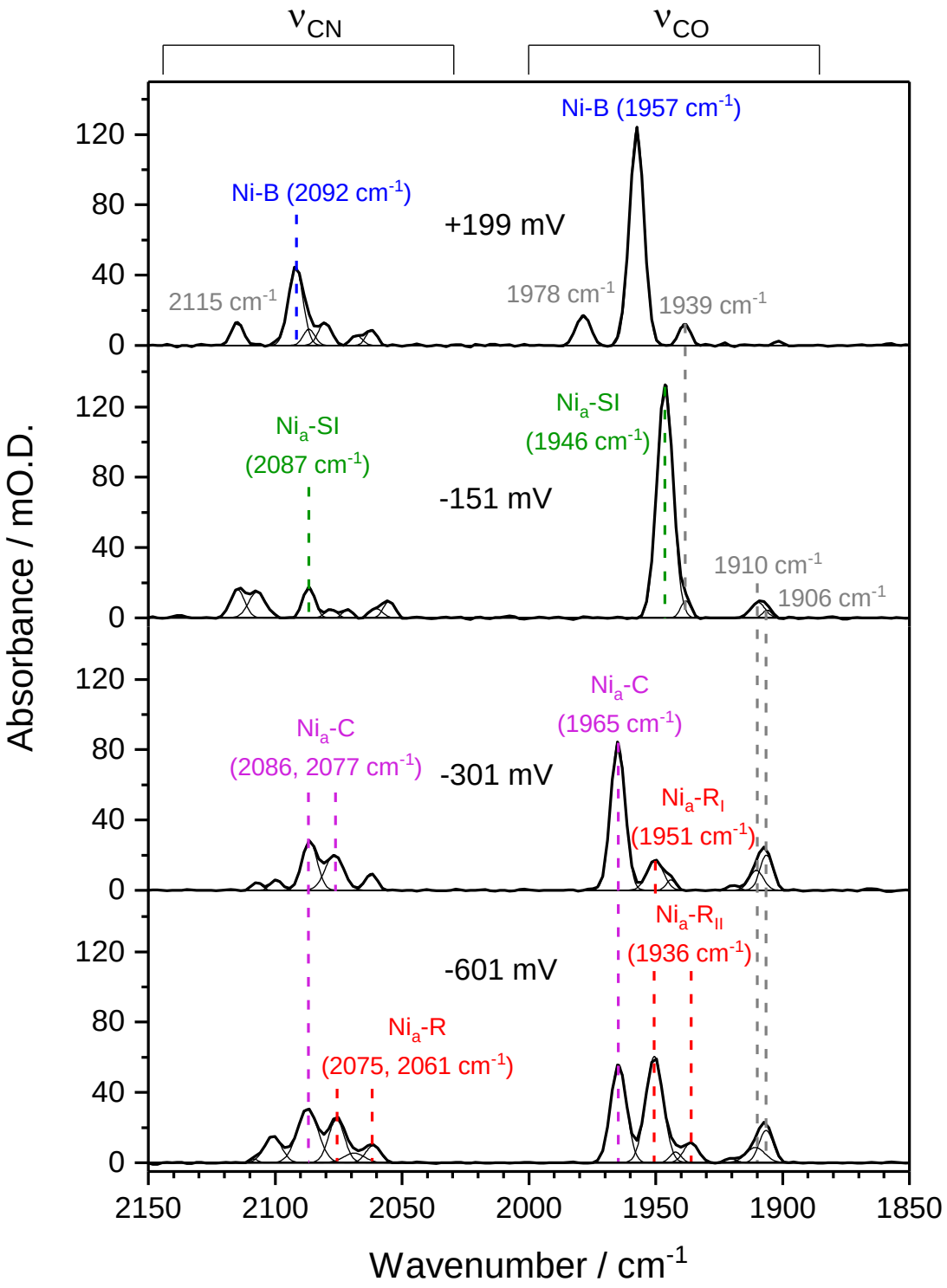


Figure 7.1 Baseline-corrected IR spectra of a single crystal of Hyd-2 at pH 5.9, poised at selected potentials which reflect those where the maximum intensity for each active site redox species is observed during the redox titration. Dashed lines mark the wavenumber positions of the intrinsic ν_{CO} and ν_{CN} bands of the Hyd-2 active site redox states. Bands in grey are unassigned. Fitted Gaussian peaks are shown by the thin black curves.

There are five bands visible in the ν_{CO} region of the IR spectrum recorded at -601 mV indicating five different active site redox species are present. Ni_a-C and Ni_a-R are expected to be detected in an equally large proportion at low potentials. This is a result of Hyd-2 catalysing H^+ reduction, resulting in partial oxidation of Ni_a-R to Ni_a-C. As such the high wavenumber 1965 cm^{-1} band can be assigned to the Ni_a-C state, with the peaks at 1951 cm^{-1} and 1936 cm^{-1} representing two sub-species of Ni_a-R (Ni_a-R_I ν_{CO} = 1951 cm^{-1}; Ni_a-R_{II} ν_{CO} = 1936 cm^{-1}). The remaining two bands detected at -601 mV are at 1910 and 1906 cm^{-1}. Low wavenumber ν_{CO} bands are usually associated with Ni(I) species such as Ni_a-L.

Moving to -301 mV shows an increase in the 1965 cm^{-1} and decrease in the bands at 1951 and 1936 cm^{-1}. This corroborates their assignments as the Ni_a-C and Ni_a-R states respectively as stepping to more oxidative potentials results in the oxidation of the Ni_a-R species to Ni_a-C. The low wavenumber bands also experience a minor increase in absorbance, suggesting they represent an active site state which also forms a result of Ni_a-R oxidation.

At -151 mV, a new ν_{CO} band appears at 1946 cm^{-1}. This is accompanied by loss of the Ni_a-C bands and decrease in the absorbances of the peaks at 1910 and 1906 cm^{-1}. Therefore, the 1946 cm^{-1} band can be assigned to the Ni_a-SI species as it forms from the oxidation of the Ni_a-C state.

Finally, at the highest potential, a large peak at 1957 cm^{-1} is detected along with two low intensity bands at 1978 and 1939 cm^{-1}. The most oxidised redox state, the inactive Ni-B, is expected to form at this potential and thus the intense band at 1957 cm^{-1} can be assigned as this species. The identities of the low absorbance bands are more difficult to assign as usually only Ni-B is formed at high potential. As the spectra displayed in Figure 7.1 was collected after complete activation of Hyd-2 *via* electrochemical reduction, no slowly

activating inactive redox species such as Ni-A are expected to be present upon subsequent re-oxidation of the sample. This illustrates that the ν_{CO} bands at 1978 and 1939 cm^{-1} most likely represent new high potential active site species.

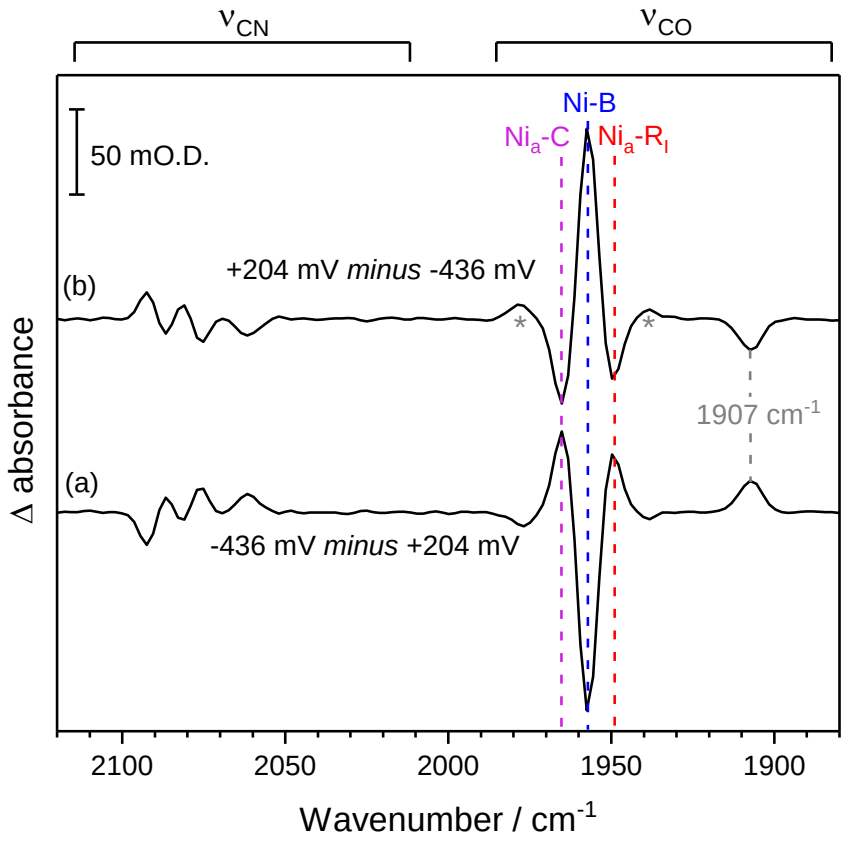


Figure 7.2 A: Reduced *minus* oxidised difference spectrum following a potential step from +204 mV to -436 mV, and B: re-oxidised *minus* reduced difference spectrum following an oxidative potential step back to +204 mV from -436 mV. Grey asterisks represent the minor ν_{CO} bands at 1978 and 1939 cm^{-1} observed at high potential.

The presence of low wavenumber ν_{CO} bands in the low potential spectra of crystalline Hyd-2 is unexpected as no equivalent species were detected in the PFIRE studies performed by Chung.[6] Formation of this low wavenumber species is reversible, as shown in Figure 7.3, indicating that it represents a 'real' species produced in response to a change in potential. It is possible that this band indicates the presence of the Ni_a-L state. If this is

the case, then illumination of the Ni_a-C species at low temperatures should show conversion between the Ni_a-C and this low wavenumber species.

7.3. Investigating a new low wavenumber ν_{CO} species

Low wavenumber ν_{CO} bands are often assigned to the Ni_a-L species in [NiFe]-hydrogenases. The low valence Ni(I), lack of bridging ligand and predicted metal-metal bond between the Ni and Fe results in delocalisation of electron density onto the Fe.[10] This in turn increases the degree of π-back bonding, therefore decreasing the wavenumber of the ν_{CO} IR bands (Equation 2.3). Ni_a-L species have been observed across a range of standard and O_2-tolerant [NiFe]-hydrogenases, with some showing multiple Ni_a-L sub-species and others merely one.[1,11–14] Initially, these species were only observed upon illumination of the Ni_a-C species under cryogenic conditions and thus not thought to be catalytically relevant.[11,14,15] Whilst the involvement of the Ni_a-L state as an intermediate in the Ni_a-C / Ni_a-SI transition has since been elucidated,[1,16] low temperature illumination of the Ni_a-C state remains a convenient way to establish whether a [NiFe]-hydrogenase can form Ni_a-L species.

Figure 7.3 presents the light difference IR spectrum of H_2-reduced Hyd-2 solution at 110 K. The spectra are presented as light *minus* dark, i.e. with and without illumination. Difference spectra calculated from both unprocessed and baseline-corrected IR spectra are shown. The negative peaks at 1965 cm^{-1} and 2089, 2079 cm^{-1} correspondingly represent the ν_{CO} and ν_{CN} bands of Ni_a-C. These align with the IR bands assigned as Ni_a-C using the PFIRE technique and *in crystallo* (Table 7.1, Figure 7.1). The positive peaks at 1914 cm^{-1} and 2064, 2048 cm^{-1} represent a different active site redox species that appears alongside the loss of Ni_a-C, namely the Ni_a-L species. Importantly, no other active site

redox species are detected in the IR difference spectrum, implying that illumination of only the Ni_a-C state results in the formation of Ni_a-L.

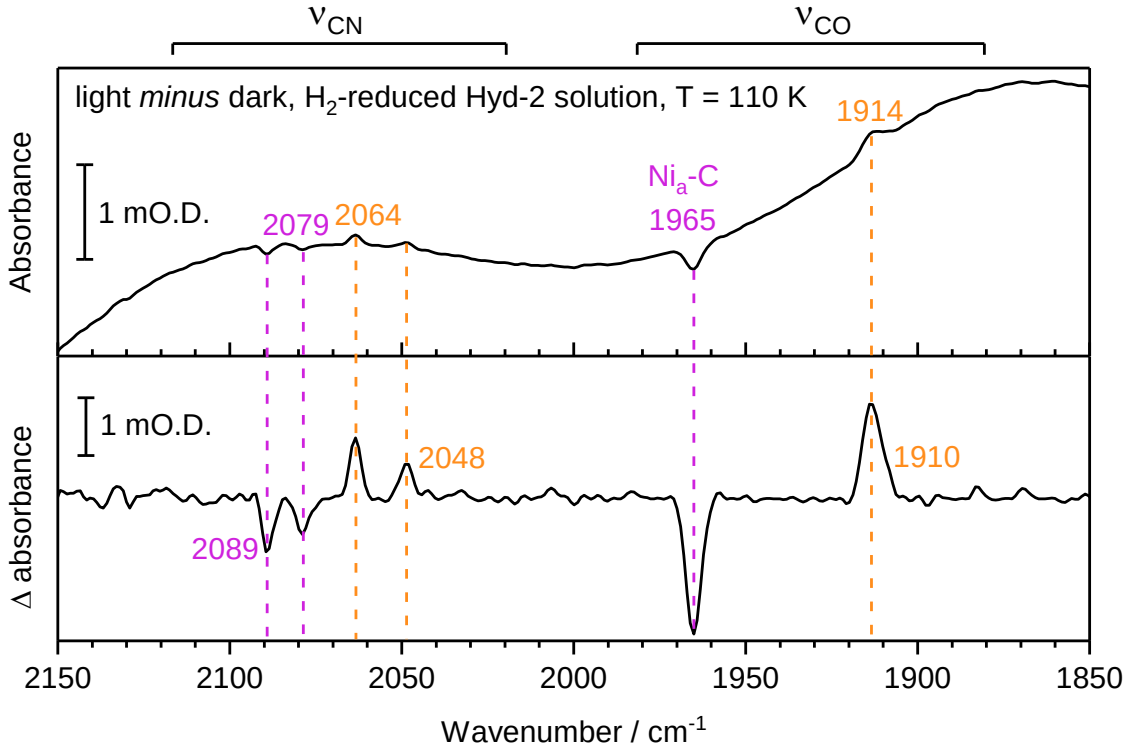


Figure 7.3 Light-induced transition between Ni_a-C and Ni_a-L in Hyd-2 at 110 K. Difference spectra presented as light minus dark. Bands representing the Ni_a-C species are in purple whereas those representing Ni_a-L are in yellow. Top: Difference spectrum calculated from unprocessed IR spectra. Bottom: Difference spectrum calculated from baseline-corrected IR spectra. Gaussian peak fitting shows an additional peak at 1910 cm^{-1} not visible in the unprocessed spectrum but is labelled in the spectrum alongside the yellow dotted line indicating the peak at 1914 cm^{-1} is still present.

In the single crystal IR spectra of Hyd-2, Gaussian peak fitting indicated that the ν_{CO} band centred at 1907 cm^{-1} was actually composed of two low wavenumber peaks at 1910 and 1906 cm^{-1}. Similarly, Gaussian peak fitting suggests the positive peak at 1914 cm^{-1} in the light-triggered difference spectrum of frozen Hyd-2 solution contains a small shoulder at 1910 cm^{-1}. Multiple Ni_a-L sub-species are known to exist in other [NiFe]-hydrogenases. It is possible that the total of three Ni_a-L bands (1914, 1910 and 1906 cm^{-1}) observed in the

frozen solution and in the single crystal represent the three Ni_a-L species. However, usually the ν_{CO} bands for sub-species differ by approximately 10 cm^{-1} (e.g. 1877 and 1867 cm^{-1} Ni_a-L species for Hyd-1) and thus it is difficult to tell whether it is an exception in Hyd-2.

Nevertheless, this experiment has indicated that like other [NiFe]-hydrogenases, Ni_a-C is shown to convert to a Ni_a-L species upon illumination under cryogenic conditions in Hyd-2.

7.4. Discussion and summary

Performing a preliminary IR spectroelectrochemical characterisation of single crystals of Hyd-2 has shown that all active site redox species present in solution and electrode absorbed are also obtainable within the crystalline state (Table 7.2). Furthermore new information regarding the active site redox species present in Hyd-2 have been revealed. Most notable is the appearance of two low wavenumber species at potentials corresponding the Ni_a-C redox level. Further study through comparing IR spectra collected on frozen Hyd-2 solution under dark and light conditions supports the assignment of the ν_{CO} band at 1914 cm^{-1} as the Ni_a-L redox state. Multiple low wavenumber ν_{CO} bands have been detected, hypothesised to represent multiple sub-species of Ni_a-L as seen in other [NiFe]-hydrogenases including standard [NiFe]-hydrogenases. A much deeper analysis of the behaviour of these species is required to confirm this.

As it has been established that proton transfer equilibria are maintained with the crystal, changing the pH of the Hyd-2 crystals should influence the relative distributions of the Ni_a-C and Ni_a-L species, as was observed in Hyd-1 (Chapter 5). Therefore it would be beneficial to repeat the electrochemical redox titrations on single crystals of Hyd-2 at higher and lower pH. This would allow further confirmation of the low wavenumber species in Hyd-2 as Ni_a-L.

Table 7.2 Wavenumber positions of the ν(CO) and ν(CN) bands for each of the identified active site redox species observed in Hyd-2 solution and single crystals, measured at pH 5.9. n.d. signifies that no band was detected.

Redox species	Wavenumber / cm^{-1}	
	ν(CO)	**ν(CN)**
Ni-B	1957	2092, n.d.
Ni_a-SI	1946	2087, n.d.
Ni_a-C	1964	2086, 2077
Ni_a-L	1914[n], 1910[n,o], 1906[o]	2064, 2048
Ni_a-R_I	1951	2075, 2061
Ni_a-R_{II}	1936	n.d.
Ni_a-R_{III}	n.d.	n.d.

It is important to emphasise that the observation of a Ni_a-L species in single crystals and frozen solution does not mean it is catalytically relevant in Hyd-2. Neither method used in this Chapter allow simultaneous control over catalytic activity, unlike the PFIRE technique, and thus the species is not generated under turnover conditions.

In Chapter 4, the single crystal IR microspectroscopic-electrochemical technique was used to monitor the equilibration of the redox states upon application of a small potential step where the Ni_a-C / Ni_a-SI transition occurs to show that Ni_a-L directly converts to the Ni_a-SI state. It was then proposed that O_2-tolerant [NiFe]-hydrogenases undergo stepwise proton-coupled electron transfer during the Ni_a-C / Ni_a-SI transition, with the Ni_a-L species acting as an intermediate, whereas O_2-sensitive [NiFe]-hydrogenases proceed by

[n] Observed upon illumination of Ni_a-C at low temperatures
[o] Observed in single crystals at pH 5.9

concerted PCET (Section 4.4). As Ni_a-L has been identified in single crystals of Hyd-2, an O_2-sensitive [NiFe]-hydrogenase, performing a similar experiment would show the involvement or lack of involvement of the Ni_a-L in the PCET Ni_a-C / Ni_a-SI transition.

7.5. References

1 R. Hidalgo, P. A. Ash, A. J. Healy and K. A. Vincent, *Angew. Chem., Int. Ed.*, 2015, **54**, 7110–7113.

2 P. A. Ash, S. E. T. Kendall-Price and K. A. Vincent, *Acc Chem Res*, 2019, **52**, 3120–3131.

3 P. A. Ash, S. E. T. Kendall-Price, R. M. Evans, S. B. Carr, A. R. Brasnett, S. Morra, J. S. Rowbotham, R. Hidalgo, A. J. Healy, G. Cinque, M. D. Frogley, F. A. Armstrong and K. A. Vincent, *Chem Sci*, 2021, **12**, 12959–12970.

4 L. Forzi, P. Hellwig, R. K. Thauer and R. G. Sawers, *FEBS Lett*, 2007, **581**, 3317–3321.

5 M. Senger, K. Laun, B. Soboh and S. T. Stripp, *Catalysts*, 2018, **8**, 530.

6 M.-W. Chung, D.Phil. thesis, University of Oxford, 2015.

7 M. Saggu, I. Zebger, M. Ludwig, O. Lenz, B. Friedrich, P. Hildebrandt and F. Lendzian, *J. Biol. Chem.*, 2009, **284**, 16264–16276.

8 G. E. Vansuch, C. H. Wu, D. K. Haja, S. A. Blair, B. Chica, M. K. Johnson, M. W. W. Adams and R. B. Dyer, *Chem Sci*, 2020, **11**, 8572–8581.

9 S. v. Hexter, M. W. Chung, K. A. Vincent and F. A. Armstrong, *J Am Chem Soc*, 2014, **136**, 10470–10477.

10 M. Kampa, M. E. Pandelia, W. Lubitz, M. van Gastel and F. Neese, *J Am Chem Soc*, 2013, **135**, 3915–3925.

11 H. Tai, K. Nishikawa, S. Inoue, Y. Higuchi and S. Hirota, *J Phys Chem B*, 2015, **119**, 13668–13674.

12 B. L. Greene, C. H. Wu, P. M. McTernan, M. W. W. Adams and R. B. Dyer, *J Am Chem Soc*, 2015, **137**, 4558–4566.

13 P. A. Ash, R. Hidalgo and K. A. Vincent, *ACS Catal*, 2017, **7**, 2471–2485.

14 M. E. Pandelia, H. Ogata and W. Lubitz, *ChemPhysChem*, 2010, **11**, 1127–1140.

15 S. Foerster, M. Stein, M. Brecht, H. Ogata, Y. Higuchi and W. Lubitz, *J Am Chem Soc*, 2003, **125**, 83–93.

16 B. L. Greene, C. H. Wu, G. E. Vansuch, M. W. W. Adams and R. B. Dyer, *Biochemistry*, 2016, **55**, 1813–1825.

Chapter 8. Conclusions and Outlook

The work presented in this Thesis has utilised two IR spectroelectrochemical approaches for studying the catalytic mechanism of an O_2-tolerant and standard [NiFe]-hydrogenases. This has not only revealed new insight into H^+/H_2 catalysis by [NiFe]-hydrogenases, but also shown the benefit of utilising different methods to build a comprehensive understanding of complex metalloenzymes.

The protein film infrared electrochemical technique was utilised to study the catalytic behaviour of Hyd-1 in Chapter 3. New active site redox species were identified: Ni_a-C^+, a protonated variant of Ni_a-C; Ni_a-R_I, a sub-species of the most reduced active site redox state; and Ni-X, a Ni-B like redox species where the proximal cluster is superoxidised. IR spectra recorded under turnover conditions in the presence of substrate were confirmed to be free of mass transport limitations which was a concern with previous PFIRE studies. Furthermore, a comparison of the steady-state distributions of the active site redox level present under turnover conditions provided new insight into the differences in standard and O_2-tolerant [NiFe]-hydrogenases. The Ni_a-C / Ni_a-SI transition was shown to be the rate limiting step in standard [NiFe]-hydrogenases, such as Hyd-2, whereas for O_2-tolerant hydrogenases, the predominance of the Ni_a-R species across all potentials demonstrated that the Ni_a-R / Ni_a-C transition is rate determining. Overall, this demonstrates that assuming a general catalytic mechanism for [NiFe]-hydrogenases is flawed.

In Chapter 4, the single crystal IR microspectroscopic-electrochemical technique was developed and improved. This allowed a full IR spectroelectrochemical redox characterisation of single crystals of Hyd-1 to be performed. The method demonstrated

that complete electrochemical control over the active site *in crystallo* is possible, and that protein crystals can be viewed as a dynamic system. Both electron transfer redox equilibria and proton transfer equilibria are unperturbed in the crystalline state, as established in Chapter 5. Moreover, the precise potential control obtained by the IR microspectroscopic-electrochemical technique allows single crystals to be poised at specific potentials to generate crystals with well-defined redox states. This is significant as it provides a more rational approach for obtaining structures of catalytic intermediate species. A current example of this is the work continued within the Vincent group at the University of Oxford, where the crystal structures of electrochemically poised crystals at the Ni_a-R, Ni_a-SI and Ni-B have been obtained for *E. coli* Hyd-1 and Hyd-2 (manuscript in preparation).

Another important feature of the IR microspectroscopic-electrochemical technique described in Chapter 4 is its ability to resolve reaction steps without needing sub-turnover frequency time resolution. Proton transfer steps are demonstrated to be retard in comparison to electron transfer, resulting in new information regarding the Ni_a-L / Ni_a-SI transition in Hyd-1 to be obtained: sequential proton followed by electron transfer steps are observed in Hyd-1 (Figure 8.1).

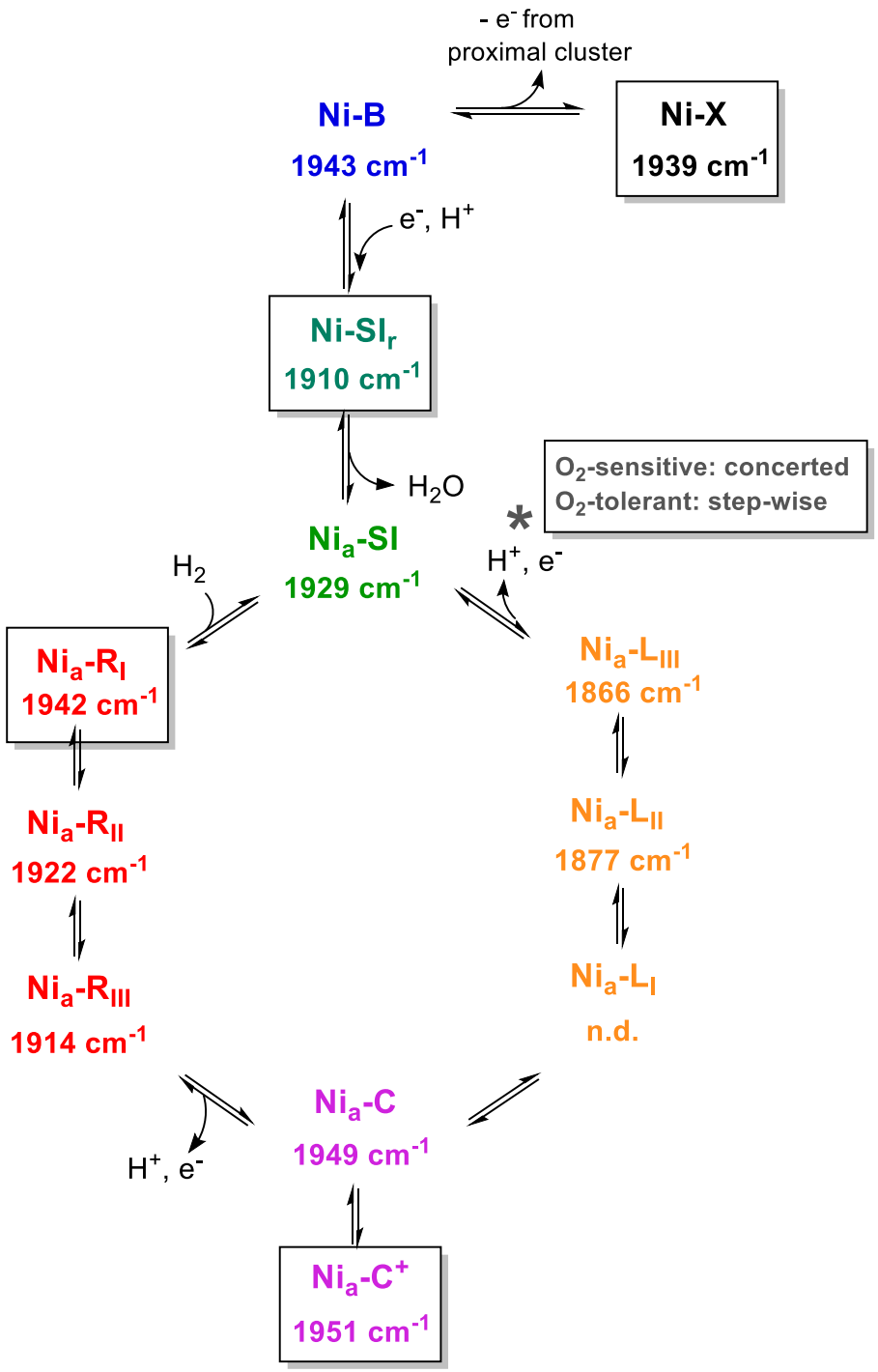


Figure 8.1 An updated outline catalytic mechanism of [NiFe]-hydrogenases based on the work in this Thesis. New active site redox species observed are highlighted in boxes. The grey asterisk marks the proton-coupled electron transfer step whose mechanism is different for O_2-tolerant and O_2-sensitive [NiFe]-hydrogenases. The ν_{CO} bands for each active site redox state observed in single crystals of the O_2-tolerant *E. coli* Hyd-1 are noted for reference.

Work in Chapter 6 demonstrated that the redox behaviour of preparations of Hyd-1 with different sub-unit compositions is inconsistent in the crystalline state. When the redox transfer sub-unit, cytochrome *b*, was present in Hyd-1 crystals, a new active site redox species was observed, assigned as the inactive, 'ready' Ni-SI_r state (Figure 8.1). This species is an intermediate in the inactivation of [NiFe]-hydrogenase and thus being able to access it in the crystal will now allow the Ni_a-SI → Ni-B transition to be monitored in finer detail. Furthermore, Chapter 6 highlighted the importance of utilising a second method to confirm the redox states present in metalloenzyme crystals, aside from x-ray crystallography.

The application of the single crystal IR microspectroscopic-electrochemical technique to a different [NiFe]-hydrogenase was demonstrated in Chapter 7. An electrochemical redox titration of single crystals of *E. coli* Hyd-2 revealed the presence of a low wavenumber active site species at the same redox level as Ni_a-C. Low temperature light-triggered IR spectra were measured to confirm the identity of the low wavenumber species as Ni_a-L. This is significant as the Ni_a-L species had not previously been conclusively identified in Hyd-2. The prospect of the Ni_a-C / Ni_a-SI transition to be investigated using the single crystal IR microspectroscopic-electrochemical technique in Hyd-2 is promising and could lead to confirmation on whether this transition is a step-wise proton coupled electron transfer step in standard [NiFe]-hydrogenases.

The main highlight of this Thesis has been the development of the single crystal IR microspectroscopic-electrochemical technique and its value in investigating the catalytic mechanisms of metalloenzymes, [NiFe]-hydrogenases in particular. This technique has already been extended to crystals of *C. pasteurianum* [FeFe]-hydrogenase I, emphasising its applicability to different metalloenzymes.[1] Other possible candidates for analysis

include molybdenum nitrogenases, where a CO bound structure has been reported to open up the molybdenum iron active site,[2] but comparison to the multiple CO-inhibited states observed in stopped-flow studies has not yet been attempted.[3]

This approach is not necessarily unique to metalloenzymes. There is plenty of scope for the technique to be utilised in studying the mechanisms of organometallic catalysts. *In crystallo* organometallic chemistry is well established,[4] and thus the single crystal IR microspectroscopic-electrochemical technique could provide a method for comparing crystalline-phase and solution reactivity.

1 S. Morra, J. Duan, M. Winkler, P. A. Ash, T. Happe and K. A. Vincent, *Dalton Trans.*, 2021, **50**, 12655–12663.

2 T. Spatzal, K. A. Perez, O. Einsle, J. B. Howard and D. C. Rees, *Science (1979)*, 2014, **345**, 1620–1623.

3 S. J. George, G. A. Ashby, C. W. Wharton and R. N. F. Thorneley, *J Am Chem Soc*, 1997, **119**, 6450–6451.

4 K. A. Reid and D. C. Powers, *Chem Comm*, 2021, **57**, 4993–5003.